

# UNIVERSITY OF CALABRIA

*Physics Department*

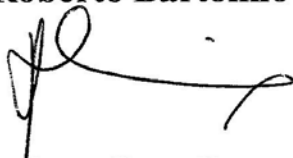
---

**BERNARDINO TELESIO-DOCTORAL SCHOOL  
IN  
“SCIENCE AND TECHNIQUE  
OF  
MESOPHASES AND MOLECULAR MATERIALS”  
“XXV° Cycle, 02/B3”**

***Micro Raman Spectroscopic Investigations on  
Soft Matter Systems***

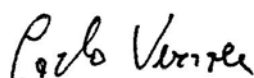
**School Director**

**Prof. Roberto Bartolino**



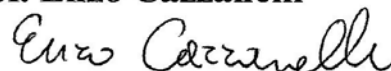
**Curriculum Coordinator**

**Prof. Carlo Versace**



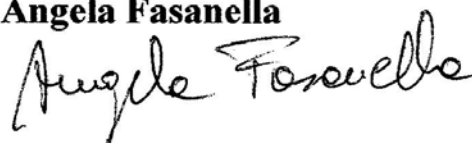
**Advisor**

**Prof. Enzo Cazzanelli**



**Ph.D Student**

**Angela Fasanella**



---

Academic Year 2011-2012

*To my FAMILY*

## TABLE OF CONTENTS

Introduction	1
Chapter 1 <i>Soft Matter</i>	4
1.1    Definition of Soft Matter	5
1.2    The features of Soft Matter systems	6
1.3    Biological Soft Matter systems	7
1.4    Chemical Soft Matter systems	10
1.5    Nanoparticles	15
1.6    Soft Matter applications	17
1.7    References	19
Chapter 2 <i>Liquid crystals and biological objects</i>	21
2.1    Nematic Liquid Crystals	22
2.2    Physical Chemistry properties of nematic liquid crystal	26
2.3    Lyotropic Liquid Crystals	29
2.4    Biological Membrane Protein	33
2.5    Mimetic models	35
2.6    Liquid Crystalline Composite Materials	36
2.7    References	38

Chapter 3	<i>Raman spectroscopy</i>	42
3.1	Raman Scattering	43
3.1.1	Raman effect	43
3.1.2	Quantum approach	46
3.1.3	Intensity of Raman scattered radiation	56
3.1.4	Raman Scattering in Solid	62
3.1.5	Raman Scattering in Polymer	65
3.2	Surfaces Enhanced Raman Spectroscopy	65
3.2.1	Fundamentals on SERS	66
3.2.1.a	Electromagnetic enhancement	67
3.2.1.b	Chemical enhancement	68
3.2.2	Substrates	70
3.3	Raman Microprobe equipment	70
3.4	References	76
Chapter 4	<i>Results And Discussion</i>	78
4.1	Raman spectroscopy on G1 ligand and GPR30 receptor	79
4.1.1	Solvent	80
4.1.2	The ligand G-1	89
4.1.3	Endogenous Receptor GPR30	91
4.1.4	Conclusions	95



4.2 Thermal structural evolutions of 1,2-dimyristoyl-sn-glycero-3-phosphatidylcholine (DMPC)-water systems investigated by micro-Raman Spectroscopy	96
4.2.1 Experimental	97
4.2.2 Discussion	98
4.2.3 Conclusions	105
4.3 Polarized Micro-Raman investigation of E7 liquid crystal in POLICRYPS	106
4.3.1 Experimental	107
4.3.2 Discussion	108
4.3.3 Conclusions	119
4.4 Thermal evolution of tungsten trioxide thin film obtained by sol gel deposition	121
4.4.1 Film preparation	122
4.4.2 Raman Spectroscopy	122
4.4.3 Discussion	122
4.4.4 Conclusions	131
4.5 Micro-Raman investigation on oil painting “Rebecca at the well”	133
4.5.1 Experimental	133
4.5.2 Discussion	135
4.5.3 Conclusions	146
4.6 References	148

Chapter 5	<i>Selected Publications</i>	159
	<i>In Molecular orientation of E7 liquid crystal in POLICRYPS holographic gratings: a micro-Raman spectroscopic analysis.</i>	160
	<i>In situ polarized micro-Raman investigation of periodic structures realized in liquid-crystalline composite materials.</i>	169
	<i>Raman scattering enhancement associated to sodium oxide formation after thermal treatment of glass substrates.</i>	177
	<i>Micro-spectroscopic Raman investigation on the canvas oil painting “Rebecca at the well”, of Neapolitan anonymous</i>	181
Chapter 6	<i>General Conclusions and Perspectives</i>	187

# **INTRODUCTION**

The importance of soft matter as a major class of materials and the increasing power of Raman spectroscopy as a characterization technique capable of questioning matter on the molecular level, is the main aim of this work.

Soft matter is a complex and flexible class of matter sometimes called as “complex fluids”. To the soft matter class belong many “kinds” of materials which includes: polymers, colloids, liquid crystals, emulsions, foams, biological tissues, proteins and so on. Very mild chemical or conformational changes in their structures can induce strong change in the physical chemistry properties of the soft matter systems: mechanical, optical and electrical changes.

At the same time Raman spectroscopy resulted to be a very useful techniques to obtain deeper chemical and physical information with regard the investigated materials. It do not need particular sample preparation and it can be usefully applied in biological systems since it is not affected by the water presence. By using the surfaces enhanced Raman spectroscopy, in the last years, Raman characterization, has been successfully performed on single molecular systems or thin films systems.

Raman spectroscopy results to be a non destructive technique that can be used for in-situ analysis and these features make it to be, in opinion of the writer, the best technique to be used to characterize soft materials systems which, as said above, are materials that can change their properties in a drastic way as answer to weak external perturbative action.

In this work, Raman spectroscopy has been used to characterize soft matter systems such as:

- *nematic liquid crystal (E7)*, in composite device with huge technological applications, i.e. ranging to holographic gratings to metamaterials systems,
- *endogenous receptor protein GPR30*, important for the breast cancer research.
- *DMPC*, a synthetic phospholipid important to make model biological membranes (biomimetic systems).

In addition, a new substrate to be used for surface enhance Raman spectroscopy has been found and studied.

The non-destructive technique has been also used to study the substances, much of them belonging to the soft matter class, present on a paint, in order to test the efficiency of this techniques as diagnostic tool for sample not made in the laboratory.

In the *Chapter 1* a brief overview regarding the soft matter has been shown. It is developed by starting from the definition of the soft matter, continues to the main properties and shows the main family of such systems.

In the *Chapter 2* the particular soft matter systems studied in work are shown. The fundamentals of liquid crystal, endogenous receptor protein, mimetic models and liquid crystalline composite materials are outlined.

In the *Chapter 3* Raman effect from both classical and quantum theories is shown. At the end of the chapter some aspect regarding the experimental set up can be found. In the paragraph 3.2 a basic introduction of the surface enhanced Raman spectroscopy is shown.

In the *Chapter 4* the research works made on the endogenous receptor protein, mimetic system, liquid crystal composite systems, new substrate for SERS and the paint are shown. All paragraphs are made introducing the scientific problematic, the experimental set-up and results and discussion and the relative conclusions.

In the *Chapter 5* the resulted publications are reported.

In the *Chapter 6* some general conclusions and perspective can be founds.

*Chapter 1*

**SOFT MATTER**

## 1.1 Definition of Soft Matter

The answer to the question: what is the matter? can be: “Objects that take up space and have mass are called matter”. The matter is usually classified as solid, liquid, gas or many mesophases taking into account the order degree, positional or orientational, of the particles that made the substances. Nevertheless, nowadays, matter can be, also, described as belonging to two different classes:

Hard Matter (which includes metals and ceramics)

Soft Matter.

While, it is quite right to state, based on the modern knowledge of the molecular theory, that many properties of hard matter are currently well understood, it cannot be said with regard to the soft matter [1]. Soft matter is, also, called *complex fluids* and it represents a novel subject of physics which involve materials such as:

- polymers,
- colloids,
- micelles/surfactants, emulsions: foams, soap solutions, liquid crystals, biological tissues (blood cells, cell membranes and proteins),
- other materials, i.e.: ink, paints, glassy materials, sponge.

De Gennes (Nobel Lecture) states that the soft matter is characterized by *complexity* and *flexibility* due to the “*unique*” molecular and supermolecular structures. The *complexity* can be explained, in certain primitive sense, in this way: thus as the modern biology has proceeded from studies on simple model systems (*bacteria*) to multicellular organisms (*plants, invertebrates, vertebrates, etc.*) the physics passed from the atomic physics studies (in the first half of XX century) to the studies of the *soft materials*.

To explain the *Flexibility* can be useful to remind a early polymer experiment made by the Indians of the Amazon basin. They collected the sap from the tree of *hevea* and let it “dry” for a short time on their foot. In this way, they have got boots.

From a physical chemistry point of view the sap is made by independent and flexible polymer chains that, after drying, and thanks to the oxygen of the atmosphere are bonded in bridges between the polymer chains passing from a liquid (sap) to a network structure which can resist to the tension called rubber. The experience of indians is quite amazing because, a very mild chemical action has induced a drastic change in the mechanical, optical, and electrical properties of the starting materials passing from the sap to the rubber; *this is a typical feature of soft matter* [2].

Matter organizes itself at many different length scales and into many different forms, each distinguished by its microscopic symmetries and dynamics. There are, for instance, non-crystalline states with various degrees of order, like liquid crystals or copolymer phases, and there are some states, glasses and gels, that are disordered but which act like solids.

Considering structural features, soft matter systems exhibit a structural ordering intermediate between that of crystalline solids and liquids, with a periodicity typically in the range between 1 - 1000 nm (ordered on nano-meso scales, respectively).

## 1.2 The features of Soft Matter systems

The main characteristics of soft matter systems are:

- Large length and time scales of motion of the constituent particles (nanoseconds to seconds, i.e. much larger than atomistic time scales femtoseconds).
- Soft Matter shows large response under external perturbation (Electric field, etc.).
- Behavior decided by entropic interactions; that is: large thermal fluctuations.
- Often very non-equilibrium systems: driven systems, active systems.

It is possible to expand a rubber band to double its size by applying relatively small forces, because the work is made against entropic forces, not against the forces originating from the chemical bond; the reorganization of the structure occurs at the macromolecular level instead of atomic length scales. In soft matter systems quantum mechanical effects and quantum fluctuations can be ignored because the effective

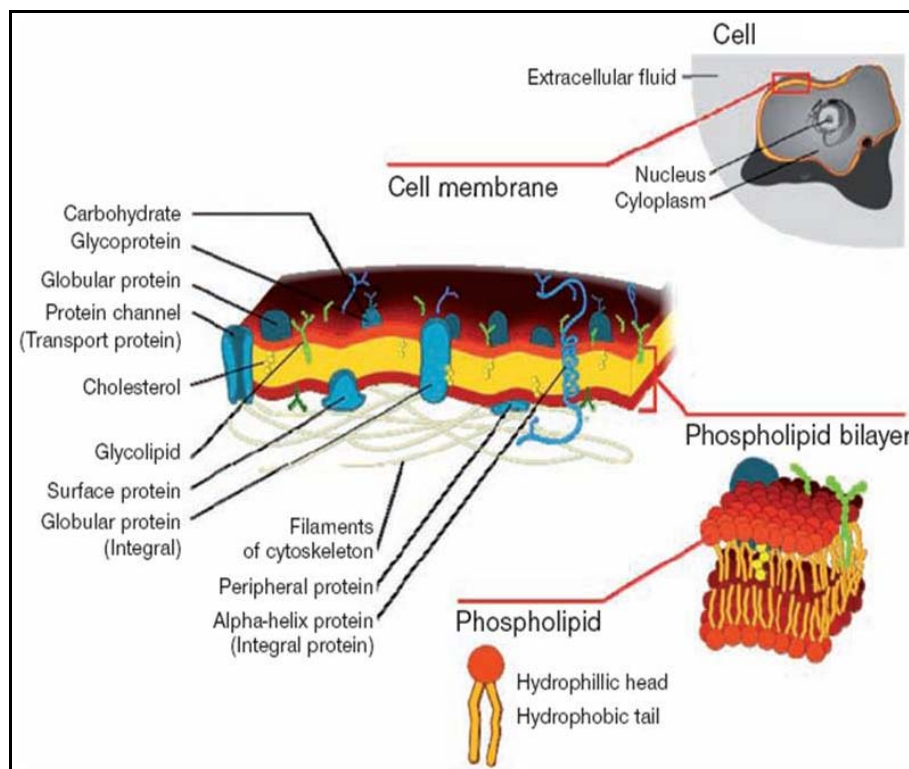


structure formed by constituent molecules is at length scales much larger than angstrom, in contrast to standard condensed systems, like metals and semiconductors.

### 1.3 Biological Soft Matter systems

The soft matter leads to many unique and exciting phenomena not seen in ordinary condensed phases, let alone the possibilities of novel technological applications. Even more exciting challenges concern applications of the soft matter physics to biological systems, especially to the biological soft matter such as proteins and membranes, which manifest, due to their low dimensional structures, unusual susceptibility to fluctuations and thus a variety of conformational transitions.

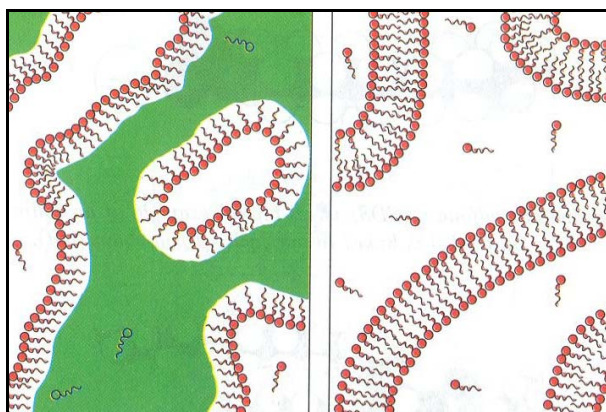
In order to identify the principle mechanism of a certain phenomenon soft matter scientist simplify and look at a model of a biological cell membrane whose picture is given in Fig. 1.3.1.



**Fig.1.3.1** Biological cell membrane model

A cell membrane is made by complex and large chemical molecules: the lipid molecules. A lipid molecule can be represented by a polar head, hydrophilic, from which emanates two aliphatic apolar tails, hydrophobic. So that, the head is surrounded by water and the cell membrane consists of two layers of lipid molecules suitably arranged.

When a large number of such molecules are dispersed in water, the tails will try to avoid the water molecules (polar). The molecules will thereby arrange themselves in a bilayer such that the heads face the water and tails face away from the water and are in contact with other tails (Fig.1.3.2). This is the simple principle by which lipid molecules self assemble and form stable cell membranes (Fig.1.3.2). It is wanted to underline that the main driving force in the formation of cell membranes is the delicate balance of hydrophilicity and hydrophobicity of the head and tail respectively of the complex lipid molecule, as shown in Fig.1.3.2.



**Fig.1.3.2** Monolayer (left), Bilayer (right)

If, instead of the water, the liquid in which the lipids were dispersed is a mixture of water and oil (the tail of lipid has an affinity for oil), then the lipids will form a monolayer of molecules instead of a bilayer, as shown in the left frame of (Fig.1.3.2). The green fluid can be assumed to be oil, and the white fluid is water. Of course the structure that will be formed also depends on the relative ratio of the oil-water mixture or the concentration of the lipid molecules dispersed in the fluid. By tuning these two quantities, it is possible, actually, get the lipids to self assemble in a wide variety of structures, including spheres, cylinders and stacks of plates.

The living cell represents the ultimate *soft-matter system*, with self-organising molecular assemblies that also form larger-scale architectures. Because cells are dynamical objects, they show the same strain and flow behavior as any polymer or surfactant solution put under stress. A better understanding of these biophysical changes can lead to new therapeutic treatments for disease and to novel biomimetic technologies.

To study such complex behavior experimentally, simplified artificial cells called giant unilamellar vesicles (GUVs), can be studied. These structures comprise a spherical lipid bilayer filled with water, which can vary from 20 to 100  $\mu\text{m}$  across, and so match the dimensions of cells and organelles. GUVs have been used to understand the transport of biomolecules between organelles [3]. Long tubular lipid vehicles are thought to form, pulled by molecular motors called kinesins along fixed protein rails. It has been shown that when these motors are bound to a GUV in contact with microtubules, the GUV is locally deformed into a long tube, just as in a real cell [3]. GUVs have been used to study changes in the shape of cell membranes triggered by protein binding. It has been demonstrated how the Shiga toxin, a protein produced by *E. coli*, binds to a specific membrane receptor, forming clusters and inducing a local spontaneous curvature [4]. This causes the membrane to bend into tubules, which then provides a conduit for the toxin to enter the cell.

The blood is a highly complex system, consisting of a fluid plasma which transports the oxygen-carrying red blood cells, the protective white blood cells, blood platelets and a myriad of essential molecules including proteins. Blood is, in fact, a typical soft composite, made for the 45% of the volume by the micron-sized red blood cells. Red blood cells flow behavior is intriguing because they are not spherical but shaped like biconcave discs which deform under stress. Red blood cells have lipid membranes supported by an internal protein network which makes them more elastic, like soft rubber. Some diseases, such as diabetes and sickle cell anaemia, render them more rigid and consequently it increases the flow resistance of blood, which then affects circulation.

By advanced simulation techniques it is has been predicted, taking into account the full hydrodynamic interactions and the deformability, how the shape of red blood cells changes when they flow in a very narrow tube (capillaries) [5]. By calculating the deformation energy due to the curvature and shear elasticity of the cell membranes, and

treating the surrounding liquid as a stream of moving, colliding particles, the simulation confirmed that above a certain flow velocity the cells do, indeed, bend back in the shape of a parachute. This is different of a simple, more fluid lipid vesicle just elongates into a rugby-ball shape aligned in the direction of the flow. The transition to the parachute shape limits the flow resistance in a way that maintains a healthy blood circulation, and regulates oxygen delivery around the body [5].

Microfluidics, whereby minute volumes of liquids are manipulated in geometrically constrained environments at the microscale, is revolutionizing clinical diagnosis and biological research, and often involves separating and manipulating cells under continuous-flow conditions in microfabricated channels.

## 1.4 Chemical Soft Matter systems

The first great pioneers to describe the liquid crystals were Georges Friedel who was the first to understand exactly what is a liquid crystal, and what are the main types. Was Charles Frank, who (after some early work of Oseen) constructed the elastic theory of nematics and described also a number of their topological defects (“disclinations”) [see Chap. 2]. Observing certain defects (“focal conics”) in smectics, Friedel was able to prove that their structure must be a set of liquid, equidistant, deformable layers [6]. By observations at the one hundred micron scale, he was thus able to infer the correct structure at the nanometer scale, an amazing achievement. Smectics bring naturally to another important feature of complex fluids - namely that, in our days, it is sometimes possible to create new forms of matter. The sponge phase was an example. Another striking case was the invention of ferroelectric smectics [7] made by using a certain molecular arrangement, with chiral molecules, which should automatically generate a phase, the C\* phase, carrying a non-zero electric dipole [7]. These materials become very important for display purposes, because they can commute  $10^3$  times faster than the nematics.

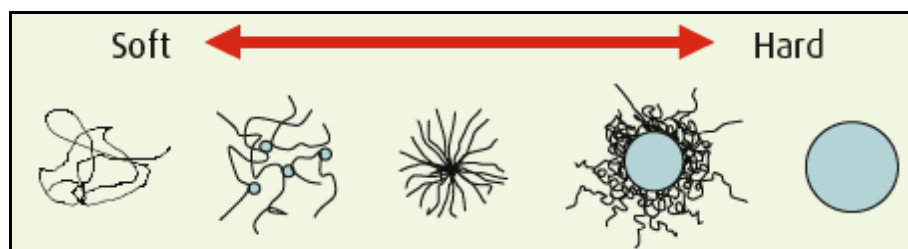
Polymer and plastics are the archetypes of soft matter: they bend and soften when subjected to heating treatment; this represents the complex behavior that emerges from their special molecular structure [8-10]. Industrial processing involves melting the

material, which is then extruded, moulded or turned into films. Understanding what happens at the molecular level as the molten plastic flows is essential in optimising production, since bulk behaviour is deeply influenced by the length and branching of the entangled constituent polymer chains and how they move.

An unusual colloidal system based on star polymers shows some very complex behavior.

Soft glasses and gels represent one of the most intriguing forms of soft matter. They are usually colloids - dispersions of particles randomly crowded together, such that their individual movement is restricted by their neighbours, as though trapped in a cage. Glasses are truly dense particle suspensions, in which the particles typically repel each other, whereas in gels the particles occupy a lower volume fraction and attract each other. In a colloidal glass, above a certain volume fraction, the particles move slowly, resulting in a variety of changes over long periods of time - in other words, they age. Like us, the exact changes that happen depend on their history. However, the particles can escape from their borders if given enough mechanical energy, in which case the material becomes a liquid. Adding other components can also alter the local environment of particles and change this “glass transition”. The challenge is to establish the rules that govern the glass transition and stability. Theorists start out with the simplest model of a colloidal glass, which treats the particles as hard spheres that mutually repel each other, and then calculate the kinetic evolution of the system [11]. Of course, real colloidal glasses are not simple spheres but more complex systems [11] which has been studied by taking into account a model system based on the use of star-shaped particles, in which a series of linear polymer chains is anchored to a central core [12]. The star polymers do not behave exactly like hard spheres but are more flexible; each particle has arms which can interpenetrate those of another particle. These systems lie between the two extremes of hard colloidal particles and soft polymeric coils. They are also very versatile: their properties can be tuned by altering the number and length of the chains.

The next figure, Fig. 1.4.4, concerns the star polymers as model soft colloids; indeed, they have microscopic intermediate properties between soft flexible polymers and hard spheres.



**Fig.1.4.1** Star polymers as model soft colloids (interpolate between polymers and hard spheres)

It turns out that star-polymer glasses show some remarkable behavior. In case of smaller star polymers, but chemically identical, added to a glass composed of big stars, they first move around the immobilised larger stars. When the volume fraction of the small stars is high enough, however, they start to knock the cages of the big stars until they break, and the glass melts into a liquid. There is also a competing scenario: using larger stars, albeit still smaller than the big ones, they can get trapped in the cages of the large stars to form a so-called double-glass system, in which both star types are immobilised. The system has yet more surprises. On adding further small stars, the cages start to push each other and the system melts again. A new type of glass appears, by more small stars, in which the cages are asymmetric.

By doing simulations, it has been calculated the glass-transition line - where the system should become liquid - for the different concentrations of small stars and showed that it followed a U-shaped curve. It has been also shown that the second glass that formed was more robust. It suggests that just by playing with simple parameters such as concentration of additives you can really tune the properties of the resulting material.

Composite liquids can show unusual organized behavior when put under stress.

Many everyday materials such as paints, cosmetics, cleaning products and even foods consist of a complex dispersion of minute particles in a liquid – a colloid. These may be fine powders, long polymer chains, surfactant micelles or some combination of all of them. Emulsion paints, for example, contain pigment particles, film-forming polymers, as well as surfactants to stabilise and maintain the paint's integrity. Not surprisingly, the physical behavior of such complex materials, especially when put under shear stress by stirring or spreading on a surface, is quite variable and can be unpredictable. Some soft-composite materials will suddenly change from a mobile liquid to a gel-like solid when sheared, while others will become thinner. Such phase transitions can be a nuisance in

processing, causing blockages in equipment, but can also be used to advantage in, say, squirting toothpaste out of a tube or applying paint to a surface. Despite the complexity, soft-matter physicists are making progress in understanding some of the surprising changes that can happen, and this will help industry to design products that are easy to process and are fit for purpose. One particular set of phenomena regard in polymer extrusion, when, at a high enough shear rate, the polymer melt would suddenly thin and “spurt” out. This flow instability, not surprisingly called the “spurt effect”, can be due to the thread like particles, whether polymer chains or worm-like surfactant micelles, suddenly untangling and stretching out, or breaking up, to form a differently organised phase. This kind of mechanism can also result in curious banded structures, and this has been revealed using the standard piece of equipment employed to study shear flow – the Couette cell. This is a narrow container with concentric cylindrical walls, where the inner wall can rotate. This creates a velocity gradient in the flow of a sample in the cell, from the outer to the inner wall. In a simple liquid, the stress increases directly with the shear rate. However, in complex liquids like polymer and micelle solutions, the material can suddenly “give way” at a given shear rate, separating into a new phase with a lower viscosity, creating distinct bands in the direction of the flow gradient [13].

Surfactants are fascinating because of the way their constituent molecules neatly organize themselves into intricate microstructures in oil and water mixtures.

A surfactant is a molecule, as said above, with two parts: a polar head, hydrophilic, and an aliphatic tail (hydrophobic). Benjamin Franklin performed a beautiful experiment using surfactants; on a pond at Clapham Common, he poured a small amount of oleic acid, a natural surfactant which tends to form a dense film at the water-air interface. He measured the volume required to cover all the pond. Knowing the area, he then knew the height of the film, something like three nanometers in our current units. This was the first measurement of the size of molecules [2].

One type of structure that has excited great interest is very long flexible cylinders, dubbed worm-like micelles. They behave a little like polymers, which also have long flexible shapes, forming viscous, elastic solutions. Nevertheless, there are some differences:

while polymers are single long-chain molecules held together by chemical bonds, worm-like micelles are molecular assemblies which continually break up and reform.

Recently, [14] it has been used a polymer- based fluid pumped at high pressure to fracture rocks so as to recover the last dregs of oil from a well. However, the highly viscous polymer then had to be removed with chemicals, which was environmentally undesirable. Therefore, it has been turned to fluids containing worm-like micelles to perform the same function. Once these come into contact with the escaping oil, they break up into spherical micelles; the material becomes runny and is easily pumped to the surface. To understand the flow behavior better, it is been developed a novel type of computer simulation in which the micelles were treated as chains of rods including properties such as the stiffness, and the breaking and fusion energies of the entangled micelles. He then simulated what would happen to the particles under shear flow [14]. The coarse-grained approach adopted allowed simulations of meaningfully large groups of micelles. At first, the computer predictions did not appear to support Schlumberger's experimental results. However, when the experiments were extended over the same length and time scales as for the simulations, they matched exactly.

The most challenging simulations are related to a type of exotic complex fluid in which the micelles are linked by a network of a polymer with 'sticky ends'—so-called "telechelic polymers". These materials are extremely viscous but also very "stretchy". The transient networks that form therefore represent an excellent model system for studying complex soft matter especially under shear forces [15]. The hydrophilic polymers have hydrophobic ends which then anchor onto the surfactant assembly to form bridges and loops. Exploring their properties using neutron-scattering techniques and rheometry, it has been found that worm-like micelles and polymers formed a double transient network.

A new type of polymer-based additive makes detergents superefficient, leading to safer, greener cleaning as well as pollution-free fuels.

One of the most intriguing types of soft composite is the microemulsion a finely dispersed mixture of water and oil, brought into intimate contact by a surfactant, or detergent, which loves both of these normally immiscible liquids. Microemulsions differ from ordinary emulsions, such as mayonnaise for example, in that the dispersion is on the nanoscale. This results in an elegantly transparent material which is extremely stable compared with even the most expertly made mayonnaise which eventually separates back into olive oil and vinegar. The stabilizing power of a microemulsion



arises from the special properties of the particular surfactants used. Traditional surfactant molecules contain both a water-loving component such as a positively charged metal ion or groups of atoms and an oil-loving hydrocarbon tail (as state above). They line up in ordered arrays, creating thin membranes separating the oil and water phases (see Fig. 1.3.2). In microemulsions, these membranes can form a range of intricate structures: they can roll up into nanosized water or oil-containing vesicles (the micelles), or form layers, or spongy networks which create bicontinuous oil and water phases throughout the material. It is quite important the knowledge of all the factors that affect the kind of microemulsion structure formed and its properties: i.e. the concentration, chemical composition, geometry and membrane flexibility.

In pursuing these goals, it has made a breakthrough in microemulsion technology [16]. Using a well-understood standard surfactant system that produces microemulsions, they add trace amounts of the new surfactant and study the phase behaviour at various concentrations and temperatures, measuring the efficiency of the system as the least amount of surfactant needed to solubilise equal amounts of oil and water. Adding very small amounts of the block copolymer greatly enhanced the surfactant efficiency, reducing the amount needed by more than a factor of ten. This meant that microemulsions could be achieved using much less of the expensive surfactant.

## 1.5 Nanoparticles

Nanoparticles, from ten to a few hundred nanometers in size, turn up everywhere: in the human body, water supply, air, many modern products such as paints, cosmetics, the highly specialized catalysts used to make chemicals, electronic device and so on.

Nanoparticles can be made by minerals, such as calcium carbonate, metals, organic compounds, or even biological molecular entities such as protein assemblies and viruses. Many natural processes such as the formation of biominerals, for example shells, or the deposition of lime scale in the washing machine, involve the initial formation of nanosized crystallites.

Understanding what controls the formation of nanoparticles is key to many technological and bio medical applications. Nanoparticles often have physical characteristics such as optical and mechanical properties uniquely related to their size

which are increasingly being exploited in the expanding field of nanotechnology. Understanding how shape and size affect these properties, and how to control their synthesis is thus an active area of research.

There is interest in making and characterising nanoparticles for industrial and technological purposes, often combining them with other materials such as polymers to control their production and behavior. Understanding how particles form and grow is extremely important in many practical processes, for example, the precipitation of salt crystals during sea-water desalination, or in the setting of concrete which involves complex recrystallisation processes that affect its strength. The standard picture of the crystallisation process was that spherical nanosized particles in the saturated water solution act as critical nuclei around which the crystals grow, but this had not been experimentally studied in detail. Electron and X-ray microscopy studies revealed that the crystallisation process is much more complicated: the particles can, for example, redissolve or cluster together into flocs. The whole story of crystallisation needs to be understood, with the aim of controlling particle formation. Studies of precipitation in the presence of polycarboxylate, which is a standard detergent additive, showed that the polymer wraps around the nanoparticles and stabilises them against further growth. Calcium carbonate represents a generic example, and the same principles can be applied to the growth of other nanoparticles, such as pigments in paints or even in natural dyestuffs used in food and drinks.

Nanoparticles which are very interesting are silver nanoplatelets and gold nanorods, which have unusual optical properties. Light impinging on the metal causes electronic surface oscillations called “plasmons”, which control how the light is reflected, and or scattered, from the particle and thus their colour. The frequency of the reflected radiation strongly depends on the shape, size and composition of the particles. Methods to obtain nanoparticles with a controlled shape – triangles, rods, decahedra, octahedra, spheres and even star shapes, so that the colour can be tuned, have been proposed [17]. Gold or silver nanoparticles, from their salt and by using a polymer stabiliser to control the nanoparticles formation results to be an highly successful chemical method to obtain gold and silver nanoparticles [17]: it is known that adding polyvinyl pyrrolidone induces the formation of nonspherical nanoparticles, but the mechanism is still not really clear.

Gold and silver nanoparticles have several exciting applications: i.e. biosensors. The particles are of the right size for attaching single molecular bio-receptors that bind with a target molecule such as a protein in the blood. Plasmons are accompanied by very high electric fields at the nanoparticle surface, which in turn enormously enhance the characteristic light scattering from the attached molecule – an effect called surface-enhanced Raman scattering (SERS) (see chap.3.). When the probes recognise their target, it can be detected through its specific vibrational signature. Another application can be found in the so-called metamaterials [18]. These are composite materials with peculiar optical properties such as a negative refractive index, with intriguing applications as “invisibility cloaks”. Metamaterials, so far, have been composed of arrays of microstructures responsive to microwaves, but the use of much smaller metallic nanoparticles is predicted to lead to similar results in the visible part of the spectrum.

## 1.6 Soft Matter applications

Nowadays, objects made by soft matter are everywhere in the life of the people.

Looking around in the house, it is possible to see that there are many kinds of soft matter: plastic containers, cleaning materials, food, soft furnishings, toys, clothes, detergent products and varnishes are made by soft-composite materials. Today, traditional materials such as metal, ceramics and wood have partly been replaced by synthetic soft materials, which may be stronger, lighter and cheaper, and which, through scientific research, can be tailored to specific requirements.

It is hard to imagine life without modern synthetic plastics and rubbers. These polymers can be moulded into almost any shape, extruded into thin films and fibres, applied as coatings, and given bright colors or made transparent. New polymer composites are continually being developed, including reinforced rubbers that are more hard-wearing.

Because soft composites are so versatile, constructed from relatively inexpensive, readily available raw materials, and capable of being processed under mild conditions of temperature and pressure, they are increasingly being exploited in advanced technological applications.

Soft materials are helping us to source and use energy efficiently. They are considerably lighter than metals, and are increasingly being used in the bodywork of vehicles, which improves fuel efficiency. Polymers incorporated in fuels themselves inhibit the formation of soot, thus reducing pollution. The amount of oil that can be recovered from an oilfield can be increased considerably by injecting polymers or surfactants into an oil well to help force the crude out of the rocks.

Because soft matter is largely constructed from molecular building blocks similar to those in living tissues, it can be designed to mimic the self-organising and molecular-recognition characteristics of biological systems. Using this approach, minute surfactant vesicles called liposomes, or coated metal nanoparticles can be used to deliver anti-cancer drugs to tumours, for example. Others issues can be the methodologies for fabricating artificial tissues or biomimetic soft materials for clinical and therapeutic applications. Soft-matter composites are generally structurally organized at the micro- or nanoscale and offer amazing potential for new technologies. The first step in this direction was liquid crystals, fluids in which molecules change their orientation in response to a voltage. Liquid crystal displays are now the device of choice for TV screens and computer monitors (see Chap. 2). Increasingly, the properties associated with soft matter are being explored in the emerging technology of microfluidics, whereby fluids are manipulated at the millimetre scale, in devices employed as sensors and used for analysis.

The further outlooks prospective for soft-matter composites are promising. With the experimental and computer techniques it is possible to investigate and predict how the many forms of soft matter behave; It would be possible to design new soft materials and structures, which have the potential to display the same diversity properties as the most complex form of matter that is the living matter.

## 1.7 References

- [1] C.N Likos, Effective interactions in soft condensed matter physics Phys. Reports, **348**, 267 – 439 (2001).
- [2] P.G. de Gennes , Soft matter Rev. Modern Phys.,**64**, 645 – 647 ( 1992 ).
- [3] A. Roux, D. Cuvelier, P. Nassoy, J. Prost, P. Bassereau, B.Goud, Role of curvature and phase transition in lipid sorting and fission of membrane tubules, EMBO J., **24**, 1537 (2005).
- [4] W. Römer, L. Berland, V. Chambon, K. Gaus, B. Windschiegl, D. Tenza, M. Aly, V. Fraisier, J.C.,Florent, D. Perrais, C. Lamaze, G. Raposo, C. Steinem, P. Sens, P. Bassereau, L. Johannes, Shiga toxin induces tubular membrane invaginations for its uptake into cells, Nature, **450**, 670 (2007).
- [5] H.Noguchi and G.Gompper , Shape transitions of fluid vesicles and red blood cells in capillary flows, Hiroshi PNAS, **102**(40), (2005).
- [6] G. Friedel, The Mesomorphic States of Matter, Annales de Physique, B1 Annales de Physique, **18**, 273–474 (1922).
- [7] R. B. Meyer, L. Liebert, L. Strzelecki, P. Keller, Ferroelectric liquid crystals, J. Physique Lett., **36**, 69-71 (1975).
- [8] I. Nicotera, C. Oliviero, G. Ranieri, A. Spadafora, M. Castriota and E. Cazzanelli, Temperature evolution of thermoreversible polymer gel electrolytes LiClO<sub>4</sub> / ethylene carbonate / poly(acrilonitrile), J. Chem. Phys., **117**, 7373-7380 (2002)
- [9] M. Castriota and D. Teeters, Impedance spectroscopy of PEO-Lithium Triflate Confined in Nanopores of Alumina Membranes, Ionics, **11**, 220 (2005),.
- [10] I. Nicotera, L. Coppola, C. Oliviero, M.Castriota, E.Cazzanelli, “Investigation of ionic conduction and mechanical properties of PMMA-PVdF blend based polymer electrolytes”.Solid State Ionics, **177**, 581, (2006).
- [11] E. Zaccarelli, Colloidal gels: equilibrium and non-equilibrium routes, J. Phys.: Condens. Matter, **19**, 323101 (50pp) (2007).
- [12] B. M. Erwin, D. Vlassopoulos, M. Gauthier and M. Cloitre, Unique slow dynamics and aging phenomena in soft glassy suspensions of multiarm star polymers, Physical Review E **83**, 061402 (2011).

- 
- [13] J.K.G. Dhont, W.J. Briels, Gradient and Vorticity banding, *Rheologica Acta*, **47**, 257-281 (2008)
- [14] J.T Padding and E.S. Boek, and W.J. Briels, Dynamics and rheology of wormlike micelles emerging from particulate computer simulations, *Journal of Chemical Physics*, **129**, 074903 (2008).
- [15] K. Nakaya, L. Ramos, H. Tabuteau and C. Ligoure, Linear viscoelasticity of entangled wormlike micelles bridged by telechelic polymers : an experimental model for a double transient network , *Journal of Rheology*, **52**, 359 (2008).
- [16] J. Allgaier and H. Frielinghaus, *Microemulsions: Background, New Concepts, Applications, Perspectives* (Chap. 4: Effects of Polymers on the Properties of Microemulsions), John Wiley and Sons, (2009).
- [17] A. F. Alvarez-Paneque, B. Rodríguez-González, I. Pastoriza-Santos, L.M. Liz-Marzán, Shape-templated growth of Au@Cu nanoparticles *J. Phys. Chem. C*, DOI: 10.1021/jp3062724.
- [18] NANOGOLD project: “Self-organized Nanomaterials for tailored optical and electrical properties” (Seventh Framework Programme Theme, NMP-2008–2.2–2, Nano-structured metamaterials grant agreement no. 228455).

*Chapter 2*

**LIQUID CRYSTALS AND BIOLOGICAL OBJECTS**

## 2.1 Nematic Liquid Crystals

The liquid crystal phase has a degree of order intermediate between the liquid isotropic state and the solid crystalline state. The molecules in liquid crystalline phases move, more or less, as in the liquid state but they maintain some degree of orientational and, sometimes, positional order, which combines order and mobility on a molecular, supramolecular and macroscopic level.

Liquid crystalline molecules are, generally, organic and many of them are elongated in shape (rod like). Some liquid crystals are made by discotic molecules, for example octa-substituted phthalocyanine derivatives, stratified in columnar shape.

The liquid crystals materials can be divided in three categories [1]:

- **Thermotropic**, the liquid crystal phase occurs when the temperature is within a precise range. If the liquid crystal phase is obtained both increasing as well as decreasing the temperature it is called enantiotropic, otherwise, if just one path conduce to the liquid crystal phase it is said monotropic. For example nematic phases, smectic phases, chiral phases, blue phases and discotic phases belong to this class.
- **Lyotropic**, when the occurrence of the liquid crystal phase depends, besides on the temperature, also by the concentration of the liquid crystal molecules dissolved in a proper solvent: i.e. amphiphilic compounds in water. For example, amphiphilic molecule.
- **Amphotropic**, when the materials are able to form thermotropic as well as lyotropic liquid crystal. For example block copolymers, amphotropic mesogeneity of other systems, flexible amphiphiles.

Different liquid crystal phases exist and they have been classify taking in account the order degree present in themselves and some of them are shown in Fig. 2.1.1



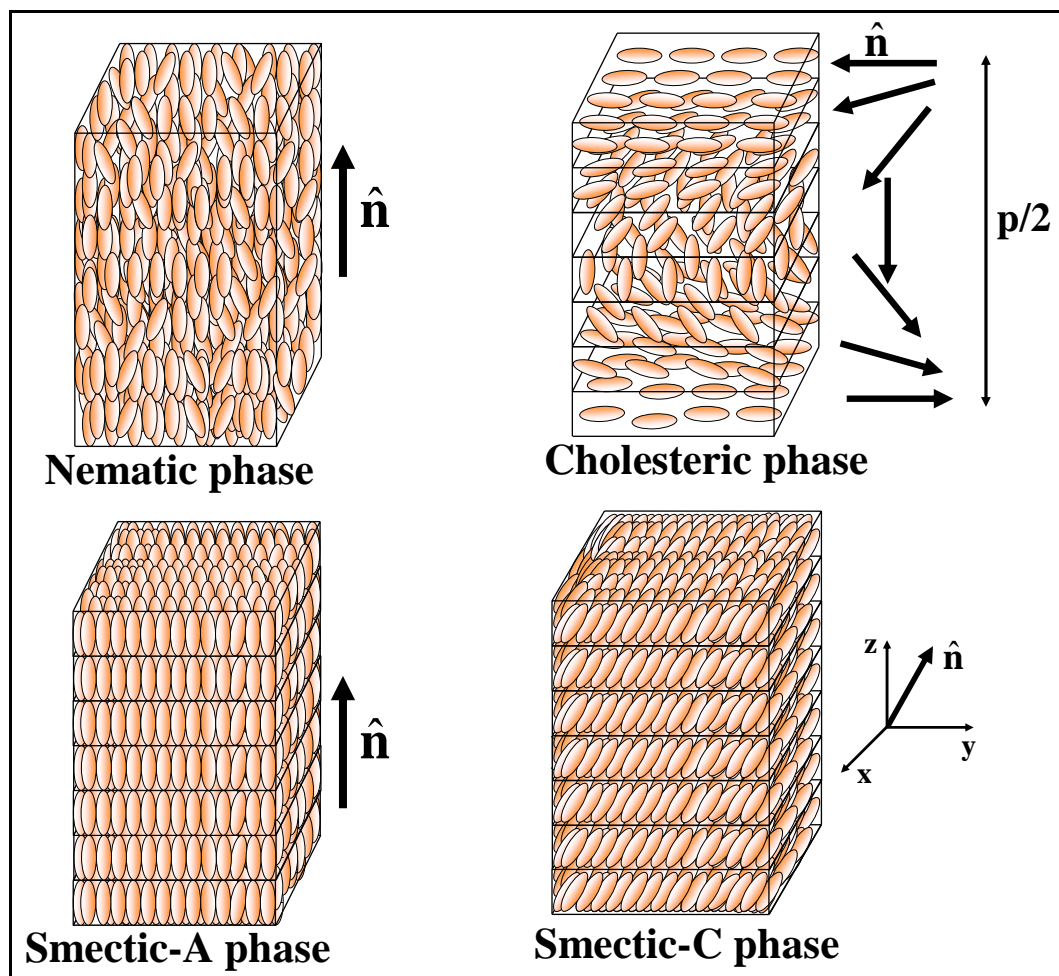


Fig.2.1.1 Liquid crystalline phases.

The nematic liquid crystal phase shows only a long range orientational order of anisotropic molecules. The direction of the average orientation of the “long axes” of the molecules is represented by a unit vector called director  $\hat{\mathbf{n}}$  (Fig.2.1.1). The molecules in the nematic phase are considered to be with cylindrical symmetry and consequently this phase will have uniaxial symmetry.

The physical properties of the nematic phase show that  $\hat{\mathbf{n}}$  and  $-\hat{\mathbf{n}}$  are equivalents:  $\hat{\mathbf{n}}$  is an apolar vector [2].

If the molecules forming a liquid crystal phase are chiral then the chiral phases take over in place of the previous phases. If this happens in the nematic liquid crystal phase then the resulting phase will be called cholesteric phase (Fig. 2.1.1). In the cholesteric phase the director rotates in helical trend about an axis perpendicular to the director. Schematically, it can be thought as different stratified nematic layers in which the

director is rotated by a constant angle coming from one layer to the next (Fig. 2.1.1). The pitch ( $p$ ) of the cholesteric phase is the distance in which the director is rotated by  $360^\circ$ . However, in the cholesteric phase, clearly, due to the equivalence of  $\hat{\mathbf{n}}$  and  $-\hat{\mathbf{n}}$  the structure repeats itself every half pitch (Fig. 2.1.1).

If the cholesteric phase is made by a mixing of two optical isomers (enantiomers) the resulting pitch will be bigger than those that occur in the cholesteric phases made with either pure enantiomer. A racemic mixture results to have an infinite pitch and for this reason it results to be as a nematic liquid crystal phase [2-3].

The helical structure exhibit very different and interesting optical properties that are very useful in practical applications: electro-optic display and thermographic use, due to the dependence on the temperature of the pitch length and therefore of the selective reflection of the light.

Liquid crystal phases with layered structures are said smectic. In these phases in addition to the orientational order of nematic phase there is positional order due to the molecular's centres of mass, arranged in layers. If the directors is perpendicular to the layers then the phase is called smectic A, while, if the director results to be with an angle different than  $90^\circ$  with the layers (tilted) then the resulting phase is said smectic C (Fig. 2.1.1). The molecules in the smectic A and C phases are randomly ordered in the layers and they can rotate around their long axes, with very small hindrance.

Many others smectic phases with layered structure have been discovered and are listed in Table 2.1.1.

<b>Phase type</b>	<b>Molecular orientation</b>	<b>Molecular packing</b>	<b>Orientalional ordering</b>	<b>Positional ordering</b>
A	Orthogonal	Random	Short range	Short range
C	Tilted	Random	Short range	Short range
B (hexatic)	Orthogonal	Hexagonal	Long range	Short range
I	Tilt to apex of hexagon	Pseudo Hexagonal	Long range	Short range
F	Tilt to side of hexagon	Pseudo Hexagonal	Long range	Short range
L (B Cryst.)	Orthogonal	Hexagonal	Long range	Long range
J (G')	Tilt to apex of hexagon	Pseudo Hexagonal	Long range	Long range
G	Tilt to side of hexagon	Pseudo Hexagonal	Long range	Long range
E	Orthogonal	Orthorhombic	Long range	Long range
K (H')	Tilted to side a	Monoclinic	Long range	Long range
H	Tilted to side b	Monoclinic	Long range	Long range

**Table 2.1.1** Main features of the smectic phases [1].

In Table 2.1.1 phases with increased positional order can be found, until to arrive to three dimensional positional order.

In the B (hexatic), I, F phases inside the layers the molecule are oriented on a two dimensional lattice and however, the layers do not have long range correlation, while the others phases show three dimensional long range order; their character is more crystalline like and the rotation of the molecules, around to the molecular long axes, is strongly hindered.

The transition from one phase to another one is generally of the first order but there are some second order transitions: smectic C / smectic A.

When the molecules of the smectic phases are chiral, as well as in the nematic case, (nematic/cholesteric), phases with different physical properties are obtained: these phases are indicated by the asterisk symbol as apex (\*). All the smectic phases with tilted structure with chiral molecules show ferroelectric properties: spontaneous polarization and piezoelectric behaviours.

## 2.2 Physical Chemistry properties of nematic liquid crystal

How stated above, the nematic liquid crystals do not have positional order but they have orientational order. In order to quantify the amount of orientational order an parameter, S, as been defined as:

$$S = \left\langle \frac{3\cos^2\theta - 1}{2} \right\rangle \quad (2.2.1)$$

where  $\theta$  is the polar angle made by the long axis of each individual molecule with the director  $\hat{\mathbf{n}}$  and the angular brackets point out a statistical average.

The order parameter S is a function of the temperature T, but a closed analytical relation is not possible because it is strongly dependent of the chemical nature of the molecules. However, for practical purposes, the relation derived from the Mayer- Saupe theory [2, 4-7] can be used:

$$S = \left( 1 - \frac{yT}{T_{Clp}} \right)^\beta \quad (2.2.2)$$

where  $T_{Clp}$  corresponds to the nematic-isotropic transition temperature, y is the order of 0.98 and  $\beta$  is an exponent in the range 0.13 - 0.18 depending of the specific material. When an material is in the liquid crystalline phase it is turbid and when it becomes

isotropic appears transparent. For this reason the nematic-isotropic transition temperature is often called temperature of the clearing point.

Due to the presence of a preferred direction  $\hat{\mathbf{n}}$  of the molecules of liquid crystal many of properties of this phase are anisotropic.

The dielectric permittivity  $\epsilon$ , as well as the refractive index  $n$ , (which at optical or higher frequencies are related by  $\epsilon = n^2$ ), are second rank tensors and for this reason they can be always referred to a principal system axes such for which :

$$\vec{\epsilon} = \begin{pmatrix} \epsilon_x & 0 & 0 \\ 0 & \epsilon_y & 0 \\ 0 & 0 & \epsilon_z \end{pmatrix} = \epsilon_0 \begin{pmatrix} n_x^2 & 0 & 0 \\ 0 & n_y^2 & 0 \\ 0 & 0 & n_z^2 \end{pmatrix} \quad (2.2.3.)$$

where  $\epsilon_x, \epsilon_y, \epsilon_z$  and  $n_x, n_y, n_z$  are the principal components which respect to the principal axes of the dielectric permittivity and refractive index, respectively.

For uniaxial systems it will be:

$$\epsilon_x = \epsilon_y = \epsilon_{\perp} \qquad \epsilon_z = \epsilon_{\parallel} \quad (2.2.4.a)$$

$$n_x = n_y = n_{\perp} \qquad n_z = n_{\parallel} \quad (2.2.4.b)$$

where the symbols  $\perp$  and  $\parallel$  indicate the perpendicular and parallel components with respect to the director  $\hat{\mathbf{n}}$  whose direction is supposed to be coincident with that of the z-axis.

It has been defined dielectric anisotropy  $\Delta\epsilon$  the difference:

$$\Delta\epsilon = \epsilon_{\parallel} - \epsilon_{\perp} \quad (2.2.5)$$

which can be either positive or negative, depending of the permanent dipole moment and of the polarizability of the molecules.

The dielectric anisotropy is related to the capacity of an external electrical field  $\vec{E}$  of aligning the liquid crystal molecules.

In fact, when the nematic liquid crystal is subject to an applied electrical field  $\vec{E}$  a dipole moment per unit volume is produced ( $\vec{P}$ ), called polarisation:

$$\vec{P} = \varepsilon_0 \vec{\chi}_0 \vec{E} \quad (2.2.6)$$

where  $\vec{\chi}_0$  is the electrical susceptibility and  $\varepsilon_0$  is the permittivity of the free space.

The electric field and the polarisation together define the vector electric displacement  $\vec{D}$ :

$$\vec{D} = \varepsilon_0 \vec{E} + \vec{P} = \vec{\varepsilon} \vec{E} \quad (2.2.7)$$

where  $\vec{\varepsilon} = \varepsilon_0 (\vec{I} + \vec{\chi}_e)$  and  $\vec{I}$  is the unit tensor.

The electrical energy per unit volume ( $U_e$ ) is given by:

$$U_e = \frac{1}{2} \vec{D} \cdot \vec{E} = -\frac{1}{8\pi} \Delta\varepsilon (\hat{n} \cdot \vec{E})^2 = -\frac{1}{8\pi} \Delta\varepsilon E^2 \cos^2 \theta \quad (2.2.8)$$

where  $\theta$  is the angle between the direction of the electric field and the director  $\hat{n}$ . The minimum values of  $U_e$  are obtained for  $\Delta\varepsilon > 0$  when  $\theta = 0^\circ$  and for  $\Delta\varepsilon < 0$  when  $\theta = 90^\circ$ .

Analogue consideration can be made regarding the magnetic susceptibility [2].

How said above, the nematic liquid crystal appear turbid as milky fluid. This is due to the random refractive index fluctuation present in the liquid crystalline phases. After the alignment of the nematic liquid crystal the two refractive indexes (eq. 2.2.4.b) can be observed. Therefore, as well as for dielectric permittivity, the optical anisotropy, better known as birefringence, can be defined:

$$\Delta n = n_e - n_o = n_{//} - n_{\perp} \quad (2.2.9)$$

where  $n_o$  is the refractive index corresponding to the “ordinary” ray with the electric field perpendicular to the optic axis of the molecule and  $n_e$  the refractive index corresponding to the “extraordinary” ray with the electric field parallel to the optic axis of the molecule.

The discussion done above assumes that the director is perfectly uniform. Actually, quite small variations can be found at molecular level depending by the position. However, these variations are not so remarkable to induce modifications of the order parameter.

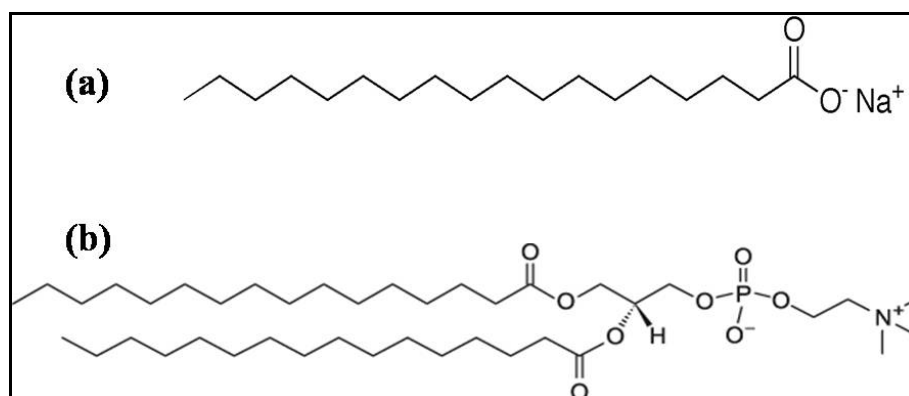
### 2.3 Lyotropic Liquid Crystals

As stated above, when the occurrence of the liquid crystal phase depends, besides on the temperature, also by the concentration of the liquid crystal molecules dissolved in a right solvent the liquid crystals is said lyotropic.

There are many different types of lyotropic liquid crystal phase structures, with different extent of molecular ordering within the solvent. However, it is possible to change the type of exhibited lyotropic phase to each concentration by changing the temperature.

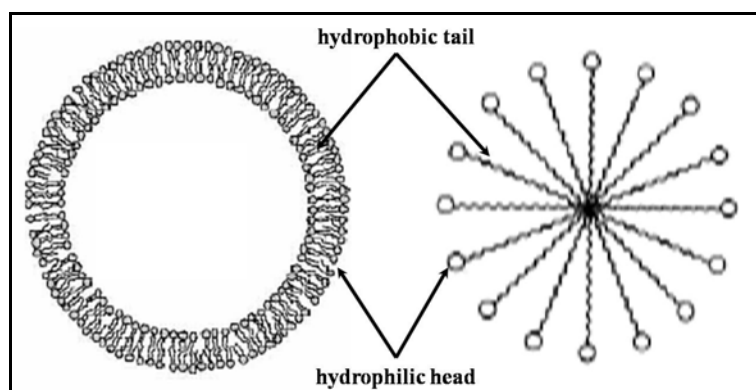
In everyday life many kinds of lyotropic liquid crystal phases can be seen; for example: surfactants in water give lyotropic liquid crystal phases as soap used with water. Very important is the occurrence of lyotropic liquid crystal phases in biological systems, for example: phospholipid, mixtures of lipid, micelles, membranes cells, blood and so on (see Chap.1). Lyotropic liquid crystal molecular structure consists in amphiphilic molecules. Amphiphilic molecules form liquid crystal phases, that are slightly different from the calamitic and discotic phases, that at low concentrations form micelles and vesicles. There is orientational and sometime positional order of the molecules within these structures, but there is no ordering of the micelles or vesicles themselves. At higher concentration, the structure changes to one in which the micelles or vesicles themselves are also ordered.

Amphiphilic molecules have both polar head group, made by a carboxylate salt, and by a non-polar tail group, that is a long hydrocarbon chain. Lyotropic liquid crystal phases are formed on the dissolution of amphiphilic molecules in a right solvent (usually water). In Fig. 2.3.1 amphiphilic molecules as surfactants and phospholipid are shown.



**Fig.2.3.1** Two lyotropic liquid crystals, soap sodium stearate (a), and synthetic phospholipid 1,2-Dimyristoyl-*sn*-Glycero-3-Phosphocholin (DMPC) (b).

When amphiphilic molecules are dissolved in a polar solvent, like water, the hydrophobic “tails” assemble together and show the hydrophilic “heads” to the solvent. Two structures are known to arise from this reorganization: micelles and vesicles (Fig. 2.3.2).



**Fig.2.3.2** Representation of a micelle cross-section(a) and vesicle (b).

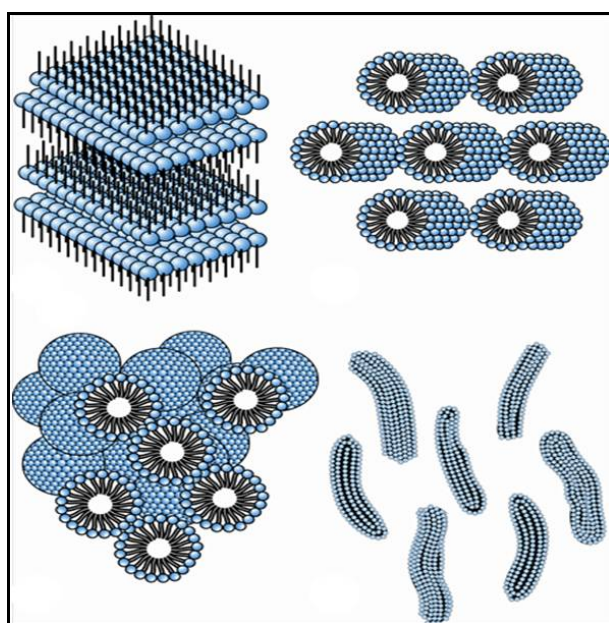
Both soaps and phospholipid molecules also form a bilayer structure, with the hydrocarbon chains separated from the water by the “head” groups [3].



Soaps improve the efficiency in removing dirt and grease of the pure water because the non-polar parts inside of the micelles dissolve non-polar substances that otherwise are not dissolved in water. In non polar solvent, polar substances can be removed, since the micelles are made with the polar head inside the micelles and the non-polar part are outside (inverse micelles). Soaps also help water dissolve more because the molecules tend to remain at the surface, hydrocarbon tail away from the water, thus lowering the surface tension of the water and allowing more material to enter it the water and be dissolved [3].

Self-assembled structures of lyotropic liquid crystals are not covalently bonded and they can assume several different geometry dependently by the thermodynamic conditions and the chemical nature of the molecule. These aggregates can be rod-like or disk-like which can be orientationally and/or positionally ordered to exhibit a high number of liquid crystalline phases including, nematic, lamellar, hexagonal and cubic phases [8].

The hexagonal phase (or middle soap phase),for example, shows an hexagonal arrangement of long cylindrical rods of amphiphilic molecules. At some concentrations the lamellar phase (sometimes called the neat soap phase) forms with a uniform amount of water separating the bilayers. Cross-sections of the hexagonal and lamellar phases are illustrated in Figure 2.3.3.



**Fig. 2.3.3** Lamellar and micelles of lyotropic liquid crystal phase.

Sometimes a cubic (or viscous isotropic) phase is made between the hexagonal and lamellar phases. In this phase the amphiphilic molecules arrange themselves in spheres, which in turn form a cubic lattice. These spheres may be closed or they may be connected to one another, thus forming a bicontinuous phase.

Under particular conditions, a mixture of highly polar liquid, slightly polar liquid and amphiphilic molecules form micelles that are not spherical. They can be rod-like, disc-like, or biaxial (all three axes of the micelles are different). These anisotropic micelles sometimes order in the solvent just as liquid crystal molecules order in thermotropic phases. There is a nematic phase of rod-shaped micelles, another nematic phase of disc-shaped micelles, and even a biaxial nematic phase, in which the molecular axes transverse to the long molecular axis partially order. Chiral versions of these phases with the same structure as the chiral nematic phase also form [3].

As state above, lipids exhibit both water-soluble and water-insoluble domain. Many properties are coming up from their interactions (of such domains and the water molecules). In micelles the lipids regroup through tail associations creating a three dimensional structure (i.e. sphere or cylinder), where only the polar headgroups are exposed to the solvent [9]. Because their cores are non-polar while the outside surface remains water soluble, micelles are ideal for encapsulating other non-polar molecules. For example, artificial amphiphilic (lipid-like) copolymers are designed to assemble into micelles for the encapsulation of single wall carbon nanotubes [10]. This encapsulation is found to change the fluorescent properties of the nanoparticles. It is also important to note that the reverse structure can assemble inside non-polar solutions (i.e. oil) and are know as reverse-micelles.

In vesicles, the lipids stack in two reflecting layers, in a head-tail-tailhead manner, such that only the head groups are exposed to the water molecules on both sides of the dual-layer. Because the hydrophobic tails are sandwiched between sheets of polar head groups, vesicles are ideal for the encapsulation of various solvents. This is the primary structure of animal cells where both the interior and exterior of the cells are aqueous.

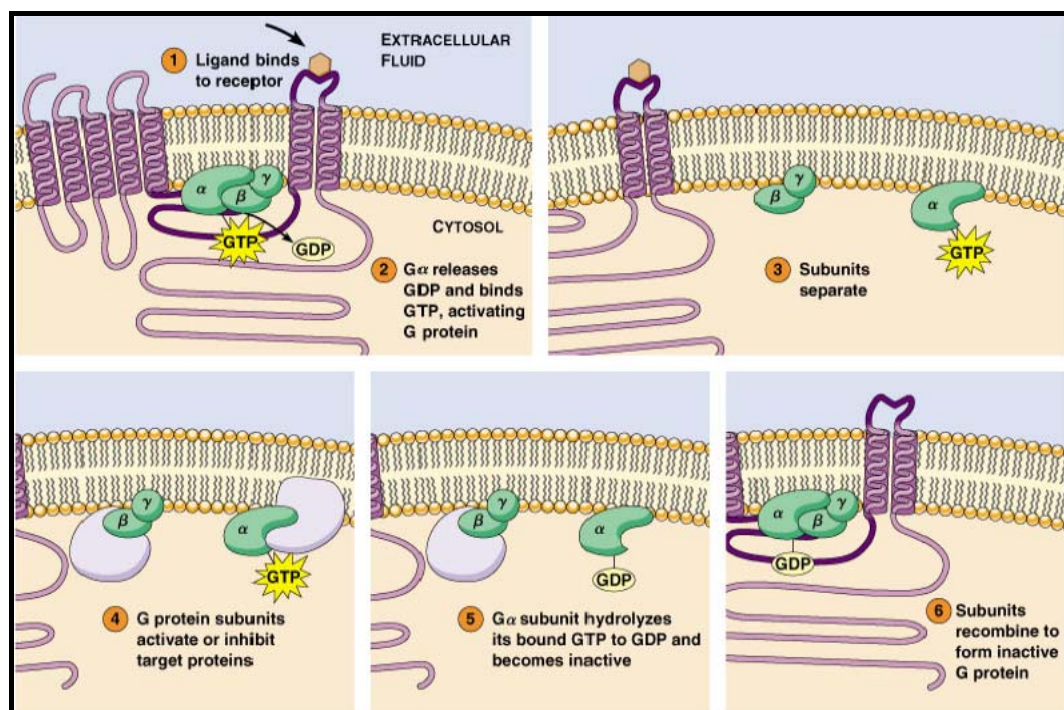
If these amphiphilic molecules are mixed with a non-polar solvent such as hexane, similar structures are made but now the polar “heads” assemble together with the non-polar “tail” groups in contact with the solvent. These are called reversed phases to distinguish them from the phase that occur in polar solvents.

Solution of biomolecules such as protein and sufficiently concentrated solutions of surfactants can make interesting class of liquid crystals such as synthetic polypeptides, biomimetic vesicles and membranes cells.

## 2.4. Biological Membrane Protein

Membrane proteins are crucial players in the cell and take center stage in processes ranging from basic small-molecule transport to sophisticated signaling pathways [11].

Many membrane protein are also prime targets of contemporary or future drugs, and it has been estimated that more than half of all drugs currently on the market are directed against membrane proteins [12]. By contrast, it is still frustratingly hard to obtain high-resolution three-dimensional (3D) structures of membrane proteins, and they represent less than 1% of the structures in the Protein Data Bank [13]. Among the membrane proteins, one of the most important class is represented by the transmembrane (TM) proteins. To the TM class protein belongs the G-protein-coupled receptor (GPCR) superfamily. The GPCR, upon their activation by extracellular signals, initiate an intracellular chemical signal cascade to transduce, propagate, and amplify these signals. GPCR has a single chain with seven helical TM domains threading through the membrane. Signal transduction begins when an extracellular agonist “ligand” binds and switches the receptor from an inactive state to an active state conformation. In particular a ligand such as a hormone, neurotransmitter, glycoprotein or syntetic agonist interacts with a heptahelical receptor on the surface of the cell and the ligand can stabilize or induce a different conformation of the receptor (GPCR) that activates the heterotrimeric G protein (composed of  $\alpha$ ,  $\beta$ , and  $\gamma$  subunits) on the inner surface of the membrane cells. [14,15]. The G protein bind the guanilic nucleotides (GDP and GTP). In the inactive heterotrimeric state, GDP is bound to the  $G_\alpha$ -subunit. Upon activation, GDP is released, GTP binds to  $G_\alpha$ , and subsequently  $G_\alpha$ -GTP dissociates from both  $G_{\beta\gamma}$  and the receptor, as shown in the Fig. 2.4.1. Both  $G_\alpha$ -GTP and  $G_{\beta\gamma}$  are then free to activate downstream effectors. The duration of the signal is determined by the intrinsic GTP hydrolysis rate of the  $G_\alpha$ -subunit and the subsequent reassociation of  $G_\alpha$ -GDP with  $G_{\beta\gamma}$  [14,16].



**Fig.2.4.1** Receptor-mediated G protein activation. The interaction of an ligand with its cell surface receptor facilitates the coupling of the activate receptor with intracellular heterotrimeric G proteins.

As said above, the GPCR play a crucial role in many essential physiological processes, ranging from the detection of the light (involving rhodopsin) and odorant signal, to the mediation of neurotransmission, hormonal actions, cell growth and immune defense. GPCRS mediate responses interacting with a variety of bioactive molecules including ions, lipids, aminoacid, peptides, proteins and small organic molecules.

To the GPCR superfamily belong the GPR30 which is an estrogenic membrane receptor found in the human breast cancer cells [16-19]. Although, usually, the GPCRs are found on the plasmatic membrane the GPR30 is found in major amount on the endoplasmic reticulum [16-20]. The localization of the GPR30, of course, is well understood also by taking into account its function since the endogenous estrogen ligand is permeable to the membrane.

The chance to characterize (by doing in situ analysis) the GPR30, its synthetic ligand (G-1) (see Chap.4) and maybe the physical chemistry mechanism of their interaction can strongly help to understand how to project the right drugs in order to solve the diseases that regard this receptor.

## 2.5 Mimetic models

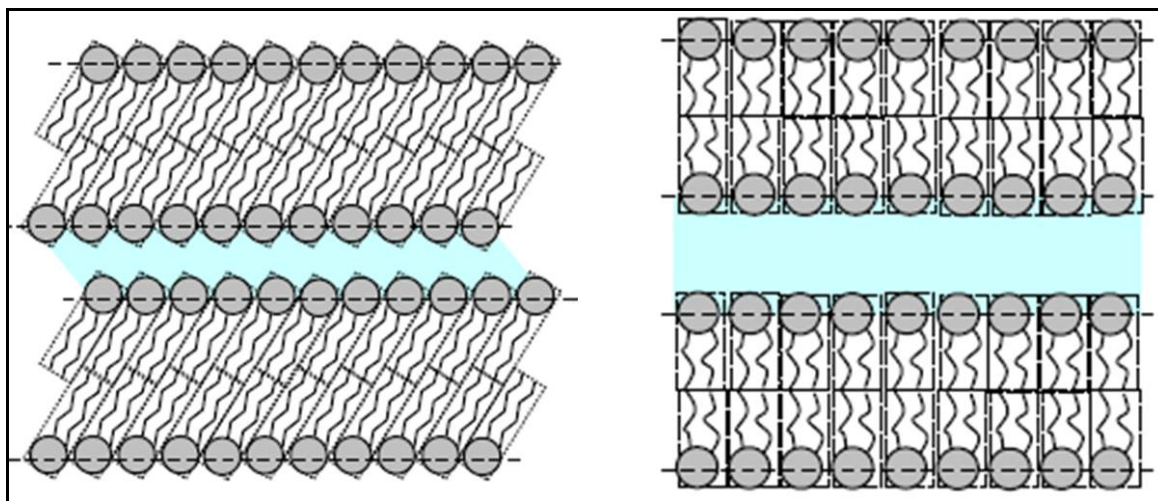
Lipids are integral parts of the cell membrane. The understanding of their behavior is therefore essential for the study of cell functions.

Among them, during the last years great interest was devoted to the study of phospholipids-water mixtures in order to evaluate the structural and functional properties of these systems [21]. In fact, cells of living organisms can be thought as phospholipids membranes, sometime functionalized by proteins, which are immersed into water environment [22]. Among the usual topics, including protein misfolding diseases, drug discovery, pathogenesis, gene therapy, etc. [23, 24], the membranes of the cells are attracting great attention as possible components for applications such as sensors, electronics and bioprocessing [25]. The great incentive coming from the different kind of applications has supported the development of membrane mimetic models made, usually, by phospholipids layers that represent the major component of most cell membranes with its typical chemical structure made by a hydrophilic charged head group bonded by glycerol backbone to hydrophobic long acyl chains [26].

It is well know, that phospholipids spontaneously adopt the bilayer organization when dispersed in water to form closed vesicles (liposomes) [27]. The vesicle is a compartment, formed in vitro, where the interior is made by a small water volume enclosed by one or few layers constituted by amphiphilic molecules [28]. By selecting the preparation method it is possible to obtain vesicle with different diameters in the range between some nanometer up to tens of micrometer: large unilamellar vesicle (LUV), giant unilamellar vesicle (GUV) and multilamellar vesicle (MLV) [28, 29].

The phospholipids bilayer vesicles (multilamellar and unilamellar) as a function of the temperature can be found in three different phases: gel ( $L_{\beta'}$ ), ripple ( $P_{\beta'}$ ) and liquid crystalline ( $L_{\alpha}$ ) [30,31]. In the  $L_{\beta'}$  phase the acyl chains are arranged in ordered way which approximate an hexagonal lattice, while above chain-melting temperature the lamellar liquid crystal phase ( $L_{\alpha}$ ) is found (Fig. 2.5.1), characterized by a fast diffusion of the molecules in the plane of bilayer. The intermediate phase  $P_{\beta'}$  is characterized by a long range periodicity of the structure in the plane of the bilayer [30,31]. Nevertheless, much efforts need to be done in order to obtain information about the hydrocarbon

chain order and mobility in the bio-mimetic membrane in order to fully understand of “order degree” of the different phases and the mechanisms of the phase transition.



**Fig. 2.5.1** Schematic illustration of PC bilayer structure  $L_\beta$  and  $L_\alpha$  phases

## 2.6 Liquid Crystalline Composite Materials

In recent decades, great attention has been devoted to the realization of electrically switchable holographic gratings in liquid crystalline composite materials. It has been shown, indeed, that devices based on holographic polymer dispersed liquid crystals (HPDLCs) are of low cost and can exhibit a good diffraction efficiency (DE) [1, 2].

However, application oriented utilization of these devices is limited, in general, by their strong scattering of light, due to the circumstance that the droplet size of the nematic liquid crystal (NLC) component inside the polymer matrix is comparable to the wavelength of the impinging light. It has been recently proposed a new kind of holographic grating called POLICRYPS (Polymer Liquid Crystal Polymer Slices), made of polymer slices alternated to films of regularly aligned NLC. These structures do not present those optical inhomogeneities that are due to the presence of NLC droplets in usual HPDLC samples [3], and can therefore exhibit good optical characteristics, with values of the diffraction efficiency as high as 98%.

POLICRYPS, as novel technology for making switchable holographic gratings, is characterized by the formation of periodic structures in liquid crystalline composite

materials cured by the periodic intensity distribution of a UV (or visible) interference pattern [4].

Following this model, diffusion and curing intensity are the two features that play the main roles during the curing process, determining the morphology of the sample. In particular, only a good diffusion of monomer molecules (realized, in fact, only when the NLC component is in the isotropic phase) can avoid the formation of NLC droplets, thus allowing a complete separation between polymeric structures and pure NLC in the cured mixture.

These considerations explain why, in order to fabricate POLICRYPS, before starting the curing process it is necessary to heat the initial mixture above the nematic–isotropic transition temperature and allow a very slow cooling down to room temperature only after the whole curing process has come to an end. In the equations of the model, two control parameters can be singled out, which are related to the monomer diffusion coefficient and to the curing intensity respectively; actual values of these parameters determine which kind of structure (HPDLC or POLICRYPS) is going to be formed. The high diffusion allowed during the curing process determines a morphology of the POLICRYPS that is quite different from the HPDLC one. Optical microscope and scanning electronic microscope (SEM) investigations have shown that the structure consists of rigid slices of almost pure polymer alternated to films of almost pure NLC, with a periodicity that reflects the pitch of the curing interference pattern. The polymeric slices are well glued to the cell glasses and represent a rigid frame that, somehow, “stabilizes” the NLC component and, therefore, the whole sample. Separation interfaces between polymer slices and NLC films are quite regular and sharp.

The uniform and regular alignment of the director in the NLC films of the structure determines the main optical and electro-optical properties of the POLICRYPS. From the optical point of view, losses due to the scattering of the visible light (which is eventually brought to impinge onto the POLICRYPS) are reduced to less than 2%, thanks to the absence of droplets, which exist in HPDLC samples, with an average size comparable to the light wavelength and an arbitrary director alignment. Afterwards, by suitably choosing the values of the refractive index of the polymer and the



ordinary/extraordinary refractive index of the NLC, this director reorientation can be exploited to vary the spatial modulation of the refractive index of the POLICRYPS.

Low scattering losses and good switchability of the POLICRYPS open a wide range of possible applications. In fact, POLICRYPS has been designed and patented [5] to work as a good “switchable” diffraction grating [28], but it is well known that this structure is suitable for different interesting exploitations, depending on the way a light beam propagates through the structure. In particular, we have found that, in addition to the possibility of using the refractive index modulation with light also propagating “in the plane” of the structure, the polymeric rigid frame of POLICRYPS can not only be exploited to realize a good “physical confinement” (stabilization) of the NLC molecules, but also can become an array of regular “channels” where light can be guided and, eventually, amplified.

## 2.7 References

- [1] D. Demus, in *Liquid Crystals Applications and Uses*, edited by B. Bahadur, World Scientific Publishing Co. Pte. Ltd, Singapore, (1990).
- [2] L. Pohl and U. Finkenzeller, in *Liquid Crystals Applications and Uses*, edited by B. Bahadur, World Scientific Publishing Co. Pte. Ltd, Singapore, (1990).
- [3] P. J. Collings and M. Hird, *Introduction to liquid crystals: Chemistry and Physics*, Taylor and Francis Ltd, London, (1997).
- [4] F. J. Bock, H. Knepe and F. Scheider, *Liq. Cryst*, **3**, 239 (1986).
- [5] W. Maier and A. Saupe, *Z.Naturforsch*, **14A**, 882 (1959).
- [6] W. Maier and A. Saupe, *Z.Naturforsch*, **15A**, 287 (1960).
- [7] M. Castriota in PhD Thesis, *Development and Spectroscopic Characterization of Materials for Applications in Electrochromic Devices and Novel liquid Crystalline Cells*, University of Calabria, ITALY, (2004).
- [8] Maher S. Amer, *Raman spectroscopy for soft matter applications*, John Wiley & Sons, Inc., USA, (2009).
- [9] K. A Dill and P. J. Flory, *Molecular organization in micelles and vesicles*, **78**, 676-680 (1981).



- [10] Y. Kang and T. A. Taton, Micelle-encapsulated carbon nanotubes: a route to nanotube composites, *J Am Chem Soc.*, **14**, 125(19):5650-1 (2003).
- [11] A. Elofsson and G. von Heijne, Membrane Protein Structure: Prediction versus Reality, *Annu. Rev. Biochem.*, **76**, 125-140 (2007).
- [12] T. Klabunde and G. Hessler, Drug Design strategies for Targeting G-Protein-Coupled Receptors, *ChemBioChem*, **3**, 928-944 (2002).
- [13] H. M. Berman, J. Westbrook, Z. Feng, G. Gilliland, T. N. Bhat, H. Weissig, I. N. Shindyalov and P. E. Bourne, The Protein Data Bank, *Nucleic Acids Research*, **28**, 235-242 (2000).
- [14] T.M. Cabrera-Vera, J. Vanhauwe, T. Thomas, M. Medkova, A. Preininger, M. R. Mazzoni, and H. E. Hamm, Insights into G Protein Structure, Function, and regulation, *Endocrine Reviews*, **24**, 765–781 (2003).
- [15] H.E. Hamm, The many faces of G protein signaling. *J Biol Chem*, **273**, 669–672 (1998).
- [16] S.R. Sprang, G protein mechanisms: insights from structural analysis, *Annu Rev Biochem*, **66**, 639–678 (1997).
- [17] E. R. Prossnitz, J. B. Arterburn and L. A. Sklar, GPR30: a G-protein-coupled receptor for estrogen, *Mol. Cell. Endocrinol.*, **265-266**, 138-142 (2007).
- [18] C. Carmeci, D. A. Thompson, H. Z. Ring, U. Francke and R. J. Weigel, Identification of a gene (GPR30) with homology to the G-protein-coupled receptor superfamily associated with estrogen receptor expression in breast cancer, *Genomics*, **45**, 607-617 (1997).
- [19] E. J. Filardo, J. Quinn, Y. Pang, C. Graeber, S. Shaw, J. Dong, and P. Thomas, Activation of the Novel Estrogen Receptor G-Protein-Coupled Receptor 30 (GPR30) at the Plasma Membrane, *Endocrinology*, **148**, 3236-3245 (2006).
- [20] E. J. Filardo, C. T. Graeber, J. A. Quinn, M. B. Resnick, D. Giri, R. A. De Lellis, M. M. Steinhoff and E. Sabo, Distribution of GPR30, a seven-membrane-spanning estrogen receptor, in breast cancer and its association with clinicopathological determinants of tumor progression, *Clin. Canc. Res.*, **12**, 6559-6566 (2006).

- [21] E. A. Disalvo , F. Lairion , F. Martini , E. Tymczyszyn, M. Frías , H. Almaleck, and G. J. Gordillo, Structural and functional properties of hydration and confined water in membrane interfaces, *Biochimica et Biophysica Acta*, **1778**, 2655-2670 (2008).
- [22] Y. Nagata and S. Mukamel, Spectral Diffusion at the Water/Lipid Interface Revealed by Two-Dimensional Fourth-Order Spectroscopy: A Classical Simulation Study, *J. Am. Chem. Soc.*, **133**, 3276-3279 (2011).
- [23] K. M. Sanchez, G. Kang, B. Wu, and J. E. Kim, Tryptophan-Lipid Interactions in Membrane Protein Folding Probed by Ultraviolet Resonance Raman and Fluorescence Spectroscopy, *Biophysical Journal*, **100** ,2121–2130 (2011).
- [24] M. P. Nieh, T. A. Harroun, V. A. Raghunathan, C. J. Glinka, and J. Katsaras, Spontaneously Formed Monodisperse Biomimetic Unilamellar Vesicles: The Effect of Charge, Dilution, and Time, *Biophys J.*, **86**, 2615–2629 (2004).
- [25] C. W. Meuse, G. Niaura, M. L. Lewis, and A. L. Plant, Assessing the Molecular Structure of Alkanethiol Monolayers in Hybrid Bilayer Membranes with Vibrational Spectroscopies, *Langmuir*, **14**, 1604-1611 (1998).
- [26] R. A. Walker, J. A. Gruetzmacher and G. L. Richmond, Phosphatidylcholine monolayer structure at a liquid-liquid interface, *J. Am. Chem. Soc.*, **120**, 6991-7003 (1998).
- [27] M. J. Hope, M. B. Bally, L. D. Mayer, A. Janoff and P. R. Cullis, Generation of multilamellar and unilamellar phospholipid vesicles, *Chemistry and Physics of Lipids*, **40**, 89-107 (1986).
- [28] P. Walde, K. Cosentino, H. Engelc, and P. Stano, Giant Vesicles: Preparations and Applications, *ChemBioChem*, **11**, 848-865 (2010).
- [29] N. Kucerka, Y. Liu, N. Chu, H. I. Petrache, S. Tristram-Nagle, and J. F. Nagle, Structure of Fully Hydrated Fluid Phase DMPC and DLPC Lipid Bilayers Using X-Ray Scattering from Oriented Multilamellar Arrays and from Unilamellar Vesicles, *Biophysical Journal*, **88**, 2626–2637 (2005).
- [30] S. Ahmed and S. L. Wunder, Effect of High Surface Curvature on the Main Phase Transition of Supported Phospholipid Bilayers on SiO<sub>2</sub> Nanoparticles, *Langmuir*, **25**, 3682-3691 (2009).

- [31] D. Needham and E. Evans, Structure and Mechanical Properties of Giant Lipid (DMPC) Vesicle Bilayers from 20°C below to 10°C above the Liquid Crystal-Crystalline Phase Transition at 24 °C, *Biochemistry*, **27**, 8261-8269 (1988).
- [32] R. Caputo, A. DeLuca, L. De Sio, L. Pezzi, G. Strangi, C. Umeton, A. Veltri, R. Asquini, A. d'Alessandro, D. Donisi, R. Beccherelli, A. V. Sukhov and N. V. Tabiryan, POLICRYPS: a liquid crystal composed nano/microstructure with a wide range of optical and electro-optical applications, *J. Opt. A: Pure Appl. Opt.*, **11**, 024017 (2009).
- [33] J. D. Margerum, A. M. Lackner, E. Ramos, G. W. Smith, N. A. Vaz, J. L. Kohler and C. R. Allison, Polymer dispersed liquid crystal film devices US Patent Specification, **5**, 096,282 (March 17) (1992).
- [34] R. L. Sutherland, V. P. Tondiglia, L. V. Natarajan, T. J. Bunning and W. W. Adams, Electro-optical switching characteristics of volume holograms in polymer dispersed liquid crystals, *J. Nonlinear Opt. Phys. Mater.*, **5**, 89–98 (1996).
- [35] R. L. Sutherland, V. P. Tondiglia, L. V. Natarajan, T. J. Bunning and W. W. Adams, Electrically switchable volume gratings in polymer-dispersed liquid crystals, *Appl. Phys. Lett.*, **64**, 1074–6 (1994).
- [36] R. Caputo, A. V. Sukhov, N. V. Tabiryan, C. Umeton and R. F. Ushakov Mass transfer processes induced by inhomogeneous photo-polymerisation in a multicomponent medium *Chem. Phys.*, **271**, 323–35 (2001).
- [37] R. Caputo, C. Umeton, A. Veltri, A. Sukhov and N. Tabiryan, Holographic diffraction grating, process for its preparation and opto-electronic devices incorporating it European Patent Request 1649318; US Patent Request 2007/0019152A1 (2005–2007).
- [38] R. Caputo, L. De Sio, A. V. Sukhov, A. Veltri and C. Umeton, Development of a new kind of switchable holographic grating made of liquid crystal films separated by slices of polymeric material (policryps), *Optics Letters*, **29**, 1261-1263 (2004).

*Chapter 3*

**RAMAN SPECTROSCOPY**

### 3.1 Raman Scattering

#### 3.1.1 Raman effect

Since the discovery of the Raman scattering in the 1928 a huge number of related reports and monographs have been written regarding the theories, instrumentations, applications and interpretations of the spectra [1-6].

When a radiation, monochromatic of frequency  $\omega_I$  is incident on a material, some “part” of the radiation is transmitted, some reflected and some scattered. The scattered radiations may show three kind of frequencies ( $\omega_s$ ):  $\omega_I$  and  $\omega_I \pm \omega_M$ , where  $\omega_M$  are the frequencies of some transitions which occur in the material.

The scattering without change of frequency is called Rayleigh and it is also said elastic scattering whereas the scattering that depends on the transitions of the material is called Raman scattering or inelastic scattering.

In the Raman scattering the lines or bands with frequencies lower than the frequency of the incident radiation are called Stokes while those with increased frequencies are called anti-Stokes.

In both classical and quantum models the origin of the scattered radiation is attributed to the oscillating electric dipole moments induced by the incident electromagnetic radiation. The contributions of the oscillating magnetic dipole and electric quadrupole are several order of magnitude smaller with respect to the dipole electric contribution, and for this reason they will not be considered in this treatment.

The intensity ( $I$ ) of the scattered radiation radiated by an oscillating electric dipole induced by the electrical field of the radiation incident ( $\omega_I$ ) is given by:

$$I = \frac{\omega_s^4 p_0^2 \sin^2 \theta}{32\pi^2 \varepsilon_0 c_0^3} = \frac{\pi^2 c_0 \tilde{\nu}_s^4 p_0^2 \sin^2 \theta}{2\varepsilon_0} \quad (3.1.1)$$

where  $\omega_s$  ( $\omega_s = 2\pi c_0 \tilde{\nu}_s$ ) and  $p_0$  are the frequency and the amplitude of the induced electrical dipole and  $\theta$  is the angle between the electrical field of the radiation and the axis of the dipole.

The induced electric dipole moment vector  $\vec{P}$  (time dependent) is linearly dependent on the electric field  $\vec{E}$  of the incident radiation:

$$\vec{P} = \vec{\alpha}\vec{E} \quad (3.1.2)$$

where  $\vec{\alpha}$  is the polarizability tensor, that is a II rank tensors.

Let consider just one molecule that is able to vibrate only (it cannot rotate). In this case, the polarizability can be modified during the molecular vibration and so the variation of the polarizability can be expressed by expanding each component (for instance  $\alpha_{xy}$ ) of the polarizability tensor in a Taylor series with respect to the normal coordinates of vibration:

$$\alpha_{xy} = (\alpha_{xy})_0 + \sum_k \left( \frac{\partial \alpha_{xy}}{\partial Q_k} \right)_0 Q_k + \frac{1}{2} \sum_{k,l} \left( \frac{\partial^2 \alpha_{xy}}{\partial Q_k \partial Q_l} \right)_0 Q_k Q_l + \dots \quad (3.1.3)$$

where  $(\alpha_{xy})_0$  is the value of  $\alpha_{xy}$  at the equilibrium configuration and  $Q_k, Q_l$  are normal coordinates of vibration associated with the molecular frequencies  $\omega_k, \omega_l$  and the summations are over all the normal coordinates.

In “harmonic approximation” the eq. 3.1.3 is taken with the term that involve only the first power of  $Q$ .

The eq. 3.1.3 can be rewritten as:

$$(\alpha_{xy})_k = (\alpha_{xy})_0 + (\alpha'_{xy})_k Q_k \quad (3.1.4)$$

where

$$(\alpha'_{xy})_k = \left( \frac{\partial \alpha_{xy}}{\partial Q_k} \right)_0 \quad (3.1.5)$$

The  $(\alpha'_{xy})_k$  are the components of a new tensor  $\vec{\alpha}'_k$  called derived polarizability tensor because all its elements are polarizability derivatives with respect to the normal coordinate.

Therefore, the eq. 3.1.4 in vector form becomes:

$$\vec{\alpha}_k = \vec{\alpha}_0 + \vec{\alpha}'_k Q_k \quad (3.1.6)$$

The scalar quantity  $Q_k$ , in the harmonic approximation, is given by:

$$Q_k = Q_{k_0} \cos(\omega_k t + \delta_k) \quad (3.1.7)$$

where  $Q_{k_0}$  is the amplitude of the normal coordinate and  $\delta_k$  is a phase factor.

The frequency dependence of the electric field of the incident radiation can be given by:

$$\vec{E} = \hat{E}_0 \cos \omega_1 t \quad (3.1.8)$$

Substituting, the eq. 3.1.7, into eq. 3.1.6 and then taking in account the eq. 3.1.8 the eq. 3.1.2 can be written as:

$$\vec{P} = \vec{\alpha}_0 \hat{E}_0 \cos \omega_1 t + \frac{1}{2} \vec{\alpha}'_k \hat{E}_0 [\cos(\omega_1 t + \omega_k t + \delta_k) + \cos(\omega_1 t - \omega_k t - \delta_k)] \quad (3.1.9)$$

where the term  $\vec{\alpha}_0 \hat{E}_0 \cos \omega_1 t$  represents the “classical” Rayleigh scattering, whereas the others two terms  $\frac{1}{2} \vec{\alpha}'_k \hat{E}_0 \cos(\omega_1 t + \omega_k t + \delta_k)$  and  $\frac{1}{2} \vec{\alpha}'_k \hat{E}_0 \cos(\omega_1 t - \omega_k t - \delta_k)$  are indicating the anti-Stokes and Stokes bands of the Raman scattering, respectively.

It can be noticed that the Rayleigh scattering has the same phase of the incident radiation while the Raman scattering does not: the quantity  $\delta_k$  defines the phase of the normal vibration  $Q_k$  respect to the electrical field. Raman scattering arise from electric dipole oscillating at  $\omega_1 \pm \omega_k$  frequencies that are produced when the electrical dipole

oscillating at frequency  $\omega_l$  is modulated by the “system” oscillation at frequency  $\omega_k$ . Indeed, Rayleigh scattering come up by the oscillation at  $\omega_l$  of the electric dipole induced by the electrical field of the incident radiation and where  $\omega_l$  represents the frequency of the electrical field.

The necessary condition for obtaining Raman scattering is that at least one component of the derived polarizability tensor  $\tilde{\alpha}'_k$  be non-zero. From eq. 3.1.5, each component  $(\alpha'_{xy})_k$  of the derived polarizability tensor  $\tilde{\alpha}'_k$  is the derivative of the corresponding component of the polarizability tensor with respect to the normal coordinate of vibration  $Q_k$  in its equilibrium position. Therefore, the condition for Raman activity is that, for at least one component of the polarizability tensor the gradient with respect to the normal coordinate, in its equilibrium position, must be non-zero.

It is worth to remember, that in order to obtain the eq. 3.1.9, the harmonic approximation has been done. Actually, if the mechanical anharmonicity is considered, the time dependence of the normal coordinate  $Q_k$  (eq. 3.1.7) will include terms as  $\cos(2\omega_k t + \delta_{2k})$ ,  $\cos(3\omega_k t + \delta_{3k})$  and so on, which produce bands called overtones and may be also terms as  $\cos(\omega_k t + \delta_{kl})\cos(\omega_l t + \delta'_{kl})$  which produce combinations tones. The resulting induced electric dipoles will oscillate with additional frequency terms as  $\omega_l \pm 2\omega_k$  etc, and  $\omega_l \pm (\omega_k \pm \omega_l)$  etc.

### 3.1.2 Quantum approach

The classical theory of Raman scattering is not able to explain thoroughly the Raman phenomena: for example it can not be applied to the molecular rotation whose discrete rotational energy levels, are typical quantum states. Furthermore the intensity difference between Stokes and anti-Stokes is not accounted for in a classical approach.

A general quantum approach for explaining this phenomena starts by considering the radiation as a photon population. Let be the incident radiation made with  $n_l$  photons and  $E_i$  the initial energetic level of the system. After the interaction with the system the radiation will have  $(n_l - 1)$  photons with the same frequency of the incident radiation ( $\omega_l$ ), the system will be in the  $E_f$  level and the one photon scattered will have frequency



$\omega_s$  which, in order to respect the conservation of the energy the frequency, will be:  $\omega_s = \omega_I - \omega_M$  where  $\omega_M = 2\pi(E_f - E_i)/h$ . Anyway, not real absorption process, spectroscopically speaking, are involved in this process: the amount  $\hbar\omega_I$  does not induce any electronic transition but just perturbs the system. Moreover, if it does approaches to the electronic transition energy an enhancement of the intensity of the scattered radiation can occur.

The global scattering process evokes two photon global process: one incident and one scattered. If  $E_f = E_i$  then  $\omega_s = \omega_I$  ( $\omega_M = 0$ ) and this is the case of the Rayleigh scattering otherwise if  $E_f > E_i$  then  $\omega_s = \omega_I - \omega_M$  and this is the Stokes Raman scattering while if  $E_f < E_i$  then  $\omega_s = \omega_I + \omega_M$  that is anti Stokes Raman scattering.

Absorption without the conservation of the energy is usually called “virtual” and the same adjective is used for the state of the energy where the material is found after an “virtual absorption” process.

Anyway, in order to explain the Raman effect deeper considerations have to be done.

The time dependent perturbation theory can be usefully applied in order to better describe the Raman effect.

In quantum mechanical treatments the induced electrical dipole of classical theory is replaced by the transition electric dipole associated to the transition from an initial state  $i$  to a finale state  $f$  induced by the electric field of the radiation which frequency  $\omega_I$ .

The total induced transition electric dipole vector is given by:

$$\left(\vec{P}\right)_{fi} = \left(\vec{P}^{(1)}\right)_{fi} + \left(\vec{P}^{(2)}\right)_{fi} + \left(\vec{P}^{(3)}\right)_{fi} + \dots \quad (3.1.10)$$

where  $\left(\vec{P}^{(1)}\right)_{fi}$  is the term which is linear with  $\vec{E}$ , and so, it will be the only one considered in this simplified approach to Raman scattering.

The term  $\left(\vec{P}^{(0)}\right)_{fi}$  due to the permanent electric dipole transition is independent from the electrical field of the incident radiation and it is not involved in Raman effect and for this reason here it was not considered.

The total transition electric dipole is given by:

$$\langle \psi'_f | \hat{P} | \psi'_i \rangle \quad (3.1.11)$$

where  $\psi'_i$  and  $\psi'_f$  are the time dependent perturbed wave functions of initial and final states, respectively and  $\hat{P}$  is the electric dipole moment operator. The  $\psi'_i$  and  $\psi'_f$  wave functions can be represented by:

$$\psi'_i = \psi_i^{(0)} + \psi_i^{(1)} + \psi_i^{(2)} + \dots + \psi_i^{(n)} \quad (3.1.12.a)$$

$$\psi'_f = \psi_f^{(0)} + \psi_f^{(1)} + \psi_f^{(2)} + \dots + \psi_f^{(n)} \quad (3.1.12.b)$$

where the apexes (0), (1), (2) ... indicate the order of the modification induced by the electric field:  $\psi^{(0)}$  unperturbed state,  $\psi^{(1)}$  first order modification,  $\psi^{(2)}$  second order modification and so on. Because the field acts on  $\psi^{(0)}$  once to give  $\psi^{(1)}$  and twice to give  $\psi^{(2)}$ , it is possible for Raman effect treatment to neglect the higher orders. So that, taking in account the eqs. 3.1.12 and by considering the terms linearly dependent to the electric field, the eq. 3.1.11 becomes

$$\left( \hat{P}^{(1)} \right)_{fi} = \langle \psi_f^{(1)} | \hat{P} | \psi_i^{(0)} \rangle + \langle \psi_f^{(0)} | \hat{P} | \psi_i^{(1)} \rangle \quad (3.1.13)$$

In order to maintain the treatments general the amplitudes of the electrical field should be considered to be complex and thus the eq. 3.1.13 can be written as:

$$\left( \tilde{P}^{(1)} \right)_{fi} = \langle \psi_f^{(1)} | \hat{P} | \psi_i^{(0)} \rangle + \langle \psi_f^{(0)} | \hat{P} | \psi_i^{(1)} \rangle \quad (3.1.14)$$

and define the real induced transition electric dipole moment  $\left( \hat{P}^{(1)} \right)_{fi}$  as

$$\left( \hat{P}^{(1)} \right)_{fi} = \left( \tilde{P}^{(1)} \right)_{fi} + \left( \tilde{P}^{(1)} \right)_{fi}^* \quad (3.1.15)$$

where  $(\tilde{P}^{(1)})_{fi}^*$  is the conjugate complex of  $(\tilde{P}^{(1)})_{fi}$ .

In order to express the component  $(P_x^{(1)})_{fi}$ , let be  $\psi_i$ ,  $\psi_r$  and  $\psi_f$  the wave functions time independent unperturbed of the states  $i$ ,  $r$  and  $f$ , respectively. The relationship between the time dependent function  $\Psi_r$  and the unperturbed correspondent wave function is given by:

$$\Psi_r = \psi_r e^{-i(\omega_r - i\Gamma_r)t} \quad \text{where} \quad \omega_r = \frac{E_r}{\hbar} \quad (3.1.16)$$

The coefficient  $(2\Gamma_r)$  is related to the full width of the level  $r$ . The lifetime  $\tau_r$  of the level  $r$  will be given, by the uncertainty principle by:

$$\tau_r = \frac{\hbar}{2\Gamma_r} \quad (3.1.17)$$

Thus,  $(P_x^{(1)})_{fi}$  is given by:

$$\begin{aligned}
(P_x^{(1)})_{fi} = & \frac{1}{2\hbar} \sum_{r \neq i} \left\{ \frac{\langle \psi_f | \hat{P}_x | \psi_r \rangle \langle \psi_r | \hat{P}_y | \psi_i \rangle}{\omega_{ri} - \omega_1 - i\Gamma_r} \tilde{E}_{y_0} e^{-i(\omega_1 - \omega_{fi})t} + \right. \\
& \left. + \frac{\langle \psi_f | \hat{P}_x | \psi_r \rangle \langle \psi_r | \hat{P}_y | \psi_i \rangle}{\omega_{ri} + \omega_1 + i\Gamma_r} \tilde{E}_{y_0}^* e^{i(\omega_1 + \omega_{fi})t} \right\} + \\
& + \frac{1}{2\hbar} \sum_{r \neq f} \left\{ \frac{\langle \psi_f | \hat{P}_y | \psi_r \rangle \langle \psi_r | \hat{P}_x | \psi_i \rangle}{\omega_{rf} - \omega_1 - i\Gamma_r} \tilde{E}_{y_0}^* e^{i(\omega_1 + \omega_{fi})t} + \right. \\
& \left. + \frac{\langle \psi_f | \hat{P}_y | \psi_r \rangle \langle \psi_r | \hat{P}_x | \psi_i \rangle}{\omega_{rf} + \omega_1 + i\Gamma_r} \tilde{E}_{y_0} e^{-i(\omega_1 - \omega_{fi})t} \right\} + \\
& + \text{complex conjugate}
\end{aligned} \tag{3.1.18}$$

where,  $\tilde{E}_{y_0}$ , is the component y of the complex amplitude of the harmonic electromagnetic wave incident and the double subscript on  $\omega$  indicates a correspondence of the frequency with the energy difference between the levels.

The initial and final states have their lifetime infinite and so that their total wave functions will be:

$$\Psi_i = \psi_i e^{-i\omega_i t} \tag{3.1.19.a}$$

$$\Psi_f = \psi_f e^{-i\omega_f t} \tag{3.1.19.b}$$

Two types of terms, can be seen in the eq. 3.1.18, looking at the exponential terms in regards their frequency dependency: namely,  $(\omega_1 - \omega_{fi})$  and  $(\omega_1 + \omega_{fi})$ .

The terms that in eq. 3.1.18 involve the factor  $(\omega_1 + \omega_{fi})$  describe the induced emission of two quanta:  $(\omega_1 + \omega_{fi})$  and  $(\omega_1)$  from an initial state, which is an excited level  $i$ , to a lower energy level  $f$ , if  $\omega_1 + \omega_{fi} > 0$ .

The others terms in eq. 3.1.18 which involve the frequency dependency described by  $(\omega_1 - \omega_{fi})$  are at the origin of the scattering (if  $\omega_1 - \omega_{fi} > 0$ ) and dependently to  $\omega_{fi}$  it will have:

$\omega_{fi} > 0$  Stokes Raman scattering

$\omega_{fi} = 0$  Rayleigh scattering

$\omega_{fi} < 0$  anti-Stokes Raman scattering.

For the rotational and vibrational transitions that do not involve electronic transitions the condition that  $\hbar\omega_1 - \hbar\omega_{fi} > 0$  is always satisfied for frequency of the incident radiation that fall in the visible –ultraviolet regions.

So that, considering what has been said above, the Stokes and anti-Stokes part of the x component of the real induced transition electric dipole moment are given by:

$$\begin{aligned} (P_x^{(1)})_{fi} = \frac{1}{2\hbar} \sum_{r \neq i, f} \left\{ \frac{\langle \psi_f | \hat{P}_x | \psi_r \rangle \langle \psi_r | \hat{P}_y | \psi_i \rangle}{\omega_{ri} - \omega_1 - i\Gamma_r} + \right. \\ \left. + \frac{\langle \psi_f | \hat{P}_y | \psi_r \rangle \langle \psi_r | \hat{P}_x | \psi_i \rangle}{\omega_{rf} + \omega_1 + i\Gamma_r} \right\} \tilde{E}_{y_0} e^{-i\omega_s t} + \end{aligned} \quad (3.1.20)$$

+ complex conjugate

where

$$\omega_s = \omega_1 - \omega_{fi} \quad (3.1.21)$$

that is the absolute frequency of the scattered radiation.

Therefore, the equation,

$$\boxed{(\alpha_{xy})_{fi} = \frac{1}{\hbar} \sum_{r \neq i, f} \left\{ \frac{\langle \psi_f | \hat{P}_x | \psi_r \rangle \langle \psi_r | \hat{P}_y | \psi_i \rangle}{\omega_{ri} - \omega_1 - i\Gamma_r} + \frac{\langle \psi_f | \hat{P}_y | \psi_r \rangle \langle \psi_r | \hat{P}_x | \psi_i \rangle}{\omega_{rf} + \omega_1 + i\Gamma_r} \right\}} \quad (3.1.22)$$

defines the component of the general transition polarizability  $(\hat{\alpha})_{fi}$ .

The restriction  $r \neq i, f$  is only due to simplify the treatment, and however, the initial and the final state in a lot of cases do not add any contributions to the polarizability or if they do the contributions are smaller respect to that obtained from the rest part of the summation and thus negligible.

Independently from the sign of the term  $i\Gamma_r$ , which makes the eq. 3.1.22 complex, the interest is devoted to those frequencies conditions where the term  $i\Gamma_r$  can be ignored and the transition polarizability becomes real and it will be given by:

$$(\alpha_{xy})_{fi} = \frac{1}{\hbar} \sum_{r \neq i, f} \left\{ \frac{\langle \psi_f | \hat{P}_x | \psi_r \rangle \langle \psi_r | \hat{P}_y | \psi_i \rangle}{\omega_{ri} - \omega_1} + \frac{\langle \psi_f | \hat{P}_y | \psi_r \rangle \langle \psi_r | \hat{P}_x | \psi_i \rangle}{\omega_{rf} + \omega_1} \right\} \quad (3.1.23)$$

So that, the eq. 3.1.20 becomes:

$$\left( P_x^{(1)} \right)_{fi} = \frac{1}{2} (\alpha_{xy})_{fi} \left( \tilde{E}_{y_0} e^{-i\omega_s t} + \tilde{E}_{y_0}^* e^{i\omega_s t} \right) \quad (3.1.24)$$

that can be conveniently expressed as

$$\left( P_x^{(1)} \right)_{fi} = \frac{1}{2} \left( \left( \tilde{P}_{x_0}^{(1)} \right)_{fi} e^{-i\omega_s t} + \left( \tilde{P}_{x_0}^{(1)} \right)_{fi}^* e^{i\omega_s t} \right) \quad (3.1.25)$$

where the x component of the time independent complex transition moment amplitude and its conjugate complex have been used:

$$\left(\tilde{P}_{x_0}^{(1)}\right)_{fi} = \left(\alpha_{xy}\right)_{fi} \tilde{E}_{y_0} \quad (3.1.26.a)$$

$$\left(\tilde{P}_{x_0}^{(1)}\right)_{fi}^* = \left(\alpha_{xy}\right)_{fi} \tilde{E}_{y_0}^* \quad (3.1.26.b)$$

When the amplitude of the electrical field is real then  $\tilde{E}_{y_0} = \tilde{E}_{y_0}^* = E_{y_0}$  and

$$\left(\tilde{P}_{x_0}^{(1)}\right)_{fi} = \left(\tilde{P}_{x_0}^{(1)}\right)_{fi}^* \text{ which may be substituted by } \left(P_{x_0}^{(1)}\right)_{fi}.$$

Then the eq. 3.1.25 becomes:

$$\left(P_x^{(1)}\right)_{fi} = \frac{1}{2} \left(P_{x_0}^{(1)}\right)_{fi} \left(e^{-i\omega_s t} + e^{i\omega_s t}\right) = \left(P_{x_0}^{(1)}\right)_{fi} \cos \omega_s t \quad (3.1.27)$$

where:

$$\left(P_{x_0}^{(1)}\right)_{fi} = \left(\alpha_{xy}\right)_{fi} E_{y_0}. \quad (3.1.28)$$

Replacing the eq. 3.1.28 in the eq. 3.1.27 then:

$$\left(P_x^{(1)}\right)_{fi} = \left(\alpha_{xy}\right)_{fi} E_{y_0} \cos \omega_s t \quad (3.1.29)$$

that is “similar” to that obtained from the classical treatment.

The electric field has still the same classical form. Indeed, the transition electric dipole and polarizability are defined in terms of wave functions and energy levels of the system which relate that the characteristics of the scattered radiations to the properties of the materials.

In order to derive the eq. 3.1.22 no restriction regarding the relationship between the frequency of the incident photon ( $\hbar\omega_i$ ) and to any absorption energy material gap ( $\hbar\omega_{ri}$ ) have been requested. Idem, for the energy of the state  $\psi_r$ , which in principle can lie above or below the energies correspondent to  $\psi_f$  and  $\psi_i$  states (Fig. 3.1.1).

These aspects are important to determine the general transition polarizability given in the eq. 3.1.22.

In the first denominator  $(\omega_{ri} - \omega_1 - i\Gamma_r)$  (eq. 3.1.22) the relative magnitude of  $\omega_1$  and  $\omega_{ri}$  can be determinant because the difference of those is involved.

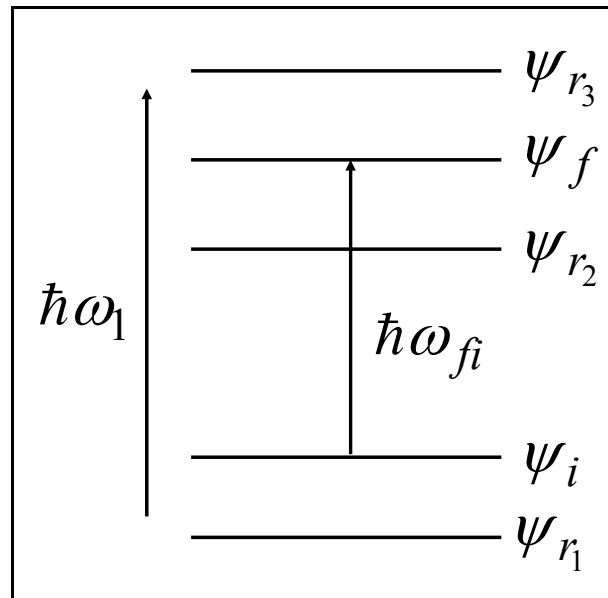


Fig.3.1.1 Energy levels of the  $\Psi_r$  states.

Two cases are possible in order to analyze the behaviour of this denominator:

- 1)  $\omega_1 \ll \omega_{ri}$  the frequency of the incident radiation  $\omega_1$  is much smaller than any absorption frequency  $\omega_{ri}$ . If this happens then  $\omega_{ri} - \omega_1 \approx \omega_{ri}$  for all the states  $\Psi_r$  and the factors  $\Gamma_r$  can be considered negligible with respect to  $\omega_{ri}$ .
- 2)  $\omega_1 \approx \omega_{ri}$  the frequency of the incident radiation  $\omega_1$  is close to one or more particular absorption frequencies  $\omega_{ri}$ . It makes the denominator to tend to  $-i\Gamma_r$  for a particular state  $\Psi_r$  which will result predominant in all the sum over  $r$ .

The case  $\omega_1 \ll \omega_{ri}$  is illustrated in Fig.3.1.2.a, where the incident radiation induces an transition from the initial stationary state to a, so said, virtual state from which it makes a transition to a final stationary state. The virtual states are not stationary states and do



not correspond to a well defined energy values; they are not solutions of the Schrodinger equation.

When the frequencies of the incident radiation approach to the molecular transition frequency others characteristic Raman scattering occur (Fig. 3.1.2).

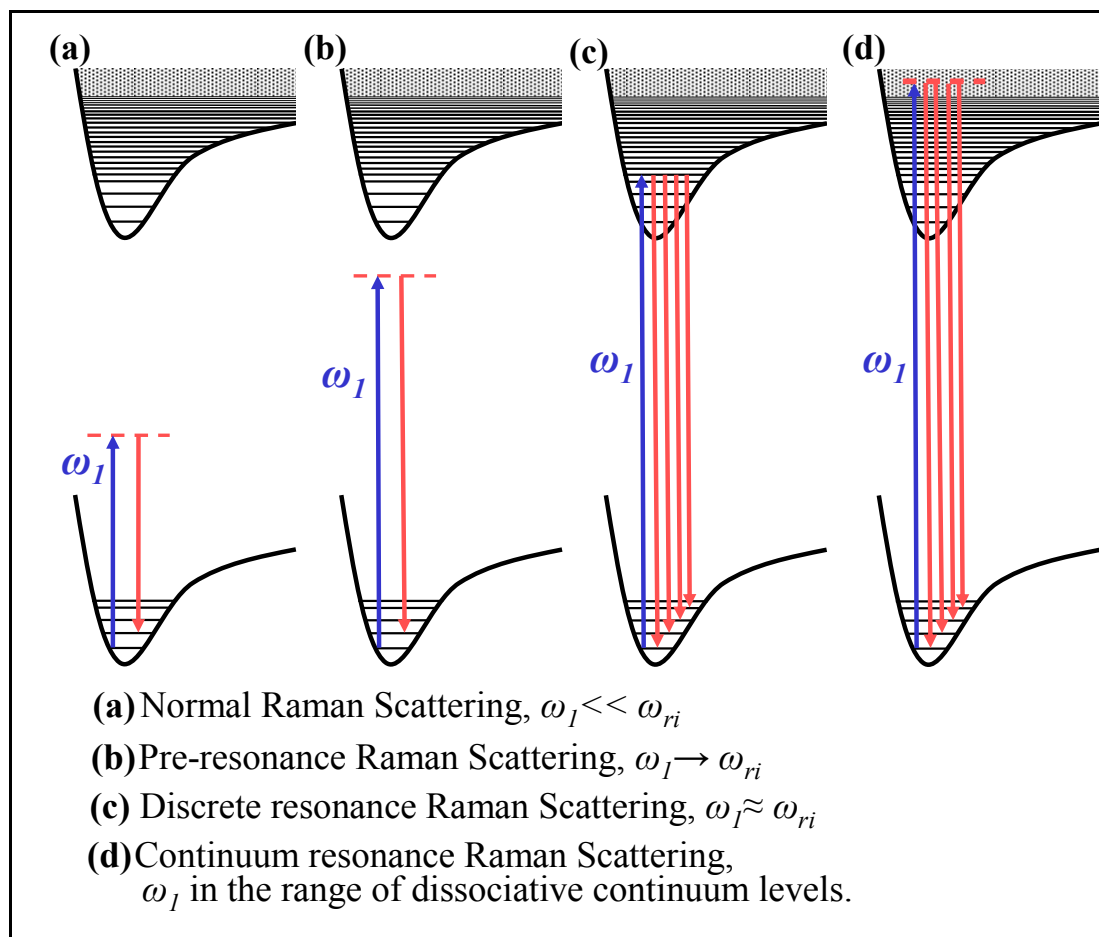


Fig.3.1.2 Raman scattering processes.

The intensity of the resonance Raman scattering, can be orders of magnitude greater than normal Raman scattering.

The second denominator  $(\omega_{ri} + \omega_1 + i\Gamma_r)$  in the eq.3.1.22 can not be zero because it involve the sum of  $\omega_{ri}$  and  $\omega_1$ . Thus, the contribution, coming from it, to  $(\alpha_{xy})_{fi}$  can be neglected when the first term has one or more dominant terms. Only if stimulated emission occurs the effect of the second term cannot be neglected.

The numerator of the first term in the eq.3.1.22 has two transition dipole terms:  $\langle \psi_r | \hat{P}_y | \psi_i \rangle$  and  $\langle \psi_f | \hat{P}_x | \psi_r \rangle$ . The first one represents the transition from the initial state  $\psi_i$  to the virtual state  $\psi_r$ , and the second one the transition from the virtual state  $\psi_r$  to the final state  $\psi_f$ . Therefore, for normal Raman scattering,  $\omega_1 \ll \omega_{ri}$ ,  $(\alpha_{xy})_{fi}$  is determined by a sum over the  $\psi_r$  states, weighted by factors  $(\omega_{ri} - \omega_1 - i\Gamma_r)^{-1}$ , of the products  $\langle \psi_f | \hat{P}_x | \psi_r \rangle \langle \psi_r | \hat{P}_y | \psi_i \rangle$ .

Therefore, the normal Raman scattering can be considered as the transition between the initial state and the final state passing to all the virtual states  $\psi_r$  where the electric dipole transition between the  $\psi_r$  states and the  $\psi_i$  and  $\psi_f$  states are not zero.

In resonance Raman scattering, the state  $\psi_r$  for which the condition  $\omega_1 \approx \omega_{ri}$  is obtained, is predominant in the sum and the properties of  $(\alpha_{xy})_{fi}$  reflected the properties of a limited number of  $\psi_r$  states.

### 3.1.3 Intensity of Raman scattered radiation

Let be  $\mathfrak{R}$  (the amount of the radiation which passes through a surface of unit area perpendicular to the propagation direction in one second) the irradiance of the incident radiation given by:

$$\mathfrak{R} = \frac{1}{2} c_0 \varepsilon_0 E_0^2 \quad [W \ m^{-2}] \quad (3.1.30)$$

and  $I$ , the radiant intensity of a point source (is the ratio of the time-average power  $d\Phi$ , in a given direction contained in a conical beam of solid angle  $d\Omega$  about this direction, to the solid angle  $d\Omega$ ), given by:

$$I = \frac{d\Phi}{d\Omega} \quad [W \ sr^{-1}] \quad (3.1.31)$$

Then, the relationship between the intensity of the Rayleigh or Raman scattered radiation from a single molecule and the irradiance ( $\mathfrak{R}$ ) of the incident radiation can be given by:

$$I = \sigma' \mathfrak{R} \quad (3.1.32)$$

where  $\sigma'$  is the first differential scattering cross-section per molecule and it has the units  $[m^2 sr^{-1} molecule^{-1}]$ .

The total scattering cross section per molecule,  $\sigma$ , is defined as:

$$\sigma = \int_0^{4\pi} \sigma' d\Omega \quad [m^2 molecule^{-1}] \quad (3.1.33)$$

If the scattered intensity is function also of the wavenumber then the second differential cross section  $\sigma''$  will consider the last dependence:

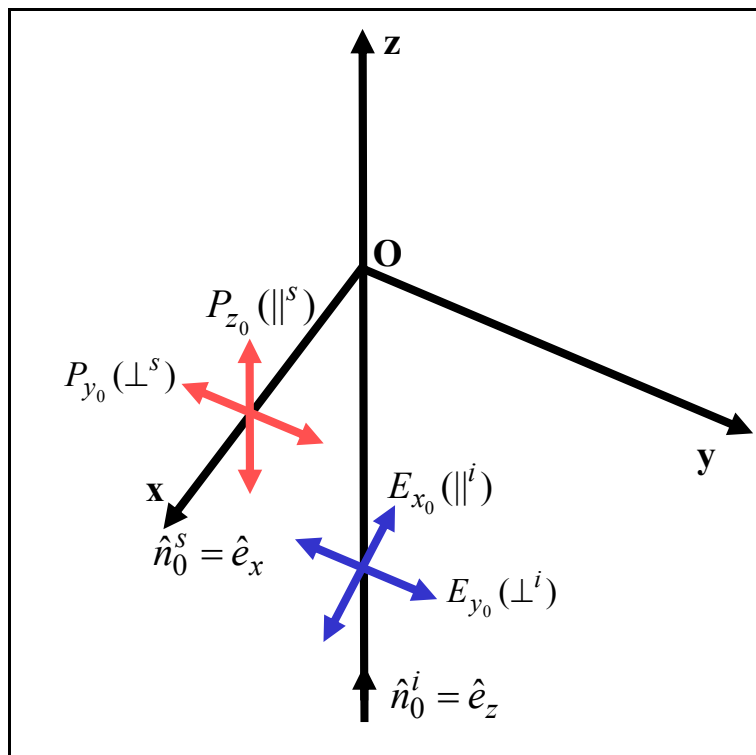
$$\sigma'' = \frac{\partial \sigma'}{\partial \tilde{\nu}} = \frac{\partial^2 \sigma}{\partial \tilde{\nu} \partial \Omega} \quad [m sr^{-1} molecule^{-1}] \quad (3.1.34)$$

It is wanted to underline that differently from ( $I$ ) the cross sections do not depend by the incident irradiance and are characteristic of the materials.

Before to go ahead with the considerations regarding the scattering geometry shown in Figure 3.1.2 is useful to write in explicit form the relation between the amplitude of the components of the induced electric moment vector and the components of the electric field:

$$\begin{cases} p_{x_0} = (\alpha_{xx})E_{x_0} + (\alpha_{xy})E_{y_0} + (\alpha_{xz})E_{z_0} \\ p_{y_0} = (\alpha_{yx})E_{x_0} + (\alpha_{yy})E_{y_0} + (\alpha_{yz})E_{z_0} \\ p_{z_0} = (\alpha_{zx})E_{x_0} + (\alpha_{zy})E_{y_0} + (\alpha_{zz})E_{z_0} \end{cases} \quad (3.1.35)$$

Let be considered the geometry shown in Fig. 3.1.3 where  $\hat{e}_x, \hat{e}_y$  and  $\hat{e}_z$  are the unit vectors associated to the Cartesian axis system x, y, z.



**Fig.3.1.3** Components of  $E_0$  and  $P_0$  when  $\hat{n}_0^i = \hat{e}_z$  and  $\hat{n}_0^s = \hat{e}_x$ , respectively.

The terms  $\hat{n}_0^i, \hat{n}_0^s$  are the unit vector defining the directions of propagation of the incident and scattered observed radiations, respectively. These vectors define the scattering plane, and the field directions, in the following, will be described as parallel ( $\parallel$ ), when they belong to the plane, or perpendicular ( $\perp$ ) to this plane. For linear polarized incident radiation the components of the electric field of the incident radiation, propagated along z, are restricted to  $E_{x_0}(\parallel^i), E_{y_0}(\perp^i)$  and for scattered radiation with (i.e scattering angle  $\theta = 90^\circ$ ) the components of the polarization are restricted to  $P_{y_0}(\perp^s), P_{z_0}(\parallel^s)$ . The symbols in the brackets ( $\parallel^{s \text{ or } i}$ ), ( $\perp^{s \text{ or } i}$ ), indicate if the components of the scattered (s) or incident (i) radiations are parallel or

perpendicular, respectively, to the scattering plane defined by the unit vectors  $\hat{n}_0^i$  and  $\hat{n}_0^s$ .

If the intensity of the radiation polarized perpendicular to the scattering plane  $I(\pi/2, \perp^s, \perp^i)$  is observed, the only active components of the transition polarizability tensor along the diagonal will be  $(\alpha_{yy})$ , and  $I(\pi/2, \perp^s, \perp^i)$  will involve its isotropic average  $\langle (\alpha_{yy})^2 \rangle$  whereas in others configurations off diagonal terms of the transition polarizability tensor will be active and the relative intensity will involve their averages values.

Thus, for  $I(\pi/2, \parallel^s, \perp^i)$ ,  $(\alpha_{zy})$  will be the active components and  $\langle (\alpha_{zy})^2 \rangle$  will be the term involved in the intensity of the scattered radiation, for  $I(\pi/2, \parallel^s, \parallel^i)$ ,  $(\alpha_{zx})$  will be the active components and  $\langle (\alpha_{zx})^2 \rangle$  will contribute to the intensity and the last possibility, for the geometry shown in Fig.3.1.3, will be  $I(\pi/2, \perp^s, \parallel^i)$ , where  $(\alpha_{yx})$  will be the active component and  $\langle (\alpha_{yx})^2 \rangle$  will be involved in the intensity of the scattered radiation.

It is remarkable that all the isotropic average of the off diagonal components of the transition polarizability are equal between them but they are different from those obtained by the diagonal components.

Moreover, only in the first case ( $I(\pi/2, \perp^s, \perp^i)$ ) the components of the electrical field and the polarization are parallel each other while in the others cases they are always perpendicular. Therefore, just two appropriate measures of intensity of the scattered radiation are enough in order to characterize a symmetric transition polarizability tensor in the Cartesian basis: one should be  $I(\pi/2, \perp^s, \perp^i)$  and the other one can be any of the others three also if generally  $I(\pi/2, \parallel^s, \perp^i)$  is chosen.

Let be the components of the electric field of the incident radiation  $E_{x_0}(\parallel^i) = 0$  and  $E_{y_0}(\perp^i) \neq 0$ .

For a single molecule the components of the amplitude of the transition electric dipole moment  $\vec{P}_0$  will be:

$$P_{y_0}(\perp^s) = (\alpha_{yy})E_{y_0}(\perp^i) \quad (3.1.36)$$

$$P_{z_0}(\parallel^s) = (\alpha_{zy})E_{y_0}(\perp^i) \quad (3.1.37)$$

The intensity of the scattered radiation by  $N_{v^i}$  molecules of an ideal gas which are in the initial state  $v^i$ , in the geometry above described, will be obtained by multiplying for  $N_{v^i}$  the eq. 3.1.1 in which where  $\theta = 90^\circ$ , taking in account the eqs.3.1.36-3.1.37 where at the place of the square of the component of the transition polarizability tensor the corresponding isotropic average are used. Thus,

$$I(\pi/2, \perp^s, \perp^i) = \frac{N_{v^i} \omega_s^4 \langle (\alpha_{yy})^2 \rangle E_{y_0}^2(\perp^i)}{32\pi^2 \varepsilon_0 c_0^3} = \frac{\pi^2 c_0 N_{v^i} \tilde{\nu}_s^4 \langle (\alpha_{yy})^2 \rangle E_{y_0}^2(\perp^i)}{2\varepsilon_0} \quad (3.1.38)$$

$$I(\pi/2, \parallel^s, \perp^i) = \frac{N_{v^i} \omega_s^4 \langle (\alpha_{zy})^2 \rangle E_{y_0}^2(\perp^i)}{32\pi^2 \varepsilon_0 c_0^3} = \frac{\pi^2 c_0 N_{v^i} \tilde{\nu}_s^4 \langle (\alpha_{zy})^2 \rangle E_{y_0}^2(\perp^i)}{2\varepsilon_0} \quad (3.1.39)$$

For symmetric tensor, as the polarizability, the isotropic average can be expressed as:

$$\langle (\alpha_{yy})^2 \rangle = \frac{45a^2 + 4\gamma^2}{45} \quad (3.1.40)$$

$$\langle (\alpha_{zy})^2 \rangle = \frac{\gamma^2}{15} \quad (3.1.41)$$

The general definition of  $a^2$  and  $\gamma^2$  are:

$$a = \frac{1}{3}(\alpha_{xx} + \alpha_{yy} + \alpha_{zz}) \quad (3.1.42)$$

$$\begin{aligned} \gamma^2 = & \frac{1}{2} \left\{ |\alpha_{xx} - \alpha_{yy}|^2 + |\alpha_{yy} - \alpha_{zz}|^2 + |\alpha_{zz} - \alpha_{xx}|^2 \right\} + \\ & \frac{3}{4} \left\{ |\alpha_{xy} + \alpha_{yx}|^2 + |\alpha_{xz} + \alpha_{zx}|^2 + |\alpha_{yz} + \alpha_{zy}|^2 \right\} \end{aligned} \quad (3.1.43)$$

Introducing the irradiance  $\mathfrak{R}$  defined in eq.3.1.30 and, taking in account the eqs. 3.1.40-3.1.41, then the eqs. 3.1.38-3.1.39 become:

$$I(\pi/2, \perp^s, \perp^i) = \frac{N_{v,i} \omega_s^4}{16\pi^2 \varepsilon_0^2 c_0^4} \left\{ \frac{45a^2 + 4\gamma^2}{45} \right\} \mathfrak{R} = \frac{\pi^2 N_{v,i} \tilde{V}_s^4}{\varepsilon_0^2} \left\{ \frac{45a^2 + 4\gamma^2}{45} \right\} \mathfrak{R} \quad (3.1.44)$$

$$I(\pi/2, \parallel^s, \perp^i) = \frac{N_{v,i} \omega_s^4}{16\pi^2 \varepsilon_0^2 c_0^4} \left\{ \frac{\gamma^2}{15} \right\} \mathfrak{R} = \frac{\pi^2 N_{v,i} \tilde{V}_s^4}{\varepsilon_0} \left\{ \frac{\gamma^2}{15} \right\} \mathfrak{R} \quad (3.1.45)$$

The sum of the eqs 3.1.44 and 3.1.45 gives the total intensity of the radiation scattered when no care is devoted to the polarization of the scattered radiation:

$$I(\pi/2, \perp^s + \parallel^s, \perp^i) = \frac{N_{v,i} \omega_s^4}{16\pi^2 \varepsilon_0^2 c_0^4} \left\{ \frac{45a^2 + 7\gamma^2}{45} \right\} \mathfrak{R} = \frac{\pi^2 N_{v,i} \tilde{V}_s^4}{\varepsilon_0^2} \left\{ \frac{45a^2 + 7\gamma^2}{45} \right\} \mathfrak{R} \quad (3.1.46)$$

Continuing, the ratio of the eq. 3.1.45 by the eq. 3.1.44 define the depolarization ratio (also known as degree of polarization)  $\rho(\pi/2, \perp^i)$ :

$$\boxed{\rho(\pi/2, \perp^i) = \frac{I(\pi/2, \parallel^s, \perp^i)}{I(\pi/2, \perp^s, \perp^i)} = \left\{ \frac{3\gamma^2}{45a^2 + 4\gamma^2} \right\}} \quad (3.1.47)$$

If the components of the electric field of the incident radiation are inverted, that is,  $E_{x_0}(\parallel^i) \neq 0$  and  $E_{y_0}(\perp^i) = 0$  the active components of the transition polarizability tensor will be off diagonal, (eq. 3.1.35) and  $I(\pi/2, \perp^s, \parallel^i)$  will be equals to  $I(\pi/2, \parallel^s, \parallel^i)$  and is given in eq. 3.1.45. If  $\gamma \neq 0$  then the depolarization ratio  $\rho(\pi/2, \parallel^i)$  will be equals to 1.

Let consider the cases in which  $\theta = 0$  and  $\theta = -\pi$  (forward scattering and backscattering, respectively). In this particular case the scattering plane is not defined and the electric vectors are no more defined parallel or perpendicular to the plane. In any case we can still analyze the depolarization ratios.

$P_{y_0}^{(s)}$  and  $P_{x_0}^{(s)}$  are the components of the amplitude of the electric dipole moment  $\vec{P}_0$  involved. The active components of the polarizability tensor, from the eq. 3.1.35, if  $E_{x_0}(\parallel^i) = 0$  and  $E_{y_0}(\parallel^i) \neq 0$  are  $(\alpha_{yy})$ ,  $(\alpha_{xy})$  and the corresponding intensity of the scattered radiations  $I(0 \text{ or } -\pi, s \parallel i)$  and  $I(0 \text{ or } -\pi, s \perp i)$  will be given by the eq. 3.1.45 and eq. 3.1.44, respectively. It should be underlined that all the relationship for the intensity conduce to two geometries: the first one is that where the electrical vectors of the incident and the scattered radiations are parallel to each other and this case conduce to the expression containing  $\alpha$  and  $\gamma$ , while the second one is the case where the electric vectors are perpendicular and in this case only  $\gamma$  is involved.

### 3.1.4 Raman Scattering in Solid

In the previous paragraphs the Raman effect has been presented and it has been seen that the vibration is quantized.

Also in solid system the reticular vibration or elastic wave is quantized [7-8]. As well as for the electromagnetic wave the energy quantum is the photon for the reticular vibration the quantum of energy is called phonon. Nearly all the concepts developed for photon are valid for the phonon, for example: the wave-particle duality, and so on.



Let be, as above, a monochromatic light beam of frequency  $\omega_1$ . The light will propagate with the propagation vector  $\vec{k}_1$ ,  $|\vec{k}_1| = \omega_1 \cdot \eta(\omega_1) / c_0$  where  $\eta(\omega_1)$  is the refractive index.

The propagation vector of the scattered light is  $\vec{k}_s$ ,  $|\vec{k}_s| = \omega_s \cdot \eta(\omega_s) / c_0$ .

Thus, it is possible to define the scattering frequency as:

$$\omega = \omega_1 - \omega_s \quad (3.1.48)$$

and the scattered wave vector as

$$\vec{k} = \vec{k}_1 - \vec{k}_s \quad (3.1.49)$$

In order to have Raman scattering the conservation of the energy and of the moment laws (eqs. 3.1.48-3.1.49) must be satisfied.

In a perfect crystal the elementary excitations (phonon) are represented by the wave vector  $\vec{q}$  and frequency  $\omega_q$ , connected by a dispersion relation that specifies a frequency  $\omega_q$  for each value of  $\vec{q}$ .

In the first order process only one elementary excitation will take place and thus the scattered wave vector as well the scattering frequency will be equals to  $\vec{q}$  and  $\omega_q$  respectively.

For typical visible –near infrared set up the maximum phonon wave vector excited by the light has an order of magnitude  $\cong 10^4 \text{ cm}^{-1}$  that is much smaller (about three order of magnitude) of the wavevectors corresponding to the Brillouin zone boundary of typical crystals ( $\cong 10^7 \text{ cm}^{-1}$ ). Thus, for first order process that conserves the wave vector only elementary excitations close to the centre of the Brillouin zone must be considered. This, means intuitively,  $\vec{q} \cong 0$ , thus the incident radiations “sees” the many unit cells of a perfect crystal to vibrate in phase.

This allows to evaluate the symmetry of the vibrations by considering the point group symmetry of the unit cell instead of the space group symmetry, treating the unit cells as molecules, with the consequent reduced difficulty because the point groups are just 32 while the space group are 230.

The theoretical treatment of the Raman effect on solid crystalline systems can, therefore, be deal with the above exposed theories.

In imperfect crystals, with a small concentration of defects, as well as in solid solution or in amorphous solids the conservations of the wave vector is not anymore respected and Raman spectra display such features, reflecting the density of the states of the particular excitation and this aspect make the Raman spectroscopy to play a fundamental role in the characterization of such systems.

However, the condition of the conservation of the wave vector has to be studied with some attention when the systems are constitute by quantum structure such as artificial multilayer systems which display size quantization along one or more directions.

The size quantization, also known as confinement, occurs when there is a small characteristic length, so that along that direction the motion is quantized into distinct energy levels, as in a quantum well: for electrons typical lengths are in the nanometers range and the structures are said nanostructures.

The Raman spectra collected on amorphous materials will generally consist in broad bands with maxima approximately close to the frequency of the same mode of the materials in the crystalline phase, that shows a narrow bands. For this reason, Raman spectroscopy is a useful tools in order to study the structural phase transitions. Most studies show effects, on the materials, due to thermal or pressure treatment that usually are opposite: the increases of the temperature tends to increase the inter atomic distance while the increase of the pressure tends to reduce that.

The thermal expansion is usually associate to a decrease of vibrational frequencies, as observed in Raman measurements, while the bandwidth usually increase vs. temperature.

In addition to these general trend, specific interactions among vibrational modes in some narrow temperature range can occur, generating particular dependences on temperature, like anomalous band broadening at some temperature and anomalous decrease or increase of the frequency [9-11].

### 3.1.5 Raman Scattering in Polymer

Raman spectroscopy has been a useful tool for studying both amorphous and crystalline polymer structures. Raman spectroscopy in polymer science, is nowadays very common, because it can give information regarding the characterization of the molecular compositions, segmental orientational, chains conformation and, quite important, regarding intermolecular interactions. Moreover, since the Raman scattering from water is very much weak, it is used often in biological systems.

An area of current interest in polymer science is to use Raman spectroscopy in systems that show disordered chains that can affect macroscopic properties such as ionic conductivity, mechanical properties, solvation efficiency, corrosion inhibition and etc. In fact, the frequency and the relative intensity of the Raman bands depends on the relative concentrations of the specific localized structures. For systems that involve well defined structures and precise assignments to the Raman band the technique works very well. However, it is not easy to reach the results, because for disorder systems, the Raman bands are generally broad and weak and often they are overlapped. The efforts that should be done in order to have information regarding the macroscopic properties are often behind these features that have to be resolved.

However, changes of the polarizability associated with different carbon-carbon backbone conformations are shown in the Raman spectra. Being the Raman scattering associated to the transition of the polarizability tensor, Raman spectra collected in polarization way contains still considerable structural information for samples that are partially disordered or even those in melt or solution.

## 3.2 Surfaces Enhanced Raman Spectroscopy

Surfaces enhanced Raman spectroscopy was discovered, though not recognized as such, by Fleischmann et al. in 1974 [12] who observed intense Raman scattering from pyridine adsorbed onto a roughened silver electrode surface from aqueous solution. Jeanmaire and Van Duyne [13] and Albrecht and Creighton [14] recognized independently that the large intensities observed could not be accounted for simply by the increase in the number of scatterers present and proposed that an enhancement of the

scattered intensity occurred in the adsorbed state. Jeanmaire and Van Duyne tentatively proposed an electric field enhancement mechanism whereas Albrecht and Creighton speculated that resonance Raman scattering from molecular electronic states, broadened by their interaction with the metal surface, might be responsible; they were both right in concept, though not in detail [15].

Recently, SERS has been used extensively as a signal transduction mechanism in biological and chemical sensing. Examples are trace analysis of pesticides, anthrax, prostate-specific antigen, glucose, and nuclear waste[16]. SERS has also been implemented for identification of bacteria, genetic diagnostics and immunoassay labeling. A miniaturized, inexpensive, and portable SERS instrument makes the technique practical for trace analysis in clinics and urban settings.

In the 28 years since the discovery of SERS, the technique has progressed from model system studies of pyridine on a roughened silver electrode to state-of-the-art surface science and real world sensor applications. SERS technique is also cited in many other manuscripts as an application for nanotechnology.

Over the past decade, the development of spectroscopic instrumentation, nanofabrication methods, theoretical modeling, and novel detection schemes has spawned wide-spread interest in the use of SERS and has established the technique as a powerful analytical tool.

### 3.2.1 Fundamentals on SERS

SERS has been observed for a very large number of molecules adsorbed on the surfaces of relatively few metals: silver, copper and gold have been far and away the dominant SERS substrates but work has been reported on the alkali metals and a few others.

The largest enhancements occur for surfaces which are rough on the nanoscale (10–100 nm).

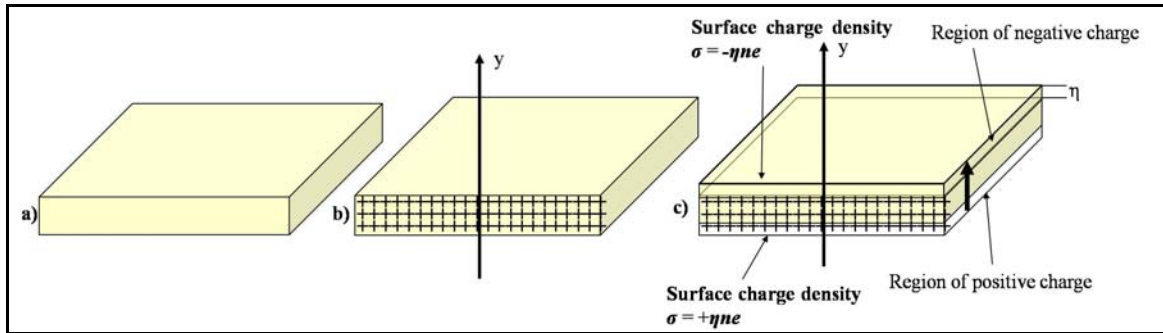
Two mechanisms are proposed to explain the SERS effect:

- *Electromagnetic*, based on the enhanced electromagnetic fields which can be supported on metal surfaces with appropriate morphologies

- *Chemical*, based on the changes in the electronic structure of molecules which occur upon adsorption and which can lead to resonance Raman scattering

### 3.2.1.a Electromagnetic enhancement

The collective excitation of the electron gas of a conductor is called a plasmon; if the excitation is confined to the near surface region it is called a surface plasmon.



**Fig.3.2.1** (a) Thin metallic layer, (b) section of the metallic layer with the positive charges indicated by the “+” sign and the electron gas by the background colour (c) the negative charge is shifted towards the top of the metallic layer of a small length  $\eta$ . This induces a negative surface charge density on the top of the metallic layer and a positive surface charge density on the bottom of the metallic layer.

Surface plasmons can either be propagating, on the surface of a grating, or localized, on the surface of a spherical particle. The plasmon is a quantized plasma oscillation. The excitation can be described, in the simplest way, as a uniform shift of the electron gas in a thin metallic layer. The electron gas moves as a whole structure with respect to the positive charges. So that, a shift of amplitude  $\eta$  induces a restoring electric field of :  $E=4\pi\eta ne$ . The equation of motion of a unit volume of electron gas is:

$$nm \frac{d^2\eta}{dt^2} = -neE = -4\pi\pi^2 e^2 \eta \quad (3.2.1)$$

that is,

$$\frac{d^2\eta}{dt^2} + \omega_p^2 \eta = 0 \quad \text{with } \omega_p = \left( \frac{4\pi\pi n^2}{m} \right)^{1/2} \quad (3.2.2)$$

Where  $\omega_p$  is the *plasma frequency* that is the frequency of the *charge density oscillations*.

Surface roughness or curvature is required for the excitation of surface plasmons by light. The electromagnetic field of the light at the surface can be greatly enhanced under conditions of surface plasmon excitation; the amplification of both the incident laser field and the scattered Raman field through their interaction with the surface constitutes the electromagnetic SERS mechanism.

For simplicity, the model is referred to a spherical particle. In the case of spherical particle whose radius is much smaller than the wavelength of light, the electric field is uniform across the particle and the electrostatic (Rayleigh) approximation is a good one. The field induced at the surface of the sphere ( $E_{induced}$ ) is related to the laser field ( $E_{laser}$ ) by the following equation:

$$E_{induced} = \frac{\epsilon_1(\omega) - \epsilon_2}{\epsilon_1 + 2\epsilon_2} \cdot E_{laser} \quad (3.2.3)$$

where  $\epsilon_1(\omega)$  is the complex, frequency dependent dielectric function of the metal and  $\epsilon_2$  is the ambient phase. This function is resonant at the frequency for which  $\text{Re}(\epsilon_1) = -2\epsilon_2$ . Excitation of the surface plasmon greatly increases the local field experienced by a molecule adsorbed on the surface of the particle.

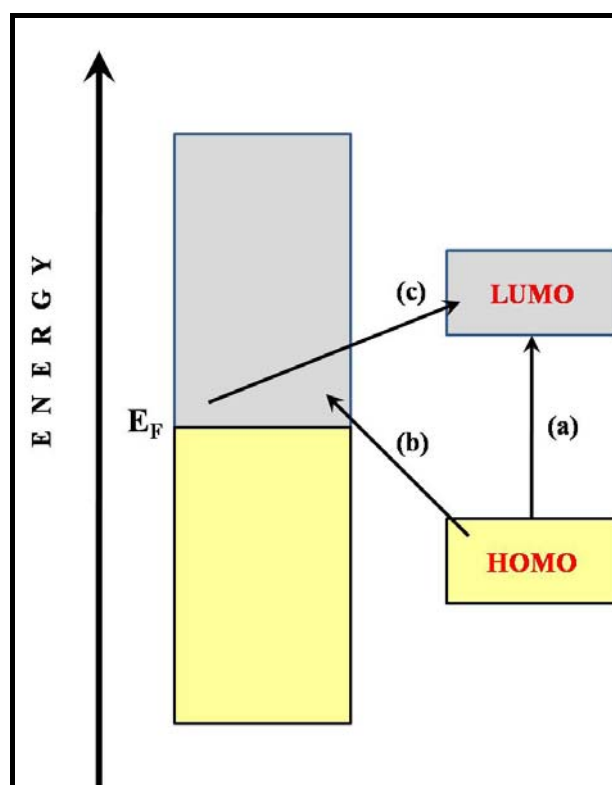
### 3.2.1.b Chemical enhancement

A second enhancement mechanism which operates independently of the electromagnetic mechanism should be introduced in order to explain the SERS effect; for systems in which both mechanisms are simultaneously operative the effects are multiplicative.

Electromagnetic enhancement should be a non selective amplifier for Raman scattering by all molecules adsorbed on a particular surface yet the molecules CO and N<sub>2</sub> differ by a factor of 200 in their SERS intensities under the same experimental conditions. This result is very hard to explain invoking only electromagnetic enhancement. If the

potential is scanned at a fixed laser frequency, or the laser frequency is scanned at fixed potential broad resonances are observed. These observations can be explained by a resonance Raman mechanism in which either (a) the electronic states of the adsorbate are shifted and broadened by their interaction with the surface or (b) new electronic states which arise from chemisorption serve as resonant intermediate states in Raman scattering (Fig. 3.2.2).

It is not uncommon that the highest occupied molecular orbital (HOMO) and lowest unoccupied molecular orbital (LUMO) of the adsorbate are symmetrically disposed in energy with respect to the Fermi level of the metal (Fig. 3.2.2).



**Fig.3.2.2** Typical energy level diagram for a molecule adsorbed on a metal surface. The occupied and unoccupied molecular orbitals are broadened into resonances by their interaction with the metal states; orbital occupancy is determined by the Fermi energy. Possible charge transfer excitations are shown.

In this case charge-transfer excitations (either from the metal to the molecule or vice versa) can occur at about half the energy of the intrinsic intramolecular excitations of the adsorbate.

Molecules commonly studied by SERS typically have their lowest-lying electronic excitations in the near ultraviolet which would put the charge transfer excitations of this simple model in the visible region of the spectrum.

### 3.2.2 Substrates

The most critical aspect of performing a SERS experiment is the choice and/or fabrication of the noble-metal substrates. Because the SERS intensity depends on the excitation of the local surface plasmon resonance (LSPR), it is important to control all of the factors influencing the LSPR to maximize signal strength and ensure reproducibility [16]. These factors which include the size, shape, and inter-particle spacing of the material as well as the dielectric environment, must be chosen carefully to ensure that the incident laser light excites the LSPR. Traditional SERS substrates, chosen because they provide the desired optical properties, include electrodes roughened by the oxidation–reduction cycle (ORC), island films, colloidal nanoparticles, and surface-confined nanostructures. The development of novel SERS substrates to provide stable and optimized enhancement factors, to increase of substrate lifetime, and to allow SERS studies in different environments is the aim of many research teams all around the world.

## 3.3 Raman Microprobe equipment

The instrument used in order to perform Raman spectroscopy is microRaman-LABRAM bought from Horiba Jobin Yvon Srl.

This instrument use a quite novel intuition, where it has been shown that the back scattering geometry ( $\theta = \pi$ ) allows to combine a Raman spectrometer with an optical microscope and this allows to collected Raman spectra from very small regions of the samples: as order of magnitude  $\cong 2 - 5 \mu m$  [17,18].

The main parts of the instruments are summarised in Table 3.3.1:



<b>Element</b>	<b>Characteristics</b>
<i>Laser</i>	HeNe 17mW laser, polarised 500:1 with wavelength 632.817 nm
<i>Holographic Notch Filter</i>	Super Notch Plus used a dichroic mirror. Drop off Stokes edge $<120\text{cm}^{-1}$ ; Now $200\text{cm}^{-1}$ .
<i>Confocal hole</i>	Adjustable between 0 and 1500 $\mu\text{m}$ (scaled on the sample by a factor: 1.4xObjective magnification)
<i>Microscope</i>	High stability BX40. Focus graduation 1 $\mu\text{m}$ . Objectives 10x NA 0.25, 50x NA 0.7, 100x NA 0.9. Other objectives available (Long work distance 20x, 50x). Illumination by transmission and reflection for opaque samples. Macro adapter for mounting of macro 40 mm objective under microscope. Colour camera for the observation of the sample.
<i>External Lasers available and Laser entrance</i>	(notch exchange is required) $\text{Ar}^+$ , 457.8, 514.532 nm, $\text{Kr}^+$ 647.1, 752,5 nm, Yag doubled, diode pumped 532 nm, Laser diode 785 nm. Removable mirrors for external Laser. HeNe beam can be directed externally through the external laser entrance for easier external laser alignment.
<i>Spectrograph</i>	Stigmatic 300mm focal length spectrograph. Two gratings mounted on the same shaft 1800 g/mm (holographic) and 600 g/mm (ruled or holographic). Sinus arm drive. Laser diode for alignment.
<i>CCD Dector</i>	Peltier cooled 1024 $\times$ 256, 16 bit dynamic range (pixel size 27 $\mu\text{m}$ ).
<i>Computer</i>	Labspec software and VITEC video card for TV image digitalisation.
<i>Separated electronic box</i>	Alimentation of the Laser, drive of hole, slit, gratings, shutters, scanners, alimentation of the Laser diode for alignment.
<i>Options</i>	Motorised XY microscope stage for point by point or laser scanning imaging. Resolution 0.1 $\mu\text{m}$ , reproducibility 1 $\mu\text{m}$ . Raman 90 $\times$ 60 mm. Y piezo table for imaging with laser scanning (X direction), range 100 $\mu\text{m}$ . "PIFOC" Z-actuator for automatic focusing of microscope objective or z-scanning (range 0-100 $\mu\text{m}$ ). Autofocus device for microscope objective (correction of focus beatween + / -5 $\mu\text{m}$ ). Temperature controlled cells. Set of filters (notch + interferential) for external laser.

**Table 3.3.1** Main features of the Raman Instrument.

Raman spectroscopy is widely used for analysis of small samples or small heterogeneities in larger samples. Since the small spot size it is possible to collect Raman spectra from several points on the sample but only at one location at a time. The spectra collected from different points of the sample is often called point to point mapping (Fig.3.2.1).

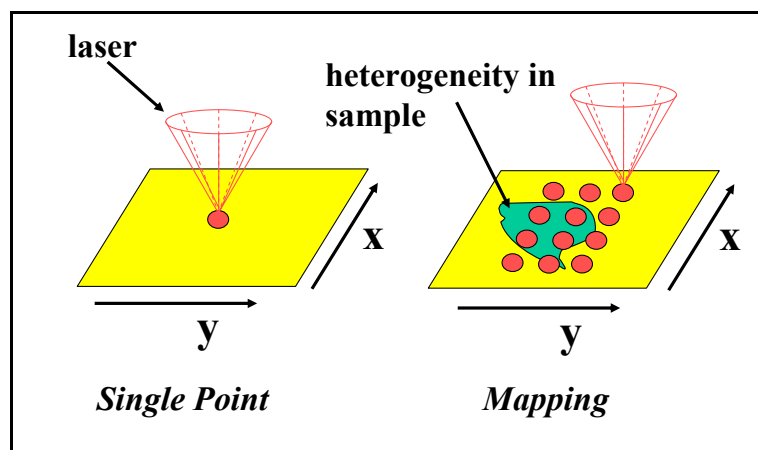


Fig.3.3.1 Two imaging modes for microRaman spectroscopy.

The developing of the two dimensional detectors has allowed to improved very much the microspectroscopy technique because the instruments shows the spectra obtained from different points of the sample in one time. This method are categorized as *Raman imaging* and the results are sample image based on the spectroscopic information [19].

For example the image can be obtained from light having a particular Raman shift of a particular component and the spatial distribution could be followed, or it is possible to choose some point on the stored spectroscopic image and then display its Raman spectra or one more possibility is the profiling where the variation of intensity of a particular Raman feature is observed along a straight line on the sample.

With this set up is possible to acquire or display the spectroscopic results from a data set of intensity as a function of four independent variables:  $x$ ,  $y$ ,  $z$ (depth) and Raman shift.

In the mapping the laser is focused on the sample plane then the Raman spectra are displayed, through an imaging spectrograph onto a charge coupled device (CCD) to generate a two dimensional data set of intensity vs Raman shift and the position is on the selected region of the sample; if the observed spectra corresponds to a specific sample component then global imaging results in a chemically selective two dimensional image.

The spatial resolution is determined by either the laser spot size or the optic used in order to collect the spectra. The diameter of the laser beam at the focal spot is given by

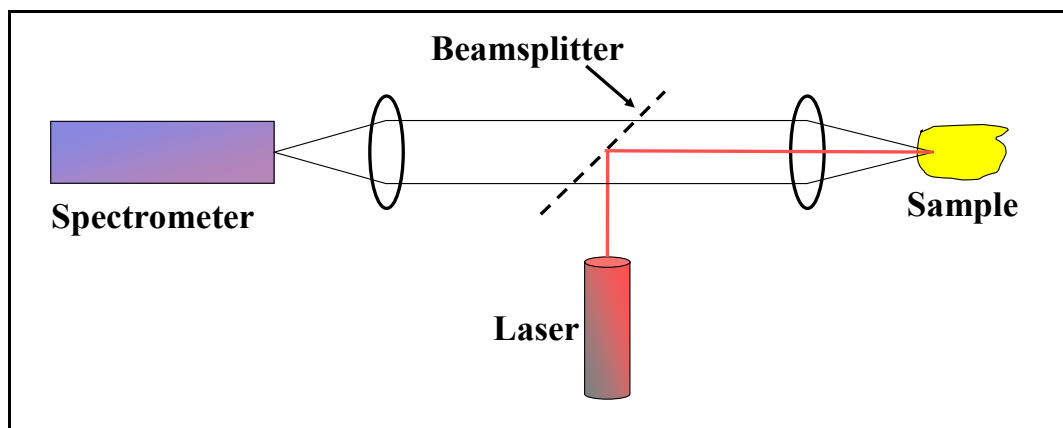
$$\text{Spot diameter} = 2w_0 = f\theta_d \quad (3.2.1)$$

where,  $w_0$  is the beam waist,  $f$  is the objective lens focal length and  $\theta_d$  is the full angle divergence of the laser in radiant. An alternative relationship is:

$$\text{Spot diameter} = 2w_0 = 1.27\lambda f / w_e \quad (3.2.2)$$

where the spot diameter is related to the pupil (aperture) of the objective lens  $w_e$ .

The insertion of a laser in a optical axis of a microscope for micro-Raman applications can be done by using a dichroic mirror which selectively reflects the laser wavelengths (Fig. 3.3.2).

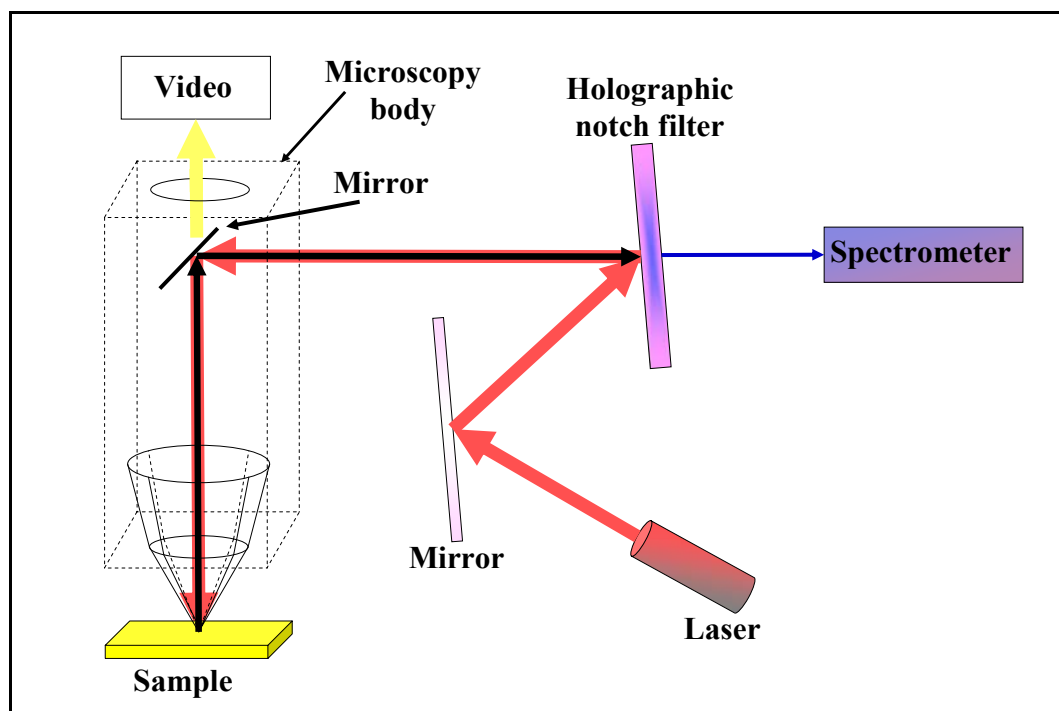


**Fig.3.3.2** The beam splitter combines the laser and collection axes.

In micro-Raman instrument the beam splitter (or dichroic mirror) is, nowadays, based on holographic optical element. The reflectivity of this element is strongly dependent on wavelength and for this reason different beam splitter are used for different laser sources. It should be very reflective to the laser radiation and highly transmissive for the Raman shifted radiations.

However, the Labram is equipped by holographic notch filter characteristic of the He:Ne laser sources. The holographic notch filter, as the same function of the beam splitter but the efficiency is higher than those. Since the filter is quite close to be

perpendicular to the collection axis it transmits high fraction of the Raman shifted light into the spectrometer. In addition, the filter rejects the Rayleigh scattered radiations (elastic scattering). Thus, the holographic notch filter behaves as both an very efficient beam splitter as well as notch filter that is able to reduce the radiations in the spectrograph which are not coming by Raman scattering.



**Fig. 3.3.3** Back scattering geometry in Raman microprobe equipped with holographic notch filter.

In Fig. 3.3.3 can be seen that the laser (coloured in red) is transmitted by mirrors to the sample. The back scattered radiation (coloured in black) is transmitted to the holographic notch filter which cuts the elastic scattered radiation (Rayleigh scattered) so that only the inelastic scattered radiation (Raman scattering) arrives to the spectrograph. The yellow arrow indicates the optical path of the microscope.

Often, the microscope used in microRaman are confocal that is, they have an additional aperture called confocal hole that has the effect of decreasing the depth of the focus.

This characteristic is quite useful for studying thin films, samples made of multiple layers where it is researched the Raman spectra of each layer, or simply because the signal of the substrate can overlap the signal of the thin film studied. In fact, if the layers are thinner than the depth of the focus then the spectrum will represent an

average of the layers. The principle of a confocal microscope is illustrated in Fig. 3.3.4, by comparison to a conventional microscope.

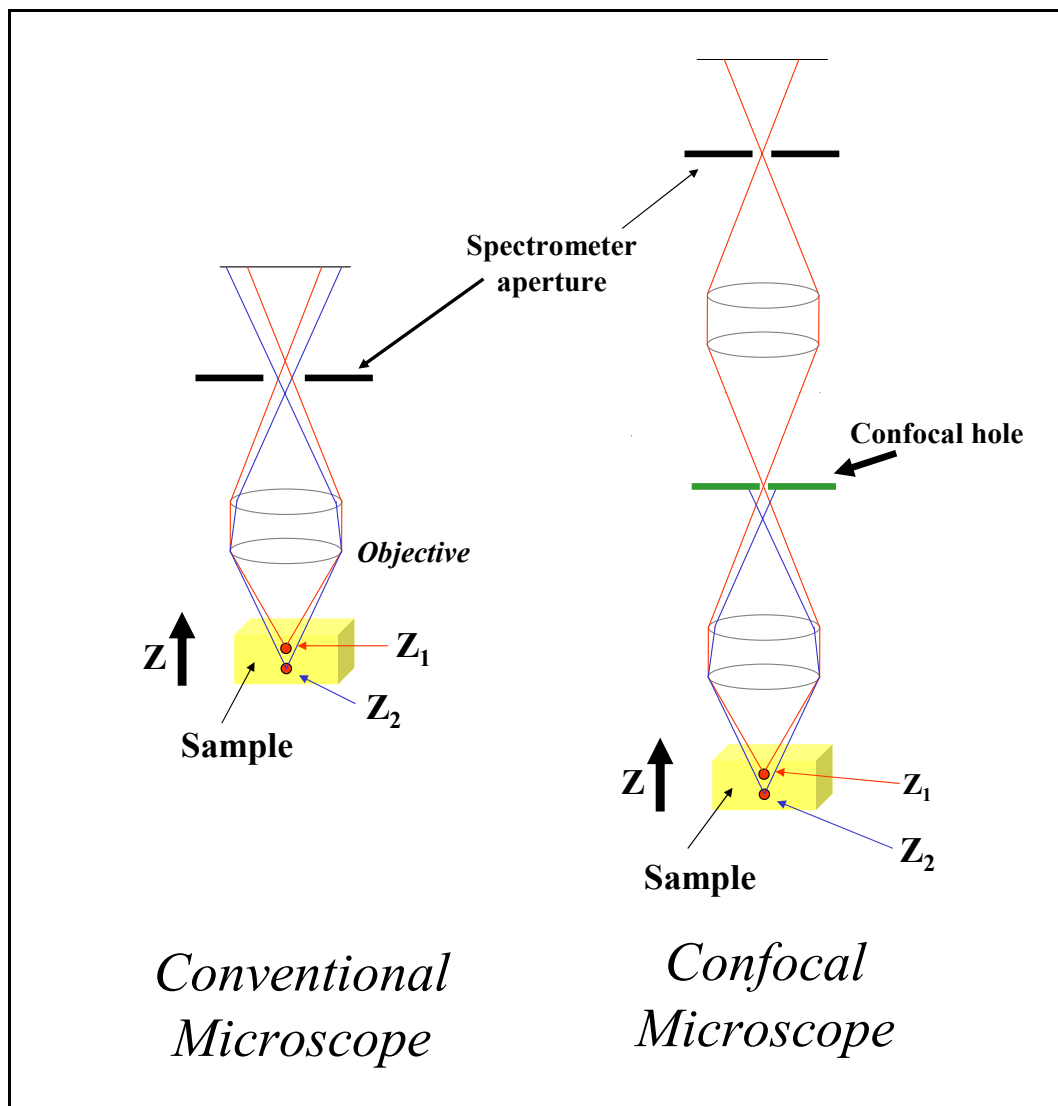


Fig.3.3.4 Confocal and conventional microscopes.

In Fig. 3.3.4 are shown the radiations scattered by two points of the samples that are situated at different depths  $Z_1$  and  $Z_2$ . It can be seen that through the spectrometer aperture (usually the slit) the light of both the points can enter in the spectrometer. If both the points are involved in the focal cylinder of the laser beam, as said above, the resulting Raman spectra will reflect the average sample composition between the two points. The confocal hole limits the sampling depth to a smaller region by blocking the radiation scattered by  $Z_2$  before it enters in the spectrometer. For homogeneous samples

the confocal hole will conduce also to a decreased intensity of the signals since it decrease the effective path length. Labram micro-Raman offer the possibility to perform z-scans, controlled by computer, thanks to confocal optics.

The degree to which the confocal hole reduce the focal cylinder of the laser beam is a quite complex function of the objective power and of the numerical aperture (NA) (defined as the sine of the half angle of the collection cone) as well as the position and the size of the confocal hole. The depth resolution improves (decreasing of the size of the focal cylinder of the laser beam) for higher objective power, higher numerical aperture and smaller confocal hole.

### 3.4 References

- [1] R. L. McCrerry, Raman Spectroscopy for Chemical Analysis, John Wiley & Sons, New York, (2000).
- [2] D. A. Long, The Raman Effect, John Wiley & Sons, Chichester, (2002).
- [3] R. S. Krishnan and R. K. Shankar, J. Raman Spectrosc., **10**, 1 (1981).
- [4] D. A. Long, Raman Spectroscopy, McGraw-Hill, Inc., New York, (1977).
- [5] M. Diem, Introduction to Modern Vibrational Spectroscopy, John Wiley & Sons, New York, (1993).
- [6] R. Loudon, The quantum theory of light, Oxford University Press, Oxford, (1973).
- [7] C. Kittel, Introduction to Solid State Physics, John Wiley & Sons, New York, (1995).
- [8] R. Merlin, A. Pinczuk and W. H. Weber, in Raman Scattering in Material Science, edited by W. H. Weber and R. Merlin, Springer, Berlin, (2000).
- [9] E. Cazzanelli, R. Frech, Temperature dependent Raman spectra of monoclinic and cubic  $\text{Li}_2\text{SO}_4$ , J. Chem. Phys., **81**, 11 (1984).
- [10] E. Cazzanelli, R. Frech, Evidence from Raman spectroscopy for progressive disordering of the lithium sulfat structure in monoclinic and plastic phases, Philosophical Magazine B **59**, 133-142 (1989).
- [11] E. Cazzanelli, A. Fontana, F. Rocca, R. Frech, Low-temperature behaviour of the lithium modes in monoclinic  $\text{Li}_2\text{SO}_4$ , Physica Status Solidi (b)**140**, 621-630 (1987).

- 
- [12] M. Fleischmann, P. J. Hendra and A.J. McQuillan, *Chem. Phys. Lett.*, **26**, 163 (1974).
- [13] D. L. Jeanmaire and R. P. Van Duyne, *J. Electroanal. Chem.*, **84**, 1 (1977).
- [14] M. G. Albrecht and J. A. Creighton, *J. Am. Chem. Soc.*, **99**, 5215 (1977).
- [15] A. Campion and P. Kambhampati, Surface enhanced Raman scattering, *Chem Soc.Rev.*, **27**, (1998).
- [16] C. H. Haynes, A. D. McFarland, R. P. Van Duyne, Surface Enhanced Raman spectroscopy, *Anal. Chem.*, **77**, 338A-346A (2005).
- [17] A. K. Ramdas, in *Raman Scattering in Material Science*, edited by W. H. Weber and R. Merlin, Springer, Berlin, (2000).
- [18] G. Turrell and J. Corset, *Raman Microscopy: Developments and Applications*, Academic Press, San Diego, (1996).
- [19] M. Shaeberle, H. R. Morris, J. F. Turner and P. J. Treado, *Anal. Chem.*, **71**, 175A (1999).

*Chapter 4*

**RESULTS AND DISCUSSION**

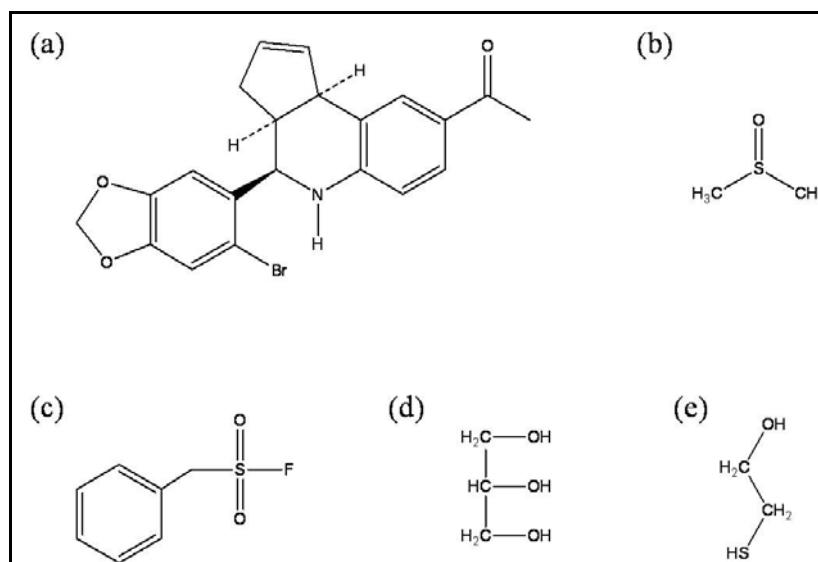


## 4.1 Raman spectroscopy on G1 ligand and GPR30 receptor

In this work the ligand G1 *1-((3a*S*,4*R*,9*bR*)-4-(6-bromobenzo[*d*][1,3]dioxol-5-yl)-3*a*,4,5,9*b*-tetrahydro-3*H*-cyclopenta[*c*]quinolin-8-yl)ethanone*, (Fig. 4.1.1.) and the GPR30 protein receptor (G protein coupled receptor) were studied by micro Raman spectroscopy, to evaluate the chemical composition and to set the possible Raman feature to be used as marker of the ligand-receptor interaction.

The experimental setup up was a LABRAM Jobin Yvon, spectral resolution of about 2  $\text{cm}^{-1}$  equipped with a CCD detector, a laser He:Ne (633 nm) and with an Mplan Olympus objective of 50X which focus on a spot area of 2-3  $\mu\text{m}$  of diameter.






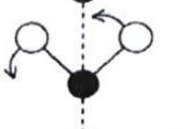
Some pre-treatments has been perfermed to the samples before to be analyzed. In fact, the G-1 ligand was dissolved in dimethyl sulfoxide (DMSO) (Fig. 4.1.1) while the GPR30 was solubilized with phenylmethsulphonyl fluoride (PMFS) in ethanol and washed many times with a PBS soluzion (Phosphate Buffered Saline System, 1M  $\text{KH}_2\text{PO}_4$ , 1M  $\text{K}_2\text{HPO}_4$ , 5M NaCl), glycerol and  $\beta$ - mercaptoethanol (Fig. 4.1.1). To assign properly the Raman features of the ligand and receptor the Raman spectra of all the solvents have been collected.



**Fig. 4.1.1** Structural formula of G-1 (a), DMSO (b), PMFS (c), Glycerol (d) e  $\beta$ - mercaptoethanol (e).

### 4.1.1 Solvents

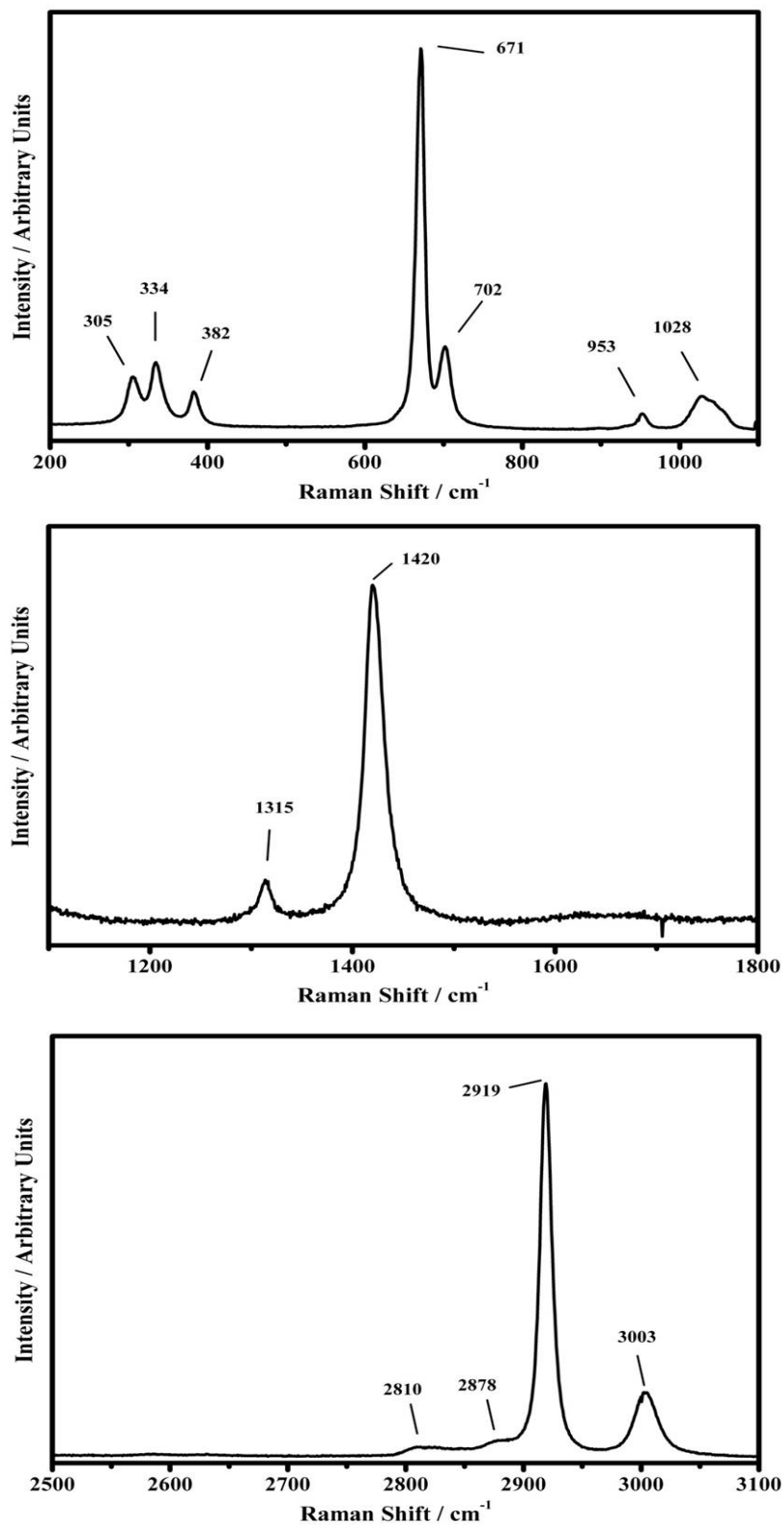
To better understand the spectroscopic modifications of the substances investigated, it is useful to have, for comparison, the spectra of the solvents. The first solvent analyzed is the DMSO. The Raman spectra were collected in the range between 200 e 4000  $\text{cm}^{-1}$  but the data shown concern the Raman features more representative of the performed analysis. In figura 4.1.2 the Raman spectra of the DMSO is shown. The attribution of the Raman peaks has been done by research in the current literature, very abundant, because of the common use of such solvents. The table below is useful to summarize the current terminology for the molecular vibrational modes used in the following.

Symbol	Designation	Example Illustration
s	symmetric	$\nu_s$
as	antisymmetric (asymmetric)	$\nu_{as}$
ip	in-plane (ip)	$\delta$
oop	out-of-plane (oop)	$\gamma$
$\nu$	stretching	
$\delta$	ip deformation	
$\gamma$	oop deformation	
$\omega$	wagging	
$\tau$	twisting	
$\rho$	rocking	

**Table 4.1.1:** Commonly used symbols and terminology for molecular vibrational modes (From D. C. Harris and M. D. Bertolucci, *Symmetry and Spectroscopy*, Dover Publication, New York, (1978).)

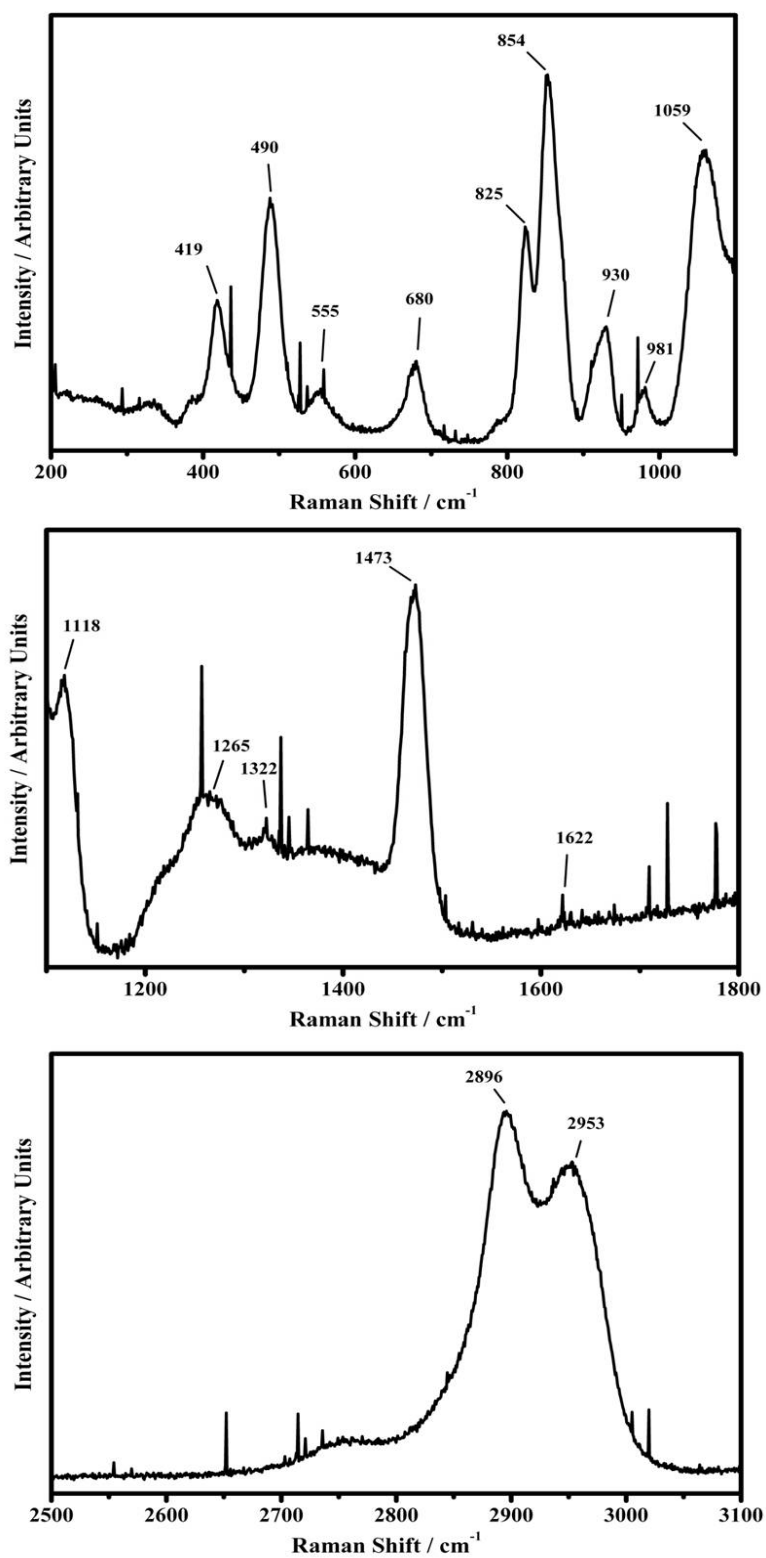
The bands at 305 and 334  $\text{cm}^{-1}$  were assigned to the “out of plane bending” mode of the CSO, while the peak at 382  $\text{cm}^{-1}$  is due to the “plane rocking” mode (of CSO) [1-5]. The more intense bands at 671 e 702  $\text{cm}^{-1}$  are assigned to the stretching modes C-S-C, symmetric and asymmetric, respectively, whereas the bands at 1028  $\text{cm}^{-1}$  is due to the S=O stretching mode and the peak at 953  $\text{cm}^{-1}$  to a rocking mode of the HCH group [1-5].

The two bands at 1315 e 1420  $\text{cm}^{-1}$  (Fig. 4.1.2. on the middle spectrum) are assigned to the H-C-H deformation mode, the peaks at 2810, 2878, 2919  $\text{cm}^{-1}$  (Fig. 4.1.2. on the bottom spectrum) are assigned to the C-H symmetric stretching whereas the mode at 3003  $\text{cm}^{-1}$  is due to the C-H asymmetric stretching [1-5].



**Fig. 4.1.2.** Raman spectra of DMSO in the range between 200 and 1100  $\text{cm}^{-1}$  (top), 1100 e 1800  $\text{cm}^{-1}$  (middle) and 2500 e 3100  $\text{cm}^{-1}$  (bottom).

In Fig. 4.1.3 the spectra of the glycerol it is shown.



**Fig. 4.1.3** Raman spectra of glycerol in the range between 200 and 1100 cm<sup>-1</sup> (top), 1100 e 1800 cm<sup>-1</sup> (middle) and 2500 e 3100 cm<sup>-1</sup> (bottom).

The peaks at 419 e 490  $\text{cm}^{-1}$  (Fig. 4.1.3., top spectra) are assigned to the CCO mode while the Raman feature at 555  $\text{cm}^{-1}$  is assigned to the “CCC deformation” mode [6].

Quite difficult was to assign the mode at 680  $\text{cm}^{-1}$ , assigned by some authors to the “out of plane” mode of the hydroxyl group, while others say that it is due to the “in plane” bending mode of the hydroxyl group and some others define this peak as the “CCO deformation” mode [6].

The peaks at 825 and 854  $\text{cm}^{-1}$  are assigned to the “C-C stretching” mode, while those at 930 e 981  $\text{cm}^{-1}$  are due to “CH<sub>2</sub> rocking” mode. The band at 1059  $\text{cm}^{-1}$  is assigned to the alcoholic hydroxyl group present as primary alcohol (the carbon which carries the -OH group is only attached to one alkyl group) [6].

The peak at 1118  $\text{cm}^{-1}$  (Fig. 4.1.3 on the middle) is assigned to the CO stretching of the alcoholic hydroxyl groups present as secondary alcohol (the carbon with the -OH group attached is joined directly to two alkyl groups) [6]. The modes at 1265 and 1322  $\text{cm}^{-1}$  are assigned to the “CH<sub>2</sub> twisting” mode and the intense band at 1473  $\text{cm}^{-1}$  is due to the “CH<sub>2</sub> deformation” mode.

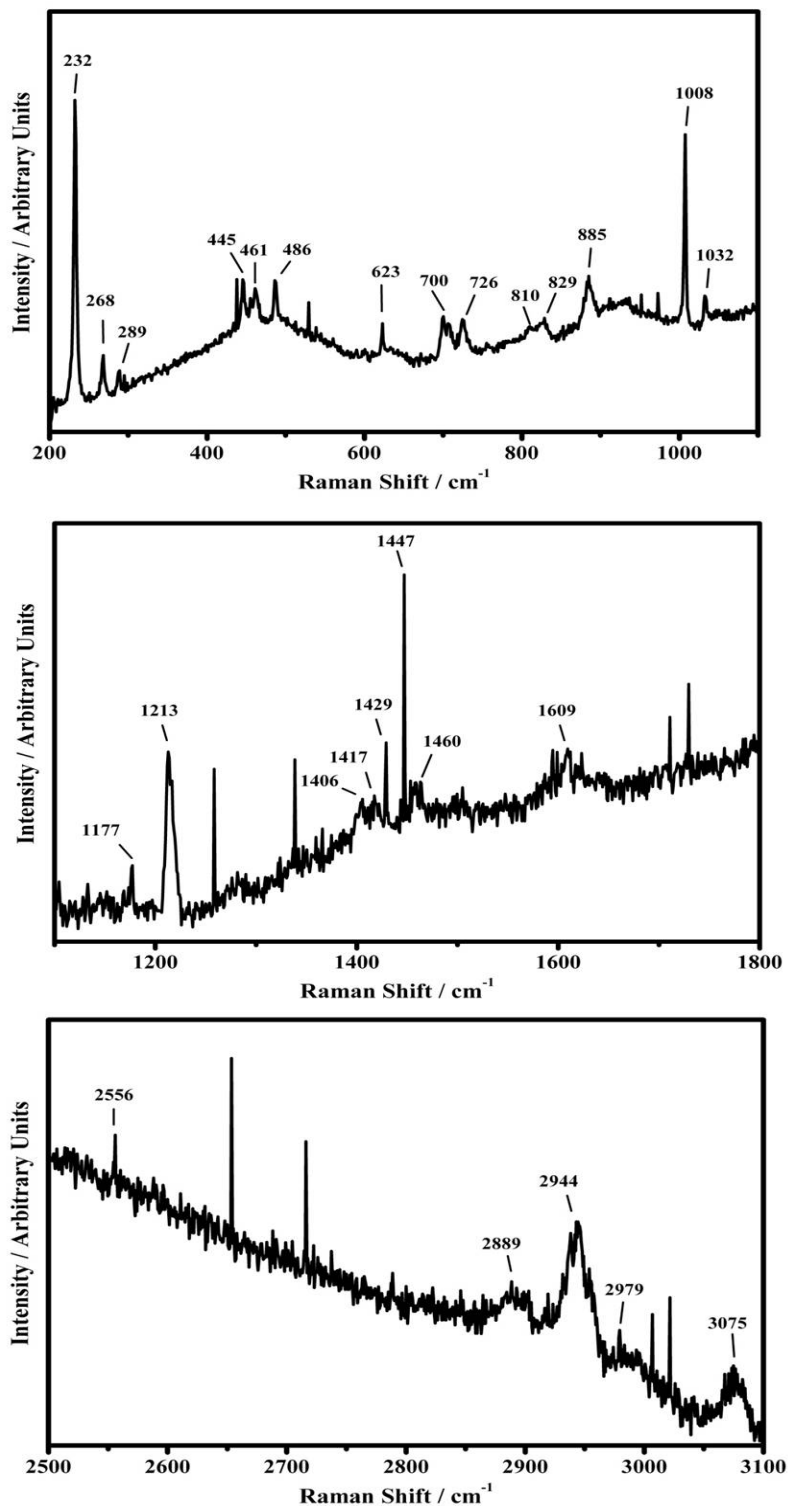
The band at 2896 e 2953  $\text{cm}^{-1}$  (Fig. 4.1.3. on the bottom) are assigned to the C-H symmetric and asymmetric stretching [6].

In Fig. 4.1.4 the Raman spectra of the PMSF(phenylmethylsulfonyl fluoride) solution it is shown [7-10].

The band at 232  $\text{cm}^{-1}$  is assigned to the “CH<sub>3</sub> torsion” mode, the peak at 268  $\text{cm}^{-1}$  is due to the  $\delta(\text{CH}_3)$  mode, that at 289  $\text{cm}^{-1}$  to the SO<sub>2</sub>F skeletal vib mode, while those features which fall at 445, 461 e 486  $\text{cm}^{-1}$  are assigned to the SO<sub>2</sub> modes (rocking, twisting, wagging). The peak at 623  $\text{cm}^{-1}$  can be due to both “in plane ring deformation” mode and to the C-S stretching mode. The peaks at 700 e 726  $\text{cm}^{-1}$  are assigned to the “C-S stretching” and the bands at 810, 829 e 885  $\text{cm}^{-1}$  are due to the “S-F stretching” mode. Il peak at 1008  $\text{cm}^{-1}$  is attributed to the stretching “=C-H” of the aromatic ring and the mode at 1032  $\text{cm}^{-1}$  to the S-O asymmetric stretching.

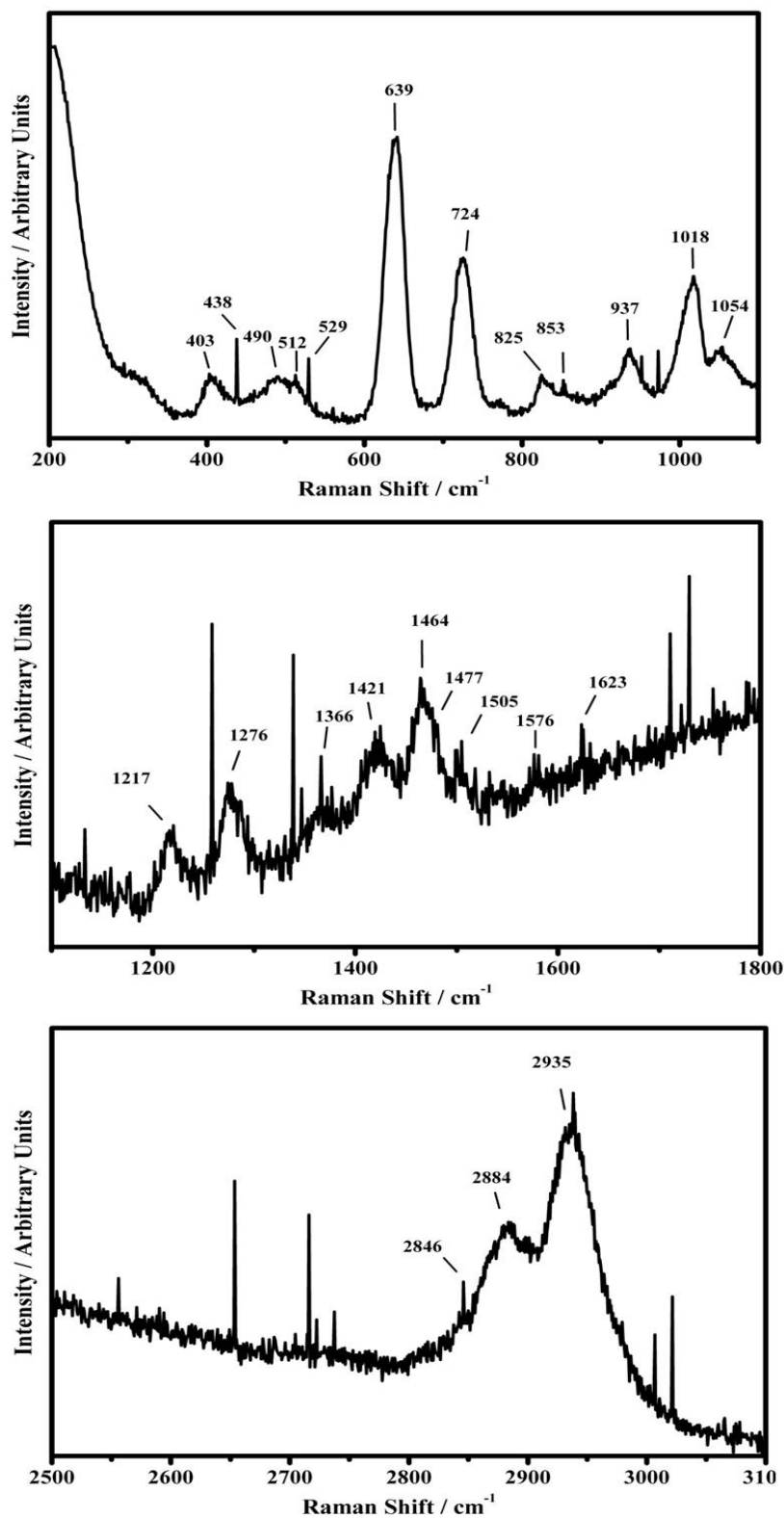
The bands at 1177 e 1213  $\text{cm}^{-1}$  (Fig. 4.1.4. in the middle) are assigned to the (SO<sub>2</sub>) symmetric stretching whereas, the bands at 1406, 1417, 1429  $\text{cm}^{-1}$  are due to the (SO<sub>2</sub>) asymmetric stretching. The peaks at 1447 e 1460  $\text{cm}^{-1}$  are assigned to the “CH<sub>3</sub> deformation” deformation mode and the mode at 1609  $\text{cm}^{-1}$  is due to the aromatic ring.

The bands at 2889, 2944, 2979 e 3075  $\text{cm}^{-1}$  are assigned to the C-H symmetric and asymmetric stretching.



**Fig. 4.1.4.** Raman spectra of PMFS in the range between 200 and 1100  $\text{cm}^{-1}$  (top), 1100 e 1800  $\text{cm}^{-1}$  (middle) and 2500 e 3100  $\text{cm}^{-1}$  (bottom).

In Fig. 4.1.5 the Raman spectra of the PBS solution it is shown.



**Fig. 4.1.5.** Raman spectra of PBS in the range between 200 and 1100 cm<sup>-1</sup> (top), 1100 and 1800 cm<sup>-1</sup> (middle) and 2500 and 3100 cm<sup>-1</sup> (bottom).



PBS is a saline solution which contains the following salts: NaCl, Na<sub>2</sub>HPO<sub>4</sub>, KH<sub>2</sub>PO<sub>4</sub>. So that, the main Raman signals that should be detected have to be those characteristic of the phosphate anions.

In fact, the bands at 937 and 1018 cm<sup>-1</sup> (Fig. 4.1.5. on the top) are assigned to the P-O bonds symmetric and asymmetric stretching and the wide band at 490 cm<sup>-1</sup> is due to the H<sub>2</sub>PO<sub>4</sub><sup>-</sup> anion symmetric bending. The mode at 1054 cm<sup>-1</sup> is due to the asymmetric stretching of the phosphate ion. While, the small peaks (403, 438, 512, 529, 825 and 853 cm<sup>-1</sup>) may be assigned to the presence of phosphate polyanion. It is, still, quite difficult to assign the bands at 639 e 724 cm<sup>-1</sup> [11-13]. Same difficult also to assign the bands which fall in the range between 1100 and 1800 cm<sup>-1</sup>, since in this range, there are not Raman modes due to the any forms of phosphate ions. For this reason the Raman bands at 1217, 1276, 1366, 1421, 1464, 1477, 1505, 1576, 1623 cm<sup>-1</sup> indicate the presence of some additional compound present of the solution and not declared by the company that sold it.

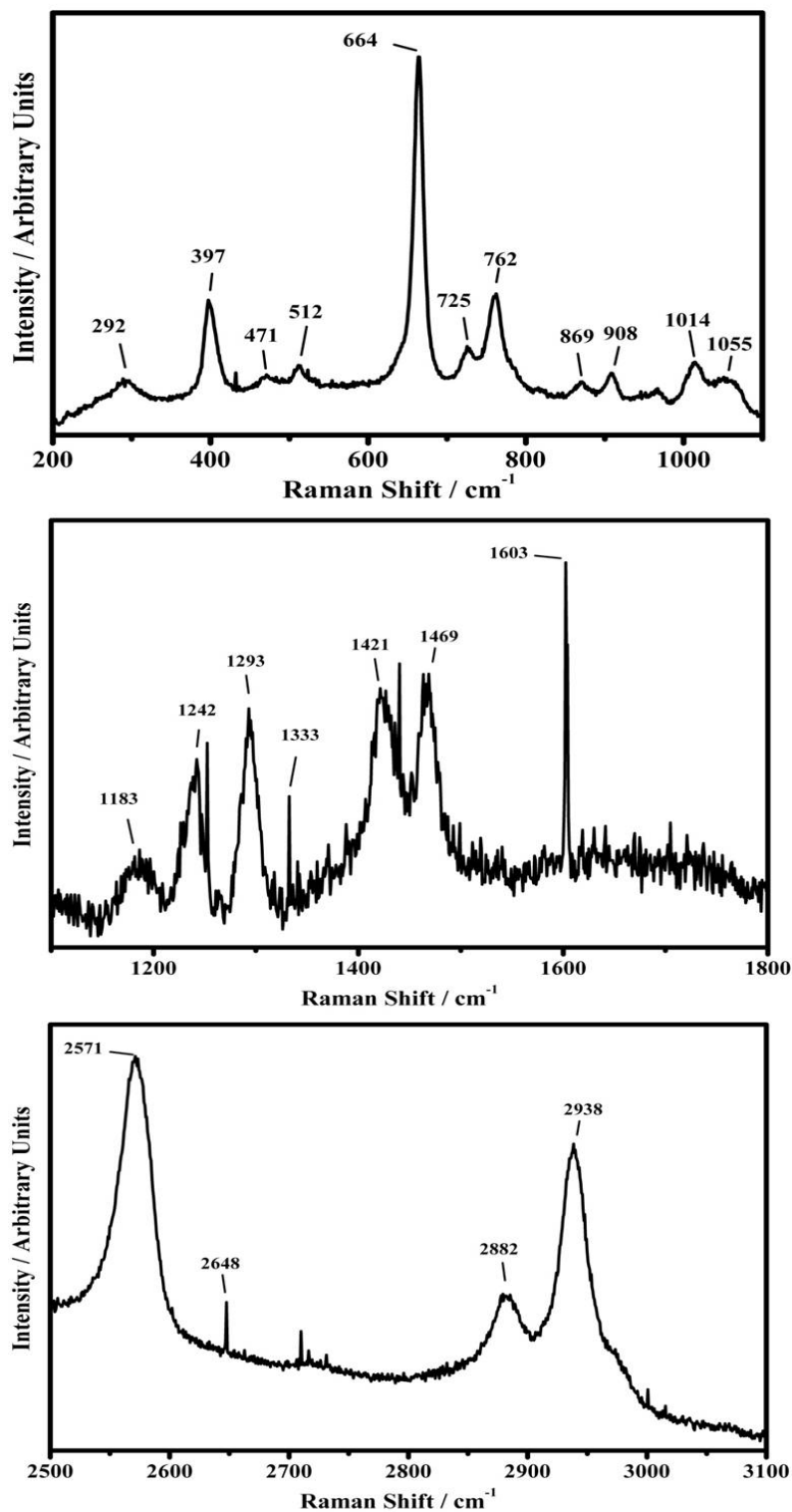
In addition, also in the range between 2500 and 3100 cm<sup>-1</sup> there are evidences of the presence of an organic compound with the bands at 2846, 2884 e 2935 cm<sup>-1</sup>, assigned to the C-H stretching. So that, the Raman bands at 639 e 724 cm<sup>-1</sup> (Fig. 4.1.5 on the top), those at 1217, 1276, 1366, 1421, 1464, 1477, 1505, 1576, 1623 cm<sup>-1</sup> (Fig. 4.1.5 on the middle) e those at 2846, 2884 e 2935 cm<sup>-1</sup> (Fig. 4.1.5. on the bottom) indicate the presence of an organic compound, most probably an anti-fungal added to the tampon phosphate solution, that, by the comparison with the bibliographic data, seems to be the 2-phenylbromobenzene [14].

In Fig. 4.1.6 are shown the Raman spectra of the β- mercaptoethanol.

The Raman band at 292 cm<sup>-1</sup> (Fig. 4.1.6 on the top) is due to C-C-S bending mode, the modes at 397, 471 e 512 cm<sup>-1</sup> are assigned to the CCO bending and the bands at 664 e 725 cm<sup>-1</sup> are due to the CS stretching. The peaks at 762 e 869 cm<sup>-1</sup> are assigned to the CSH bending, the peak at 908 cm<sup>-1</sup> to the “CH<sub>2</sub> rocking” mode and that at 1014 cm<sup>-1</sup> is due to the C-H stretching while the peak at 1055 cm<sup>-1</sup> is assigned to the C=O stretching [15].

The peaks at 1183 e 1242 cm<sup>-1</sup> (Fig. 4.1.6 on the middle) are assigned to the CH<sub>2</sub> stretching, the peak at 1293 cm<sup>-1</sup> is due to the CH<sub>2</sub> wagging mode and the peaks at 1421 e 1469 cm<sup>-1</sup> are assigned to the CH<sub>2</sub> scissoring mode [15]. The Raman bands (Fig. 4.1.6

on the bottom) at 2571 and 2882  $\text{cm}^{-1}$  are assigned to the S-H stretching modes, while the band at 2938  $\text{cm}^{-1}$  is due to the C-H stretching mode [15].



**Fig. 4.1.6** Raman spectra of 2-mercaptoethanol in the range between 200 and 1100  $\text{cm}^{-1}$  (top), 1100 e 1800  $\text{cm}^{-1}$  (middle) and 2500 e 3100  $\text{cm}^{-1}$  (bottom).

### 4.1.2 The ligand G-1

The analyzed sample was made by the G-1 ligand dissolved in DMSO (Fig.4.1.1.). The representative spectra of the G-1 ligand dissolved in DMSO is shown in Fig. 4.1.7.

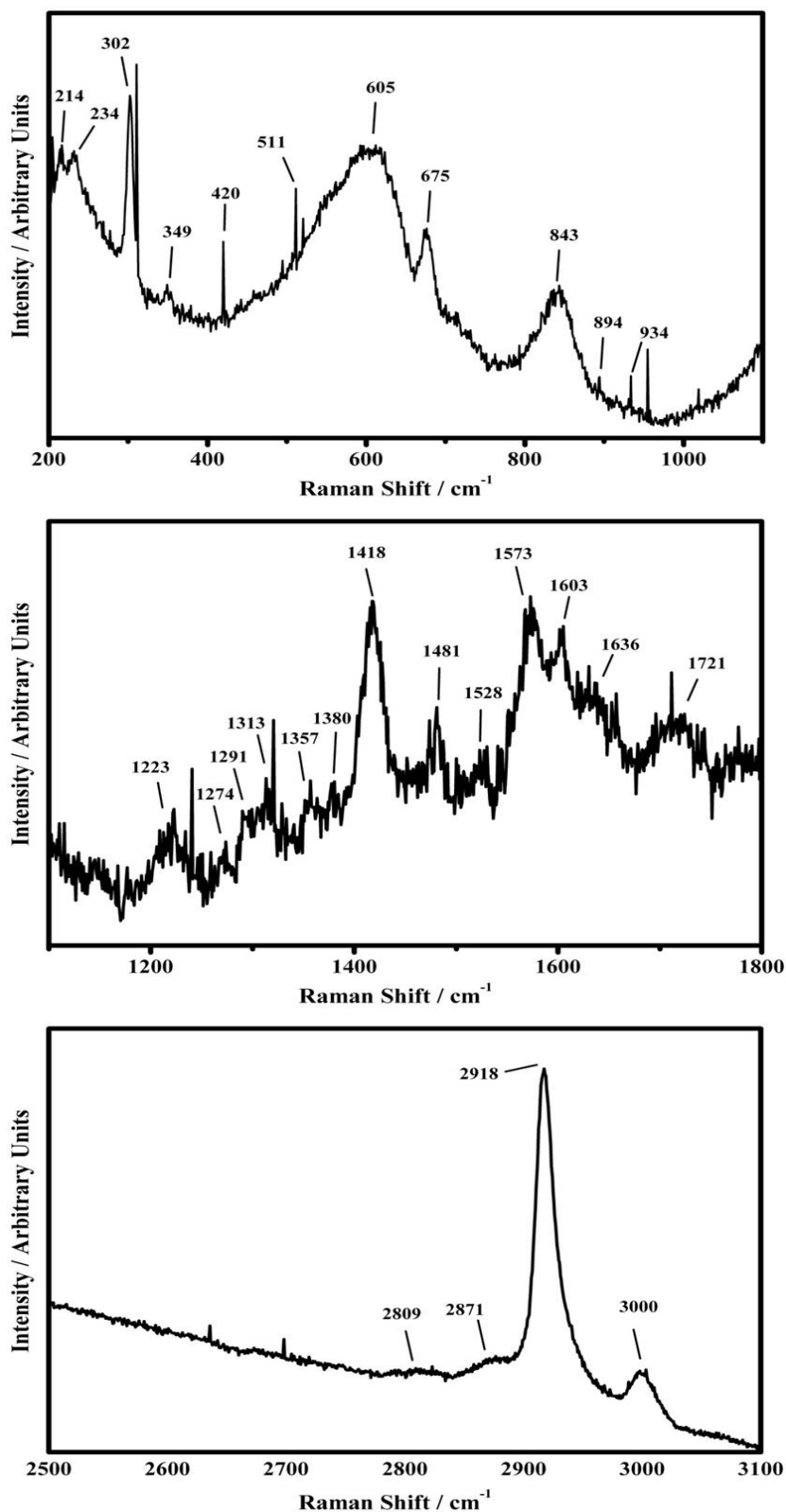
The Raman band at  $675\text{ cm}^{-1}$  (Fig. 4.1.7. on the top) can be assigned to the solvent DMSO (see Fig. 4.1.2), while the doublet at  $214$  and  $234\text{ cm}^{-1}$ , the sharp band  $302\text{ cm}^{-1}$ , the band at  $349\text{ cm}^{-1}$  and the two wide bands centered at  $605$  and  $843\text{ cm}^{-1}$ , by the comparison with the spectra of the DMSO (Fig. 4.1.2) are due to the vibrational spectra of the G-1 ligand.

Since a complete work of assignation for the G-1 Raman spectrum has not been done, in our knowledge, tentative attributions of the G-1 (Fig. 4.1.1.a) Raman features have been performed on the basis of characteristic groups of the molecule.

The Raman spectra of the 5-bromo-1,3-benzodioxole [16] shows a similar Raman patterns of that shown in Fig. 4.1.7. The attribution of the Raman features has been performed by taking into account the results obtained for the high symmetric molecule 1,3-benzodioxole[17]. So that, the bands at  $214$  e  $234\text{ cm}^{-1}$  have been assigned to the “flap ring” mode, the band at  $605\text{ cm}^{-1}$  it is assigned to the aromatic rings bending while the band at  $843\text{ cm}^{-1}$  is due to the “C-H oop wagging” mode. The peak at  $302\text{ cm}^{-1}$ , characteristic of the molecule with low symmetry (similar to G-1), can be assigned to the “-C-Br in plane bending” mode.

The band at  $1223\text{ cm}^{-1}$  (Fig. 4.1.7, on the middle) is assigned to “sat. ring stretching” mode, the bands at  $1357$  e  $1380\text{ cm}^{-1}$  are due to the “C-C phenyl stretching” mode, the peak at  $1418\text{ cm}^{-1}$  is assigned to the “CH<sub>2</sub> wagging”, while the peak at  $1481\text{ cm}^{-1}$  is assigned to the “C-C stretching” mode, the peak at  $1636\text{ cm}^{-1}$  again to the “phenyl C-C stretching” mode. The peaks at  $1274$ ,  $1291$  and  $1313\text{ cm}^{-1}$  are assigned to “C-H +ring” modes, the band at  $1528\text{ cm}^{-1}$  is most probably due to the “N-H+ ring” mode and that at  $1573\text{ cm}^{-1}$  is assigned to the “C=C stretching” mode. The band at  $1603\text{ cm}^{-1}$  is attributed to the “C=O stretching” mode and that at  $1721\text{ cm}^{-1}$  is assigned to the C=O in  $\alpha$  position with respect the aryl group and to the C=C stretching [8, 16-19].

The bands at  $2809$ ,  $2871$ ,  $2918$  and  $3000\text{ cm}^{-1}$ , shown in Fig. 4.1.7 on the bottom, are assigned to the symmetric and asymmetric C-H stretching modes [8].



**Fig. 4.1.7** Raman spectra of G-1 ligand dissolved in DMSO in the range between 200 and 1100 cm<sup>-1</sup> (top), 1100 and 1800 cm<sup>-1</sup> (middle), 2500 and 3100 cm<sup>-1</sup> (bottom).

### 4.1.3 Endogenous Receptor GPR30

The sample of GPR30 is made by a cell lysate protein. The Raman spectra of a protein shows mainly the vibrational characteristic modes of the skeleton polypeptide together with the Raman bands due to the characteristic groups of the side chain of the twenty natural amino acids.

A protein, typically, shows about 30 Raman bands in the spectral region between 400 and 2000  $\text{cm}^{-1}$  (fingerprint region) and some other bands in the range 2500 - 4000  $\text{cm}^{-1}$  due to vibrational modes of localized groups for example: NH, OH, CH<sub>3</sub>, CH<sub>2</sub> and SH.

The NH, OH and SH groups may do hydrogen bonds which results in a broadening of the Raman bands dependently of the degree of hydrogen interactions [20].

The interpretation of the bands due to the polypeptide skeleton is quite important in order to determine the secondary protein structure while the bands assigned to the groups of the side chains allow to obtain information with regard the intermolecular interaction, hydrogen bonds and the chemical environment.

The chance to obtain information with regard the secondary structure of the protein is due to the degree of the hydrogen interactions; it is quite different dependently if the protein structure is:  $\alpha$ -helix,  $\beta$ -sheet or disordered structures.

The Raman bands of peptide bond are indicated as amide bands followed by a roman number which indicate the contribution of different normal modes of N-methylacetamide chosen as “model” for the peptide bond [21]. In table 4.1.2 is reported the meaning of each “amide mode” in terms of different normal vibrational modes.

NAME OF THE VIBRATIONAL BAND	MEANING
Ammide I	$\approx 80\%$ CO stretching + $\approx 10\%$ CN stretching + $\approx 10\%$ NH bending vib.
Ammide II	$\approx 60\%$ NH bending vib + $\approx 40\%$ CN stretching
Ammide III	30% CN stretching + 30% NH bending vib.+10% CO stretching + 10% O=C-N bending vib. + 20 % altre vibrazioni.
Ammide IV	40% O=C-N bending vib. + 60 % altre vibrazioni.
Ammide V	N-H bending vib.
Ammide VI	CO bending vib.
Ammide VII	C-N torsional vib.

**Table 4.1.2** Meaning of the name of some Raman bands of protein systems.

The first band studied in order to evaluate the secondary structure of a protein is the band Amide I. If the conformation of the polypeptide skeleton is  $\alpha$ -helix, then the hydrogen bonds occur between the C=O carbonylic and the N-H aminic groups of the same chain and the Amide I band falls at  $1655\text{ cm}^{-1}$ . This band is shifted at higher frequencies,  $\approx 1670\text{ cm}^{-1}$ , when the conformation of the skeleton is  $\beta$ -sheet, where the hydrogen bonds occur between C=O carbonylic and the N-H aminic groups of near chains. On the contrary, this band is down-shifted, at  $\approx 1640\text{ cm}^{-1}$ , in the case of disordered structures.

Among the band Amide I also the band Amide III reflects the secondary structure of the polypeptide; in fact, it falls at  $1300\text{--}1340\text{ cm}^{-1}$  in the case of  $\alpha$ -helix conformation and at  $1235\text{--}1250\text{ cm}^{-1}$  in the case of  $\beta$ -sheet.

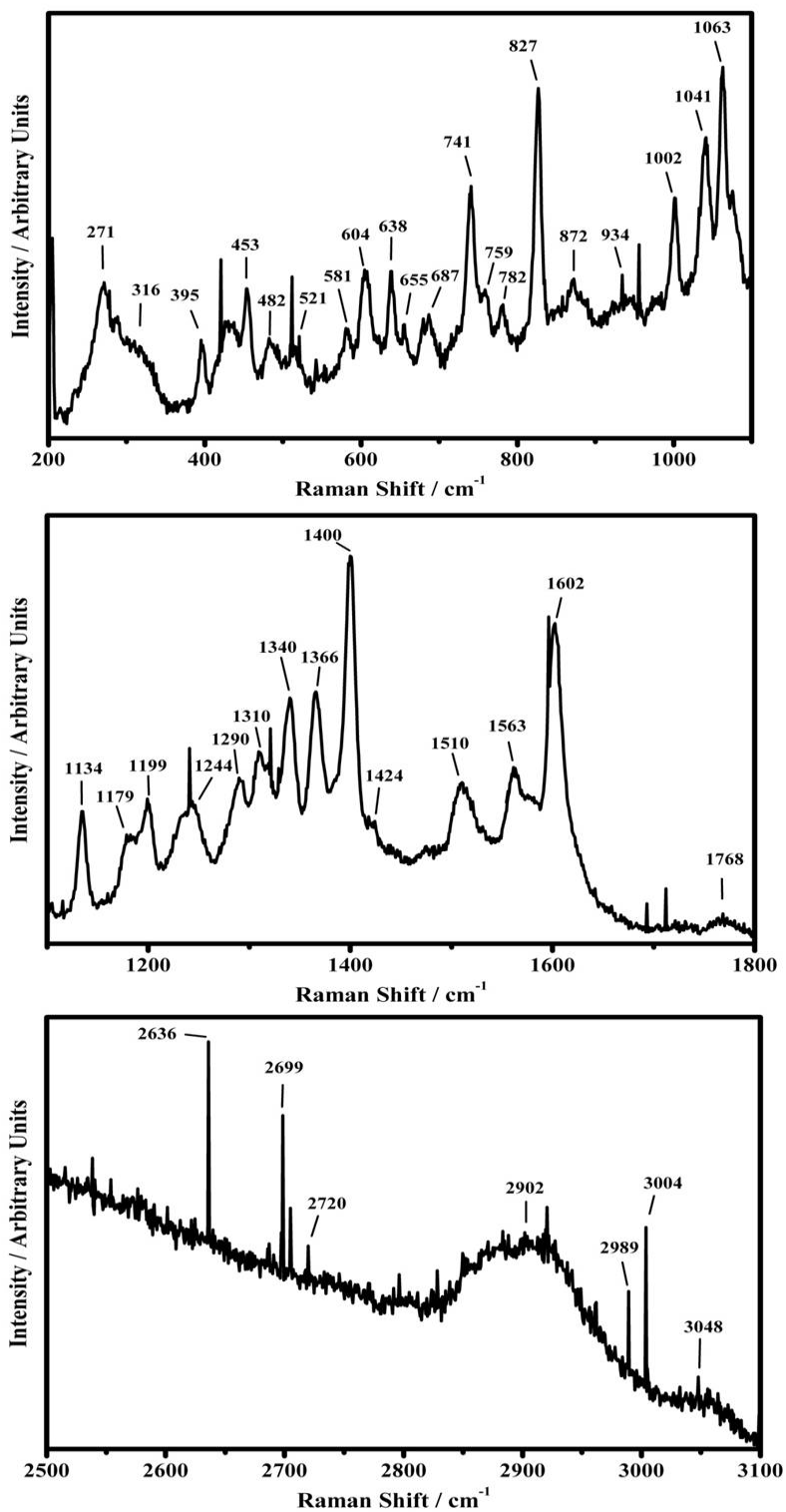
The occurrence of the weak band at  $\sim 950\text{ cm}^{-1}$ , assigned to the stretching mode of the protein structure, has been proposed has a good marker for the  $\alpha$ -helix structure.

As state above, the Raman band of the side chains of proteins are due to localized vibrational modes of specific amino-acids. For example, the characteristic modes of aromatic amino-acids have relatively high intensity and can be well detected also if sometime can be overlapped by others amide bands or other groups.

The phenylalanine shows a strong band at  $1002\text{ cm}^{-1}$ , (stronger in a hydrophobic chemical environment). The tryptophan and tyrosine have a Raman “*cross section*” ten times higher than phenylalanine; for this reason they results easier to detect by Raman spectroscopy.

The tryptophan shows a doublet (Fermi doublet) at  $1340$  and  $1360\text{ cm}^{-1}$ . The intensity ratio of such bands has been suggested has a good marker to determine the hydrophobic or hydrophilic chemical environment of the indole ring of the tryptophan amino-acid: hydrophobic if the band at  $1360\text{ cm}^{-1}$  is higher than that at  $1340\text{ cm}^{-1}$  (the ring is in contact with aliphatic side chains ) otherwise hydrophilic (the ring interacts with water molecules or similar). The band at about  $1550\text{ cm}^{-1}$  reflects the angle between the indole ring and the plane of the peptide bond whereas the band at  $\sim 875\text{ cm}^{-1}$  reflects the hydrogen bond of the N-H group of the indole ring. The bands at  $763$ ,  $1228$ ,  $1370$ ,  $1560$  and  $1776\text{ cm}^{-1}$  have been assigned to the interaction between cationic side chains and the aromatic  $\pi$  system of the tryptophan [20].

Many proteins shows thio- groups, both as free standing S-H or as disulphur bridge S-S, coming from the cysteine amino acid.



**Fig. 4.1.8** Raman spectra of the receptor GPR30 in the range between 200 and 1100  $\text{cm}^{-1}$  (top), 1100 and 1800  $\text{cm}^{-1}$  (middle), 2500 and 3100  $\text{cm}^{-1}$  (bottom).

The Raman bands due to the S-H group are usually weak and fall in the range between 2500 and 2700  $\text{cm}^{-1}$ , where, fortunately, others protein modes do not occur.

The Raman bands of the disulfide bridges fall in the range 450- 700  $\text{cm}^{-1}$ . In particular the bands at 508-512  $\text{cm}^{-1}$ , 523-528  $\text{cm}^{-1}$ , 540-545  $\text{cm}^{-1}$  can be assigned to the C-S stretching while the bands that fall at 655 and 704  $\text{cm}^{-1}$  can be assigned to the S-S [20].

In Fig. 4.1.8 representative Raman spectra collected on the GPR30 receptor are shown. The strong band at 1602  $\text{cm}^{-1}$  is an overposition of three modes: phenylalanine aromatic ring stretching, tryptophan aromatic ring stretching (indole ring) [22] and  $\text{COO}^-$  carboxylate ion stretching present as group of a side chain of an amino acid [8]. This indicate the presence of aspartic acid in the polypeptide skeleton [17], to which is ascribed also the mode at 1400  $\text{cm}^{-1}$ .

Even though the band at 1602  $\text{cm}^{-1}$ , two weak peaks at 1642 e 1658  $\text{cm}^{-1}$  can be detected and assigned to disordered  $\alpha$ -helix structures. The  $\alpha$ -helix structure is confirmed also by the Amide III mode which falls at 1310  $\text{cm}^{-1}$  and by the protein skeleton stretching that occurs at  $\sim 950 \text{ cm}^{-1}$  (Fig. 4.1.8). To the mode Amide III is also assigned the band that falls at 1244  $\text{cm}^{-1}$  (N-H bending) [23]. Moreover, it is possible to notice the presence of the bands at 759, 1233, 1366, 1563, 1768  $\text{cm}^{-1}$  assigned, as state above, to the interaction between the cationic side chains and the aromatic ring of the tryptophan [20]. This, confirms the hypothesis concerning the presence of the charged species and of the tryptophan in the investigated protein sample. The presence of the tryptophan is also confirmed by the occurrence of the “Fermi doublet” at 1340  $\text{cm}^{-1}$  and 1360  $\text{cm}^{-1}$  (shoulder of the band at 1366  $\text{cm}^{-1}$ ); the intensity ratio of the band of the Fermi doublet suggests that the indole ring is into hydrophilic chemical environment. The band at 1002  $\text{cm}^{-1}$  is assigned to the phenylalanine, while the bands at 511, 521, 543 e 655  $\text{cm}^{-1}$  are ascribed to the disulphur bridges, due to the presence of the cysteine amino acid [20]. The band at 827  $\text{cm}^{-1}$  is typical of the phenylalanine amino acid [24]. The others Raman features that can be seen in Fig. 4.1.8 are assigned in the following way [17]: 741  $\text{cm}^{-1}$  “ $\text{CH}_2$  rocking”, 782  $\text{cm}^{-1}$  “ring vibrational”, 872  $\text{cm}^{-1}$  “C-C stretching”, 1063  $\text{cm}^{-1}$  “C-N stretching”, 1310  $\text{cm}^{-1}$  “C-H deformation” and 1510  $\text{cm}^{-1}$  to a NH mode [8]. The bands at 316, 482, 581, 638, 687, 872, 1041, 1134, 1199, 1290 and 1424  $\text{cm}^{-1}$  are ascrive to the tryptophan amino acid [25]. The peaks at 934 and 1179



$\text{cm}^{-1}$  are due to the cysteine [26]. The bands at 271, 395, 453, 604  $\text{cm}^{-1}$  indicate the presence of the alanine amino acid in its charged form [27].

The broad band at about 2900  $\text{cm}^{-1}$  is due to the C-H stretching. The sharp peaks at 2636, 2699 e 2720  $\text{cm}^{-1}$  are assigned to the presence of disulphur bridges.

#### 4.1.4 Conclusions

The micro-Raman spectroscopy has been used to characterize the Endogenous Receptor GPR30 made by a cell lysate protein and its synthetic agonist ligand G-1.

In order to detected the Raman features of the GPR30 and of the G-1 ligand all the solvents used to obtain the samples have been characterized. For this reason the Raman spectra of dimethyl sulfoxide (DMSO) (Fig. 4.1.2), glycerol (Fig. 4.1.3), phenylmethylsulphonyl fluoride (PMFS) in ethanol (Fig. 4.1.4), PBS solution (Phosphate Buffered Saline System, 1M  $\text{KH}_2\text{PO}_4$ , 1M  $\text{K}_2\text{HPO}_4$ , 5M NaCl) (Fig.4.1.5), and  $\beta$ - mercaptoethanol (Fig. 4.1.6) have been collected and assigned to the main vibrational modes typical of each substance.

The Raman analysis of the PBS solution has shown the presence of an additive compound made by a biphenyl substituted structure, most probably the anti-fungal 2-phenylbromobenzene. The Raman spectra of the ligand was collected on sample made by the G-1 dissolved in DMSO (Fig. 4.1.7). Since, the G-1 theoretical spectrum, it has not been done, the attribution of the G-1 (Fig. 4.1.1.a) relative Raman features has been performed by comparison with characteristic parts of the molecules: 5-bromo-1,3-benzodioxole and the 1,3-benzodioxole. The Raman investigation performed on the endogenous receptor GPR30 allowed to identify some amino acid present on the peptide skeleton: tryptophan, phenylalanine, cysteine, alanine, and aspartic acid. It has been shown that the chemical environment of the indole ring of the tryptophan amino acid is hydrophilic. Moreover, it has been shown that the secondary structure of the peptide skeleton is made by disordered  $\alpha$ -helix structures.

Deeper investigation, made also by using different laser sources, to use the resonance Raman effect, in order to investigate the interaction between the ligand and the receptor are on the way. Preliminary studies not reported seems indicate that this interaction occur between the ligand and cysteine side chains.

## 4.2 Thermal structural evolutions of 1,2-dimyristoyl-sn-glycero-3-phosphatidylcholine (DMPC)-water systems investigated by micro-Raman Spectroscopy

During the last years great interest was devoted to the study of phospholipids-water mixtures in order to evaluate the structural and functional properties of these systems [28]. In fact, cells of living organisms can be thought as phospholipids membranes, sometime functionalized by proteins, which are immersed into water environment [29]. Among the usual topics, including protein misfolding diseases, drug discovery, pathogenesis, gene therapy, etc.[30-31], the membranes of the cells are attracting great attention as possible components for applications such as sensors, electronics and bioprocessing [32]. The great incentive coming from the different kind of applications has supported the development of membrane mimetic models made, usually, by phospholipids layers that represent the major component of most cell membranes with its typical chemical structure made by a hydrophilic charged head group bonded by glycerol backbone to hydrophobic long acyl chains [33].

It is well known that phospholipids spontaneously adopt the bilayer organization when dispersed in water to form closed vesicles (liposomes) [34]. The vesicle is a compartment, formed in vitro, where the interior is made by a small water volume enclosed by one or few layers constituted by amphiphilic molecules [35]. By selecting the preparation method it is possible to obtain vesicle with different diameters in the range between some nanometer up to tens of micrometer: large unilamellar vesicle (LUV), giant unilamellar vesicle (GUV) and multilamellar vesicle (MLV) [35,36].

The phospholipids bilayer vesicles (multilamellar and unilamellar) as a function of the temperature can be found in three different phases: gel ( $L_{\beta'}$ ), ripple ( $P_{\beta'}$ ) and liquid crystalline ( $L_{\alpha}$ ) [37,38]. In the  $L_{\beta'}$  phase the acyl chains are arranged in ordered way which approximate an hexagonal lattice, while above chain-melting temperature the lamellar liquid crystal phase ( $L_{\alpha}$ ) is found, characterized by a fast diffusion of the molecules in the plane of bilayer. The intermediate phase  $P_{\beta'}$  is characterized by a long range periodicity of the structure in the plane of the bilayer [37,38]. Nevertheless, much efforts need to be done in order to obtain information about the hydrocarbon chain order

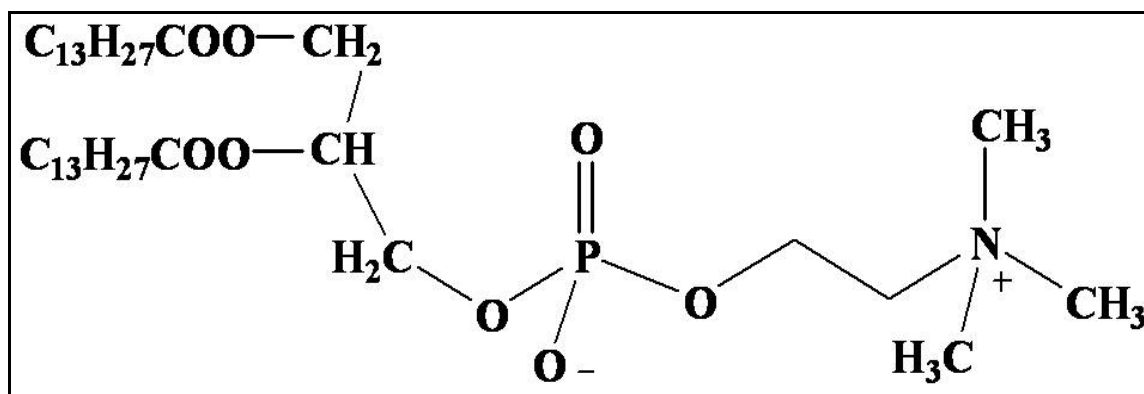
and mobility in the bio-mimetic membrane in order to fully understand of “order degree” of the different phases and the mechanisms of the phase transition.

Raman spectroscopy is a very powerful technique in this field. In fact, it has been already used to study the molecular organization of phospholipids in relation to the bilayer structure, affecting the fluidity and the conformational order in lipid mesophases, and to determine the average orientation of the mesophases molecules inside gratings [39-41].

In this framework, the thermal evolution, in the range between 10 up to 35°C, of biomimetic membranes made by the synthetic phospholipid 1,2-dimyristoyl-sn-glycero-3-phosphocholine (DMPC) and water has been studied by Raman spectroscopy, in order to investigate the mechanisms of the phase transition. Such study allow us to define the shift of a Raman band as a marker of the phospholipids bilayer phase and a qualitative model of the interaction between the water molecules and the lipid chains has been proposed.

#### 4.2.1 Experimental

The sample have been obtained by dissolving the DMPC (supplied by Echelon) in water, with weight ratio 90 to 10 respectively (see structure in Fig. 4.2.1)



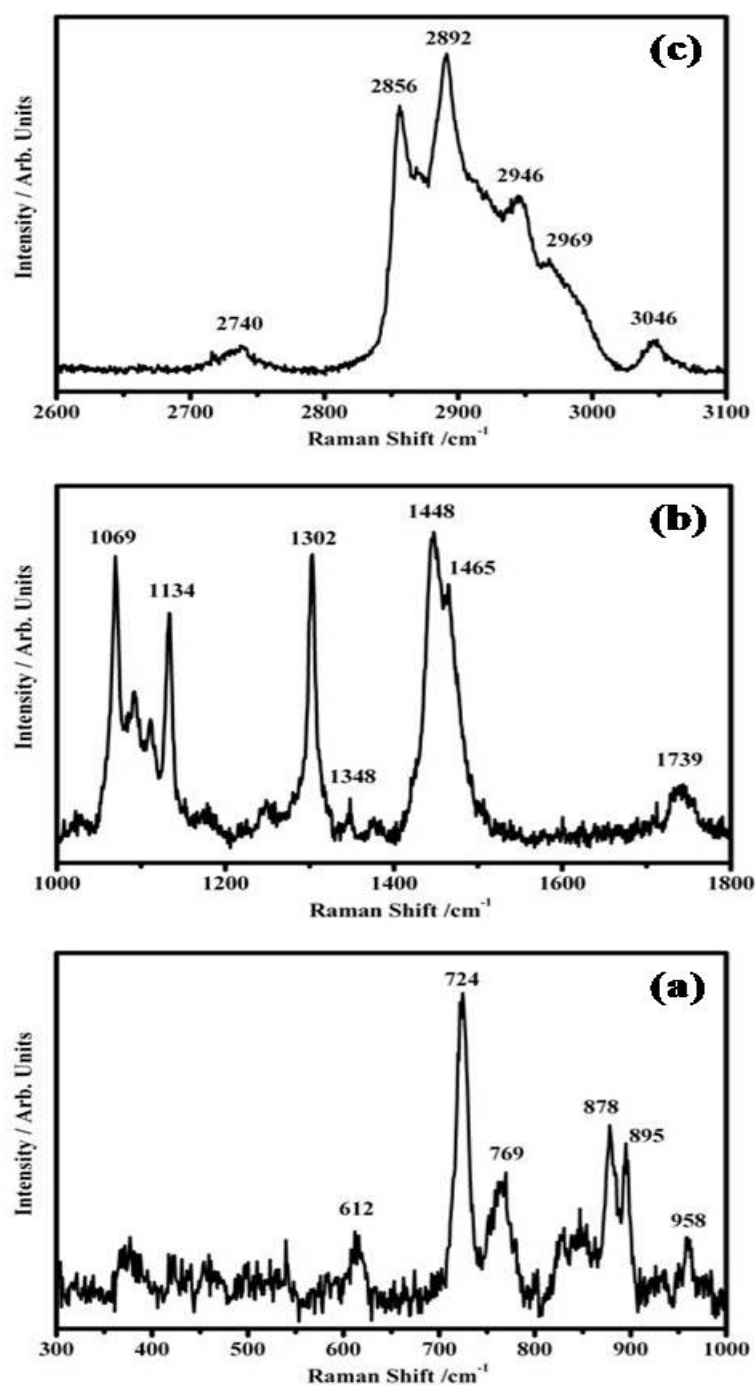
**Fig. 4.2.1.** Chemical Structure of 1,2-dimyristoyl-sn-glycero-3-phosphocholine (DMPC)

Raman spectra were recorded with the same software controlled Jobin-Yvon micro-Raman LABRAM apparatus described before, equipped by a He-Ne laser ( $\lambda=632.8\text{nm}$ ); a 50x Mplan Olympus objective (Numerical Aperture 0.90) was used, focusing the laser spot to 2-3  $\mu\text{m}$  of diameter. The spectral resolution using was of the order of 1  $\text{cm}^{-1}$ . The

temperature was controlled by placing the samples in a LINKAM THMS cell. The measurements were performed from 10 to 35°C using a heating rate of 1 °C/min. Prior to performing the measurements, the samples were held at the selected temperature for 20 min for thermal stabilization.

#### **4.2.2 Discussion**

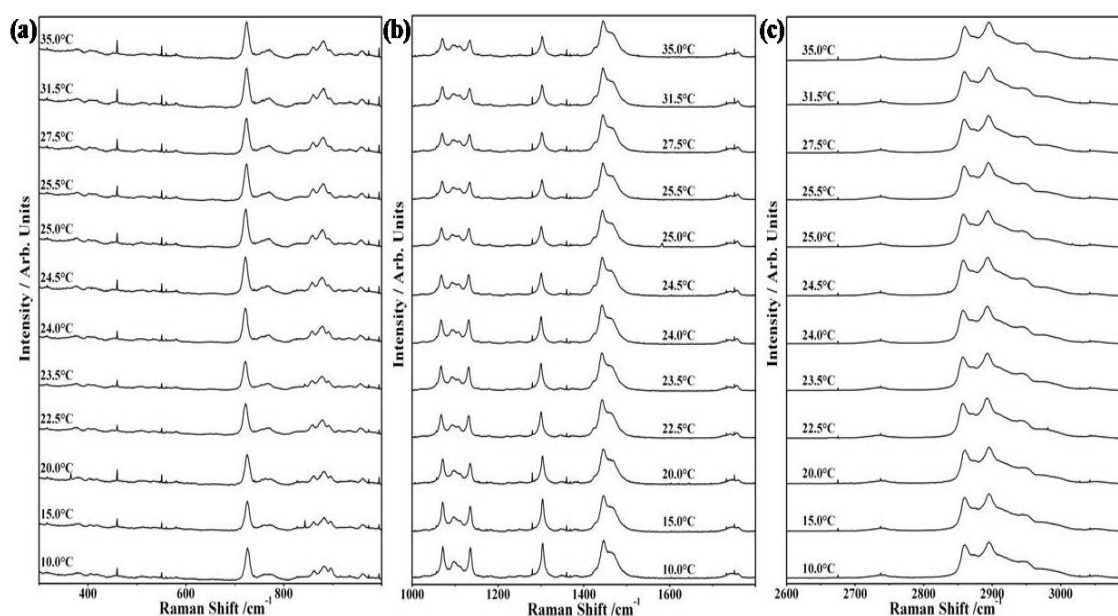
Before of the Raman investigation on thermal evolution, the attribution of the Raman modes of the DMPC was carried out. In figure 4.2.2 are shown the representative Raman spectra collected on the DMPC as powder.



**Fig. 4.2.2.** Representative Raman spectra of 1,2-dimyristoyl-sn-glycero-3-phosphocholine (DMPC) powder in the ranges 300-1000 cm<sup>-1</sup> (a), 1000-1800 cm<sup>-1</sup> (b), 2600-3100 cm<sup>-1</sup> (c).

The main Raman features are indicated in Fig. 4.2.2 and have been assigned taking into account the data reported elsewhere [39,40,42,43]. The bands at 2856 and 2892 cm<sup>-1</sup> are assigned to the symmetric ( $\nu_s(\text{CH}_2)$ ) and antisymmetric ( $\nu_a(\text{CH}_2)$ ) stretching modes of methylene groups. The band at 2740 cm<sup>-1</sup> is due to a combination of the scissoring and

wagging ( $\gamma(\text{CH}_2)$ ) methylene groups. The two modes at 2969 and 3046  $\text{cm}^{-1}$  correspond to the antisymmetric stretching modes ( $\nu_a(\text{CH}_3)$ ) of the methyl terminal groups of the chains of the phosphocholine head, respectively. The bands at 2946  $\text{cm}^{-1}$  is assigned to the overtone of the methylene scissoring mode ( $\delta(\text{CH}_2)$ ) enhanced by Fermi resonance with the  $\nu_s(\text{CH}_2)$  mode. The bands at 1302 and 1465,  $\text{cm}^{-1}$  are assigned to the methylene scissoring mode ( $\delta(\text{CH}_2)$ ) and the band at 1448  $\text{cm}^{-1}$  to the methylene twisting mode ( $t(\text{CH}_2)$ ). The modes between 1069 and 1134  $\text{cm}^{-1}$  (enclosed the modes at 1092 and 1111  $\text{cm}^{-1}$ ) are assigned to the skeletal vibrations of the C-C bonds. In particular, the modes at 1111 and 1134  $\text{cm}^{-1}$  are assigned to the *trans* C-C bonds, whereas, the mode at 1092  $\text{cm}^{-1}$  has been assigned to the stretching of the C-C skeleton of different kinds of *gauche* structures. The C=O ester groups stretching is responsible of the mode at 1739  $\text{cm}^{-1}$ . The modes at 769 and 895  $\text{cm}^{-1}$  are assigned to the C-N stretching of the O-C-C-N<sup>+</sup> (see Fig. 4.2.1) in the *trans* conformation while the choline *gauche* conformation it is associated to the modes at 724 and 878  $\text{cm}^{-1}$ . The mode at 958  $\text{cm}^{-1}$  is assigned to the CH<sub>2</sub> rocking mode.

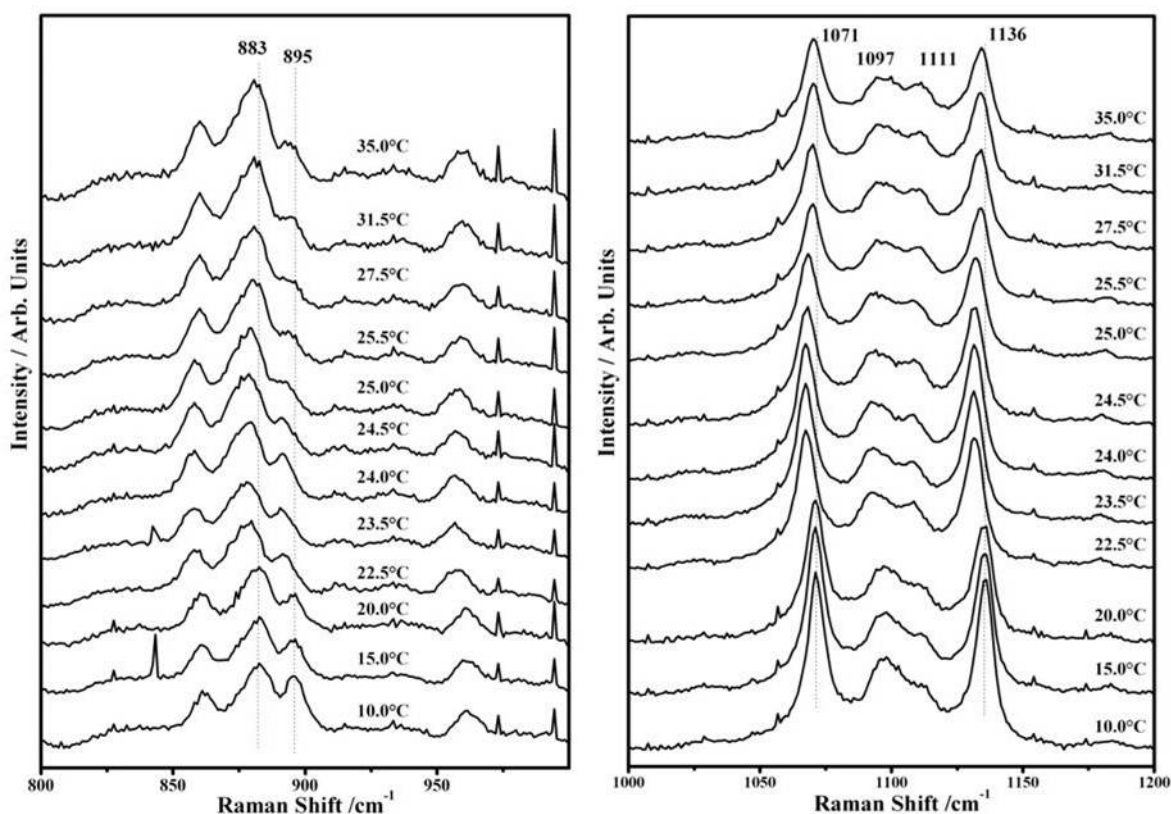


**Fig. 4.2.3.** Representative Raman spectra collected on the 1,2-dimyristoyl-sn-glycero-3-phosphocholine (DMPC) and water mixture with weight ratio 90 to 10 in the range between 300 and 1000  $\text{cm}^{-1}$  (a), 1000 and 1800  $\text{cm}^{-1}$  (b) and 2600 and 3100  $\text{cm}^{-1}$  (c).

In Fig. 4.2.3 are shown the representative Raman spectra collected on the mixture made by DMPC and water as a function of the temperature.

As it can be noticed from Fig. 4.2.3, only weak modifications occur on the Raman spectra of such sample as a function of the temperature. It can be seen as the band assigned to the C-N stretching of the O-C-C-N<sup>+</sup> (Fig. 4.2.3.a) due to choline gauche conformation at 878 cm<sup>-1</sup> (in solution at 883 cm<sup>-1</sup>) increases as the temperature increases, while that at 895 cm<sup>-1</sup>, assigned to the *trans* conformation of choline group seems to decrease vs. temperature [39]. Such evidence seems to be confirmed by the observed behaviour seen in Fig. 4.2.3.b where the modes at 1111 and 1134 cm<sup>-1</sup> (assigned to the *trans* C-C bonds) increase against the mode at 1097 cm<sup>-1</sup> (assigned to the stretching of the C-C skeleton of different kinds of *gauche* structures).

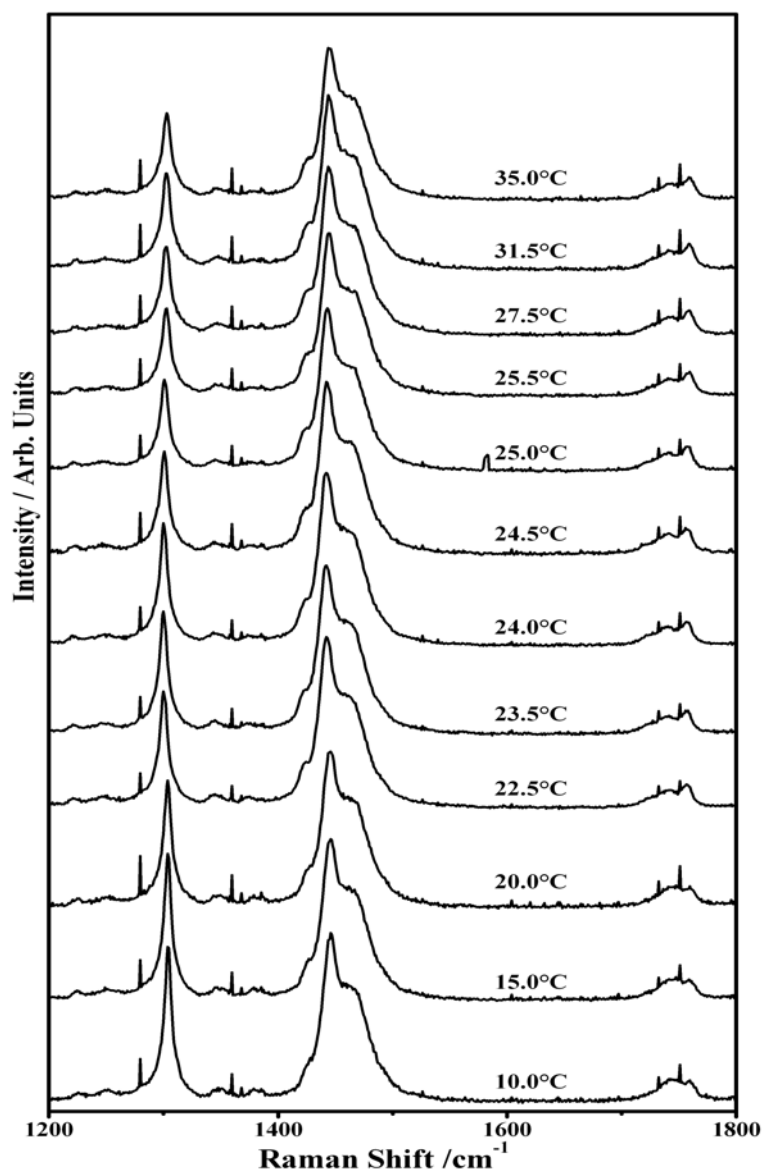
In order to better understand the evidence obtained by the Raman analysis, some parts of the Raman spectra shown in Fig. 4.2.3 have been magnified.



**Fig. 4.2.4.** Magnification of the representative Raman spectra collected on the 1,2-dimyristoyl-sn-glycero-3-phosphocholine (DMPC) and water mixture with weight ratio 90 to 10 in the range between 800 and 1000 cm<sup>-1</sup> (on the left) and between 1000 and 1200 cm<sup>-1</sup> (on the right).

The observations stated above are confirmed from the Fig. 4.2.4. In fact, the described trends of the ratio between the bands at 883 and 895  $\text{cm}^{-1}$  as well as the ratio between the bands at 1097 on 1111  $\text{cm}^{-1}$  indicate that both choline groups and carbon chains change from *trans-trans* conformation to the *gauche* conformation during the phase transition of the system DMPC-WATER from the well ordered gel phase to the liquid crystalline phase as the temperature increases[42,44-45].

In Fig. 4.2.5 is shown the magnification of the spectra in the range between 1200 and 1800  $\text{cm}^{-1}$ .

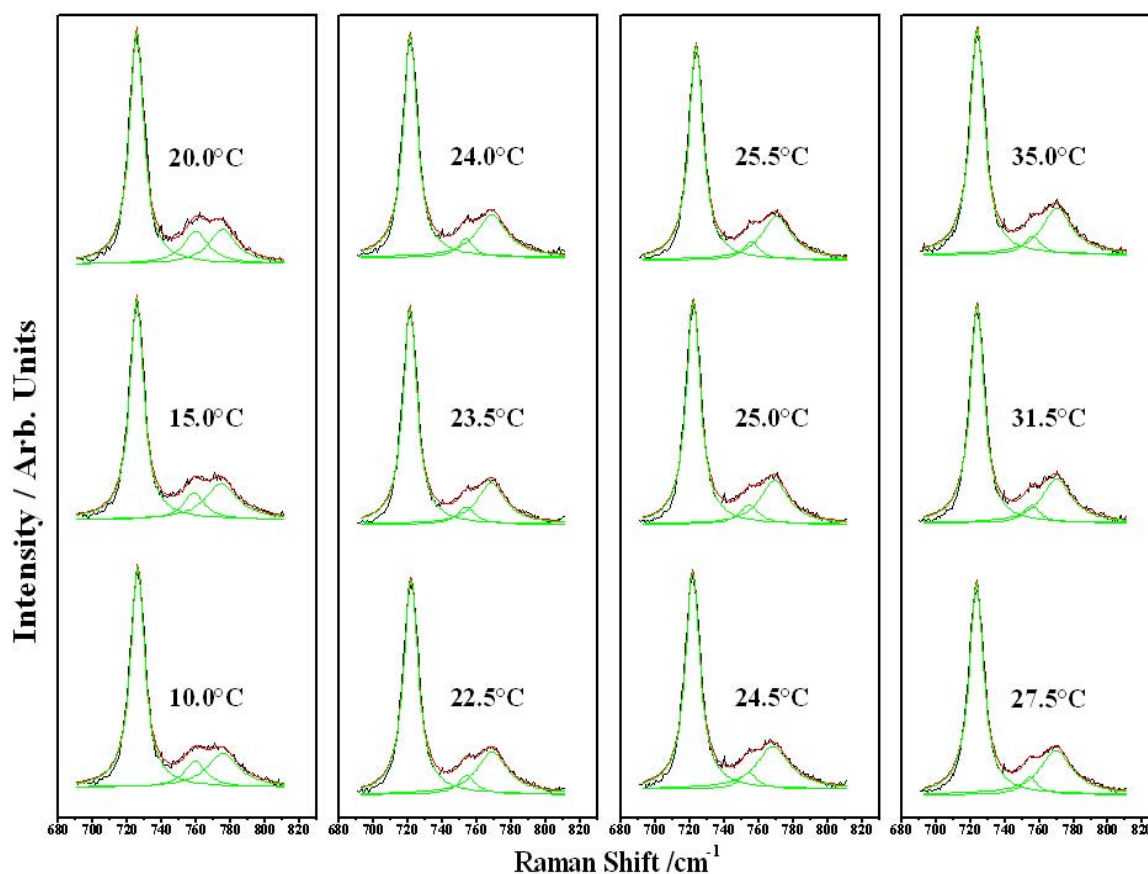


**Fig. 4.2.5.** Magnification of the representative Raman spectra collected on the 1,2-dimyristoyl-sn-glycero-3-phosphocholine (DMPC) and water mixture with weight ratio 90 to 10 in the range between 1200 and 1800  $\text{cm}^{-1}$ .



As it can be seen a remarkable modification in the Raman spectra of the systems subjected to heating treatment is the occurrence of the band at  $1427\text{ cm}^{-1}$  near the strongest band at  $1444\text{ cm}^{-1}$  (with its shoulder at  $1463\text{ cm}^{-1}$ ) induced by the increased temperature. Such Raman features assigned to the acyl chain  $\text{CH}_2$  deformation indicate a change in the lattice packing [44].

Of great interest it has been for us the observation of a light up-shift of the band at  $724\text{ cm}^{-1}$ . For such reason, the parts of the Raman spectra, at the different temperatures, in the range between  $690$  and  $810\text{ cm}^{-1}$  have been detailed studied and the deconvolution fit of each spectra has been done (Fig. 4.2.6).



**Fig. 4.2.6.** Deconvolution of the Raman bands in the range between  $690$  and  $810\text{ cm}^{-1}$  where are shown the experimental spectra (black lines), the single lorentzian functions (green lines) and the calculated spectra (red lines).

As it can be seen only three lorentzian curves have been used to obtain the experimental spectrum. The increased intensity of the band at  $769\text{ cm}^{-1}$  with respect the one at  $724\text{ cm}^{-1}$  confirm the change from *trans* to *gauche* conformation of the choline group during

the phase transition (Fig.4.2.6). Anyway, the frequencies of the bands at  $724\text{ cm}^{-1}$  obtained for the spectra collected at different temperature have been plotted as a function of temperature (Fig. 4.2.7).

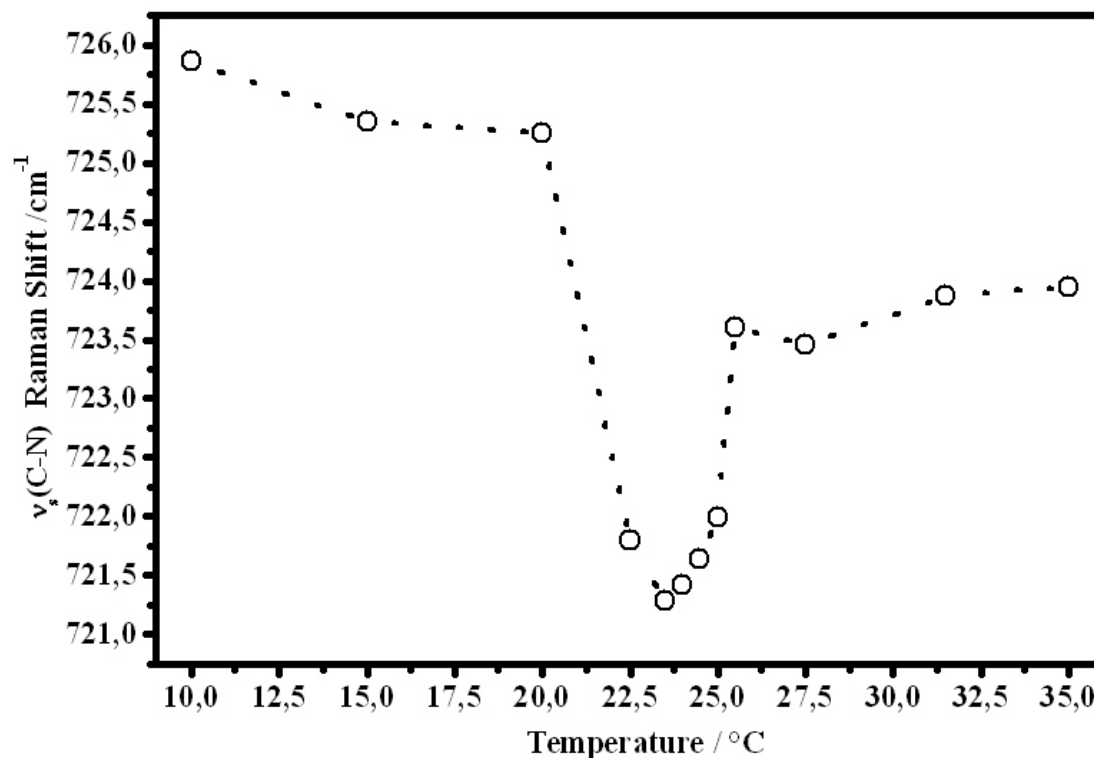


Fig. 4.2.7. Plot of the calculated frequencies of the band at  $724\text{ cm}^{-1}$  versus the temperature.

From Fig. 4.2.8 it is possible to see that temperature dependent frequencies are grouped in three ranges. In particular, from 10 to 20 °C the bands frequency falls in the range between 726 and  $725\text{ cm}^{-1}$ , from 21 to 25°C the frequency range is between  $722.5$  and  $721\text{ cm}^{-1}$  and for temperature from 25.5 to 35°C the frequency range goes from  $723$  to  $724.5\text{ cm}^{-1}$ . The blue shift of the bands at  $724\text{ cm}^{-1}$  assigned to the C-N stretching of the  $\text{O-C-C-N}^+$  is due to the water molecules that dependently by the phase of the system can be able or not to offer their lone pair, to the positive charge of the nitrogen in the choline groups. In the gel phase longer chains and greater chain ordering of DMPC should produce a greater hydrophobic barrier to the water molecules. Of course, in the liquid crystalline phase, the order is reduced and the water molecules are able to interact to the cationic site. It is however evident by Fig. 4.2.7, that between the ripple phase and the liquid crystalline phase an increased interaction of the water molecules with the

nitrogen of the choline group is found, suggesting a “more” disorder phase with respect to the liquid crystalline one.

However, in this work, the use of the Raman band of the C-N stretching in the O-C-C-N<sup>+</sup> group is proposed, for the first time in our knowledge, to detect the “order degree” and subsequently the phases of a biomimetic membranes made by DMPC.

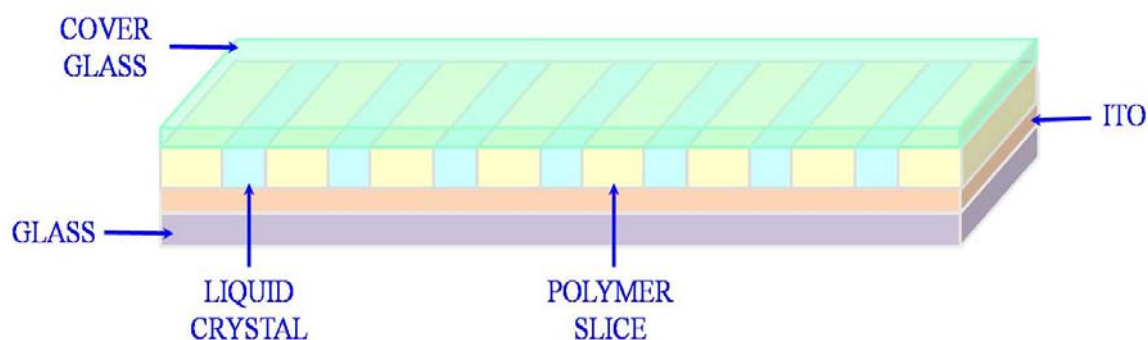
### 4.2.3 Conclusions

The attribution of the Raman modes of the DMPC powder has been given. It has been shown that as the temperature increases the conformation of the choline groups and of the hydrocarbon chains change from *trans* to *gauche*. In addition, it has been shown that the C-N stretching band shows a peculiar frequency shift across the transition gel-ripple-liquid crystalline phases. This behaviour could even provide a useful diagnostic marker of such kind of transition.

A more extensive and accurate investigation on the temperature dependence of all the Raman modes across the phase transitions of this systems are planned, to better characterize the relationship between the vibrational dynamics, the change of packing and the degree of disorder.

### 4.3 Polarized Micro-Raman investigation of E7 liquid crystal in POLICRYPS

During the recent years great interest was aroused by the POLICRYPS (Polymer Liquid Crystal Polymer Slices), as novel technology for making switchable holographic gratings [46]. As it can be seen in Fig. 4.3.1, POLICRYPS consist in polymer slices alternated to films of regularly aligned nematic liquid crystal cell. All the electro-optical applications of POLYCRYPS are due to the uniform and regular alignment of the molecular director inside the nematic liquid crystal films.



**Fig. 4.3.1.** Schematic view of a POLICRYPS.

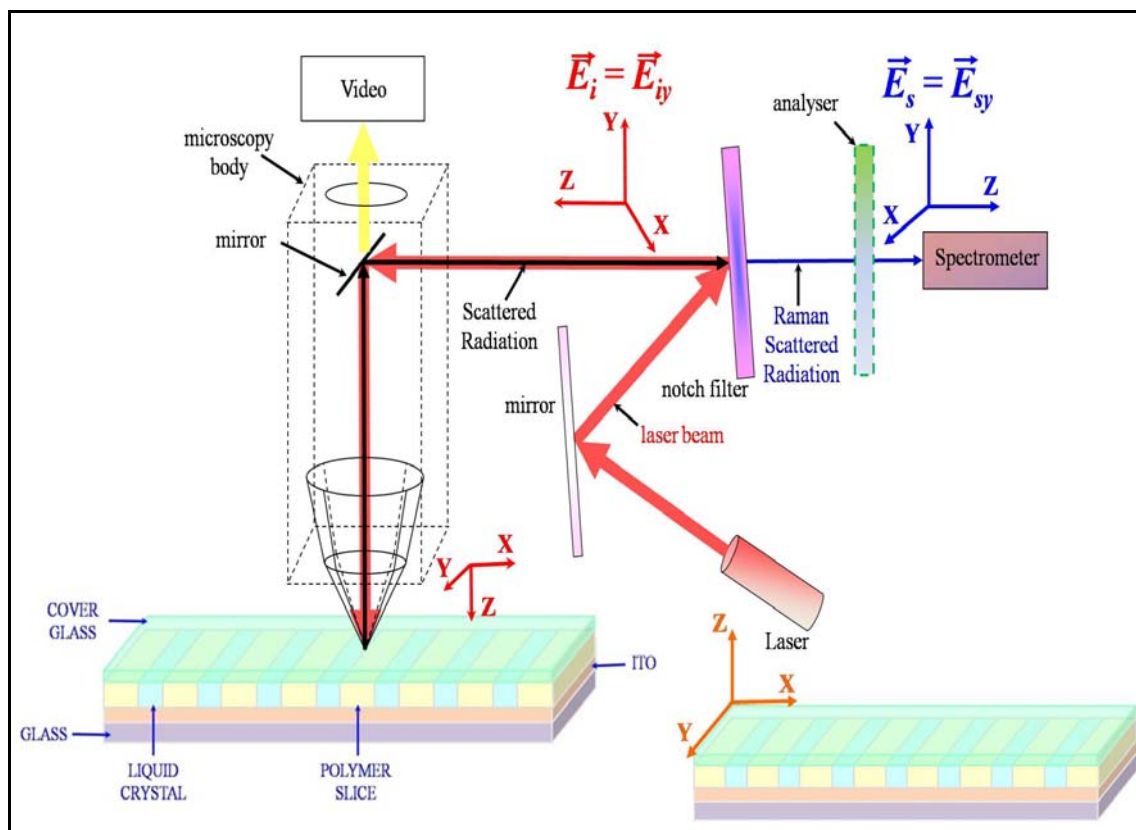
Nevertheless, in our knowledge, a direct estimation of the orientation of the director of Nematic liquid crystal was never performed. Polarized Raman spectroscopy can be considered a very useful technique in order to follow the orientations of the nematic liquid crystal molecules inside the POLYCRYPS device, and its application to this aim will be presented in this paper. In this work a specific investigation of the liquid crystal E7, of the monomer (Norland Optical Adhesive NOA-61) and its derived polymeric form will be carried out, in order to assign the main Raman features to be used for the polarized Raman spectroscopy investigation. The orientation of the director of the nematic liquid crystal POLYCRYPS will be determined by a modified experimental setup used for polarized Raman spectroscopy.

### 4.3.1. Experimental

The POLYCRYPS studied in this work are prepared by using liquid crystal E7 (supplied by Merk) and the monomer NOA-61 (Norland Optical Adhesive). The used procedure to make the POLYCRYPS is described elsewhere [46,47]. Briefly, the mixture made by the nematic liquid crystal, monomer and photo-initiator is heated above the nematic–isotropic transition temperature of the E7 component and then cured by interference pattern of a UV radiation. When the curing process is finished the sample is slowly cooled down at room temperature. An Ar-ion laser is the source of a single-mode radiation at the wavelength  $\lambda_B = 351$  nm. The beam is broadened up to a diameter of about 25 mm by a beam expander BE and divided into two beams of almost equal intensity by the beam splitter BS. These two beams overlap and give rise to the ‘curing’ light beam, spatially modulated by the interference pattern at the entrance plane of the sample cell. Depending on the required nano/microscale dimensions of the structure, the spatial period of the interference pattern can be varied in the range  $\Lambda = 0.2\text{--}15$   $\mu\text{m}$  by adjusting the total interference angle  $2\theta_{\text{cur}}$ . A commercial, metal-coated, reflective diffraction grating (Edmund Optics) placed above the sample is used as a test element for the interferometric monitoring of vibrations. Part of each of the curing beams is reflected and diffracted by this grating. The set-up is adjusted to make the reflected part of one beam spatially coincident with the diffracted part of the second one. These two radiations are wave coupled by the test grating and their interference pattern is detected by an additional photodiode. The signal of this photodiode is sent to a computerized active feedback system, which exploits a software based on a proportional–integral–derivative protocol; this drives a mirror-holder whose position can be controlled by a piezoelectric mechanism, used in feedback configuration. This control system has proved to be able to continuously compensate for changes in the optical path length due to vibrations as well as variations in environmental conditions such as room pressure, temperature or humidity; residual fluctuations are of the order of 6–7 nm, which correspond to the sensitivity of the piezo-system used.

Raman spectra were collected by a Raman microprobe Jobin-Yvon Labram (spectral resolution  $\sim 2$   $\text{cm}^{-1}$ ) equipped with a CCD detector and a He-Ne laser (632.8 nm

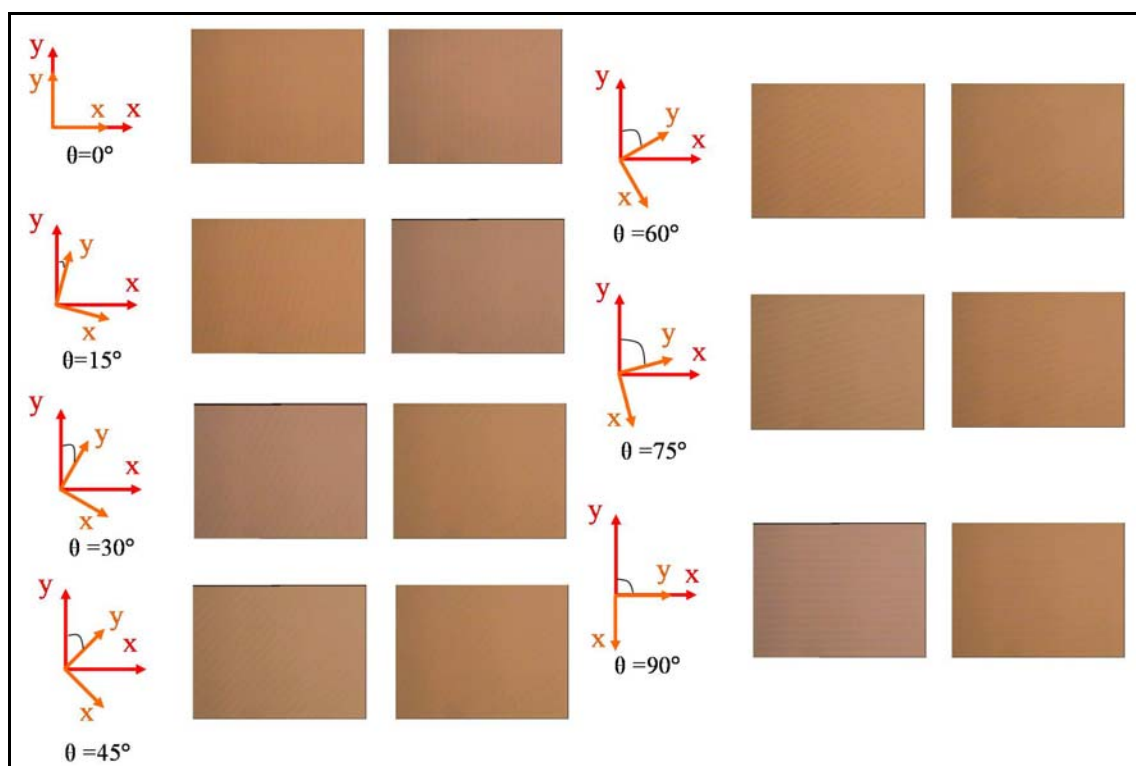
emission). A 50x Mplan Olympus objective was used (Numerical Aperture 0.90), focusing a laser spot of 2-3  $\mu\text{m}$  apparent diameter. Polarized spectra have been collected by using the experimental set-up shown in Fig. 4.3.2.



**Fig. 4.3.2** Experimental set up used for polarized Raman spectra and laboratory frame axes: in red the axis systems of the laser source, in orange those of the sample and in blue the system of the scattered radiations.

As it can be seen, the laser source (He:Ne, 633nm) is polarized in the plane **YZ**. In this configuration the sample is placed under the microscope in such way that the walls of the polymeric slices are parallel to the polarization of the incident light. The analyser allows only the transmission of the scattered radiation component polarized in the plane **YZ**. By using this setup only the component **YY** of the polarizability tensor will be detected (labelled after the laboratory axes). The sample is placed on a goniometric axis rotation stage supplied by Thorlabs. The spectra have been collected for different values of the angle  $\theta$ , between incident light polarization and the direction of POLYCRIPS grating grooves, starting from  $\theta=0^\circ$  (polymeric wall parallel to the laser sources polarization) up to  $\theta=90^\circ$  (polymeric wall perpendicular to the light polarization), with

angular steps of  $15^\circ$ , as shown in Fig. 4.3.3. In Fig. 4.3.3 can be observed how the polymeric wall are aligned with respect to laser polarization as a function of the angle  $\theta$ .



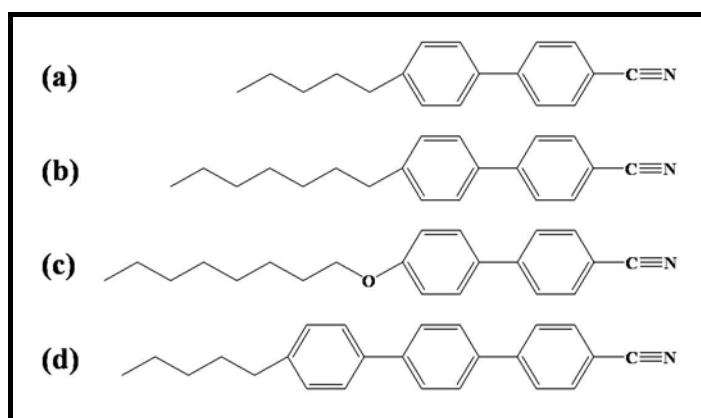
**Fig. 4.3.3** Optical images of POLICRYPS and relative angles used in order to collect the Raman spectra. In red is indicated the light axes and in orange the samples axes references.

### 4.3.2 Discussion

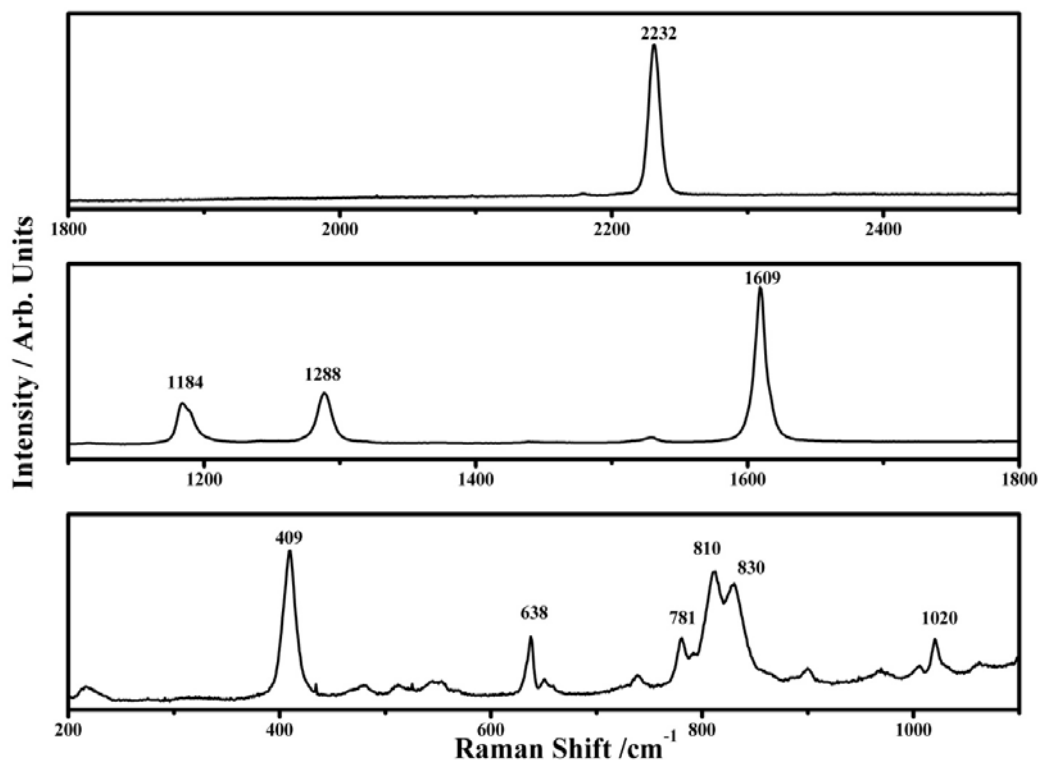
The liquid crystal E7 is a multicomponent nematic mixture made mainly by substituted 4-cianobiphenyls (Fig. 4.3.4) [48].

The relative Raman spectra collected on the isotropic liquid crystal are shown in Fig. 4.3.5. In the collected spectra the major Raman bands are assigned to the ring deformations. The attribution of such modes has been performed taking into account that biphenyl belong to the  $C_{2v}$  point group [49-51]. So that the skeletal vibrational modes of the biphenyl can be described just in four symmetry species; in particular the bands at  $1020$  ( $\nu_{18a}$ ),  $1184$  ( $\nu_{9a}$ ),  $1529$  ( $\nu_{19a}$ ) and  $1609$  ( $\nu_{8a}$ )  $\text{cm}^{-1}$  are described by the  $A_1$  symmetry representation; the modes with symmetry  $A_2$  falls at  $781$   $\text{cm}^{-1}$  ( $\nu_{10a}$ ) while the peaks at  $810$  ( $\nu_4$ ) and  $830$  ( $\nu_{11}$ )  $\text{cm}^{-1}$  have  $B_1$  symmetry and the modes with  $B_2$  symmetry are at  $638$  ( $\nu_{6b}$ ) and  $1288$  ( $\nu_3$ )  $\text{cm}^{-1}$  [49-51]. In addition the vibrations which

fall at 1020 ( $\nu_{18a}$ ), 1184 ( $\nu_{9a}$ ), 1529 ( $\nu_{19a}$ ) and 1609 ( $\nu_{8a}$ )  $\text{cm}^{-1}$  occur in the molecular plane while the others occur out of the molecular plane.



**Fig. 4.3.4** Main components of the E7 liquid crystal: (a) 4'-pentylbiphenyl-4-carbonitrile,  $\text{C}_{18}\text{H}_{19}\text{N}$ , (5CB); (b) 4'-heptylbiphenyl-4-carbonitrile,  $\text{C}_{20}\text{H}_{23}\text{N}$ , (7CB); (c) 4'-(octyloxy)biphenyl-4-carbonitrile,  $\text{C}_{21}\text{H}_{25}\text{NO}$ , (8OCB); (d) 4'-Pentyl-p-terphenyl-4-carbonitrile,  $\text{C}_{24}\text{H}_{23}\text{N}$  (5CT).



**Fig. 4.3.5** Representative Raman spectra collected on isotropic liquid crystal E7 in the ranges 200-1100  $\text{cm}^{-1}$  (bottom), 1100-1800  $\text{cm}^{-1}$  (middle) and 2000-2400  $\text{cm}^{-1}$  (top).



The others modes at 409 ( $\gamma$  deformation) and 2232 (symmetric stretching)  $\text{cm}^{-1}$  are assigned to the CN group [49-52]. A detailed attribution of the E7 liquid crystal observed modes can be found in Table 4.3.1.

Liquid Crystal E-7		
Raman Shift ( $\text{cm}^{-1}$ )	Relative Intensity	Assignments <sup>a</sup>
216	(W)	
409	(S)	$\gamma_s(\text{CN})$
479	(W)	$\gamma(\text{CC})$
512	(W)	$\delta_s(\text{CN})$
542	(W)	$\gamma(\text{CC})$ (16b)
553	(W)	$\beta(\text{CN})$
638	(M)	$\beta(\text{CC})$ (6b)
651	(VW)	$\delta_s(\text{CCC}) + \beta(\text{CC})$ (6b)
739	(VW)	$\beta_{\text{as}}(\text{CH}_2) + \gamma(\text{CH})$
781	(M)	$\gamma(\text{CH})$ (10a)
810	(M)	$\nu(\text{CCC}) + \beta(\text{CC})(1) + \beta_{\text{as}}(\text{CH}_2)$ (4b1)
830	(M)	$\gamma(\text{CH})$ (11)
899	(W)	$\nu(\text{CCC})$
970	(W)	$\nu(\text{CCC})$
1006	(W)	$\beta(\text{CC})$ (12)
1020	(W)	$\beta(\text{CH})$ (18a)
1062	(W)	$\gamma(\text{CCC}) + \beta(\text{CH})$ (18a)
1184	(S)	$\beta(\text{CH})$ (9a)
1288	(S)	$\gamma_{\text{as}}(\text{CH}_2) + \gamma_s(\text{CH}_2)$ (3b2)
1529	(VW)	$\nu(\text{CC})$ (19a)
1609	(VS)	$\nu(\text{CC})$ (8a)
2232	(VS)	$\nu(\text{CN})$

**TABLE 4.3.1.** Raman modes frequencies, relative intensities and assignments of E7 liquid crystals [2-4] (key:  $\nu$   $\equiv$  stretch,  $\delta$   $\equiv$  bend,  $\nu_{\text{ccc}}$   $\equiv$  skeletal,  $\beta$   $\equiv$  in plane deformation,  $\gamma$   $\equiv$  perpendicular deformation,  $s$   $\equiv$  symmetric,  $as$   $\equiv$  asymmetric); VS= very strong, S=strong, M=medium, W=weak, VW=very weak).

<sup>a</sup> In Wilson notation with symmetries based on  $C_{2v}$  point group.

The optical polarizability tensor for the molecular components of the E7 liquid crystal can be represented with good approximation by an ellipsoid oblate with  $\alpha_{zz} > \alpha_{yy} = \alpha_{xx}$ , if the molecular axes are the same described in Fig. 4.3.6 (In this work the molecular axes will be labeled by lowercase letters, while the laboratory frame axes are indicated by capital letters). It is well known, from the basic Raman theory, that each vibrational modes induce a dynamic distortion of the polarizability that is synchronized with the

vibrational normal coordinate  $Q_k$ :  $\left( \frac{\partial \alpha_{ij}}{\partial Q_k} \right)$ .

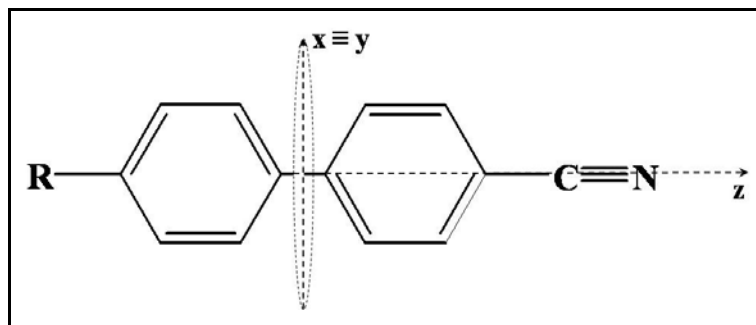


Fig. 4.3.6 Molecular reference axes of the component of the E7 liquid crystal.

The symmetric stretching of the aromatic rings of the biphenyls molecules and the stretching of the CN groups induce the major change along the long molecular axis of biphenyl molecules. In this frame, if the electric field of the incident polarized radiation is parallel to the molecular  $z$ -axis then the induced dipole moment lies along that axis and it is given by  $\mu_z = \alpha_{zz} E$ . If the electric field of the incident light is perpendicular to the molecular  $z$ -axis then the induced dipole moment is given by  $\mu_y = \alpha_{yy} E$ . Therefore, since the intensity of the scattered radiation depends on the square of the induced dipole moment, the Raman intensity of the modes which occur along the  $z$ -axis will be biggest for the biphenyl molecules with their long axes ( $z$ -axis) parallel to the electric field of the incident radiation. So that, the orientation of the liquid crystal molecules can be identified by finding the axis at which the maximum Raman signal, for the above described Raman band, occurs [52,54]. Therefore, before performing Raman spectroscopy investigations of POLICRYPS it was necessary to investigate the monomer component used to make the holographic grating. The NOA-61 has been studied before and after the polymerization process. It should be underlined that the exact composition of the NOA-61 is still unknown but it should be a mixture of a mercapto-ester with acrylate monomer as described elsewhere [55] (Fig. 4.3.7).

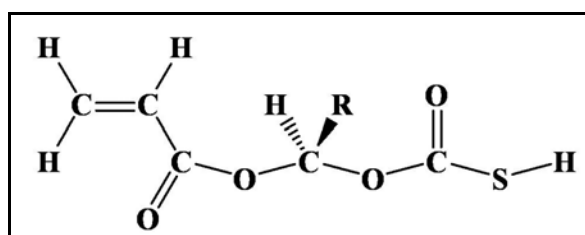
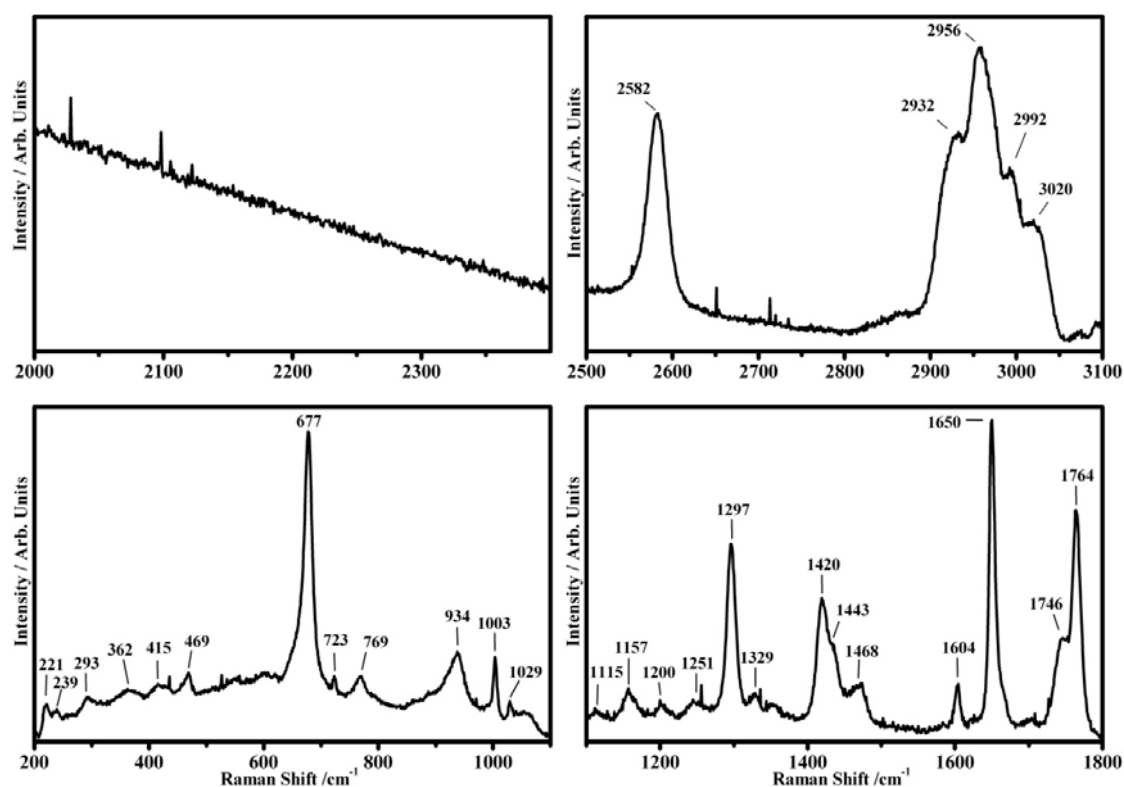


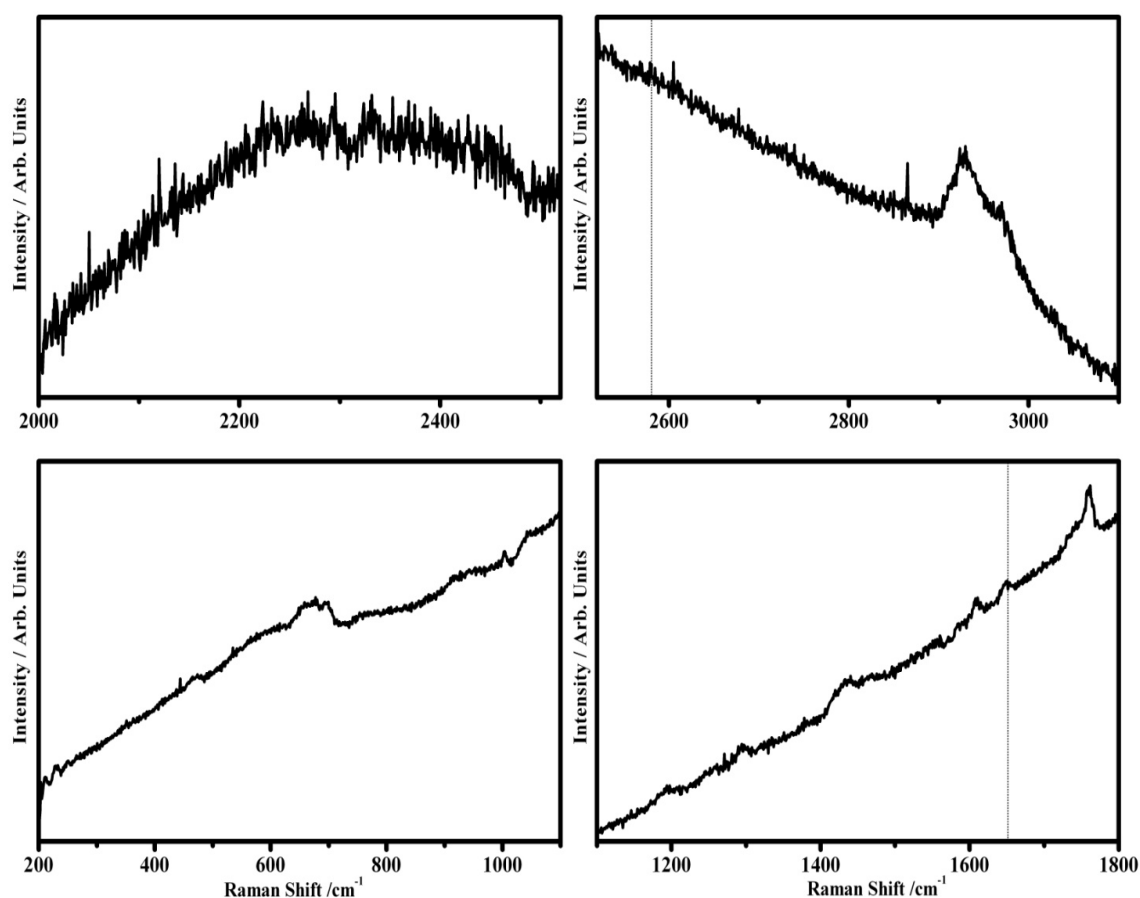
Fig. 4.3.7 Basic structure Norland Optical Adhesive NOA-61: mercapto-ester with acrylate monomer.

In Fig. 4.3.8 the Raman spectra collected on NOA-61 monomer are shown. It is possible to notice the characteristic Raman features of the thiol groups (S-H) at about  $2582\text{ cm}^{-1}$ , vinyl group (C=C symmetric stretching, non conjugated) at  $1650\text{ cm}^{-1}$  and of the carbonyl group (C=O) at  $1746$  and  $1764\text{ cm}^{-1}$  of the carboxyl group (COOR) [56-59].



**Fig. 4.3.8** Representative Raman spectra collected on the monomer Norland Optical Adhesive NOA-61.

At  $1604\text{ cm}^{-1}$  falls the aromatic ring vibration, evidently present on the R group of the molecule (Fig. 4.3.7) [56,60]. The Raman band at  $677\text{ cm}^{-1}$  is assigned to the C-S bond, while the peak at  $1297\text{ cm}^{-1}$  and the bands that fall in the region between  $1400$  and  $1500\text{ cm}^{-1}$  are assigned to the  $\text{CH}_3$  bending and those in the range between  $2900$  and  $3100\text{ cm}^{-1}$  are assigned to C-H stretching [60-64]. It is interesting to see the Raman spectra collected on the polymerized NOA-61 that is the material which make the walls in the POLICRYP gratings. It is possible to see in Fig. 4.3.9 the absence of the band at  $2582\text{ cm}^{-1}$  and, simultaneously, the strong reduction of the band at  $1650\text{ cm}^{-1}$  indicating that the curing process regard a reaction between the thiol group and the vinyl group present on the monomer [57-59].

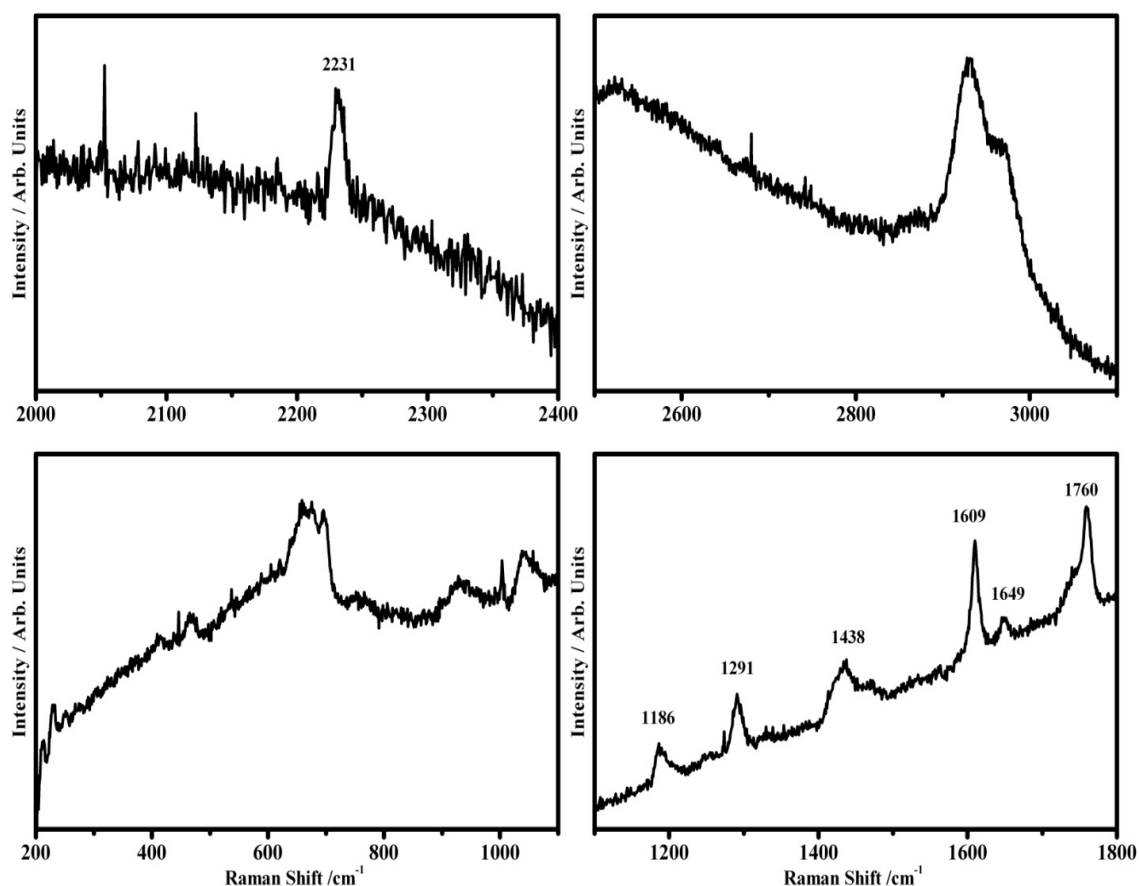


**Fig. 4.3.9** Representative Raman spectra collected on the polymerized Norland Optical Adhesive NOA-61.

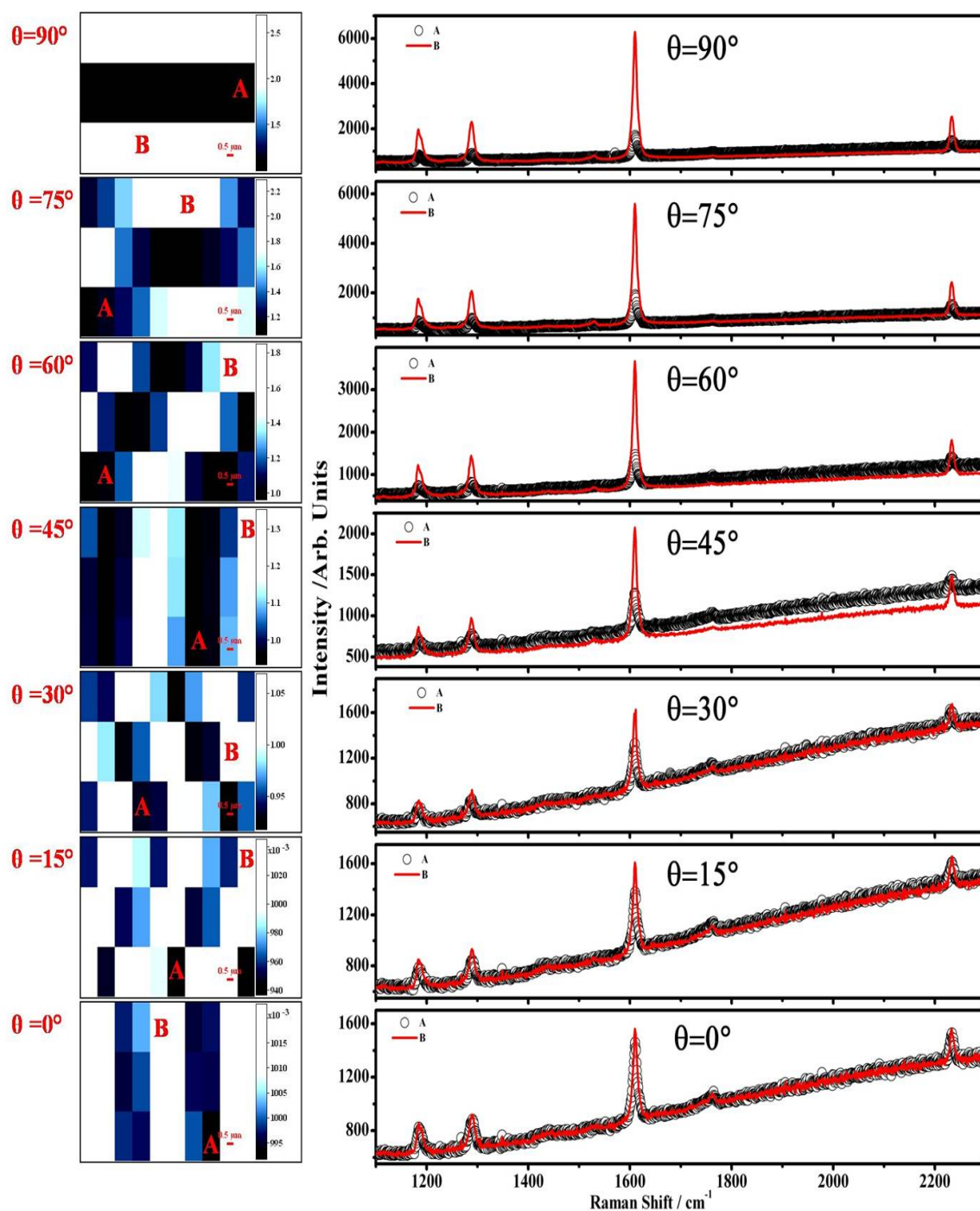
In Fig. 4.3.10 are shown the Raman spectra collected on the whole POLICRYPS (NOA-61 polymerized and E7) where it is possible to notice the typical bands at  $1609\text{ cm}^{-1}$  and  $2231\text{ cm}^{-1}$  assigned above to the liquid crystal molecules and the bands at  $1746$  and  $1764\text{ cm}^{-1}$  of the carboxyl group of the NOA-61. Such bands will be used to study the liquid crystal orientation inside POLICRYPS.

In order to study the orientation of the liquid crystal molecules with respect to the polymeric walls of the POLICRYPS, polarized Raman spectra have been collected with the experimental setup described above (Fig. 4.3.2). In Fig. 4.3.11 (on the left) are shown the Raman mapping, obtained by the intensity ratios between the frequency region  $1590\text{--}1640\text{ cm}^{-1}$  and the frequency region  $1735\text{--}1785\text{ cm}^{-1}$ . In this way, since the band intensity in the range between  $1590\text{--}1640\text{ cm}^{-1}$  is strongly dependent from the liquid crystal molecules while the other range  $1735\text{--}1785\text{ cm}^{-1}$  is assigned to the polymer then when this ratio is lower than 1 (in the pictures the darker squares) then the

analyzed point shows the prevalent presence of the polymer otherwise if the intensity ratios is higher than 1 then prevails the liquid crystal presence. It can be seen (Fig. 4.3.11, on the left) as the “colored” squares (indicating the polymer walls) turn as well as the angle  $\theta$  increases starting from the bottom to the top of the figure; so that, it has been possible to confirm through the micro-Raman investigation the initial alignment of the POLICRYPS which results to be with the polymeric walls parallel to the polarization of the laser sources. In addition, it can be seen, when the sample is turned those walls assume a perpendicular orientation with respect the polarization of the light sources. The corresponding polarized Raman spectra of the mapping are shown in Fig. 4.3.11 (on the right).



**Fig. 4.3.10** Representative Raman spectra collected on POLICRYPS grating.



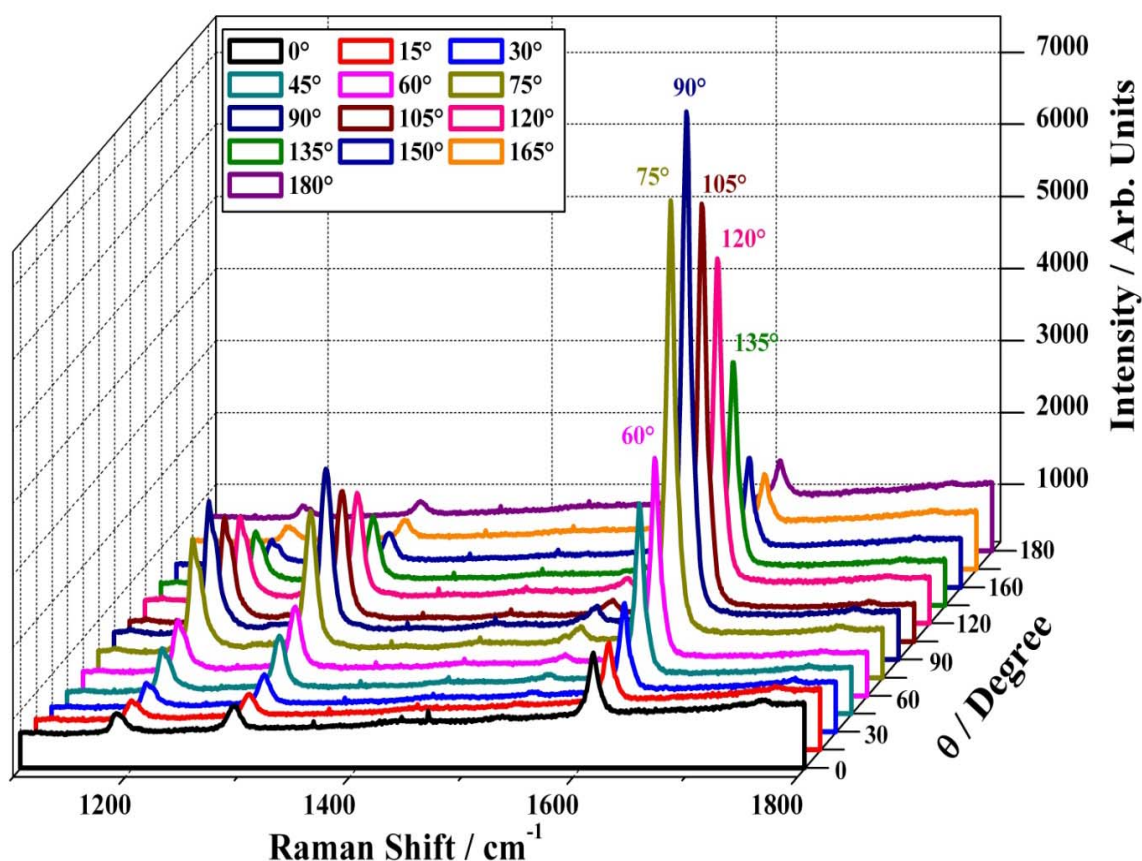
**Fig. 4.3.11** Raman mapping (on the left) and relative representative Polarized Raman spectra (on the right) collected on the POLICRYPS grating at different angle  $\theta$  between the polymeric walls and the polarization of the laser sources starting from  $0^\circ$  to  $90^\circ$ .

It can be seen that for  $\theta=0^\circ$ , there is not a remarkable difference between the spectrum collected on the point A with respect to that collected on the point B. Nevertheless, by increasing  $\theta$  the intensities of the bands of the spectra B results to be bigger than those

observed in the spectra A; in particular, for the peaks at 1184, 1288, 1610 and 2233  $\text{cm}^{-1}$  respectively assigned to the aromatic C-H in plane deformation, C-C stretch of biphenyl bond, C=C stretching of biphenyl rings and C-N stretching there is a remarkable increasing of the relative intensity. The increased intensities of such modes, as stated above, reflects the preferred E7 molecular orientation indicated by the director  $\mathbf{n}$  with respect to the polarization of the incident light [53,54, 65-69]. In particular since the biggest intensities difference is observed for  $\theta=90^\circ$ , it means that the director  $\mathbf{n}$  is parallel to the polarization of the laser for  $\theta=90^\circ$ , when, namely, the polymeric walls are perpendicular to the polarization plane of the light. So that, it can be concluded that POLICRYPS gratings are made by polymer slices regularly alternated to films of nematic liquid crystal molecules which are oriented perpendicular to the polymeric walls. Moreover, the presence of the characteristic peaks of the liquid crystal (1610 and 2232  $\text{cm}^{-1}$ ) in all the spectra collected in both the points (points A and B of Fig. 4.3.11), allows to state that during the formation of the POLYCRYPS grating there is not a complete separation of the liquid crystals molecules toward the “liquid crystals slices”, but some of them are involved inside the polymeric structures. From a qualitative analysis, it can be seen (black spectra Fig. 4.3.11) that, also, the liquid crystal molecules enclosed on the polymeric walls show the same orientation seen above (on reduced scale) which is reflected by the small increased intensities of the bands at 1610 and 2232  $\text{cm}^{-1}$ , when the sample is turned from the parallel to perpendicular alignment. This last result can be very useful in order to explain the physics involved during the POLYCRIPS formation; in fact, the polymerization which occurs along the polymeric walls trapped the E7 liquid crystal molecules in a perpendicular orientation with respect to the walls formations. Such liquid crystal molecules are distributed homogeneously in the polymeric walls and some of them are linked on the walls surfaces, as tails, inducing the alignment of the liquid crystal molecules in the “liquid crystal slices”.

In order to deeper investigate the orientation of the liquid crystal molecules inside the POLICRYPS, different polarized Raman spectra have been collected on the liquid crystal slices as a function of the angle  $\theta$  between the polymeric walls and the polarization of the incident light, in the range between  $0^\circ$  and  $180^\circ$  (Fig.4.3.12). As it can be seen in Fig. 4.3.12, the intensity of the band at 1610  $\text{cm}^{-1}$  increases as well as  $\theta$  increases until to reach its maximum for  $\theta=90^\circ$  decreasing again when  $\theta$  increases from

90° to 180°. The intensity of the band at 1610 cm<sup>-1</sup> in the spectra shown in Fig. 4.3.12 has been determined throughout baseline corrections and peak deconvolution. The ratio between the intensity of the band at 1610 cm<sup>-1</sup> collected at each angle to that collected at 90°, as function of the rotational angle  $\theta$  (Fig. 4.3.13), confirms the occurrence of the maximum for  $\theta = 90^\circ$ , indicating that the director  $\mathbf{n}$  of the liquid crystal E7 is perpendicular to the polymeric walls.



**Fig. 4.3.12.** Representative Polarized Raman spectra collected on the Liquid crystal slices of POLICRYPS grating at different angle between the polymeric walls and the polarization of the laser sources starting from 0° to 180°.



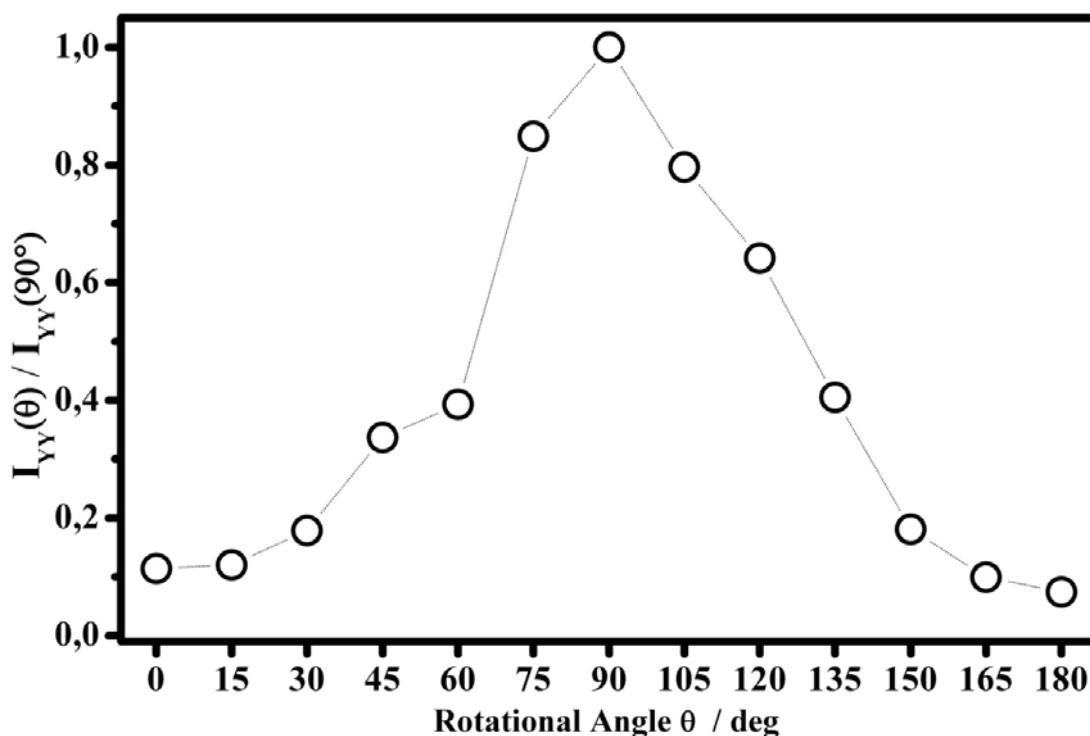


Fig. 4.3.13. Raman intensity ratios of the band at  $1610\text{ cm}^{-1}$  obtained at each angle (between  $0$  and  $180^\circ$ ) with the intensity of the band obtained at  $90^\circ$  as a function of the rotational angle  $\theta$ .

### 4.3.3 Conclusions

Polarized Raman spectroscopy has been used for the first time in order to monitor the orientation of the liquid crystal molecules in POLICRIPS holographic lattice. The Raman characterization has been performed on all the components used to make the holographic device which involve the liquid crystal E7 and the NOA-61, monomer and polymerized; the main Raman features of each component have been assigned. In particular the Raman bands due to the symmetric stretching of the aromatic rings of the biphenyls molecules and the stretching of the CN groups have been selected as “marker” of the liquid crystal orientation since they occur along the long molecular axis of biphenyl molecules. The Raman mapping of POLICRYPS, obtained by the intensities ratios of the bands between the frequency region  $1590\text{-}1640\text{ cm}^{-1}$  and the frequency region  $1735\text{-}1785\text{ cm}^{-1}$  have been shown and those reflected by false colors images the slices structure of the POLICRYPS. The presence of liquid crystal molecules inside the polymeric walls has been detected supporting an hypothesis with regard the

alignment of the liquid crystal E7 molecules in the liquid crystals slices: liquid crystal molecules are distributed homogenously in the polymeric walls and some of them are linked on the walls surfaces, as tails, inducing the alignment of the liquid crystal molecules in the “liquid crystal slices”. The orientation of the liquid crystal molecule inside the POLICRYPS holographic lattice has been detected and it results to be perpendicular to the polymeric walls of the systems.

In the future others polarized Raman investigations on POLICRYPS are planned, by changing the polarized component analyzed, to determine the order parameters,  $\langle P_2 \rangle$  and  $\langle P_4 \rangle$  of the liquid crystal molecules inside the POLICRYPS holographic grating.

#### 4.4 Thermal evolution of tungsten trioxide thin film obtained by sol gel deposition

Since long time [70-75] tungsten trioxide ( $\text{WO}_3$ ) films have attracted the interest of many researchers because of its electrochromic properties. Today it is still studied for electrochromic applications and as semiconductor gas sensor, catalyst, satellite thermal control, being an indirect band gap semiconductor with interesting photoconductive properties for solar energy applications [76-81]. Very interesting applications have been observed when films of tungsten trioxide, deposited on indium tin oxide covered glasses (ITO glasses), were inserted as electrodes in asymmetric nematic liquid crystals (ANLC) cells [82-86].

In the usual nematic liquid crystal (NLC) cell (glass-ITO-polymer-liquid crystal-polymer-ITO-glass) the electro-optical response obtained does not depend of the polarity of the applied voltage. On the contrary, the electro-optical response obtained when  $\text{WO}_3$  films are used as electrode in the ANLC cell (glass-ITO- $\text{WO}_3$ -liquid crystal-polymer-ITO-glass) results rectified namely polarity sensitive.

It has been shown that the rectified responses collected from the ANLC cells depend from the structural order of the  $\text{WO}_3$  films inserted: if the  $\text{WO}_3$  film is amorphous the rectified response will be in phase with the applied voltage otherwise if the film is crystalline the electro-optical response will be in opposition of phase with the applied voltage.

The structural order of the  $\text{WO}_3$  films used in the ANLC cells is affected by post deposition thermal treatment processes (annealing).

It has been proposed a model to explain this effect, which is, mainly based on the conductive properties of such films: the amorphous films have been considered prevalent ionic conductors whereas the crystalline have been considered electronic conductors.

Nevertheless, some additional efforts need to be done in order to understand the effects of the annealing process on such electrodes: glass, ITO and  $\text{WO}_3$  films.

The  $\text{WO}_3$  films used in this work have been obtained by sol gel synthesis and spin coating deposition. Such films were subjected to different thermal treatments in the

range between 100°C to 600°C. Such annealing processes induce some structural and/or compositions transformations of the WO<sub>3</sub> films and, also, to the substrate.

#### 4.4.1 Films preparation

Tungsten oxide thin films were obtained by sol gel route [86-89]. The mother solution was prepared in Argon atmosphere in Glove Box MBRAUN-unilab, by dissolving Tungsten(VI) oxide chloride (WOCl<sub>4</sub>) supplied by Aldrich, in isopropanol anhydrous.

Indium tin oxide (ITO) coated glasses (supplied by Balzers) and Silver (Ag) coated glasses were used as substrates. The silver coated glasses were obtained by physical vapour deposition on glasses.

The mother solution was deposited on the substrate with a spin coater SC10 CaLCTec S.r.l. at 1200 rpm for 30 s. Some films were obtained by three subsequent depositions. The samples were subjected to different thermal treatments, in the range between 100°C and 600°C for an hour, to follow the structural evolution thermal induced.

#### 4.4.2 Raman Spectroscopy

Raman spectra were collected by a Raman microprobe Jobin-Yvon Labram equipped with a CCD detector and a He-Ne laser (632.8 nm emission). The used objective was a 100x Mplan Olympus with Numerical Aperture of 0.90 with about 2-3 μm of apparent diameter of the focused laser spot. The frequency resolution on the Raman spectra is over esteemed to be equals to 2 cm<sup>-1</sup>.

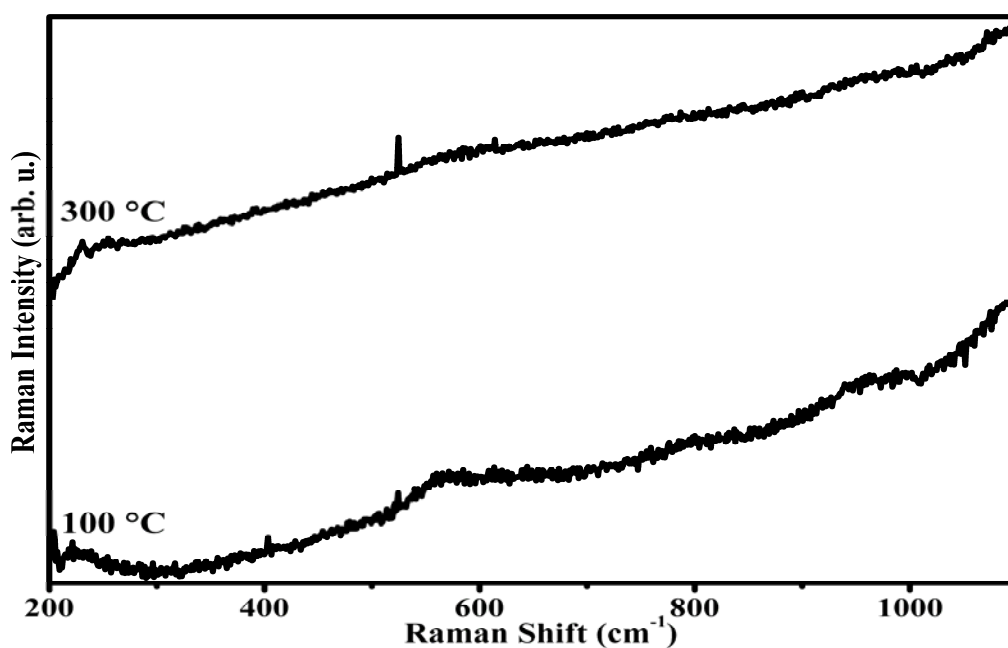
#### 4.4.3 Discussion

In order to evaluate the thermal induced structural modification micro-Raman spectroscopy has been used. In Fig. 4.4.1 the spectra collected on the single layer WO<sub>3</sub> film treated at 100°C and 300°C are shown.

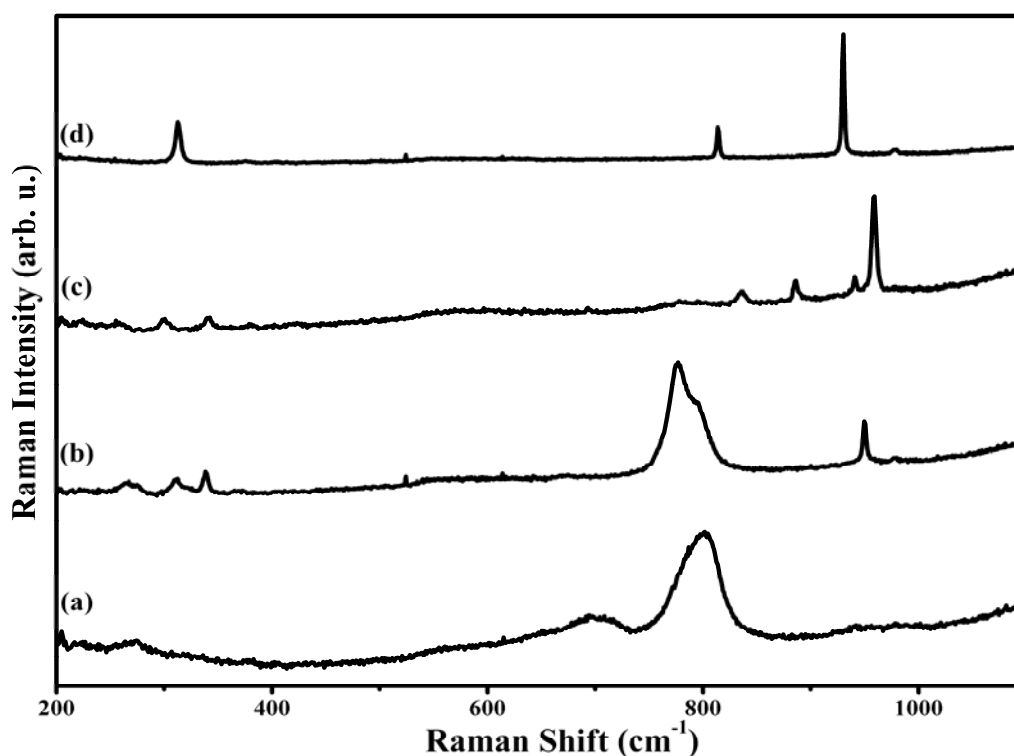
No particular features can be seen in the Raman spectra which suggest that the tungsten oxide layers are amorphous with a very low Raman cross section.

In Fig. 4.4.2 are shown the representative spectra collected on the single layer samples treated a 600°C.

As it can be seen, the spectra of Fig. 4.4.2 seems to be an evolution from the spectrum (a) to the spectrum (d). The spectrum 4 (a), shows the characteristic bands centred at about  $700\text{ cm}^{-1}$  and  $800\text{ cm}^{-1}$  with some very small features at  $\sim 265\text{ cm}^{-1}$ ,  $\sim 275\text{ cm}^{-1}$ , which are assigned to tungsten trioxide crystalline [83,90-92]; since the obtained bands are very broad they are due to the presence of nano-domains of crystalline tungsten trioxide [93-96].



**Fig. 4.4.1** Raman Spectra collected on the samples obtained on ITO coated glasses substrates annealed at 100°C and 300°C.

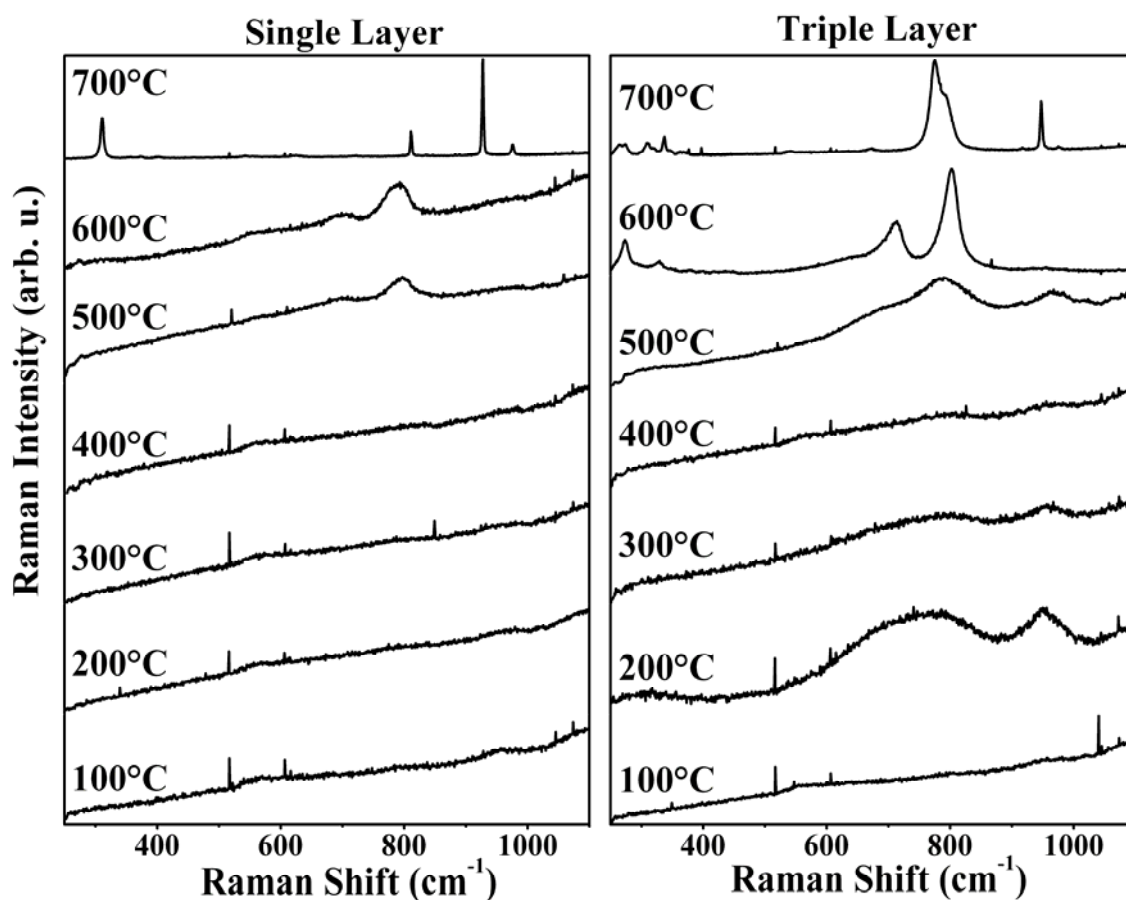


**Fig. 4.4.2** Raman Spectra collected on the samples obtained on ITO coated glasses substrates annealed at 600°C.

The spectra (d) of Fig. 4.4.2, cannot be assigned to any form of tungsten oxide. It shows its main features at about  $\sim 312$ ,  $\sim 814$ ,  $\sim 930$ ,  $\sim 980$   $\text{cm}^{-1}$ , typical of some tetragonal form of tungstate which has been identified as sodium tungstate [98-104].

Obviously, the sodium ions diffusion from the glass substrates is favoured by the thermal annealing processes and for the highest thermal annealing it become very strong to affect the tungsten films. In fact, the spectrum 4 (d) is the more characteristic of the sample after the highest thermal annealing. The spectra (b) (Raman evidences:  $\sim 265$ ,  $\sim 275$ ,  $\sim 312$ ,  $\sim 338$ ,  $\sim 524$ ,  $\sim 777$ ,  $\sim 795$ ,  $\sim 950$   $\text{cm}^{-1}$ ) and (c) (Raman evidences:  $\sim 265$ ,  $\sim 275$ ,  $\sim 298$ ,  $\sim 342$ ,  $\sim 837$ ,  $\sim 886$ ,  $\sim 941$ ,  $\sim 959$   $\text{cm}^{-1}$ ) of Fig. 4.4.2 are clearly due to intermediate phases between those above stated, which indicates the coexistence of both phases.

The thermal evolution has been followed also for three layers samples up to 700°C, to monitor the difference between surfaces and bulk effects. The relative Raman spectra together to those collected on the single layer samples are shown in Fig. 4.4.3.



**Fig. 4.4.3** Raman Spectra collected on the samples obtained on ITO coated glasses substrates annealed at 700°C.

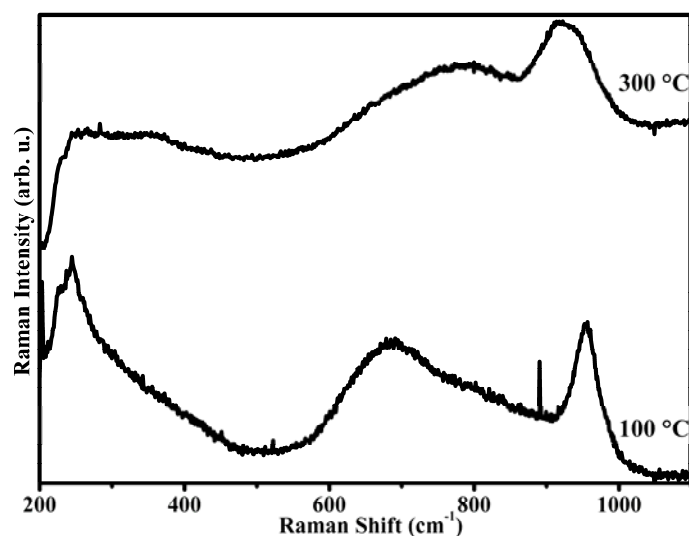
In the three layers samples, the broad Raman bands at  $\sim 750$  and  $\sim 952$   $\text{cm}^{-1}$ , present also for low temperature annealing such as 200°C and 300°C, indicates the presence of amorphous tungsten trioxide [93]. The high intensity observed for the triple layer sample treated at 200°C, is due to the presence of higher amount of the  $\text{WO}_3$  since this spectra has been collected on the centre of the samples where centrifugal force during the spin coating is minimum. Moreover, the high frequency band indicates the contribution of nanocrystalline domains whose size should be close to 4 nm [94]. The relative spectra collected on the three layer sample treated at 500°C shows the evolution from the amorphous to crystalline tungsten trioxide with its bands at  $\sim 691$ ,  $\sim 789$ ,  $\sim 963$   $\text{cm}^{-1}$  while the 600°C thermal annealing induce the formation of a well crystallized phase of tungsten trioxide with its typical modes at  $\sim 273$ ,  $\sim 327$ ,  $\sim 712$ ,  $\sim 802$   $\text{cm}^{-1}$ , which indicate the presences of the phase  $\gamma$  of monoclinic  $\text{WO}_3$  [94].

The thermal behaviour of the single layer films confirms the trends before observed. In fact, the structural evolution due to the annealing processes below 500°C are not detectable by the Raman spectra (Fig. 4.4.3). The annealing treatment at 500°C induce structural modification, on single layer samples, which are reflected on the Raman spectrum as wide bands at ~699 and ~797  $\text{cm}^{-1}$  which are typical [91-96] of nano size crystals of tungsten trioxide. The further annealing at 600 °C (on single layer films) confirms the formation of crystalline tungsten trioxide (~699,~795  $\text{cm}^{-1}$ ) and the annealing at 700°C induces the complete formation of sodium tungstate (~310, ~811, ~928, ~976  $\text{cm}^{-1}$ ) [97-103].

The highest annealing process performed on the three layers samples induce the formation of the same specie seen in the single layer films. In this case, anyway not the whole film has been transformed in sodium tungstate as it is possible to see in Fig. 4.4.3, where the bands at ~263, ~274, ~310, ~337, ~775, ~792, ~947, ~975  $\text{cm}^{-1}$  show the structural evolution from crystalline tungsten trioxide to sodium tungstate.

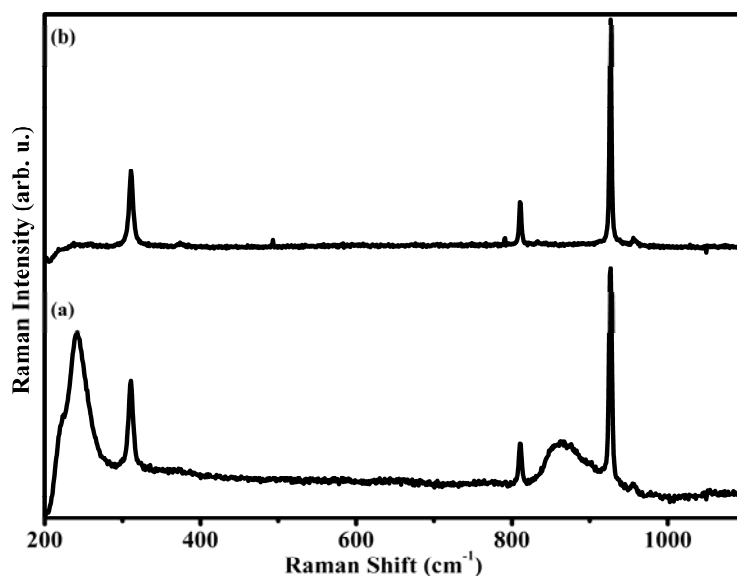
In order to obtain more information, the tungsten trioxide films have been obtained also on silver coated substrates. In this case an enhancement of the Raman scattering is offered by the noble metal surfaces (SERS) [104]. In Fig. 4.4.4 the surface enhanced Raman (SER) spectra of the sample treated at 100°C and at 300°C are shown. As it is possible to see, the intensity Raman bands observed in such spectra result to be huge with respect to those seen for the samples obtained on ITO covered substrates and treated at the same temperatures.





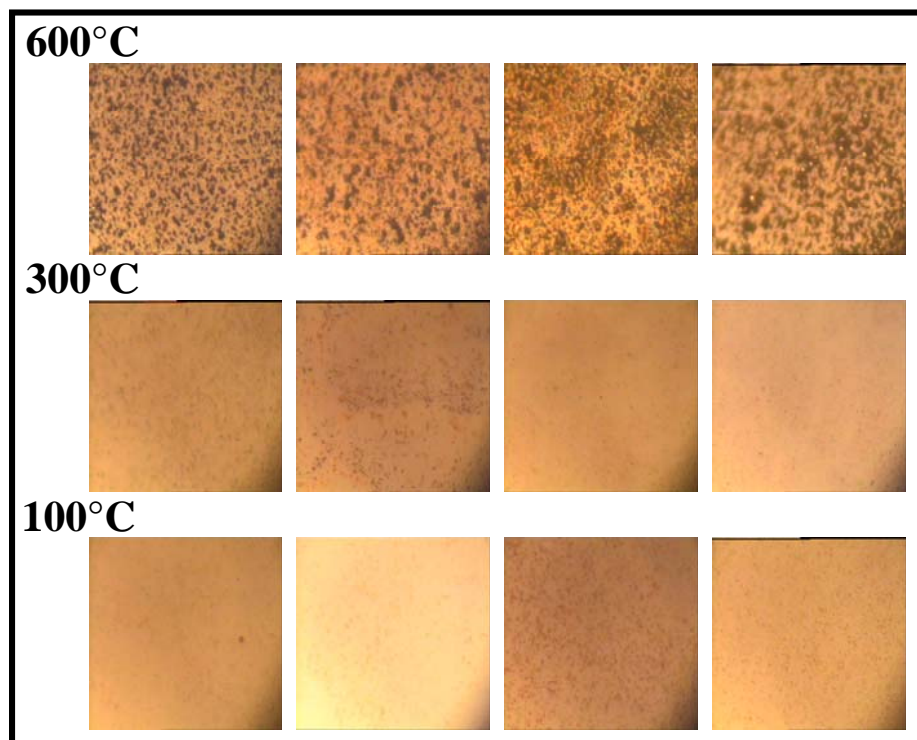
**Fig. 4.4.4** Surface Enhanced Raman Spectra collected on the samples obtained on silver coated glasses substrates annealed at 100°C and 300°C.

The SER spectra collected on the 100°C annealing treatment samples shows very broad bands centred at about  $\sim 244$ ,  $\sim 685$  and  $\sim 958$   $\text{cm}^{-1}$  which indicates the removing process of the water molecules of the gel [100] forming the nanocrystalline domain -amorphous tungsten trioxide [93], obtained in the 300°C thermal treatment samples as it can be seen on its relative SER spectra that shows very broad bands centred at about  $\sim 750$  and  $\sim 930$   $\text{cm}^{-1}$ . As well as for the ITO substrates samples, different SER spectra are obtained for silver coated samples annealed at 600°C (Fig. 4.4.5).



**Fig. 4.4.5** Surface enhanced Raman Spectra collected on different point of the samples obtained on silver coated glasses annealed at 600°C.

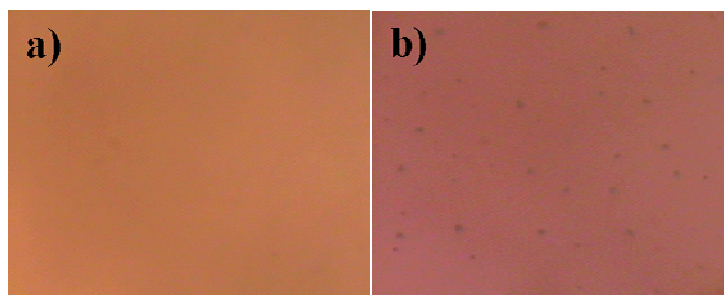
The SER spectrum (a) of Fig. 4.4.5 ( $\sim 242$ ,  $\sim 311$ ,  $\sim 812$ ,  $\sim 863$ ,  $\sim 928$  and  $\sim 958$   $\text{cm}^{-1}$ ) shows again an evolution from crystalline tungsten trioxide to sodium tungstate detectable by the analysis of the SER spectrum (b) of Fig. 4.4.5 with its typical features [97] at  $\sim 311$ ,  $\sim 811$ ,  $\sim 928$  and  $\sim 957$   $\text{cm}^{-1}$ . In Fig. 4.4.6, are reported the optical microscope images collected on the silver coated substrates samples treated at different temperatures. It can be seen as the 100°C and 300°C show homogenous surfaces the 600°C shows the presence of many holes, homogeneously distributed, on the surfaces.



**Fig. 4.4.6** Optical images collected on the silver coated glass treated at the different temperatures.

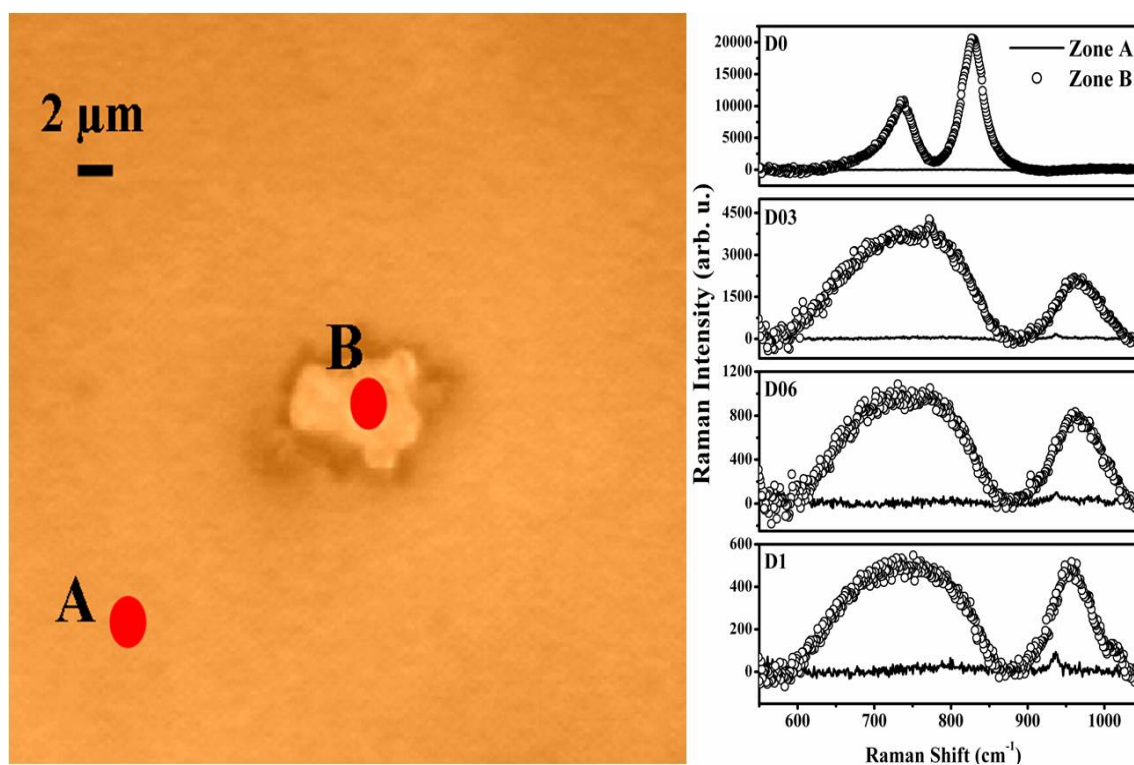
To have a more complete investigation, some ITO-glass substrates have been subjected to different thermal treatment. In Fig. 4.4.7 are shown the optical images of the surfaces of such substrates. It can be seen that the 700°C induces the formation of some micrometer eruptions homogeneously distributed on the surfaces.

Single layer of tungsten oxide samples have been obtained on the 700°C pre-treated substrates as described above and suddenly annealed at 300°C for one hour. In Fig. 4.4.8 (left) is shown an optical image collected on such samples with underline that the deposition occur on the surfaces (point A) and above the eruption generated by the thermal annealing pre-treatment.



**Fig. 4.4.7** Optical images collected on the ITO coated glass a) not annealed b) annealed at 700°C.

In Fig. 4.4.8 (right) are shown the Raman spectra collected on the different points of Fig. 4.4.8 on the left, at different power of laser.



**Fig. 4.4.8** (left) Optical image collected on the single layer sample annealed at 300°C made with ITO covered glass substrate pre-treated at 700 °C, (right) Raman spectra collected on the 300°C samples made with the ITO-covered glass substrate pre-annealed at 700°C relative to the zones A (solid line plot) and B (circles plot) of the optical image. These spectra have been collected by using filters with different optical density:  $D1=P_0/10$ ,  $D06=P_0/6$ ,  $D03=P_0/2$ ,  $D0=P_0$ , where  $P_0$  is the power source.

In fact, this spectra have been collected by using filters with different optical density ranging from D1 to D0.

As it can be seen in Fig. 4.4.8 (right), the Raman spectra collected above the eruption are much more intense of those collected on the surfaces, which means that the “eruption” enhance the Raman spectra. It is wanted to remark that the intensity enhanced induced by such eruption is of the same order of magnitude of that obtained by using the silver coated substrates.

The spectra collected above the eruption (point B) with filter D1 shows broad bands at about  $\sim 740$  and  $\sim 957$   $\text{cm}^{-1}$ , with filter D06 shows broad bands at about  $\sim 747$  and  $\sim 960$   $\text{cm}^{-1}$ , and the spectra collected with filter D03 shows broad bands at about  $\sim 749$  and  $\sim 961$   $\text{cm}^{-1}$  all attributed to the presence of tungsten trioxide amorphous [93]. When no filter is used for collecting the spectra (D0), the power of the laser heats the sample point inducing the formation of tungsten trioxide crystalline [94] with its modes at about  $\sim 707$ ,  $\sim 806$   $\text{cm}^{-1}$ .

#### 4.4.4 Conclusions

During this work, films of tungsten oxide obtained by sol gel synthesis and subjected to different thermal treatments have been studied by Raman spectroscopy.

Raman spectroscopy shown that all the layers are subject, after high temperature annealing, to become sodium tungstate. The presence of tungsten trioxide has been confirmed by monitor the evolution of the Raman spectra of three layers samples and by collecting the Raman spectra of the single layer sample on silver covered substrate in such a way to have an enhancement of the Raman scattering.

Very interesting issues came by analyzing the Raman spectra collected on the ITO substrate, which were subjected to a  $600^\circ\text{C}$  pre-treatment annealing process. In fact, this treatment induce the formation of some micrometer islands were are responsible of an anomalous enhancement of the Raman signals of the single layer film subjected at  $300^\circ\text{C}$  thermal annealing: above these island, the Raman signal is detectable out of such structures no Raman signals has been detected.

It has been purposed a qualitative model to explain such evidences Fig.4.4.9.

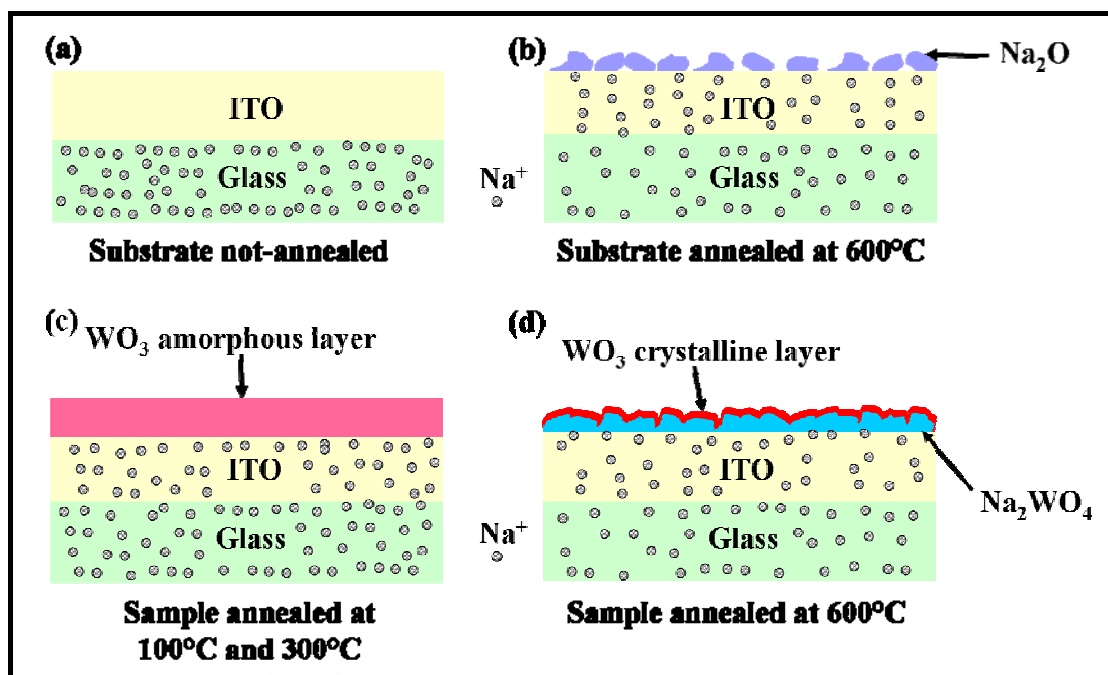


Fig. 4.4.9 Qualitative model of the ITO substrates and of the WO<sub>3</sub> samples treated at the indicated temperatures.

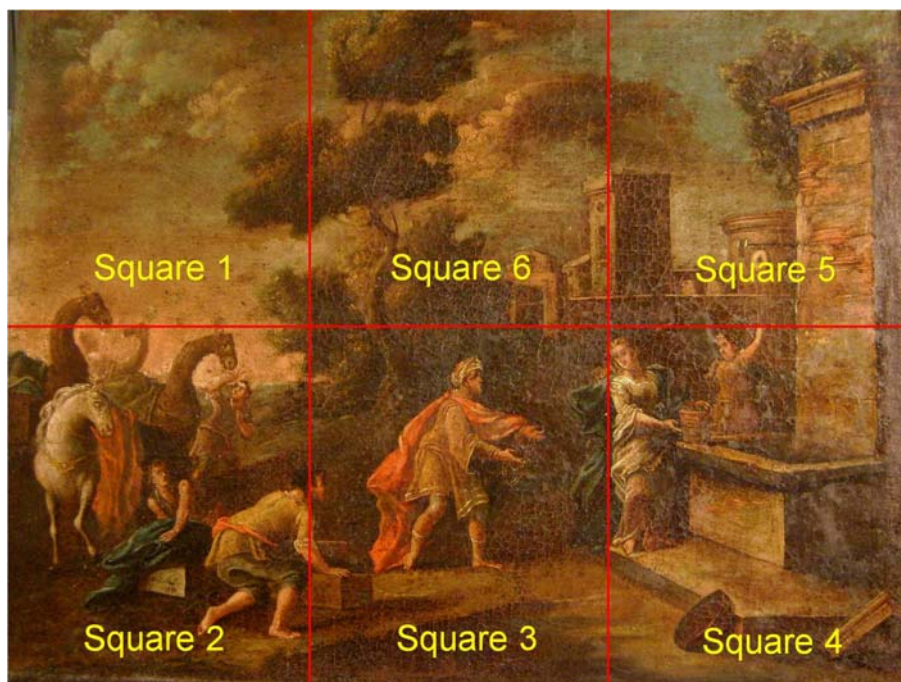
Such model is based mainly on the mobility of the sodium ions present on the glass substrate, which move to the top of the samples after the high temperature annealing treatment. When at the top of the ITO-covered substrates there is a film of tungsten trioxide these ions react to form sodium tungstate. Otherwise when there is nothing on the top of such substrates, these ions move on the top forming micrometer structure of sodium oxide. It has been shown that such structures are responsible for the enhancement of the Raman signal. Further consideration with regard to the size control and the technological application of such structures are planned for future work.

## 4.5 Micro-Raman investigation on oil painting “Rebecca at the well”

Nowadays, optical spectroscopy, and in particular Raman spectroscopy, represents one of the most powerful and useful investigation tools in many scientific areas of interest[105]. With regard to the artistic field, the technique’s application concerned different artifacts and art materials: medieval manuscripts [106,107], majolica [108], ancient glasses [109], ancient roman mortars [110], frescoes [111], canvas paintings [112], pigments, varnishes and many others. Raman Spectroscopy presents several advantages: non-destructive analysis of materials, no chemical-mechanical preparation of desiccation necessary for specimens prior to analysis, specific biomolecular spectral marker recognition for the identification of genuine and fake objects which may have been made for fraudulent purposes, high spatial resolution, analysis of organic and inorganic materials, execution of standard and *in situ* analysis [113]. In this work Raman spectroscopy was used to investigate the pigments of the canvas oil painting “Rebecca at the well” of a Neapolitan anonymous, preserved in MAON museum of Rende (Cosenza), Italy. The difficulty of the work was due to the absence of historical and scientific documents about the painting: it is the first time that scientific analysis were performed on the artwork. Art historians ascribe the painting to the XVIII century taking into account stylistic and formal studies: it seems that the canvas was painted by a Neapolitan artist. In conclusion Raman spectroscopy constituted an excellent probing tool not only to study the pigments’ composition, but also to investigate the artifacts’ history.

### 4.5.1 Experimental

The paint has been previously photographed in two manners: natural light and grazing light. A widespread craquelure phenomena has been showed by the grazing light method on the paint layer. In particular, this method allows to emphasize the texture of the painting surface. The paint was subdivided in six ideal squares, performing measurements according to the numeric increasing order of the squares (Fig. 4.5.1).



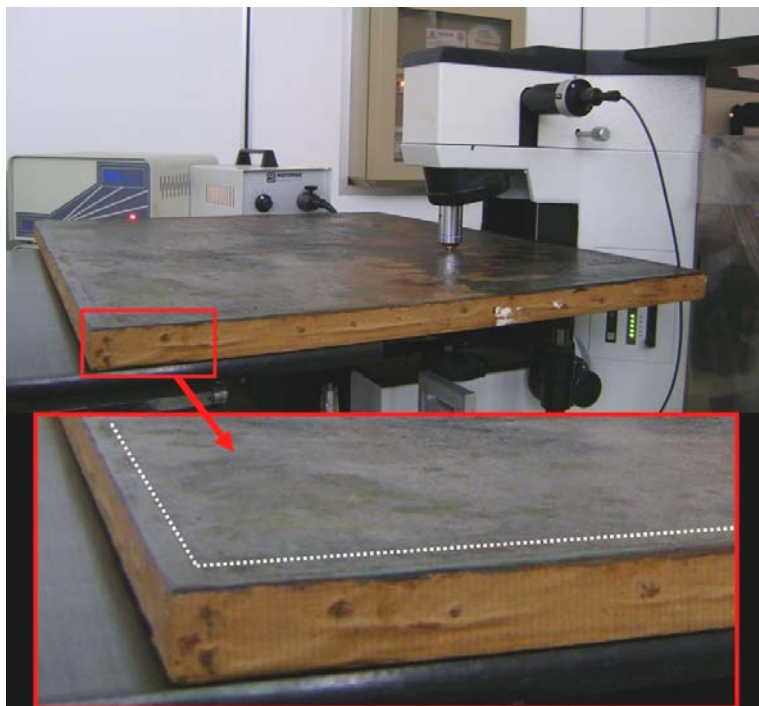
**Fig. 4.5.1** The subdivision of the painting in six ideal squares.

Different Olympus objectives (20x, 50x and 100x) were used to visually explore the painting and to collect the spectra. Raman spectra were recorded with a Jobin Yvon LABRAM instrument, equipped with a He-Ne (632.8 nm) laser.

In this work, only the spectra obtained with the 50x objective (focal length of 15mm) are shown, being the same as those obtained with the other objectives. The spectral resolution was estimated to be better than about  $2\text{ cm}^{-1}$ . The illuminated spot size was about  $5\text{ }\mu\text{m}$  in diameter. Neutral filters with different optical densities, 0.3, 0.6, 1, 2, 3 and 4, were available in order to reduce the impinging laser power and avoid damages to the painting and pigment modification.

The perimeter area has been analysed first. Since the presence of a “glue paste lining” restoration treatment (this treatment consists of positioning the original canvas on a new canvas) has been seen, it is thought that the paint layer was restored as well. Moreover, it has been seen that the lining canvas was larger than the original canvas. In fact, the perimeter area of the lining canvas was covered with a special material (Fig. 4.5.2) and painted, reproducing the original chromatic tonalism. For this reason, the analysis were first performed on the lateral borders of the painting in order to find possible recent pigments.





**Figura 4.5.2** The picture shows the papery material with which the painting's perimeter area has been covered. Broken lines define the borders of the original canvas.

Subsequently, spectra of the painting's internal points were collected. Several problems have been showed: strong fluorescence phenomena due to decay of the thick varnish layer; different areas of the painting were retouched which created the risk of collecting current pigments instead of the originals. For this reason, the painting was lighted up with a Wood lamp which distinguished the retouched areas from the originals. In particular, the different brightness observed on the painting lighted up by a Wood Lamp, are function of various factors: pigments and medium chemistry composition; time gone by after their application. The new pigments are darker than the old ones, which are more fluorescent due to chemical reactions between medium-pigment established in time [114]. In that manner, retouched areas were individuated, as well as areas with thin medium layer that allowed to optimize spectral collection. Each Micro-Raman spectrum was collected in 20 seconds and 3 accumulations.

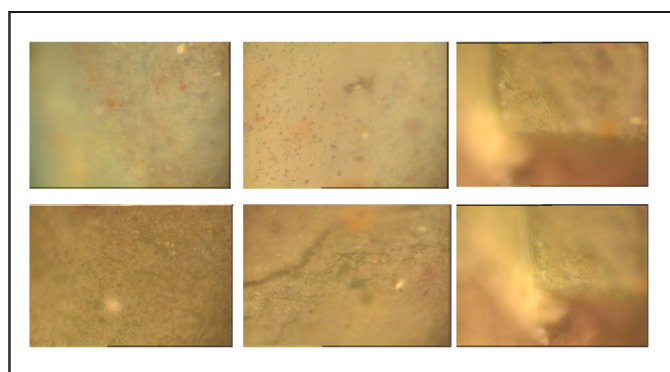
#### 4.5.2 Discussion

The probed points of the painting are shown in Fig. 4.5.3.



**Fig. 4.5.3** Probed points inside the oil painting.

The spectral collection started from lateral borders of the painting. Figg. 4.5.4-4.5.5 show optical pictures of these points, while Figg. 4.5.6-4.5.7 show the representative spectra concerning the investigated areas. Figg. 4.5.6-4.5.7 show representatives spectra relative to investigated areas.



**Fig. 4.5.4** Optical pictures of green areas concerning the painting's lateral borders and internal points.

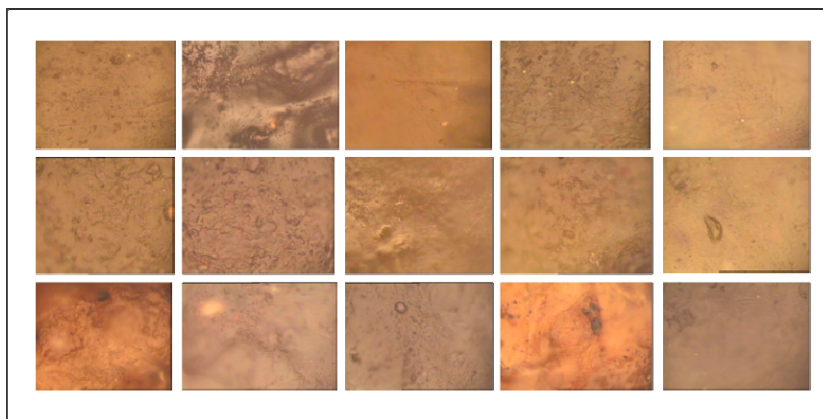


Fig. 4.5.5 Dark areas of the painting's lateral borders.

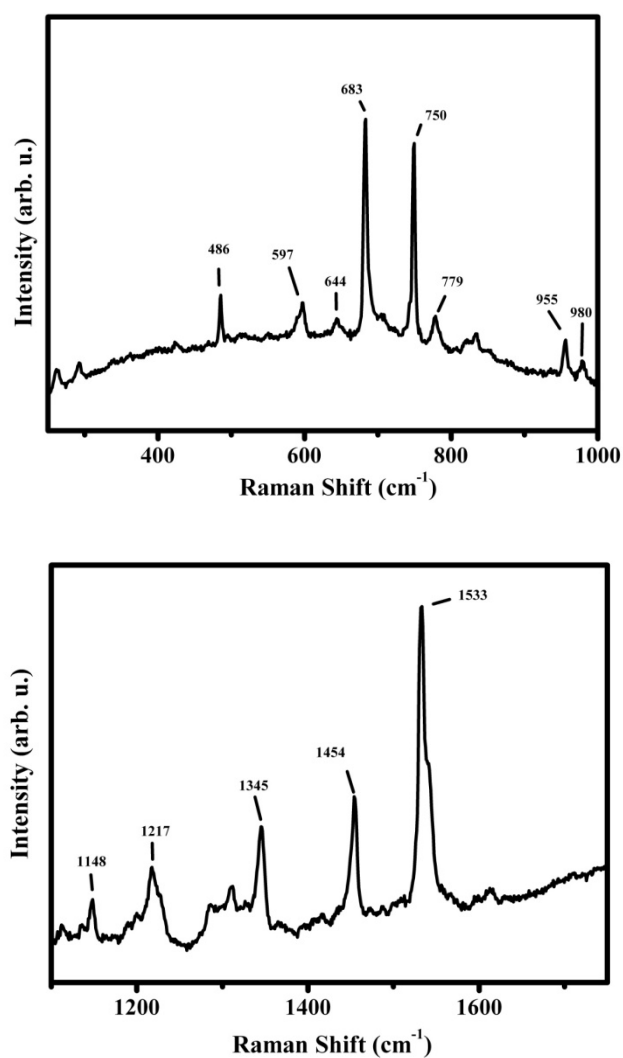
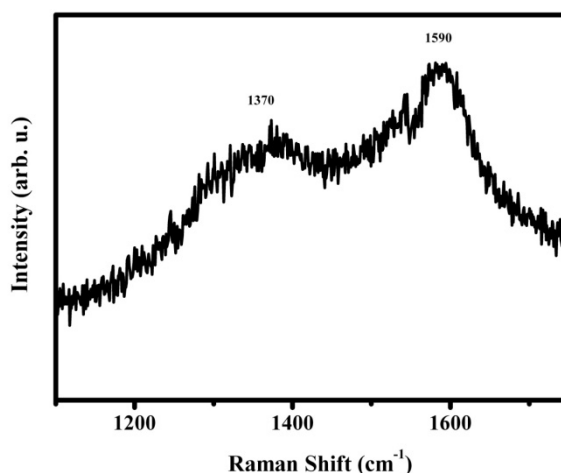


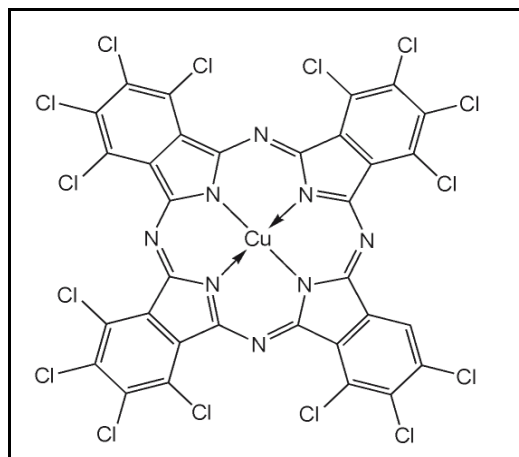
Fig. 4.5.6 Representatives Raman Spectra of the lateral borders, concerning the spectral regions: 250-1000 cm<sup>-1</sup> (at the top) and 1100 - 1750 cm<sup>-1</sup> (at the bottom).



**Fig. 4.5.7** Representative Raman spectrum of the lateral borders, concerning the 1100-1750 cm<sup>-1</sup> spectral region.

The spectrum of Fig. 4.5.6 is also characteristic of internal points of the painting. Characteristic Raman modes at about 683, 750, 779, 1217, 1345, 1454 and 1533 cm<sup>-1</sup> have been attributed to green chlorinated copper phthalocyanine [115,116].

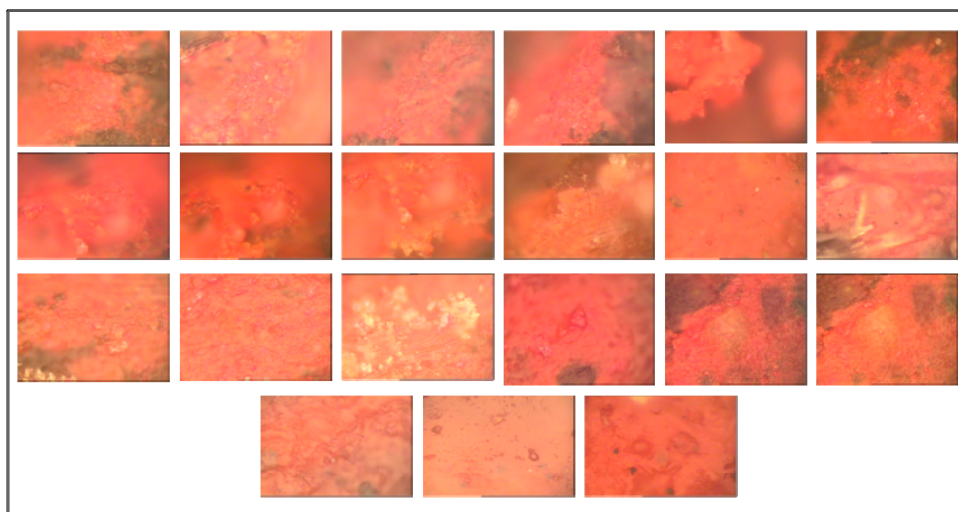
Raman modes at about 486, 597, 644, 955, 980, 1148 cm<sup>-1</sup> show the presence of blue chlorinated copper phthalocyanine[117]. These pigments synthesized since 1936 [118], are chemical complexes of copper and chlorinated phthalocyanine. In particular, in the case of the phtalo-green, a higher number of hydrogen atoms is substituted by chlorine atoms. The strong chlorine's electronegativity influences the electronic distribution of the green phtalocyanine, which is particularly stable and resistant to external agents. Chemical formulas of this pigments are: C<sub>32</sub>H<sub>3</sub>Cl<sub>13</sub>CuN<sub>8</sub> (blu phtalocyanine), C<sub>32</sub>H<sub>3</sub>Cl<sub>15</sub>CuN<sub>8</sub> (green phtalocyanine). Chemical structure of phtalo-green is showed in Fig. 4.5.8.



**Fig. 4.5.8** Phtalo-green chemical structure.

The spectrum of Fig. 4.5.7 concerns the dark areas of the painting's lateral borders and internal points. The two Raman modes at  $1370$  and  $1590\text{ cm}^{-1}$  have been attributed to D and G band of amorphous carbon [119].

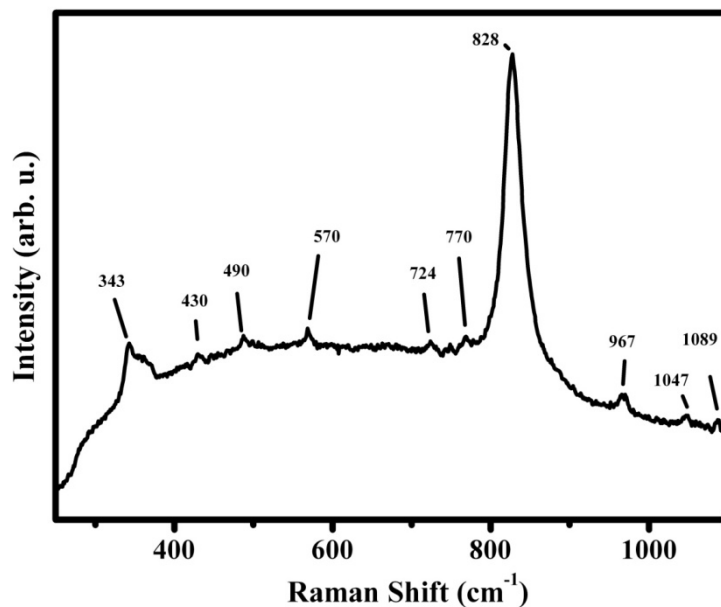
The spectral answer on the red areas is illustrated on Figg. 4.5.10-4.5.11, while Fig. 4.5.9 shows optical images of the red probed points.



**Fig. 4.5.9** Optical pictures of the red pigment performed with the 50X objective (focal length of 15mm).

Raman features at about  $343$  and  $828\text{ cm}^{-1}$  (Fig. 4.5.10) have been attributed to chrome yellow-orange<sup>6</sup> ( $\text{PbCrO}_4\cdot\text{PbO}$ ). The weak modes at about  $430$ ,  $490$ ,  $570$ ,  $724$ ,  $770$ ,  $967$ ,  $1047$ ,  $1089$  can be attributed to phosphates, carbonates and lead sulphate (white bone, gypsum and calcite) [120].

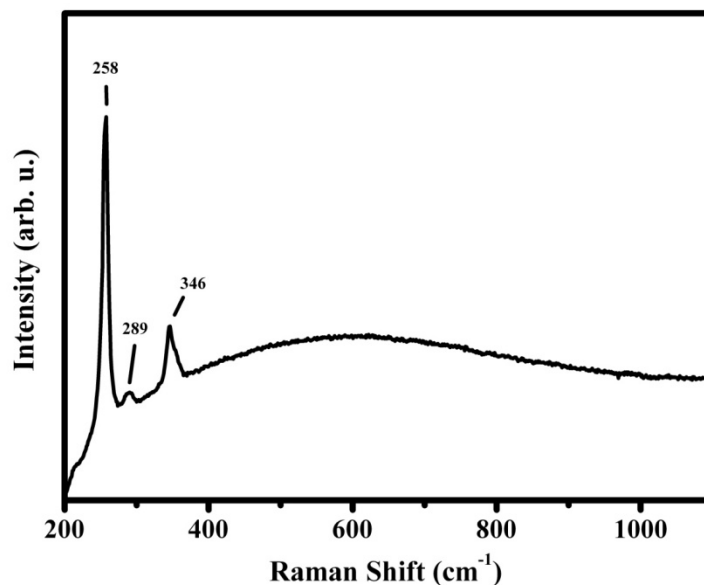
Chrome yellow-orange was introduced round about 1809 by the French chemist Louis Vaquelin, who extracted for the first time the pigment from crocoite mineral [121]. This pigment is used in oil painting because it makes the drying process [122] of the paint layer faster.



**Fig. 4.5.10** Representative Raman spectrum of red internal painting's points, concerning 250 - 1100  $\text{cm}^{-1}$  spectral region.

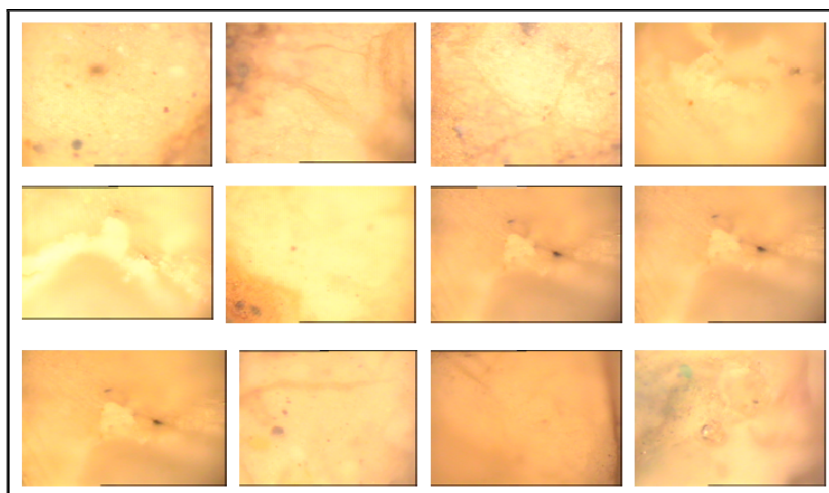
The Raman spectrum in Fig. 4.5.11 shows three vibrational modes at about 252, 282 and 343  $\text{cm}^{-1}$ . This pigment has been identified as red vermilion ( $\text{HgS}$ ) [123,124].



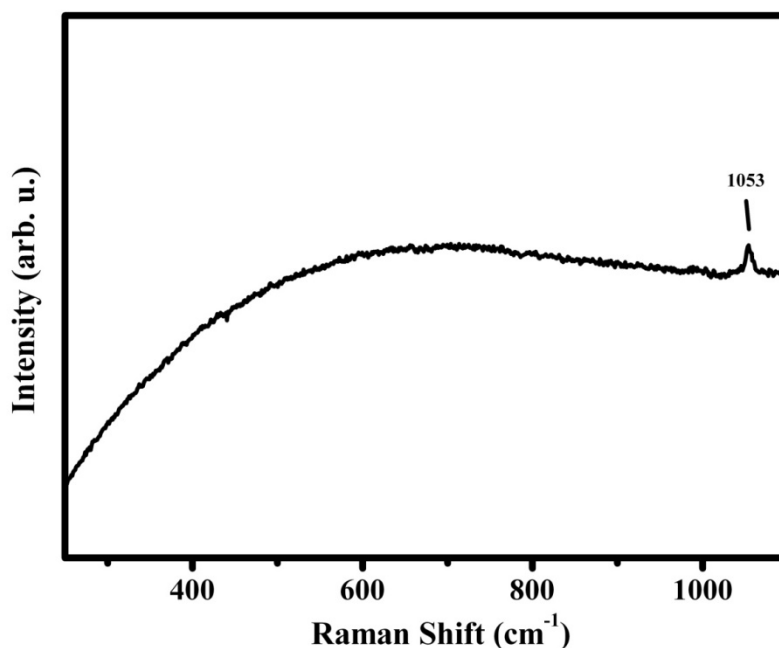


**Fig. 4.5.11** Representative Raman spectrum of red internal painting's points, concerning 200 - 1100 cm<sup>-1</sup> spectral region.

This pigment, known and used since ancient times, was obtained from cinnabar (natural mineral), and it was one of the most expensive pigments. Ancient Romans, who called it *minium*, used it for parietal paintings. In particular, the most important Pompei's families, used to paint the walls of their dwellings with red vermilion, with the purpose of boasting their richness [125]. Optical images of white probed areas are shown in Fig. 4.5.12.



**Fig. 4.5.12** Optical images of the white probed pigment taken with the 50X objective (focal length of 15mm).

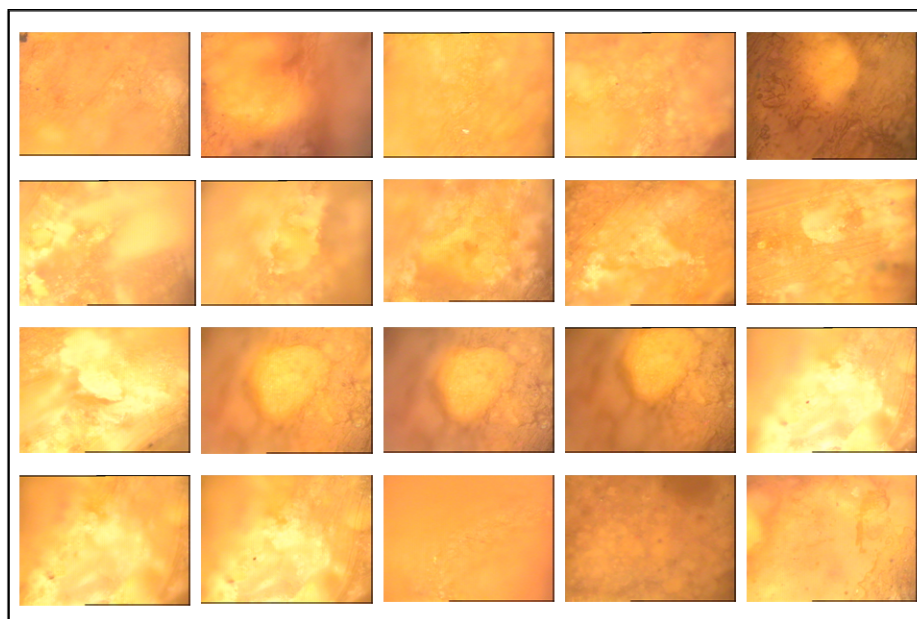


**Fig. 4.5.13** Representative Raman spectrum of red internal painting's points, concerning 250 - 1100  $\text{cm}^{-1}$  spectral region.

The Raman spectra collected on the white areas have showed a characteristic vibrational mode at  $1050 \text{ cm}^{-1}$  attributed to “lead white”. This pigment, known and used since ancient times (Theophrast, Plinius and Vitruvius illustrated the wide use of the lead white for wall paintings or as siccativ of linen oil in the oil painting [126]) was progressively substituted by zinc white during the half of XIX century and by titanium white in the half of XX century, due to its toxicity. Historical documents [127] say that the best quality of white lead was produced in Venice, while less precious qualities were produced in Holand and England. The lead white produces a very flexible paint layer, easy to apply and with a good opacity. For this reason the lead white has been the most used white in the painting history, unlike the bone white which was extremely doughy [128]. The lead white is a basic lead carbonate ( $2\text{PbCO}_3 \cdot \text{Pb(OH)}_2$ ). In spite of the high stability of this pigment, it becomes black with the time. This behavior depends on a chemical reaction where  $\text{H}_2\text{S}$  produced by atmospheric pollution reacts with the lead white, creating  $\text{PbS}$ , also known as black galena.

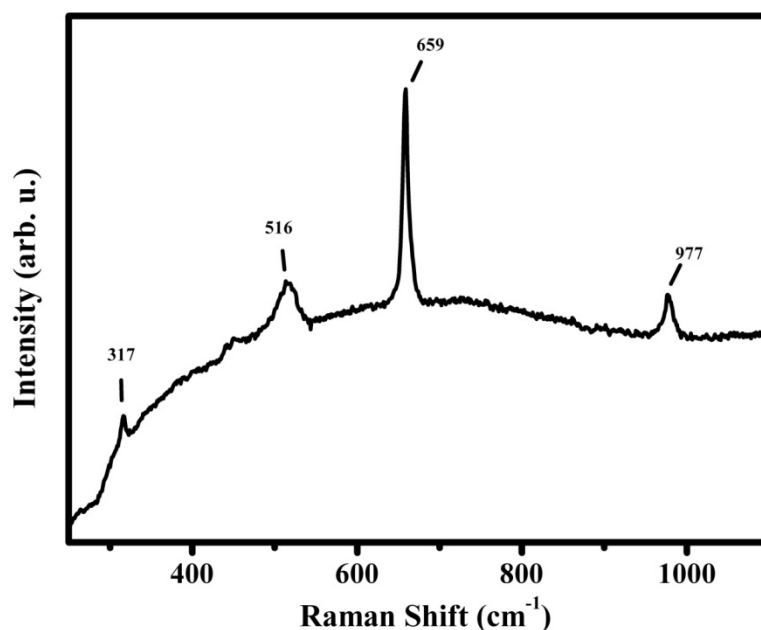
Fig. 4.5.14 shows optical pictures relative to yellow areas.





**Fig. 4.5.14** Optical pictures of the probed yellow areas, taken with a 50X objective and concerning the page's yellow tunic and the horse's ornament (square 2 of Fig. 4.5.1).

The Raman investigation provided the following spectral answer showed in Fig. 4.5.15:

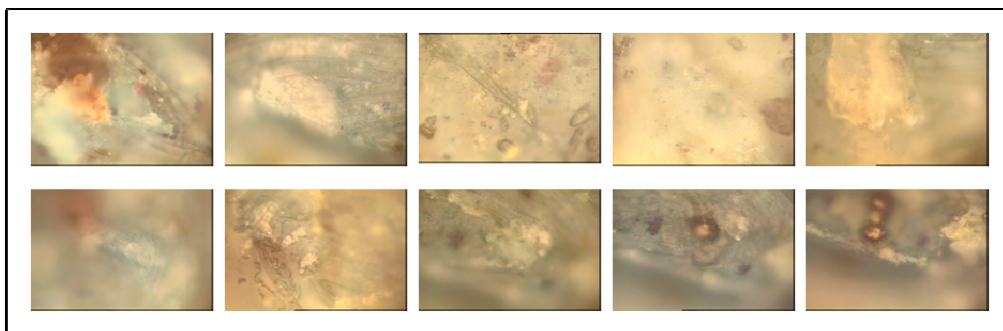


**Fig. 4.5.15** Representative Raman spectrum of red internal painting's points, concerning 200 - 1100 cm<sup>-1</sup> spectral region.

Some of the observed peaks have been identified, by using different database. Raman bands at 440, 451 and 977 [129] has been attributed to the presence of lead sulphate,

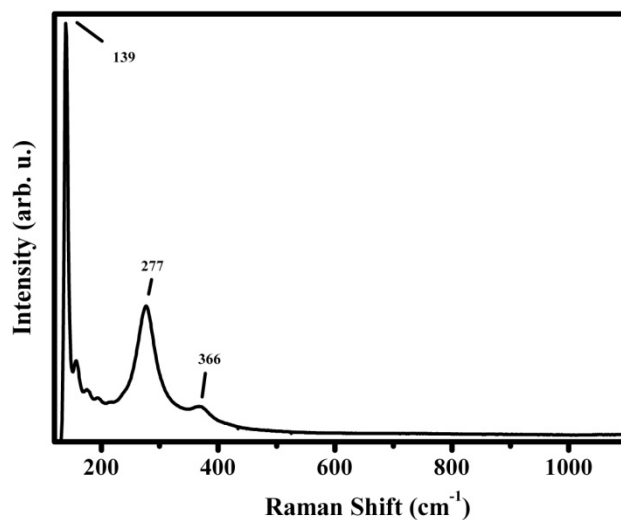
while vibrational mode at  $659\text{ cm}^{-1}$  has been attributed to magnetite ( $\text{Fe}_3\text{O}_4$ ), [130] an iron magnetic mineral known since ancient times. The Raman mode at  $317\text{ cm}^{-1}$  has been attributed to fluorite ( $\text{CaF}_2$ ).

Optical pictures of the light blue areas are showed in Fig. 4.5.16.



**Fig. 4.5.16** Optical images of the light blue areas, taken by microscopy with a 50X objective, concerning the light blue cloak put on the trunk by the page (square 2 of Fig. 4.5.1).

Raman representative spectrum is showed in Fig. 4.5.17.



**Fig. 4.5.17** Raman representative spectrum concerning  $200\text{ e }1100\text{ cm}^{-1}$  spectral region.

Raman features at  $139$ ,  $277$  and  $366\text{ cm}^{-1}$  were attributed to galena ( $\text{PbS}$ ). It is a mineral pigment (known in the past as “alquifoglio” [131]) composed for the 87% by lead; it is

the results of blackening process of the lead white [132]. Ancient Egyptians mixed galena with malachite duster and oil for maquillage [133].

The dark probed areas, whose pictures are shown in Fig. 4.5.18 , correspond to spectra as the ones reported in Fig.4.5.19. As expected, it is some kind of carbon, as in the dark region of the border, shown before.

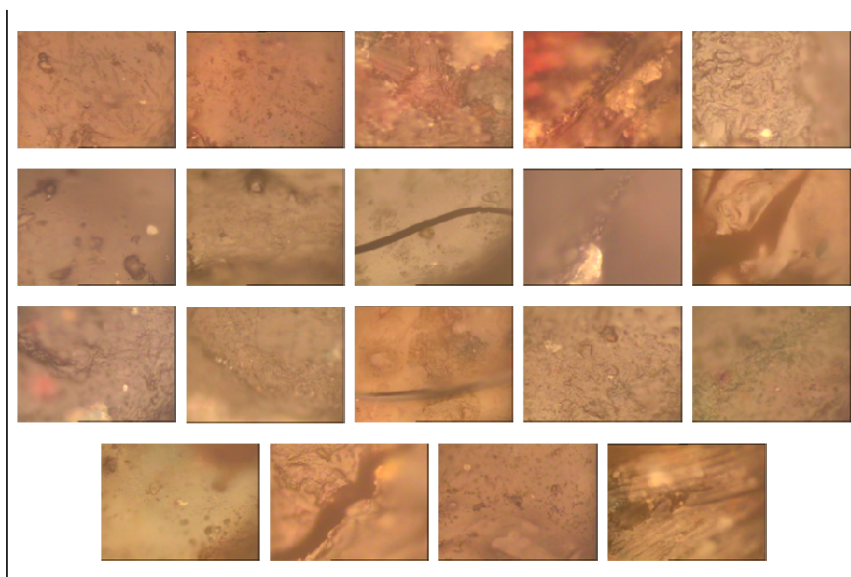


Fig. 4.5.18 Optical images of dark internal points taken with a 50X objective.

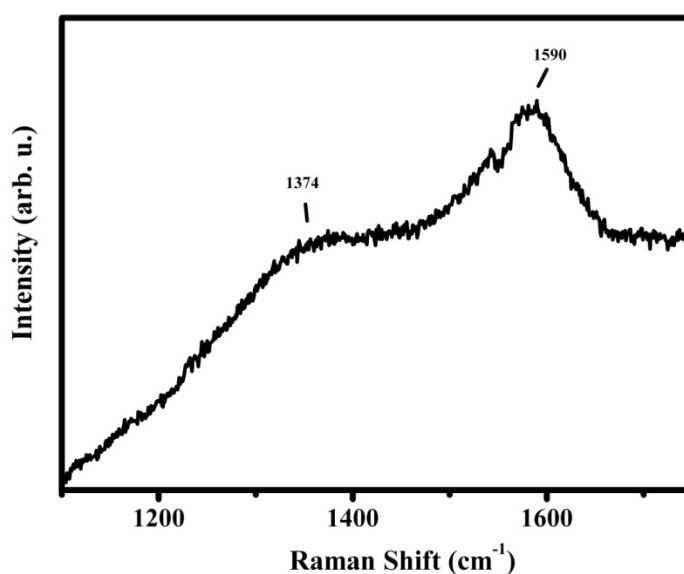


Fig. 4.5.19 Raman representative spectrum concerning 1100 e 1750  $\text{cm}^{-1}$  spectral region.

### 4.5.3 Conclusions

In this work, some of the pigments used in the painting “Rebecca at the well” were analysed and characterized by non-invasive Micro-Raman spectroscopic technique. This technique has been confirmed as non-invasive and effective for the diagnostic investigation. In particular, six pigments of the pictorial palette were characterized. The analysis of the white pigment showed the presence of lead white, commonly known as “biacca”; it was used since ancient times and it was progressively substituted by zinc white during the half of XIX century and by titanium white in the half of XX century, due to its toxicity. The identification of this pigment provided important information about the medium used by the artist. In fact, the lead white were used as siccative of linen oil and probably the artist used that kind of oil in this painting. The red pigment identified has been the red vermilion, a very precious pigment, known also as cinnabar (the mineral from which the pigment derives). The presence of a pigment so expensive suggests not only the importance and the richness of the purchaser, but also the fame of the artist who was able to buy such an expensive pictorial material. Moreover, the small extent of the painting suggests that perhaps the purchaser was a nobility’s member, and not a Church’s member, who would have preferred huge artefacts, in order to put them in holy places.

The black pigment analysed has been attributed to amorphous carbon. In particular, it is Lamp Black due to the absence of calcium phosphate vibrational mode, characteristic of Ivory Black. The yellow areas showed the presence of fluorite and silica, and of magnetite, an iron magnetic mineral, known and used since ancient times. The light blue areas showed the presence of galena. The presence of blue and green chlorinated phtalocyanine has been an extremely important discovery. In fact, these pigments, synthesized since 1936, confirm the presence of retouched areas of the paint layer, seen with the Wood Lamp analysis. Moreover, the presence of these pigments give important information about the painting’s restoration during the XX century, of which none historical document is available. The presence of yellow-orange chrome, used since 1809, confirmed the restoration hypothesis. In particular, since the pigment was widely used during the XIX century and rarely used during the XX century, two restoration

interventions are supposed: one during the XIX century and the other during the XX century.

Finally, the diagnostic studies allowed the identification of the original pigments and of those used in restoration intervention. These elements constitute important for the artefact history.

## 4.6. References

- [1] P. G. Caspers, A. C. Williams, E. A. Carter, H. G. M. Edwards, B. W. Barry, H. A. Bruining and G. J. Puppels, Monitoring the Penetration Enhancer Dimethyl Sulfoxide in Human Stratum Corneum in Vivo by Confocal Raman Spectroscopy, *Pharmaceutical Research*, **19**, 10 (2002).
- [2] K. Ohwada, Excitation profile of the resonance Raman effect of rubidium uranyl trinitrate in dimethyl sulfoxide, *Spectrochimica Acta Part A*, **53**, 501-507 (1997).
- [3] A. Milani, N.A. Fadel, L. Brambilla, M. Del Zoppo, C. Castiglioni, G. Zerbi and R. Stradi, "Hydrogen bonding in amylose/DMSO complexes studied by vibrational spectroscopy and density functional theory calculations", *J. Raman Spectrosc.*, **40**, 1119-1116 (2009).
- [4] W. A. Alves and O. A. C. Antunes, Lewis acid-base adducts: A quantitative Raman analysis of formamide and dimethylsulfoxide mixtures, *Spectrochimica Acta Part A*, **67**, 847-851 (2007).
- [5] W. N. Martens, R. L. Frost, J. Kristof and J. T. Kloprogge, Raman spectroscopy of dimethyl sulphoxide and deuterated dimethyl sulphoxide at 298 and 77 K, *J. Raman Spectrosc.*, **33**, 84-91 (2002).
- [6] E. Mendelovici, R. L. Frost and T. Kloprogge, Cryogenic Raman spectroscopy of glycerol, *J. Raman Spectrosc.*, **31**, 1121-1126 (2000).
- [7] J. R. Durig, L. Zhou, T. Schwartz and T. Gounev, Fourier transform Raman spectrum, vibrational assignment and *ab initio* calculation of methanesulfonic acid in the gas and liquid phases, *J. Raman Spectrosc.*, **31**, 193-202 (2000).
- [8] G. Socrates, *Infrared and Raman Characteristic Group Frequencies*, John Wiley & Sons Ltd, England, (2002).
- [9] R. E. Barletta, B. N. Gros and M. P. Herring, Analysis of marine biogenic sulfur compounds using Raman spectroscopy: dimethyl sulfide and methane sulfonic acid, *J. Raman Spectrosc.*, **40**, 972-981 (2009).
- [10] H. G. M. Edwards, D. R. Brown, J. A. Dale and S. Plant, Raman spectroscopy of sulfonated polystyrene resins, *Vibrational Spectroscopy*, **24**, 213-224 (2000).

- [11] A Ben Ahmed, H. Feki, Y. Abid, H. Boughzala, C. Minot and A. Mlayah, Crystal structure, vibrational spectra and theoretical studies of l-histidinium dihydrogen phosphate-phosphoric acid, *Journal of Molecular Structure*, **920**, 1-7, (2009).
- [12] G. Niaura, A. K. Gaigalas and V. L. Vilker, Surface Enhanced Raman Spectroscopy of Phosphate Anions: Adsorption on Silver, Gold, and Copper Electrodes, *J. Phys. Chem. B*, **101**, 9250-9262 (1997).
- [13] S. Simard, M. Odziemkowski, D. e. Irish, L. Brossard and H. Menard, In situ micro-Raman spectroscopy to investigate pitting corrosion product of 1024 mild steel in phosphate and bicarbonate solutions containing chloride and sulfate ions, *Journal of Applied Electrochemistry*, **31**, 913-920 (2001).
- [14] C. W. Lee, D. Pan, L. C. T. Shoute and D. L. Phillips, Transient resonance Raman spectroscopic and ab initio MO investigation of substituent effects on the T<sub>1</sub> triplet states of halobiphenyls, *J Raman spectrosc.*, **32**, 461-470 (2001).
- [15] S. K. Nandy, D. K. Mukherjee, S. B. Roy and G. S. Kastha, Vibrational Spectra and Rotational Isomerism in 2-Mercaptoethanol, *Can J. Chem.*, **51**, 1139 (1973).
- [16] <http://www.sigma-aldrich.com> (October 2009).
- [17] E. Emanuele, F. Negri and G. Orlandi, Reminescence of benzene in the spectroscopy of 1,3-benzodioxole: A computational study, *Chemical Physics*, **321**, 75-85 (2006).
- [18] N. Sundaraganesan, H. Saleem, S. Mohan, M. Ramalingam and V. Sethuraman, FTIR, FT-Raman spectra and ab initio DFT vibrational analysis of 2-bromo-4-methyl-phenylamine, *Spectrochimica Acta Part A*, **62**, 740-751 (2005).
- [19] A. Burneau and B. Teiten, Surface-enhanced raman spectra of both uranyl (VI) and 2-(5-bromo-2-pyridylazo)-5-diethylaminophenol in silver colloids, *Vibrational Spectroscopy*, **21**, 97-109 (1999).
- [20] Z. Q. Wen, Raman spectroscopy of protein pharmaceuticals, *Journal of Pharmaceutical Sciences*, **96**, 11 (2007).
- [21] S. Krimm and J. Bendekar, Vibrational spectroscopy and conformation of peptides, polypeptides, and proteins, *Adv Protein Chem.*, **38**, 81-364 (1986).

- [22] Beulah J.M. Rajkumar, V. Ramakrishnan, Infrared and laser Raman studies of L-phenylalanine, L-phenylalaninium perchlorate and bis (DL-phenylalaninium) sulphate monohydrate, *Spectrochimica Acta Part A*, **58**, 1923-1934 (2002).
- [23] F. M. Lyng, E. Ó Faoláin, J. Conroy, A. D. Meade, P. Knief, B. Duffy, M. B. Hunter, J. M. Byrne, P. Kelehan, H. J. Byrne, Vibrational spectroscopy for cervical cancer pathology, from biochemical analysis to diagnostic tool, *Experimental and Molecular Pathology*, **82**, 121-129 (2007).
- [24] S. A. Overman and G. J. Thomas Jr., Novel Vibrational Assignments for Proteins from raman Spectra of Viruses, *Journal of Raman spectra*, **29**, 23-29 (1998).
- [25] M. Tsuboi, T. Uedab, K. Ushizawab, Y. Ezakib, S.A. Overman and G. J. Thomas Jr., Raman tensors for the tryptophan side chain in proteins determined by polarized Raman microspectroscopy of oriented N-acetyl+tryptophan crystals, *Journal of Molecular Structure*, **379**, 43-50 (1996).
- [26] S. W. Raso, P. L. Clark, C. Haase-Pettingell, J. King and G. J. Thomas Jr., Distinct Cysteine Sulfhydryl Environments Detected by Analysis of Raman S-H Markers of Cys->Ser Mutant Proteins, *J. Mol. Biol.*, **307**, 899-911 (2001).
- [27] S. Kumar, A. K. Rai, S. B. Rai, D. K. Rai, A. N. Singh and V.B. Singh, Infrared, Raman and electronic spectra of alanine: A comparison with ab initio calculation, *Journal of Molecular Structure*, **791**, 23-29 (2006).
- [28] E. A. Disalvo , F. Lairion, F. Martini , E. Tymczyszyn , M. Frías , H. Almaleck , and G. J. Gordillo, Structural and functional properties of hydration and confined water in membrane interfaces, *Biochimica et Biophysica Acta* ,**1778**, 2655-2670 (2008).
- [29] Y. Nagata and S. Mukamel, Spectral Diffusion at the Water/Lipid Interface Revealed by Two-Dimensional Fourth-Order Spectroscopy: A Classical Simulation Study, *J. Am. Chem. Soc.*, **133**, 3276-3279. (2011).
- [30] K. M. Sanchez, G. Kang, B. Wu, and J. E. Kim, Tryptophan-Lipid Interactions in Membrane Protein Folding Probed by Ultraviolet Resonance Raman and Fluorescence Spectroscopy, *Biophysical Journal*, **100**, 2121–2130. (2011).



- [31] M. P. Nieh, T. A. Harroun, V. A. Raghunathan, C. J. Glinka, and J. Katsaras, Spontaneously Formed Monodisperse Biomimetic Unilamellar Vesicles: The Effect of Charge, Dilution, and Time, *Biophys J.*, **86**(4), 2615–2629. (2004).
- [32] C. W. Meuse, G. Niaura, M. L. Lewis, and A. L. Plant, Assessing the Molecular Structure of Alkanethiol Monolayers in Hybrid Bilayer Membranes with Vibrational Spectroscopies *Langmuir*, **14**, 1604-1611. (1998).
- [33] R. A. Walker, J. A. Gruetzmacher, and G. L. Richmond, Phosphatidylcholine monolayer structure at a liquid-liquid interface *J. Am. Chem. Soc.*, **120**, 6991-7003 (1998).
- [34] M. J. Hope, M. B. Bally, L. D. Mayer, A. Janoff and P.R. Cullis, Generation of multilamellar and unilamellar phospholipid vesicles” *Chemistry and Physics of Lipids*, **40**, 89-107 (1986).
- [35] P. Walde, K. Cosentino, H. Engelc, and P. Stanod, Giant Vesicles: Preparations and Applications, *ChemBioChem*, **11**, 848-865. (2010).
- [36] N. Kucerka, Y. Liu, N. Chu, H. I. Petrache, S. Tristram-Nagle, and J. F. Nagle, Structure of Fully Hydrated Fluid Phase DMPC and DLPC Lipid Bilayers Using X-Ray Scattering from Oriented Multilamellar Arrays and from Unilamellar Vesicles, *Biophysical Journal*, **88** , 2626–2637 (2005).
- [37] S. Ahmed and S. L. Wunder, Effect of High Surface Curvature on the Main Phase Transition of Supported Phospholipid Bilayers on SiO<sub>2</sub> Nanoparticles, *Langmuir*, **25**, 3682-3691 (2009).
- [38] D. Needham and E. Evans, Structure and Mechanical Properties of Giant Lipid (DMPC ) Vesicle Bilayers from 20°C below to 10°C above the Liquid Crystal-Crystalline Phase Transition at 24 °C, *Biochemistry*, **27**, 8261-8269 (1988).
- [39] F. Lhert, F. Capelle, D. Blaudez, C. Heywang, and J-M. Turllet, Raman Spectroscopy of Phospholipid Black Films, *J. Phys. Chem. B*, **104**, 11704-11707 (2000).
- [40] Chongsoo Lee, Colin D. Bain, Raman spectra of planar supported lipid bilayers, *Biochimica et Biophysica Acta* **1711** 59–71 (2005).
- [41] M. Castriota, A. Fasanella, E. Cazzanelli, L. De Sio, R. Caputo, and C. Umeton, In situ polarized micro-Raman investigation of periodic structures realized in liquid-crystalline composite materials, *Optics Express*, **19** (11),10494 (2011).

- [42] M. A. Kiselev, S. Wartewig, M. Janich, P. Lesieur, A. M. Kiselev, M. Ollivon, R. Neubert, Does sucrose influence the properties of DMPC vesicles? *Chemistry and Physics of Lipids*, **123**, 31-44 (2003).
- [43] R. Foucault, R. L. Birke, and J. R. Lombardi, SERS of Surfactants in Monolayer and Multibilayer Forms on an Electrified Ag Surface, *Langmuir*, **19**, 8818-8827 (2003).
- [44] S. Kint, Paul H. Wermer, and James R. Scherer, Raman Spectra of Hydrated Phospholipid Bilayers. Water and Head-Group Interactions, *The Journal of Physical Chemistry*, **96** (1992).
- [45] A. D. Pink, T. J. Green, and D. Chapman, Raman Scattering in Bilayers of Saturated Phosphatidylcholines. Experiment and Theory, *American Chemical Society Biochemistry*, **19**, (1980).
- [46] R. Caputo, A. De Luca, L. De Sio, L. Pezzi, G. Strangi, C. Umeton, R. Asquini, A. d' Alessandro, D. Donisi, R. Beccherelli, A. V. Sukhov, and N. V. Tabiryan, *J. Opt. A: Pure Appl. Opt.*, **11**, 024017 (2009).
- [47] R. Caputo, A. L. De Sio, A. Veltri, and C. Umeton, *Optics Letters*, **29**, 1261 (2004).
- [48] A. R. E. Brás, T. Casimiro, J. Caldeira, and A. Aguiar-Ricardo, *J. Chem. Eng.*, **50**, 1857 (2005).
- [49] Dae Seung Kang, Ki-Sun Kwon, Sung Il Kim, Myoung-Seon Gong, Sung Seok A. Seo, Tae Won Noh, and Sang-Woo Joo, *Applied Spectroscopy*, **59**, 1136 (2005).
- [50] Sang-Woo Joo, Taek Dong Chung, Won Cheoul Jang, Myoung-Seon Gong, Neri Geum, and Kwan Kim, *Langmuir*, **18**, 8813 (2002).
- [51] K. Merkel, R. Wrzalik, and A. Kocot, *Journal of Molecular Structure*, **563-564**, 477 (2001).
- [52] I. Nicotera, C. Oliviero, G. Ranieri, A. Spadafora, M. Castriota and E. Cazzanelli, Temperature evolution of thermoreversible polymer gel electrolytes LiClO<sub>4</sub> \ ethylene carbonate \ poly(acrylonitrile), *J. Chem. Phys.*, **117** (15), 7373-7380 (2002).

- [53] W. J. Jones, D. K. Thomas, D. W. Thomas, and G. Williams, On the determination of order parameters for homogeneous and twisted nematic liquid crystals from Raman spectroscopy, *J. Mol. Struct.*, **708**(1-3), 145–163 (2004).
- [54] E. W. Astrova, T. S. Perova, S. A. Grudinkin, V. A. Tolmachev, Yu. A. Pilyugina, V. B. Voronkov, and J. K. Vij, Polarized infrared and Raman spectroscopic studies of the liquid crystal E7 alignment in composites based on grooved silicon, *Semiconductors*, **39**, 759-767 (2005).
- [55] B. Pinto-Iguanero, A. Olivares-Perez, and I. Fuentes-Tapia, Holographic material film composed by Norland Noa 65® adhesive, *Opt. Mater.*, **20**(3), 225–232 (2002).
- [56] H. T. A. Wilderbeek, J. (Han) G. P. Goossens, C. W. M. Bastiaansen, and D. J. Broer, Photoinitiated bulk polymerization of liquid crystalline thiolene monomers, *Macromolecules*, **35**(24), 8962–8968 (2002).
- [57] N. B. Cramer, and C. N. Bowman, Kinetics of thiol–ene and thiol–acrylate photopolymerizations with real-time fourier transform infrared, *Journal of Polymer Science: Part A: Polymer Chemistry*, **39**, 3311 (2001).
- [58] S. M. Trey, M. Lundström, D. Ståhlberg, and M. Johansson, *Progress in Organic Coatings*, **64**, 238 (2009).
- [59] C. Nilsson, N. Simpson, M. Malkoch, M. Johansson, and E. Malmström, *Journal of Polymer Science: Part A: Polymer Chemistry*, **46**, 1339 (2008).
- [60] S. E. Barnes, Z. T. Cygan, J. K. Yates, K. L. Beers, and E. J. Amis, Raman spectroscopic monitoring of droplet polymerization in a microfluidic device, *Analyst* **131**, 1027 (2006).
- [61] M. Claudino, M. Johansson, and M. Jonsson, *European Polymer Journal*, **46**, 2321 (2010).
- [62] M. Asquier, P. Colomban, and V. Milande, *J. Raman Spectrosc.*, **40**, 1641 (2009).
- [63] K. S. Moe, T. M. Moses, and P. Johnson, *Gems & Gemology*, **43**, 149 (2007).
- [64] M.H. Jamróz, M. E. Jamróz, and J. E. Rode, *Vibrational Spectroscopy*, **50**, 231 (2009).

- [65] H. F. Gleeson, C. D. Southern, P. D. Brimicombe, J. W. Goodby, and V. Görtz, *Liquid Crystals*, **37**, 949 (2010).
- [66] Jong Kuk Lim, Ohyun Kwon, Dae Seung Kang, and Sang-Woo Joo, *Chemical Physics Letters*, **423**, 178 (2006).
- [67] W. J. Jones, D. K. Thomas, D. W. Thomas, and G. Williams, *Journal of Molecular Structure*, **614**, 75 (2002).
- [68] E. A. Büyüktanir, K. Zhang, A. Gericke, and J. L. West, *Mol. Cryst. Liq. Cryst.*, **487**, 39 (2008).
- [69] A. Sanchez-Castillo, M. A. Osipov, and F. Giesselmann, *Phys. Rev. E*, **81**, 021707 (2010).
- [70] S. K. Deb; *Philos. Mag.*, **27**, 801 (1973).
- [71] J. Blanc and D. L. Staebler; *Phys. Rev. B*, **4**, 3548 (1971).
- [72] R. S. Crandall and B. W. Faughnan; *Appl. Phys. Lett.*, **26**, 120-121 (1975).
- [73] V. Dallacasa, M. Manfredi and G. Schianchi; *Thin solid films*, **91**, 1-8 (1982).
- [74] T. Yoshimura; *J. Appl. Phys.*, **57**, 911-919 (1984).
- [75] C. M. Lampert; *Sol. Energy Mater.*, **52**, 207-221 (1998).
- [76] C.G. Granqvist; *Handbook of Inorganic Electrochromic Materials*; Elsevier: Amsterdam, (1995).
- [77] K. Bange; *Solar Energy Materials & Solar Cells*, **58**, 1-131 (1999).
- [78] A. Petra, K. Auddy, D. Ganguli, J. Livage and P. K. Biswas; *Materials Letters*, **58**, 1059-1063 (2004).
- [79] A. Bessière, C. Marcel, M. Morcrette and J-M. Tarascon, V. Lucas, B. Viana and N. Baffier; *J. Appl. Phys.*, **91**, 1589-1594 (2002).
- [80] M. Castriota; Ph.D Thesis, Development and Spectroscopic Characterization of Materials for Applications in Electrochromic Devices and Novel Liquid Crystalline Cells, University of Calabria, Rende, Cosenza, Italy, (2004).
- [81] P.K. Biswas, N. C. Pramanik, M. K. Mahapatra, D. Ganguli and J. Livage; *Materials Letters*, **57**, 4429-4432 (2003).
- [82] G. Strangi, D.E. Lucchetta, E. Cazzanelli, N. Scaramuzza, C. Versace and R. Bartolino; *Applied Physics Letters*, **74**, 534-536 (1999).
- [83] G. Strangi, N. Scaramuzza, C. Versace, E. Cazzanelli, F. Simone, A. Pennisi and R. Bartolino; *Ionics*, **5**, 275-285 (1999).

- [84] G. Strangi, E. Cazzanelli, N. Scaramuzza, C. Versace and R. Bartolino; *Physical Review E*, **62**, 2263-2268 (2000).
- [85] E. Cazzanelli, N. Scaramuzza, G. Strangi, C. Versace, A. Pennisi and F. Simone; *Electrochimica Acta*, **44**, 3101-3109 (1999).
- [86] M. Castriota, S. Marino, C. Versace, G. Strangi, N. Scaramuzza and E. Cazzanelli; *Molecular Crystals and Liquid Crystals*, **429**, 237-253 (2005).
- [87] N. Ozer; *Thin Solid Films*, **304**, 310-314 (1997).
- [88] J. Livage and D. Ganguli; *Solar Energy Materials & Solar Cells*, **68**, 365-381 (2001).
- [89] L.H.M. Krings and W. Talen; *Solar Energy Materials & Solar Cells*, **54**, 27-37 (1998).
- [90] A. Kuzmin, J. Purans, E. Cazzanelli, C. Vinegoni and G. Mariotto; *J. Appl. Phys.*, **84**, 5515-5524 (1998).
- [91] E. Cazzanelli, C. Vinegoni, G. Mariotto, A. Kuzmin and J. Purans; *J. of Solid State Chemistry*, **143**, 24-32 (1999).
- [92] E. Cazzanelli, C. Vinegoni, G. Mariotto, A. Kuzmin and J. Purans; *Solid State Ionics*, **123**, 67-74 (1999).
- [93] E. Cazzanelli, L. Papalino, A. Pennisi and F. Simone; *Electrochimica Acta*, **46**, 1937-1944 (2001).
- [94] M. Boulova and G. Lucazeau; *J. of Solid State Chemistry*, **167**, 425-434 (2002).
- [95] C.V. Ramana, S. Utsunomiya, R.C. Ewing, C.M. Julien and U. Becker; *J. Phys. Chem. B*, **110**, 10430-10435 (2006).
- [96] G.J. Fang, Z.L. Liu, G.C. Sun and K.L. Yao; *Phys. Stat. Sol. A*, **184**, 129-137 (2001).
- [97] K. Schofield; *Energy & Fuels*, **17**, 191-203 (2003).
- [98] J. Hanuza, L. Maczka, E.T.G. Lutz and J.H. van der Maas; *Journal of Molecular Structure*, **511-512**, 85-106 (1999).
- [99] M. Maczka; *J. of Solid State Chemistry*, **129**, 287-297 (1997).
- [100] M. Picquart, S. Castro-Garcia, J. Livage, C. Julien and E. Haro-Poniatowski; *Journal of Sol-Gel Science and Technology*, **18**, 199-206 (2000).
- [101] E. Gallucci, C. Goutaudier, F. Bourgeois, G. Boulon and M. Th. Cohen-Adad; *J. of Solid State Chemistry*, **163**, 506-512 (2002).

- [102] J.F. Scott, R.F. Leheny, J.P. Remeika and A.R. Sweedler; *Physical Review B*, **2**, 3883-3887 (1970).
- [103] U. Opara Krasovec, A. Surca Vuk and B. Orel; *Electrochimica Acta*, **46**, 1921-1929 (2001).
- [104] L.G. Quagliano; *Surface Science*, **566-568**, 875-879 (2004).
- [105] G Compagnini., *Raman Spectroscopy and related techniques: state of the art and future directions in Italy*, in *J. Raman Spectrosc.*, **39**, 131-133 (2008).
- [106] R. J. H Clark, *Pigment identification on Medieval Manuscripts by Raman Microscopy*, in *Journal of Molecular Structure*, **347**, 417-428 (1995).
- [107] R. J. H Clark, *Raman Microscopy: sensitive probe of pigments on manuscripts, paintings and other artefacts*, in *Journal of Molecular Structure*, **480-481**, 15-20 (1999).
- [108] K. Sakellariou, C. Miliani, A. Morresi, M Ombelli, *Spectroscopic investigation of yellow majolica glazes*, in *J. Raman Spectrosc.*, **35**, 61-67 (2004).
- [109] P Colomban, *On-site Raman Identification and dating of ancient glasses: A Review of procedures and tools*, in *Journal of Cultural Heritage*, **9**, 55-56 (2008).
- [110] M. Castriota, V. Cosco, T. Barone, G. De Santo, P. Carafa, E. Cazzanelli, *Micro-Raman characterizations of Pompei's mortars*, in *J. Raman Spectrosc.*, **39**, 295-301 (2008).
- [111] M. Castriota, E. Meduri, T Barone, G De Santo, E Cazzanelli, *Micro-raman investigations on the fresco "Trapasso della Vergine", in the Church of "S. Giovanni Battista" of Paterno Calabro in southern Italy*, in *J. Raman Spectrosc.*, **39**, 284-288. 2008.
- [112] M. Ortega- Avilés, P. Vandenabeele, D. Tenorio, G Murillo, M Jimenéz-Reyes., N Gutiérrez., *Spectroscopic investigation of a "Virgin of Sorrows" canvas painting: a multi-metod approach*, in *Analytica Chimica Acta*, **550**, 164-172 (2005).
- [113] H. G. M. Edwards, T. Munshi, *Diagnostic Raman Spectroscopy for the forensic detection of biomaterials and the preservation of Cultural Heritage*, in *J. Anal. Bioanal. Chem.*, **382**, 1398-1406 (2005).

- [114] A. Conti, R. Cassanelli, *L'Arte. Critica e Conservazione*, Jaca Book, Milano, 109 (1993).
- [115] M. Bouchard, R. Rivenc, C. Menke, T. Learner, Micro-FTIR and Micro-Raman study of paints used by Sam Francis, in *Preservation Science*, **6**, 27-37 (2009).
- [116] F. Schulte, K. W. Brzezinka, K. Lutzenberger, H. Stege, U. Panne, Raman Spectroscopy of synthetic organic pigments used in 20th century works art, in *Journal of Raman Spectroscopy*, **39**, 1455-1463 (2008).
- [117] L. I. Mc Cann, K. Trentelman, T. Possley, B. Golding, Corrosion of ancient Chinese Bronze Money Trees Studied by Raman Spectroscopy, *Journal of Raman Spectroscopy*, **30**, 121-132 (1999).
- [118] F. Rosi, C. Miliani, I. Borgia, B. Brunetti, A. Sgamellotti, Identification of nineteenth century blue and green pigments by in situ X-ray fluorescence and micro-Raman spectroscopy, in *Journal of Raman Spectroscopy*, **35**, 610-615 (2004).
- [119] I. M. Bell, R. J. H. Clark, P. J. Gibbs, Raman Spectroscopic library of natural and synthetic pigments (pre- ~1850 AD), in *Spectrochimica Acta Part A*, **53**, 2159-2179 (1997).
- [120] R. Srivastava, H.V. Lauer Jr, L.L. Chase, W.E. Bron, Raman frequencies of fluorite crystals, **36** (4), 333-334 (1971)
- [121] M. Sendova, V. Zhelyaskov, M. Scalera, C. Gulliford, Micro-Raman Spectroscopy characterization of Della Robbia glazes, in *Archaeometry*, **49**, 655-664 (2007).
- [122] (<http://www.webexhibits.org/pigments/indiv/history/cryellow.html>).
- [123] T. D. Chaplin, A. Jurado-López, R. J. Clark, D. R. Beech, Identification by Raman microscopy of pigments on early postage stamps: distinction between original 1847 and 1858-1862, forged and reproduction postage stamps of Mauritius, in *Journal of Raman Spectroscopy*, **35**, 600-604 (2004).
- [124] D. Bersani, G. Antonioli, P. Lottici, A. Casoli, Spectroscopic investigation of wall paintings in S. Giovanni Evangelista Abbey in Parma: a comparison between two artists of the 16th century, in *Spectrochimica Acta Part A*, **59**, 2409-2417 (2003).

- 
- [125] H. G. M. Edwards, D. W. Farwell, S. Rozenberg, Raman Spectroscopic Study of Red Pigments and Fresco Fragments from King Herod's Palace at Jericho, in *Journal of Raman Spectroscopy*, **30**, 361-366 (1999).
- [126] B. Wehling, P. Vandenabeele, L. Moens, R. Klockenkämper, A. Von Bohlen, G. Van Hooydonk, M. De Reu, Investigation of Pigments in Medieval Manuscripts by Micro-Raman Spectroscopy and Total Reflection X-Ray Fluorescence Spectroscopy, in *Microchimica Acta*, **130**, 253-260 (1999).
- [127] L. De Beausobre, *Introduzione generale allo studio della politica, delle finanze e del commercio*, Yverdon, Berlino, 109 (1764).
- [128] B. S. Tosatti, *Trattati Medievali di tecniche artistiche*, Jaca Book, Milano, 108 (2007).
- [129] [http://www.dst.unisi.it/geofluids/raman/spectrum\\_frame.htm](http://www.dst.unisi.it/geofluids/raman/spectrum_frame.htm).
- [130] F. Froment, A. Tournie', P. Colomban, Raman identification of natural red to yellow pigments: ochre and iron-containing ores, in *Journal of Raman Spectroscopy*, **39**, 560-568 (2008).
- [131] N. Caruso, *Ceramica viva*, Hoepli, Milano, 257 (2003).
- [132] J. G. Shapter, M. H. Brooker, W.M. Skinner, Observation of the oxidation of galena using Raman Spectroscopy, in *Journal of Raman Spectroscopy*, **60**, 199-211 (2000).
- [133] M. Firestone, Z. O'Neill, A. Sattin, R. Wlodarski, *Egitto EDT*, Torino, 43 (2008).



**SELECTED PUBLICATIONS**

*Molecular orientation of E7 liquid crystal in POLICRYPS holographic gratings: a micro-Raman spectroscopic analysis*

**A. Fasanella**, M. Castriota, E.Cazzanelli, L. De Sio, R. Caputo and C. Umeton,

*Molecular Crystals and Liquid Crystals*, **558**, 46 (2012),

# Molecular Orientation of E7 Liquid Crystal in POLICRYPS Holographic Gratings: A Micro-Raman Spectroscopic Analysis

ANGELA FASANELLA, MARCO CASTRIOTA,\*  
ENZO CAZZANELLI, LUCIANO DE SIO,  
ROBERTO CAPUTO, AND CESARE UMETON

LICRYL (Liquid Crystals Laboratory, IPCF-CNR), Center of Excellence  
CEMIF.CAL and Department of Physics University of Calabria,  
87036 Rende (CS), Italy

*Micro-Raman Spectroscopy was used to determine the orientation of the E7 nematic liquid crystal molecules inside the POLICRYPS (Polymer Liquid CRYstal Polymer Slices) holographic gratings. The POLICRYPS grating was analyzed after defining the Raman features of each single component of the system: i.e the random aligned nematic liquid crystal E7 and Norland Optical Adhesive (NOA-61). Among the Raman bands of the liquid crystal molecules, a specific one was selected, which exhibits strong anisotropy of the Raman tensor. The modulation of its intensity, depending on the sample orientation with respect to the laser polarization, provided the experimental evidence about the orientation of the E7 molecules, which occurred to be perpendicular to the polymeric slices.*

**Keywords** Holographic grating; nematic liquid crystals; polymers; Raman spectroscopy

## 1. Introduction

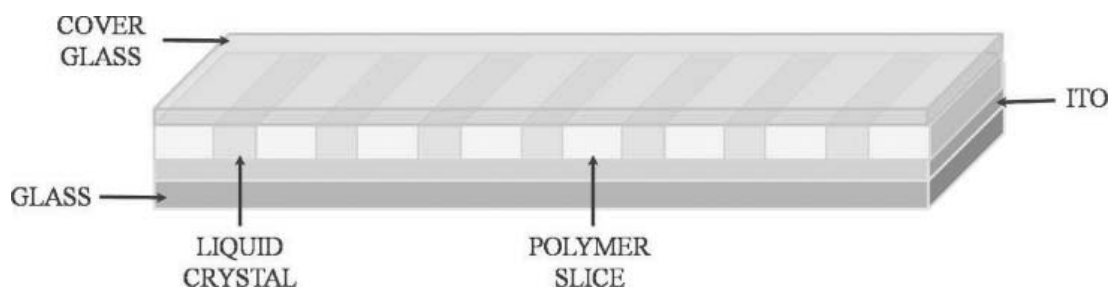
Great interest has recently been addressed to switchable holographic gratings, due to the several potential industrial applications, e.g. imaging and diffractive optics [1]. Periodic liquid crystalline composite materials like POLICRYPS (acronym of POLYmer LIQuid CRYstal Polymer Slices), represent a significant example of a novel structure in the field of optics and electro-optics [2–5]. Furthermore, if doped with metal nanoparticles, POLICRYPS could possibly be exploited for the realization of tunable metamaterials [6].

POLICRYPS, as schematized in Fig. 1, consist in polymer slices alternated to films of Nematic Liquid Crystal (NLC). The electro-optical properties of these systems, as in all liquid crystal based devices, depend on the orientation of the liquid crystal molecules, whose average value is given by the director  $\mathbf{n}$  [7].

In this work, polarized Raman spectroscopy is used to investigate the orientation of NLC molecules inside the POLYCRYPS grating. Before performing such analysis, Raman

---

\*Address correspondence to Marco Castriota, Physics Department-University of Calabria, 87036 Rende (CS), Italy. Phone: +39-0984-496145; Fax: +39-0984-496145. E-mail: marco.castriota@fis.unical.it



**Figure 1.** Schematic view of a POLICRYPS.

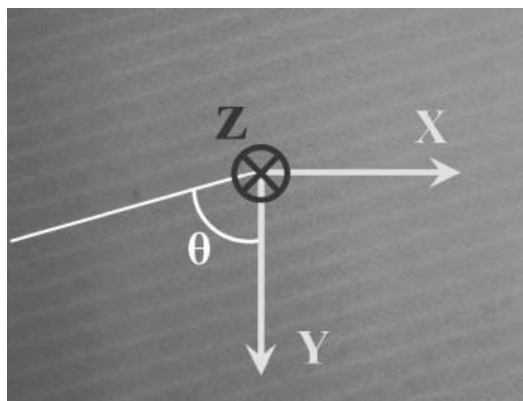
spectra of both the randomly aligned NLC E7 and the polymer (Norland Optical Adhesive NOA-61) were collected separately, in order to define the main Raman features needed for the interpretation of POLICRYPS spectra.

## 2. Experimental

POLICRYPS made with nematic liquid crystal E7 (supplied by Merck) and monomer NOA-61 (Norland Optical Adhesive), were obtained by the procedure described elsewhere [5, 8]. Briefly, the mixture made up of NLC, the monomer and the photo-initiator was heated above the nematic–isotropic transition temperature of the E7 component and then cured by exposing it to an interference pattern of a UV radiation. After the curing process is finished the sample is cooled down to room temperature with a cooling rate of  $0.3^{\circ}\text{C}/\text{min}$ . An Ar-ion laser generates a single-mode radiation at the wavelength  $\lambda_B = 351 \text{ nm}$ . The beam diameter is broadened to about 25 mm by a beam expander BE and subsequently divided by a beam splitter BS into two beams of almost equal intensity. These two overlapping beams originates the ‘curing’ interference pattern at the entrance plane of the sample cell. Depending on the required nano/microscale dimensions of the structure, the spatial period of the interference pattern can vary in the range  $\Lambda = 0.2\text{--}15 \mu\text{m}$  by adjusting the total interference angle  $2\theta_{\text{cur}}$  [5, 8]. A commercial, metal-coated, reflective diffraction grating (Edmund Optics) placed above the sample is used as a test element for the interferometric monitoring of vibrations [5, 8]. Part of each of the curing beams is reflected and diffracted by this grating. The set-up is tuned to make the reflected part of one beam spatially coincident with the diffracted part of the second one. These two radiations are wave coupled by means of the test grating and their interference pattern is detected by an additional photodiode. The signal coming from the latter is sent to a computerized active feedback system, based on a proportional–integral–derivative protocol software which controls a mirror-holder tuned by a piezoelectric mechanism, working in feedback configuration. The control system is able to continuously compensate the optical path length changes due to vibrations, as well as variations in environmental conditions such as room pressure, temperature or humidity; residual fluctuations are of the order of 6–7 nm, corresponding to the sensitivity of the piezo-system used.

The sample grating was written with a large pitch ( $6 \mu\text{m}$ ) and a 0.1 mm thick glass employed for the upper cell window [Fig. 1].

Raman spectra were collected by a Raman microprobe Jobin-Yvon Labram (spectral resolution  $\sim 2 \text{ cm}^{-1}$ ) equipped with a CCD detector and a He-Ne laser (633 nm). A 50x Mplan Olympus objective was used (Numerical Aperture 0.90), focusing a laser spot of diameter of about 2–3  $\mu\text{m}$ .



**Figure 2.** Optical micro-image of a POLICRYPS structure and laboratory reference axes;  $\theta$  is the angle between the direction of polarization of the incident radiation along Y axis of the laboratory reference system (yellow line) and the direction of polymer slices of the POLICRYPS structure (white line). In the POLICRYPS, as observed by microscopy, darker strips correspond to polymer zones and lighter narrow lines to liquid crystals zones.

Polarized Raman spectra of POLICRYPS sample were recorded at different orientations changing the angle  $\theta$ , defined as the angle formed by the light polarization direction and the polymeric slices (Fig. 2) [7]. The laser source is linearly polarized along the Y axis of the reference system of the laboratory. The analyzer is set to allow the passage of exclusively the Y polarized component of the scattered radiation: only the YY component of the polarizability tensor can be detected with this setup (small letters  $x,y,z$  refer to the molecular reference system while capital  $X,Y,Z$  indicate the laboratory reference system).

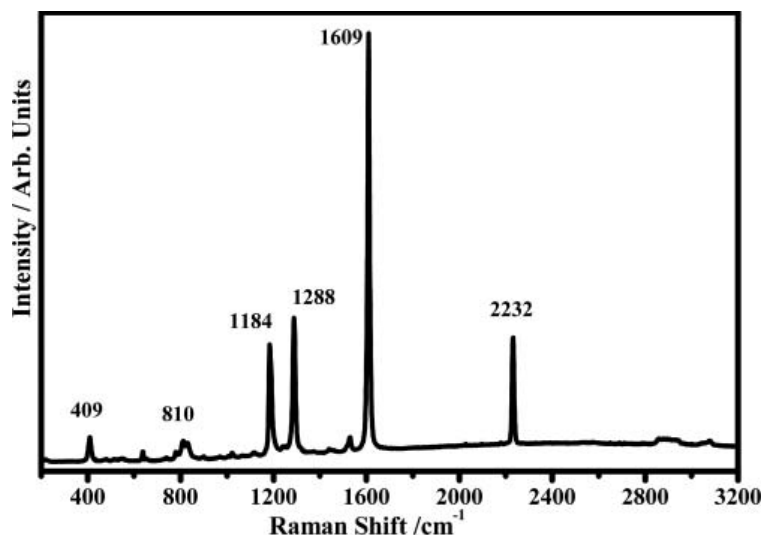
The sample holder is a goniometric rotation stage supplied by Thorlabs. Spectra were collected for different values of the angle  $\theta$ , spanning from  $0^\circ$  (polymeric slices parallel to the light polarization direction) to  $180^\circ$ , steps of  $15^\circ$ .

The spectral mappings on the POLICRYPS were recorded by using an automatic X-Y stage.

### 3. Results and Discussion

The E7 liquid crystal is a multicomponent nematic mixture mainly composed of substituted 4-cyanobiphenyls [9]. Raman spectra corresponding to the random aligned NLC are shown in Fig. 3. The higher intensity Raman bands are assigned to the ring deformations. These modes were attributed taking into account that the biphenyl group belongs to the  $C_{2v}$  point group [10–12], meaning that its skeletal vibrational modes can be defined just by four symmetry species. Specifically, the  $1184 (\nu_{9a})$  and  $1609 (\nu_{8a}) \text{ cm}^{-1}$  bands are described by the  $A_1$  symmetry representation, the peaks at  $810 (\nu_4)$  and  $830 (\nu_{11}) \text{ cm}^{-1}$  by the  $B_1$  symmetry while the modes at  $638 (\nu_{6b})$  and  $1288 (\nu_3) \text{ cm}^{-1}$  by the  $B_2$  symmetry [10–12]. One should point out that the eigenvectors of the  $1184$  and  $1609 \text{ cm}^{-1}$  modes belong to the molecular plane while the others correspond to motion out of it. The CN group modes fall at  $409 (\gamma \text{ deformation})$  and  $2232 \text{ cm}^{-1}$  (symmetric stretching) [10–13].

The optical polarizability tensor of the cyanobiphenyl NLC molecules can be represented by an oblate ellipsoid with  $\alpha_{zz} \gg \alpha_{yy} = \alpha_{xx}$ , where  $\alpha_{xx}$ ,  $\alpha_{yy}$  and  $\alpha_{zz}$  indicate the components of the polarizability tensor in the molecular reference system, where the z axis is oriented along the long molecular axis. From the basic Raman theory it is known that each vibrational mode induces a dynamic modulation of the polarizability ( $\partial\alpha_{ij}/\partial Q_k$ ) that is

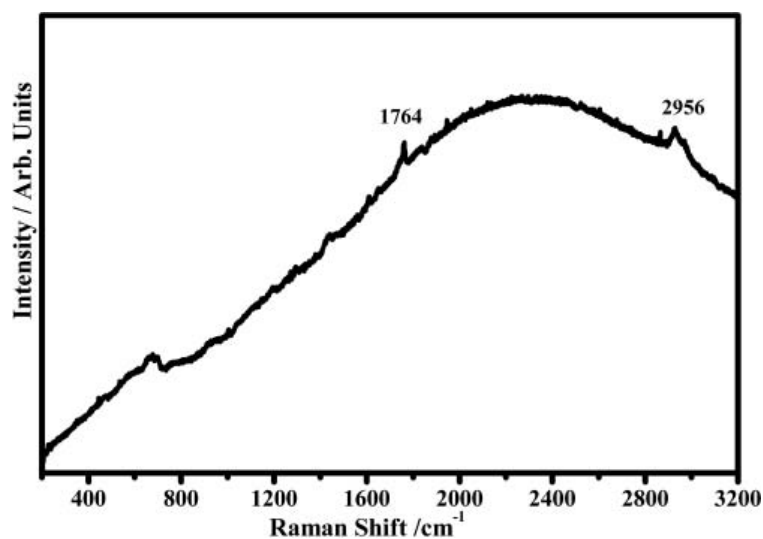


**Figure 3.** Example of a Raman spectrum acquired on randomly aligned E7 NLC in the range between 200 and 3200 cm<sup>-1</sup>.

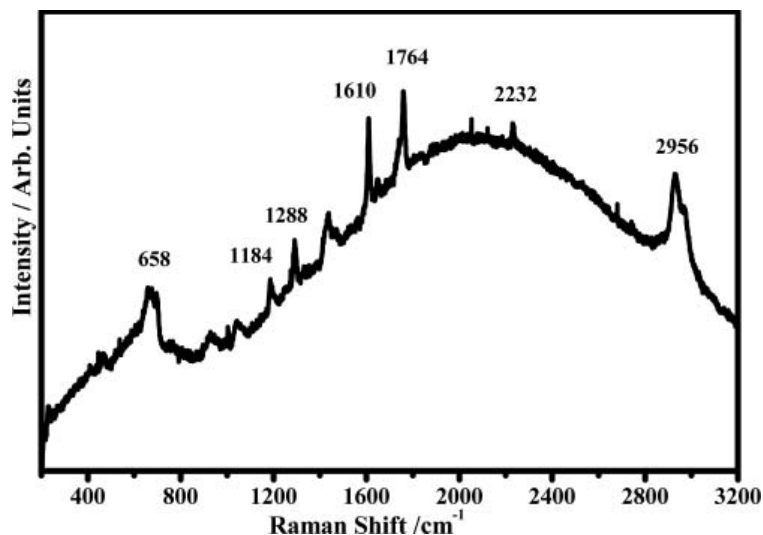
synchronized with the vibrational normal coordinate  $Q_k$ . The most significant variation of the polarizability tensor corresponds to the symmetric stretching of the biphenyls aromatic rings and the CN stretching, which occurs along the long molecular axis of the molecule. As the intensity of the scattered radiation depends on the square of the induced dipole moment, therefore the Raman intensity of the modes occurring along the  $z$ -axis, whose associate dipole moment is  $\mu_z = \alpha_{zz} E_z$ , will be higher in the case of NLC molecules  $z$ -axis being parallel to the polarization of the incident light ( $E_z$  is maximum).

The orientation of the director  $\mathbf{n}$ , (and therefore of the liquid crystal molecules), is parallel to the incident light polarization for the  $\theta$  value at which are maximized the intensities of the Raman bands of the vibrational modes occurring along the  $z$ -molecular axis [14, 15].

The Raman spectrum of the polymeric component (NOA-61) of POLICRYPS was collected, after the polymerization process, for comparative purposes (Fig. 4). NOA-61



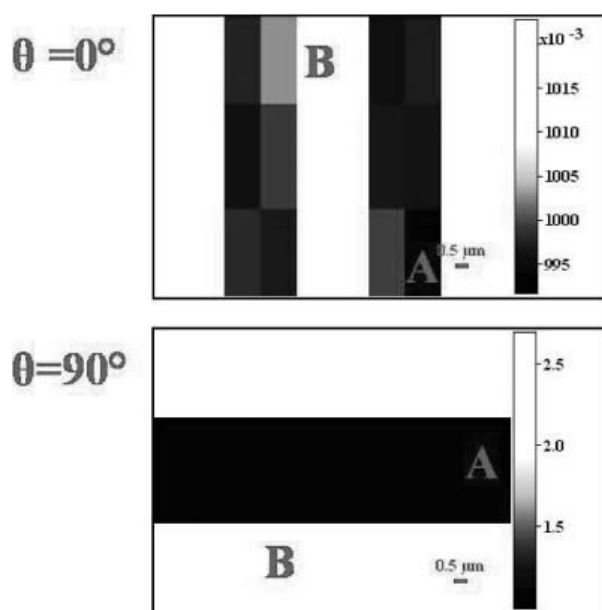
**Figure 4.** Example of a Raman spectrum of the polymerized Norland Optical Adhesive NOA-61.



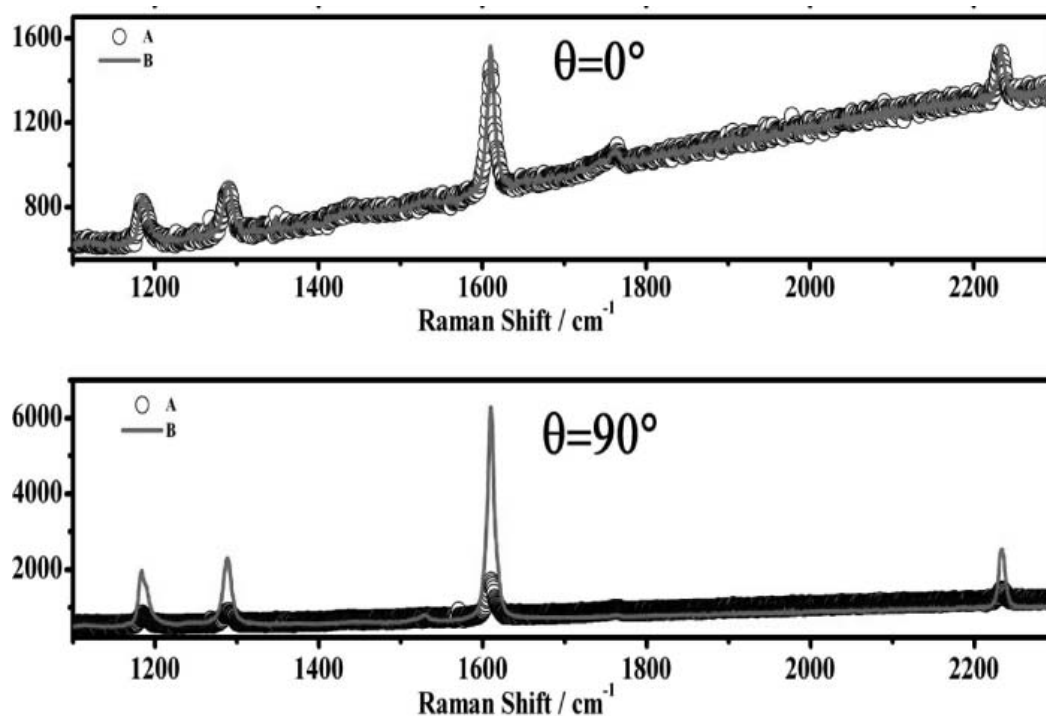
**Figure 5.** Example of a Raman spectrum of a POLICRYPS holographic grating.

exact composition is still unknown, probably consisting of a mixture of a mercapto-ester and an acrylate monomer [16]. The polymerized NOA-61 Raman spectra (Fig. 4) overlaps with a great luminescence band and it is characterized by the carboxyl group (COOR) bands at 1746 and 1764  $\text{cm}^{-1}$  [17–20] and the C–H stretching bands in the region 2900–3100  $\text{cm}^{-1}$ .

An example of POLICRYPS (NOA-61 polymerized and E7) Raman spectrum is shown in Fig. 5, where one can note bands, both at 1610  $\text{cm}^{-1}$  and 2232  $\text{cm}^{-1}$ , typical of E7 molecules, and at 1746 and 1764  $\text{cm}^{-1}$  originated by NOA-61 carboxyl groups. Hence, a Raman mapping (Fig. 6) plotting the intensity ratio between the frequency region 1590–1640  $\text{cm}^{-1}$  (E7 bands), and the 1735–1785  $\text{cm}^{-1}$  one (NOA-61 bands), is a valid indication



**Figure 6.** Raman mapping of ratio between the intensity in the frequency region 1590–1640  $\text{cm}^{-1}$  (NLC band) and that in the 1735–1785  $\text{cm}^{-1}$  region (NOA-61 polymer band). Top map:  $\theta = 0^\circ$ ; bottom map:  $\theta = 90^\circ$ .



**Figure 7.** Example of a Polarized Raman spectra of a POLICRYPS grating, acquired from A zones (polymer-circles) and B zones (liquid crystal-solid red line) in the maps of Fig. 6. Top spectra:  $\theta = 0^\circ$ ; bottom spectra  $\theta = 90^\circ$ .

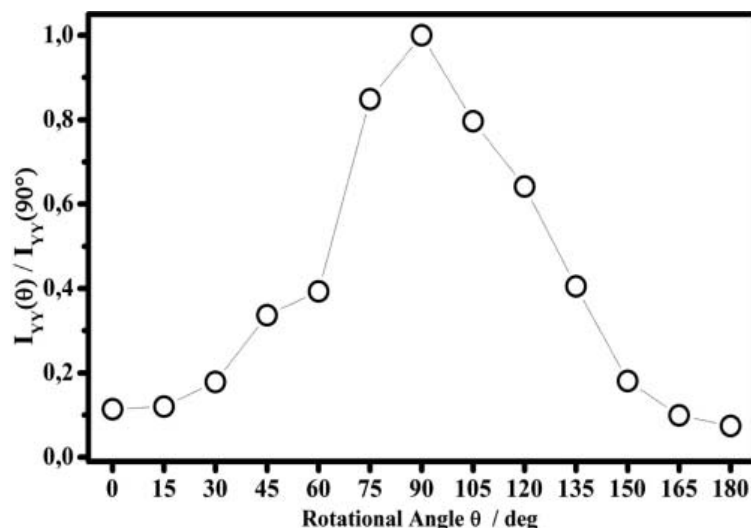
on the material distribution: when this ratio is lower than 1 (Fig. 6, dark squares) the presence of the polymer is prevalent; on the contrary, clearer squares corresponding to an intensity ratio above 1 indicate the prevalence of the E7 molecules (Fig. 6).

This “chemical map”, provided by the micro-Raman measurement, matches with the pattern of polymer slices alternating with liquid crystal zones, acquired by microscopy. Fig. 6 displays two different experimental configurations corresponding to  $\theta = 0$  at the top and  $\theta = 90^\circ$  at the bottom; the spatial distribution of the two chemical species appears well defined, with a good parallel alignment of the polymeric slices to the Y axis when  $\theta = 0$ , and perpendicular to it when  $\theta = 90^\circ$ . Since the laboratory Y axis corresponds also to the fixed direction of impinging light polarization, a strong modulation of the intensity is expected for the Raman peak, due to the total symmetric vibrational modes of E7 molecules, as a consequence of their orientational order in the regions occupied mainly by the liquid crystal.

Figure 7 shows spectra A (circles) and B (solid red line), collected from the polymeric slices and the liquid crystal zones respectively, in both  $\theta = 0^\circ$  (top), and  $\theta = 90^\circ$  (bottom) orientations of the sample. As one can notice, in the recorded spectra from A zones (polymeric slices) there is no appreciable difference of intensity of the E7 bands between  $\theta = 0^\circ$  and  $\theta = 90^\circ$ . On the contrary, in the B regions case (liquid crystal zones) bands at 1184, 1288, 1610 and 2232  $\text{cm}^{-1}$  – corresponding to the aromatic C–H in plane deformation, C–C stretch of biphenyl bond, C=C stretching of biphenyl rings and C–N stretching, respectively [14, 15, 21–25]—the intensity appears quite higher in the  $\theta = 90^\circ$  spectra than in the  $\theta = 0^\circ$  ones (see Fig. 7, top and bottom graphs, focusing in particular on the intensity scales).

A detailed analysis of the intensity modulation of NLC Raman bands, as a function of the orientation with respect to the laser polarization, is reported in Fig. 8, where the 1610  $\text{cm}^{-1}$  band of a B zone (liquid crystal) spectra was taken into consideration. The data





**Figure 8.** Raman intensity of the NLC band at  $1610\text{ cm}^{-1}$  plotted versus  $\theta$ , normalized to the intensity recorded at  $\theta = 90^\circ$  ( $\theta$  varying between 0 and  $180^\circ$ , in steps of  $15^\circ$ ).

shown in Fig. 8 were obtained acquiring Raman spectra for increasing  $\theta$  values, going from 0 to  $180^\circ$ , in steps of  $15^\circ$ , and subsequently deriving the  $1610\text{ cm}^{-1}$  band intensity, in each of them, through baseline corrections and peak deconvolution. Finally, these intensities values were normalized to that calculated from the spectrum recorded at  $90^\circ$ , and finally plotted as a function of the angle  $\theta$ . The trend of this function reaches a maximum at  $\theta = 90^\circ$  indicating that when the polymeric slices are perpendicular to the laser polarization, fixed along the laboratory **Y** axis, the director **n** is parallel to the latter. In other words, in the analyzed POLICRYPS grating, the director **n** of E7 molecules in the liquid crystal regions is aligned at right angles to the polymeric layers.

#### 4. Conclusions

Polarized Raman spectroscopy was used to determine the orientation of the E7 liquid crystal molecules in POLICRYPS holographic gratings.

The Raman characterization was first performed on the single components of which the holographic grating is made up: E7 liquid crystal mixture and polymerized NOA-61.

The Raman bands originating from the symmetric stretching of the aromatic rings and from the stretching of the cyano groups were selected as “markers” of the NLC orientation because of the extent of the Raman tensor element associated to the long molecular axis of the biphenyls.

E7 orientation inside the POLICRYPS holographic grating was detected, the NLC director **n** resulted in being perpendicular to the polymeric slices.

In the future, this study will be extended, to support the possible use of POLICRYPS as templates for fabricating metamaterials after nano-doping.

#### Acknowledgments

The research leading to these results has received funding from the European Union’s Seven Framework Programme (FP7/2007-2013) under grant agreement n° 228455.

## References

- [1] Natarajan, L. V., Sutherland, R. L., Tondiglia, V. P., Bunning, T. J., & Adams, W. W. (1996). *J. Nonlinear Opt. Phys. Materials*, 5, 89.
- [2] Caputo, R., Veltri, A., Umeton, C., & Sukhov, A. V. (2004). *J. Opt. Soc. Am. B*, 21, 1939.
- [3] Caputo, R., De Sio, L., Veltri, A., Umeton, C., & Sukhov, A. V. (2006). *J. Display. Tech.*, 2, 38.
- [4] D'Alessandro, A., Donisi, D., De Sio, L., Beccherelli, R., Asquini, R., Caputo, R., & Umeton, C. (2008). *Opt. Expr.*, 16, 9254.
- [5] Caputo, R., De Luca, A., De Sio, L., Pezzi, L., Strangi, G., Umeton, C., Veltri, A., Asquini, R., d'Alessandro, A., Donisi, D., Beccherelli, R., Sukhov, A. V., & Tabiryan, N. V. (2009). *J. Opt. A: Pure Appl. Opt.*, 11, 024017-1.
- [6] NANOGOLD project: "Self-organized Nanomaterials for tailored optical and electrical properties". (Seventh Framework Programme Theme, NMP-2008-2.2-2, Nano-structured metamaterials grant agreement n° 228455).
- [7] Castriota, M., Fasanella, A., Cazzanelli, E., De Sio, L., Caputo, R., & Umeton, C. (2011). *Optics Express*, 19, 10494.
- [8] Caputo, R., De Sio, A. L., Veltri, A., & Umeton, C. (2004). *Optics Letters*, 29, 1261.
- [9] Brás, Ana R.E., Casimiro, T., Caldeira, J., & Aguiar-Ricardo, A. (2005). *J. Chem. Eng. Data*, 50, 1857.
- [10] Dae Seung Kang, Ki-Sun Kwon, Sung Il Kim, Myoung-Seon Gong, Sung Seok A. Seo, Tae Won Noh, & Sang-Woo Joo. (2005). *Applied Spectroscopy*, 59, 1136.
- [11] Sang-Woo Joo, Taek Dong Chung, Won Cheoul Jang, Myoung-Seon Gong, Neri Geum, & Kwan Kim. (2002). *Langmuir*, 18, 8813.
- [12] Merkel, K., Wrzalik, R., & Koch, A. (2001). *Journal of Molecular Structure*, 563-564, 477.
- [13] Nicotera, I., Oliviero, C., Ranieri, G., Spadafora, A., Castriota, M., & Cazzanelli, E. (2002). *J. Chem. Phys.*, 117, 7373.
- [14] Jones, W. J., Thomas, D. K., Thomas, D. W., & Williams, G. (2004). *Journal of Molecular Structure*, 708, 145.
- [15] Astrova, E. W., Perova, T. S., Grudinkin, S. A., Tolmachev, V. A., Pilyugina, Yu.A., Voronkov, V. B., & Vij, J. K. (2005). *Semiconductors*, 39, 759.
- [16] Pinto-Iguanero, B., Olivares-Perez, A., & Fuentes-Tapia, I. (2002). *Optical Materials*, 20, 225.
- [17] Wilderbeek, H. T.A., Goossens, J. (Han) G. P., Bastiaansen, C. W.M., & Broer, D. J. (2002). *Macromolecules*, 35, 8962.
- [18] Cramer, N. B., & Bowman, C. N. (2001). *Journal of Polymer Science: Part A: Polymer Chemistry*, 39, 3311.
- [19] Trey, S. M., Lundström, M., Ståhlberg, D., & Johansson, M. (2009). *Progress in Organic Coatings*, 64, 238.
- [20] Nilsson, C., Simpson, N., Malkoch, M., Johansson, M., & Malmström, E. (2008). *Journal of Polymer Science: Part A: Polymer Chemistry*, 46, 1339.
- [21] Gleeson, H. F., Southern, C. D., Brimicombe, P. D., Goodby, J. W., & Görtz, V. (2010). *Liquid Crystals*, 37, 949.
- [22] Jong Kuk Lim, Ohyun Kwon, Dae Seung Kang, and Sang-Woo Joo. (2006). *Chemical Physics Letters*, 423, 178.
- [23] Jones, W. J., Thomas, D. K., Thomas, D. W., & Williams, G. (2002). *Journal of Molecular Structure*, 614, 75.
- [24] Büyüktanir, E. A., Zhang, K., Gericke, A., & West, J. L. (2008). *Mol. Cryst. Liq. Cryst.*, 487, 39.
- [25] Sanchez-Castillo, A., Osipov, M. A., & Giesselmann, F. (2010). *Physical Review E*, 81, 021707.

*In situ polarized micro-Raman investigation of periodic structures realized in liquid-crystalline composite materials*

M. Castriota, **A. Fasanella**, E.Cazzanelli, L. De Sio, R. Caputo and C. Umeton

*Optics Express*, **19**, 10494 (2011)

# *In situ* polarized micro-Raman investigation of periodic structures realized in liquid-crystalline composite materials

Marco Castriota,\* Angela Fasanella, Enzo Cazzanelli, Luciano De Sio, Roberto Caputo, and Cesare Umeton

LICRYL (Liquid Crystal Laboratory, IPCF-CNR), Center of Excellence CEMIF.CAL and Department of Physics, University of Calabria, 87036 Arcavacata di Rende (CS), Italy

\*marco.castriota@fis.unical.it

**Abstract:** In situ polarized micro-Raman Spectroscopy has been utilized to determine the liquid crystal configuration inside a periodic liquid crystalline composite structure made of polymer slices alternated to films of liquid crystal. Liquid crystal, Norland Optical Adhesive (NOA-61) monomer and its polymerized form have been investigated separately. The main Raman features, used as markers for the molecular orientation estimation, have been identified. In situ polarized Raman spectra indicate that the orientation of the liquid crystal director inside the structure is perpendicular to its polymeric slices. Results show the usefulness of in situ polarized micro-Raman spectroscopy to investigate liquid crystalline composite structures.

©2011 Optical Society of America

**OCIS codes:** (050.1950) Diffraction gratings; (160.3710) Liquid crystals; (160.5470) Polymers; (300.6450) Spectroscopy, Raman.

---

## References and links

1. L. V. Natarajan, R. L. Sutherland, V. P. Tondiglia, T. J. Bunning, and W. W. Adams, "Electro-optical switching characteristics of volume holograms in polymer dispersed liquid crystals," *J. Nonlinear Opt. Phys. Mater.* **5**(1), 89–98 (1996).
2. A. Veltri, R. Caputo, C. Umeton, and A. V. Sukhov, "Model for the photoinduced formation of diffraction gratings in liquid-crystalline composite materials," *Appl. Phys. Lett.* **84**, 3492–3494 (2004).
3. R. Caputo, L. De Sio, A. Veltri, C. Umeton, and A. V. Sukhov, "POLICRYPS switchable holographic grating: a promising grating electro-optical pixel for high resolution display application," *J. Display Technol.* **2**(1), 38–51 (2006).
4. A. d'Alessandro, D. Donisi, L. De Sio, R. Beccherelli, R. Asquini, R. Caputo, and C. Umeton, "Tunable integrated optical filter made of a glass ion-exchanged waveguide and an electro-optic composite holographic grating," *Opt. Express* **16**(13), 9254–9260 (2008).
5. R. Caputo, A. De Luca, L. De Sio, L. Pezzi, G. Strangi, C. Umeton, A. Veltri, R. Asquini, A. d'Alessandro, D. Donisi, R. Beccherelli, A. V. Sukhov, and N. V. Tabiryan, "POLICRYPS: a liquid crystal composed nano/microstructure with a wide range of optical and electro-optical applications," *J. Opt. A, Pure Appl. Opt.* **11**(2), 024017 (2009).
6. NANOGOLD project: "Self-organized Nanomaterials for tailored optical and electrical properties" (Seventh Framework Programme Theme, NMP-2008–2.2–2, Nano-structured metamaterials grant agreement no. 228455).
7. R. Caputo, L. De Sio, A. Veltri, C. Umeton, and A. V. Sukhov, "Development of a new kind of switchable holographic grating made of liquid-crystal films separated by slices of polymeric material," *Opt. Lett.* **29**(11), 1261–1263 (2004).
8. L. De Sio, R. Caputo, A. De Luca, A. Veltri, C. Umeton, and A. V. Sukhov, "In situ optical control and stabilization of the curing process of holographic gratings with a nematic film-polymer-slice sequence structure," *Appl. Opt.* **45**(16), 3721–3727 (2006).
9. A. R. E. Brás, T. Casimiro, J. Caldeira, and A. Aguiar-Ricardo, "Solubility of the nematic liquid crystal E7 in supercritical carbon dioxide," *J. Chem. Eng. Data* **50**(6), 1857–1860 (2005).
10. S.-W. Joo, T. D. Chung, W. C. Jang, M.-S. Gong, N. Geum, and K. Kim, "Surface-enhanced Raman scattering of 4-Cyanobiphenyl on gold and silver nanoparticle surfaces," *Langmuir* **18**(23), 8813–8816 (2002).
11. I. Nicotera, C. Oliviero, G. Ranieri, A. Spadafora, M. Castriota, and E. Cazzanelli, "Temperature evolution of thermoreversible polymer gel electrolytes LiClO<sub>4</sub>/ethylene carbonate/poly(acrylonitrile)," *J. Chem. Phys.* **117**(15), 7373–7380 (2002).
12. W. J. Jones, D. K. Thomas, D. W. Thomas, and G. Williams, "On the determination of order parameters for homogeneous and twisted nematic liquid crystals from Raman spectroscopy," *J. Mol. Struct.* **708**(1-3), 145–163 (2004).

13. E. W. Astrova, T. S. Perova, S. A. Grudinkin, V. A. Tolmachev, Yu. A. Pilyugina, V. B. Voronkov, and J. K. Vij, "Polarized infrared and Raman spectroscopic studies of the liquid crystal E7 alignment in composites based on grooved silicon," *Semiconductors* **39**(7), 759–767 (2005).
14. B. Pinto-Iguanero, A. Olivares-Perez, and I. Fuentes-Tapia, "Holographic material film composed by Norland Noa 65<sup>®</sup> adhesive," *Opt. Mater.* **20**(3), 225–232 (2002).
15. H. T. A. Wilderbeek, J. H. G. P. Goossens, C. W. M. Bastiaansen, and D. J. Broer, "Photoinitiated bulk polymerization of liquid crystalline thiolene monomers," *Macromolecules* **35**(24), 8962–8968 (2002).
16. M. Claudino, M. Johansson, and M. Jonsson, "Thiol-ene coupling of 1,2-disubstituted alkene monomers: the kinetic effect of cis/trans-isomer structures," *Eur. Polym. J.* **46**(12), 2321–2332 (2010).
17. H. F. Gleeson, C. D. Southern, P. D. Brimicombe, J. W. Goodby, and V. Görtz, "Optical measurements of orientational order in uniaxial and biaxial nematic liquid crystals," *Liq. Cryst.* **37**(6), 949–959 (2010).
18. J. K. Lim, O. Kwon, D. S. Kang, and S.-W. Joo, "Raman spectroscopy study and density functional theory calculations of the nematic liquid crystal 4-n-pentyl-4'-cyanobiphenyl under an electric field," *Chem. Phys. Lett.* **423**(1-3), 178–182 (2006).
19. W. J. Jones, D. K. Thomas, D. W. Thomas, and G. Williams, "Raman scattering studies of homogeneous and twisted-nematic liquid crystal cells and the determination of  $\langle P_2 \rangle$  and  $\langle P_4 \rangle$  order parameters," *J. Mol. Struct.* **614**(1-3), 75–85 (2002).
20. E. A. Büyüktanir, K. Zhang, A. Gericke, and J. L. West, "Raman imaging of nematic and smectic liquid crystals," *Mol. Cryst. Liq. Cryst. (Phila. Pa.)* **487**, 39–51 (2008).
21. A. Sanchez-Castillo, M. A. Osipov, and F. Giesselmann, "Orientational order parameters in liquid crystals: a comparative study of x-ray diffraction and polarized Raman spectroscopy results," *Phys. Rev. E Stat. Nonlin. Soft Matter Phys.* **81**(2), 021707 (2010).
22. R. Caputo, I. Trebisacce, L. De Sio, and C. Umeton, "Jones matrix analysis of dichroic phase retarders realized in soft matter composite materials," *Opt. Express* **18**(6), 5776–5784 (2010).
23. R. L. Sutherland, "Polarization and switching properties of holographic polymer-dispersed liquid-crystal gratings. I. Theoretical model," *J. Opt. Soc. Am. B* **19**(12), 2995–3003 (2002).
24. R. L. Sutherland, L. V. Natarajan, V. P. Tondiglia, S. Chandra, C. K. Shepherd, D. M. Brandelik, S. A. Siwecki, and T. J. Bunning, "Polarization and switching properties of holographic polymer-dispersed liquid-crystal gratings. II. Experimental investigations," *J. Opt. Soc. Am. B* **19**(12), 3004–3012 (2002).
25. K. K. Vardanyan, J. Qi, J. N. Eakin, M. De Sarkar, and G. P. Crawford, "Polymer scaffolding model for holographic polymer-dispersed liquid crystals," *Appl. Phys. Lett.* **81**(25), 4736–4738 (2002).

## 1. Introduction

Switchable holographic structures are promising for a wide range of applications such as imaging, information processing and diffractive optics [1]. Liquid crystals (LCs) are useful for the fabrication of these devices thanks to their capability to change orientational order under the influence of external stimuli. In the last years, great attention has been devoted to periodic liquid crystalline composite materials like POLICRYPS (acronym of POLYmer LIquid CRYstal Polymer Slices) (Fig. 1(a)), as novel structures with a wide range of optical and electro-optical applications [2–5]. At present, there is the possibility of exploiting the POLICRYPS as a template to be doped with metal nano-particles for the realization of controllable metamaterials [6].

In fact, possible electro-optical applications of POLICRYPS are due to the uniform and regular steady state alignment of the director  $\mathbf{n}$  of the Nematic Liquid Crystal (NLC) films inside the structure; nevertheless, at our knowledge, there is no direct estimation of this orientation, at microscopic level, like the one shown in the present work, obtained by using *in situ* polarized Raman spectroscopy.

## 2. Experimental

The investigated POLICRYPS has been realized by using E7 NLC (supplied by Merk) and the monomer NOA-61 (Norland Optical Adhesive). The used standard fabrication procedure is described elsewhere [7,8]. Spectroscopic investigations were performed by a Raman microprobe Jobin-Yvon Labram (spectral resolution  $\sim 2 \text{ cm}^{-1}$ ) equipped with a CCD detector and a He-Ne laser ( $\lambda = 632.8 \text{ nm}$  emission wavelength).

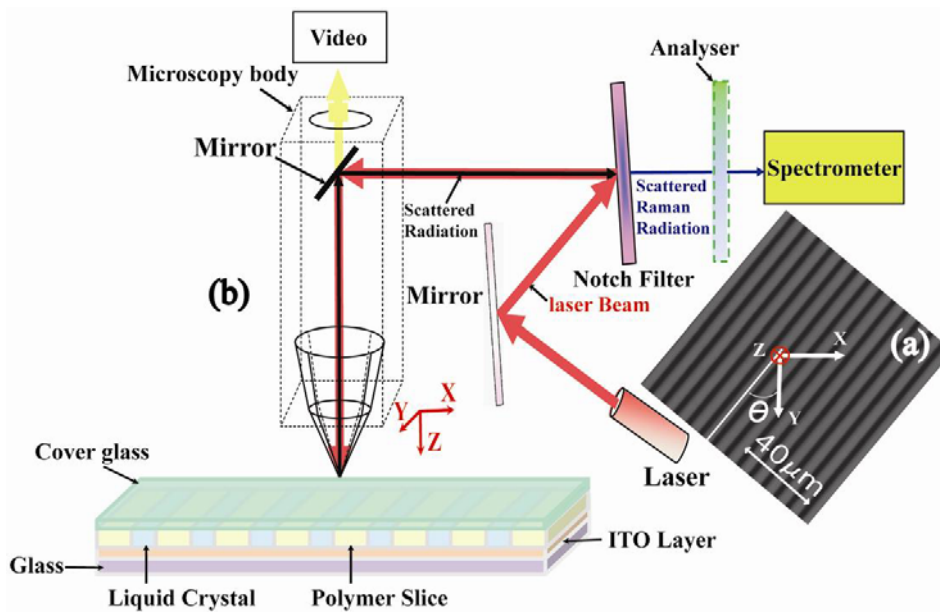


Fig. 1. (a) SEM image of a POLICRYPS structure and reference axes; (b) experimental set-up used to collect the polarized Raman spectra and reference axes.  $\theta$  is the angle between the direction of polarization of the incident radiation ( $Y$  axis of the laboratory reference system) and the polymer slice of the POLICRYPS structure.

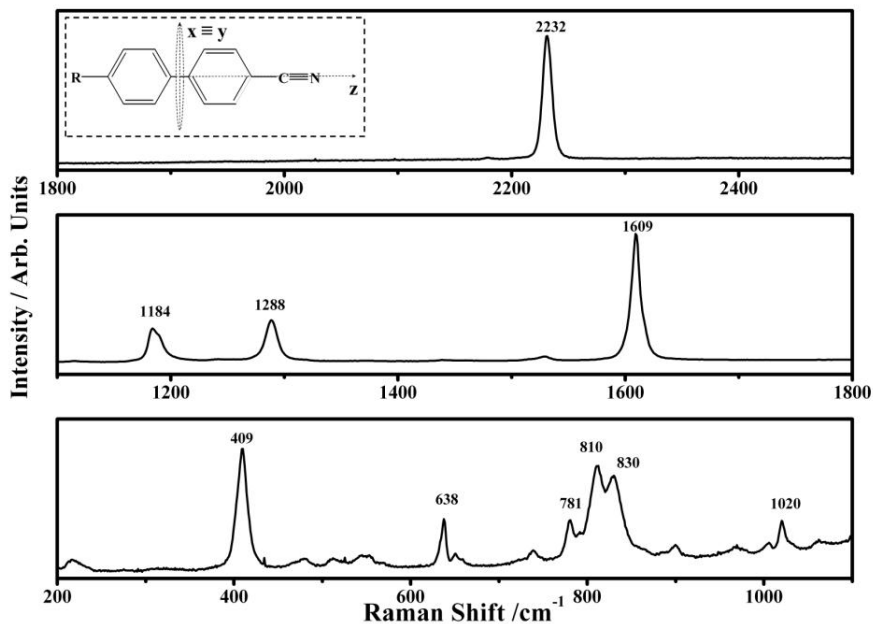


Fig. 2. Representative Raman spectra collected on randomly aligned NLC E7 in the range between 200 and 1100  $\text{cm}^{-1}$  (on the bottom), 1100 and 1800  $\text{cm}^{-1}$  (on the middle) and 1800 and 2500  $\text{cm}^{-1}$  (on the top). (For a better presentation, the graphs are shown with different intensity scales).

A 50x Mplan Olympus objective (Numerical Aperture 0.90) was used, focusing the laser spot to 2-3  $\mu\text{m}$  of diameter. The sample grating has been written with a large pitch (6  $\mu\text{m}$ ), while a very thin glass (0.1 mm thick) has been used for the upper cell window. *In situ* polarized Raman spectra have been collected by using the experimental set-up shown in Fig. 1(b). The laser source is linearly polarized along the  $Y$  axis of the reference system (in this work, small letters  $x,y,z$  are adopted for the molecular frame, while capital  $X,Y,Z$  indicate the laboratory axes). The analyzer lets only the  $Y$  polarized component of the scattered radiation reach the instrument grating; in this way, only the  $YY$  component of the polarizability tensor is detected. The sample is placed on a goniometric rotation stage (Thorlabs) and, at the beginning, it is oriented with the polymeric slices parallel to the polarization direction of the incident light. Spectra have been collected for values of the angle  $\theta$ , (formed by the light polarization direction and the polymeric slices, see Fig. 1(a)) which vary from  $0^\circ$  up to  $180^\circ$ , with steps of  $15^\circ$ . The Raman spectra shown in this paper are representative of a wider Raman investigation performed along many liquid crystal slices.

### 3. Results and discussion

The E7 NLC is a multicomponent nematic mixture made by substituted 4-cyanobiphenyls [9] (structure formula in the inset of Fig. 2). The related Raman spectra, collected on a randomly aligned NLC sample, are shown in Fig. 2. The higher intensity main Raman bands are assigned to the ring deformations; assignment of such modes has been performed by taking into account that biphenyl belongs to the  $C_{2v}$  point group [10]; therefore, the skeletal vibrational modes of the biphenyl can be described in just four symmetry species. In particular, the bands at 1020 ( $\nu_{18a}$ ), 1184 ( $\nu_{9a}$ ), 1529 ( $\nu_{19a}$ ) and 1609 ( $\nu_{8a}$ )  $\text{cm}^{-1}$  are described by the  $A_1$  symmetry representation; the mode with symmetry  $A_2$  falls at 781  $\text{cm}^{-1}$  ( $\nu_{10a}$ ) while the peaks at 810 ( $\nu_4$ ) and 830 ( $\nu_{11}$ )  $\text{cm}^{-1}$  have  $B_1$  symmetry and the modes with  $B_2$  symmetry [10] are at 638 ( $\nu_{6b}$ ) and 1288 ( $\nu_3$ )  $\text{cm}^{-1}$ . In addition, vibrations which fall at 1020 ( $\nu_{18a}$ ), 1184 ( $\nu_{9a}$ ), 1529 ( $\nu_{19a}$ ) and 1609 ( $\nu_{8a}$ )  $\text{cm}^{-1}$  occur in the molecular plane, while all other vibrations occur out of the molecular plane. Modes at 409 ( $\gamma$  deformation) and 2232 (symmetric stretching)  $\text{cm}^{-1}$  are assigned to the CN group [10,11].

The components of the optical polarizability tensor for molecules which belong to point group  $C_{2v}$  are, in principle, all different. However, due to the rotational isotropy around the long molecular axis ( $z$ -axis), the optical polarizability tensor, for the E7 NLC, can be represented by an oblate ellipsoid with  $\alpha_{zz} > \alpha_{yy} = \alpha_{xx}$ , where  $\alpha_{xx}$ ,  $\alpha_{yy}$  and  $\alpha_{zz}$  indicate the components of the polarizability tensor in the molecular frame. The symmetric stretching of the aromatic rings of the biphenyl molecules and the stretching of the CN groups induce the major change of polarizability along the long molecular axis of biphenyl molecules. Therefore, if there is a preferential orientation of the director  $\mathbf{n}$  of the NLC inside the POLICRYPS, this can be evidenced by following the behaviour of the intensities of the Raman bands, related to the above mentioned stretchings, as a function of the angle  $\theta$ : the  $\theta$  value where the maximum intensity of those Raman bands is obtained, clearly identifies the direction of  $\mathbf{n}$  [12,13].

NOA-61 has been investigated before and after the polymerization process (Figs. 3(a), 3(b)). It is worth underlining that the exact composition of NOA-61 is still unknown; however it should be a mix of a mercapto-ester with acrylate monomer as described elsewhere [14]. In Fig. 3(a), reporting spectra collected on NOA-61 monomer, we notice the characteristic features of the thiol groups (S-H) at about 2582  $\text{cm}^{-1}$ , vinyl group (C = C symmetric stretching, non conjugated) at 1650  $\text{cm}^{-1}$ , and the carbonyl (C = O) of the carboxyl group COOR [15] at 1746 and 1764  $\text{cm}^{-1}$ . At 1604  $\text{cm}^{-1}$  we find the aromatic ring vibration, evidently present on the R group (unknown part) of the molecule [15].

The band at 677  $\text{cm}^{-1}$  is assigned to the C-S bond, while the peak at 1297  $\text{cm}^{-1}$  and the bands in the region between 1400 and 1500  $\text{cm}^{-1}$  are assigned to the  $\text{CH}_3$  bending; those in the range between 2900 and 3100  $\text{cm}^{-1}$  are assigned to the C-H stretching [16]. Spectra of polymerized NOA-61 (Fig. 3(b)) show the absence of the band at 2582  $\text{cm}^{-1}$  and,

simultaneously, a strong reduction of the band at  $1650\text{ cm}^{-1}$ , indicating that the curing process involves a reaction between the thiol and the vinyl groups present in the monomer [15].

In Fig. 4, the micro-Raman un-polarized spectra of the POLICRYPS (polymerized NOA-61 and E7), representative of all the spectra collected on the whole sample, are shown. The liquid crystal characteristic bands at  $1609\text{ cm}^{-1}$  and  $2232\text{ cm}^{-1}$  and the bands at  $1746$  and  $1764\text{ cm}^{-1}$  of the carboxyl group of the NOA-61 are still well evident. For this reason, these bands are used as markers in order to evaluate the presence and the contribution of each component to the total Raman spectra.

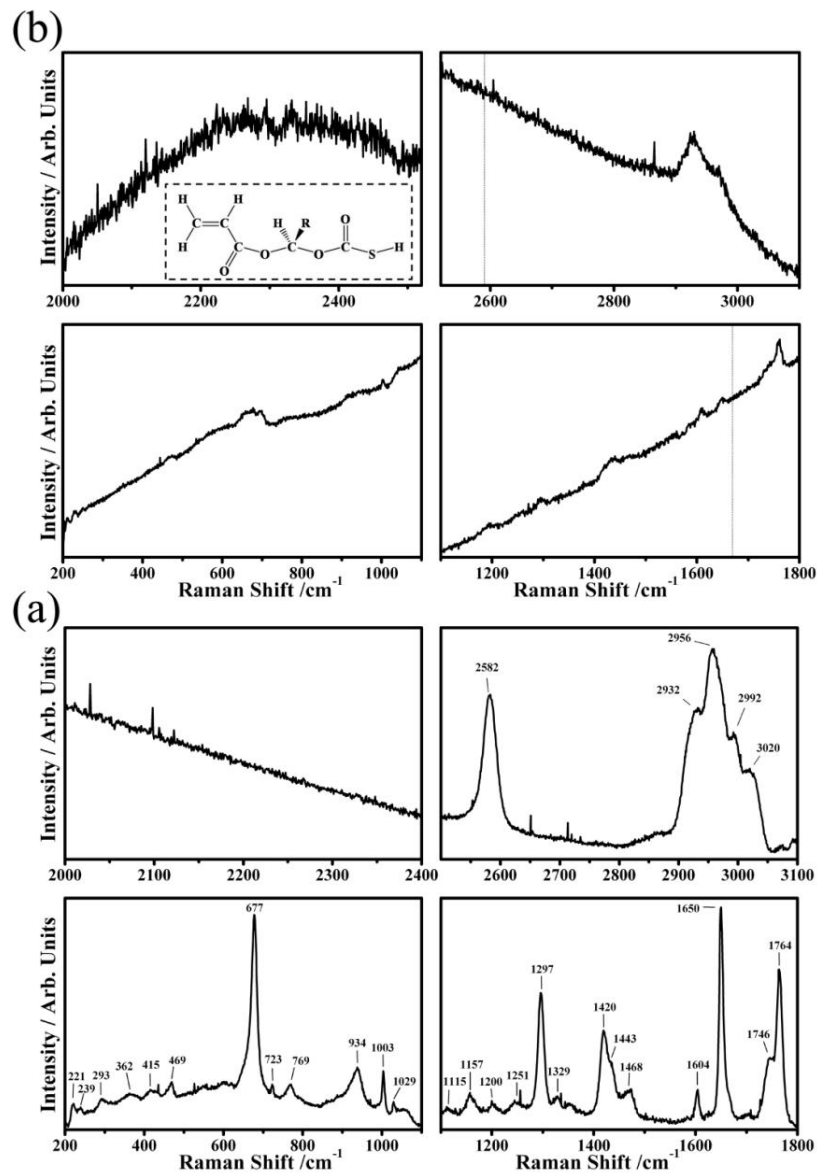


Fig. 3. Representative Raman spectra collected on Norland Optical Adhesive NOA-61 monomer (a) and (b) polymerized. (For a better presentation, the graphs are shown with different intensity scales).



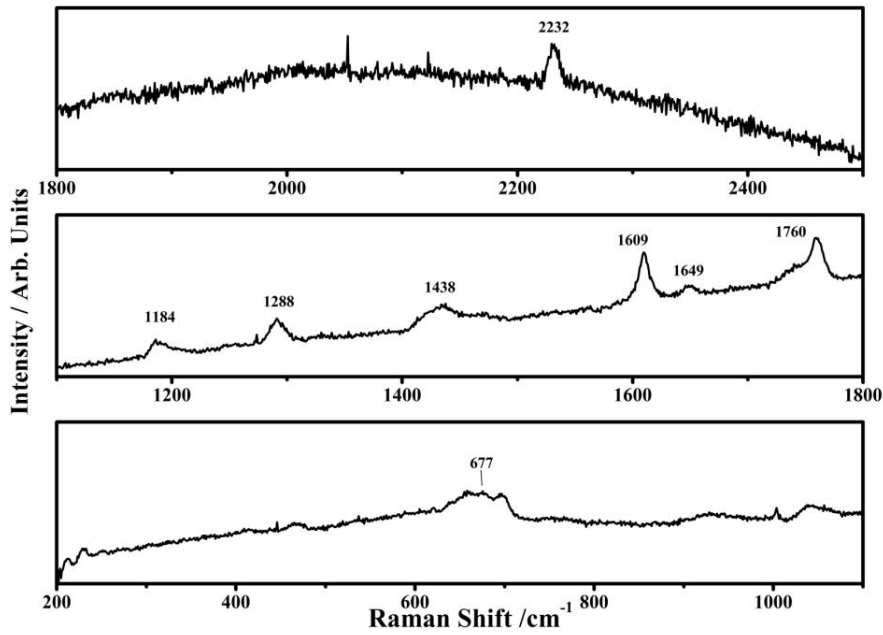


Fig. 4. Representative un-polarized Raman spectra collected on the POLICRYPS sample in the range between 200 and 1100  $\text{cm}^{-1}$  (on the bottom), 1100 and 1800  $\text{cm}^{-1}$  (on the middle) and 1800 and 2500  $\text{cm}^{-1}$  (on the top). (For a better presentation, the graphs are shown with different intensity scales).

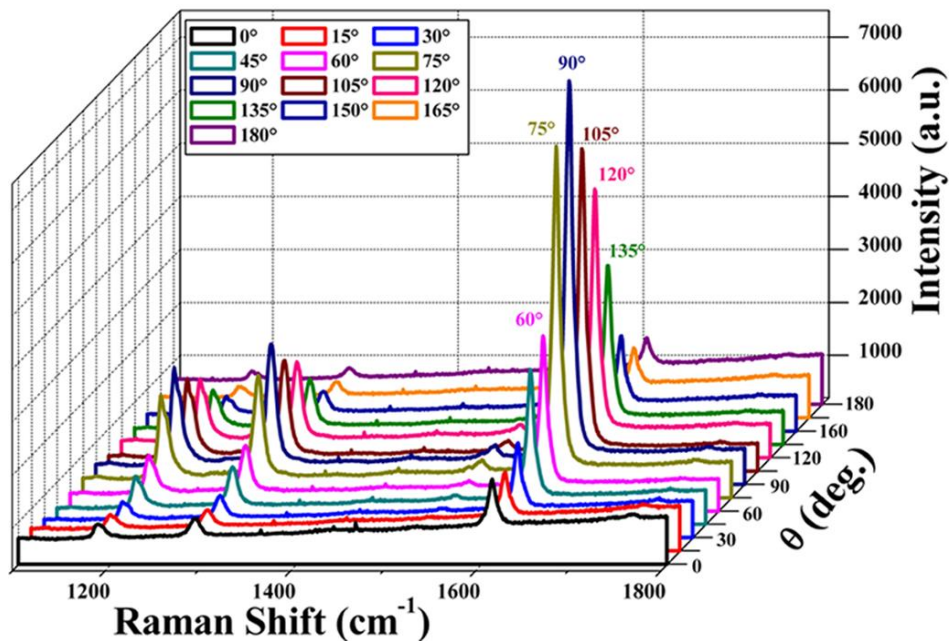


Fig. 5. Representative Polarized Raman spectra collected on the liquid crystal slices of the POLICRYPS grating at different  $\theta$  values between  $0^\circ$  and  $180^\circ$ .

*In situ* polarized Raman spectra have been collected on the NLC films (confined between the polymer slices of the POLICRYPS, see Fig. 1) as a function of the angle  $\theta$  in the range between  $0^\circ$  and  $180^\circ$  (Fig. 5). Intensities of the bands at 1184, 1288, 1610 and  $2233\text{ cm}^{-1}$  (respectively assigned to the aromatic C-H in plane deformation, C-C stretch of biphenyl bond and C = C stretching of biphenyl rings) increase with  $\theta$ , to reach the maximum value at  $\theta = 90^\circ$ ; then, a decrease occurs when  $\theta$  goes from  $90^\circ$  to  $180^\circ$ .

This behavior clearly evidences a preferential orientation of the NLC director within the POLICRYPS structure [12,13,17–21]: at  $\theta = 90^\circ$ , the Raman intensities show a maximum because the director  $\mathbf{n}$  is parallel to the polarization direction of the laser light (the molecular  $\mathbf{z}$  axis corresponds to laboratory  $\mathbf{Y}$  axis). Since, in our geometry, this corresponds to the polymeric slices being perpendicular to the polarization direction of light, it can be argued that POLICRYPS gratings are made of polymer slices regularly alternated to films of Nematic Liquid Crystal molecules whose average orientation (director  $\mathbf{n}$ ) is perpendicular to the polymeric slices. We underline that this director configuration can be directly correlated to the birefringence of the sample: in the past [22], a similar result has been demonstrated by measuring the polarization dependence of a POLICRYPS diffraction grating efficiency, which is proportional to the birefringence value. In fact, as shown by Sutherland et al. [23–25], this birefringence also gives a unique signature to the electro-optical properties of the structure as a function of the polarization direction of the probe beam. However, while birefringence measurements yield macroscopic indications only, the chemical sensitivity of Raman spectroscopy allows a detailed microscopic view of the director configuration; a Raman mapping of a large area of the sample could be conveniently used to deduce its birefringence distribution. It is our intention to perform new experiments in this direction.

#### 4. Conclusions

*In situ* Polarized Raman spectroscopy has been exploited to investigate the orientation of liquid crystal molecules in a POLICRYPS holographic grating. Raman spectra have been collected both on the NLC and NOA-61 (monomer and polymerized forms). Bands due to the symmetric stretching of the aromatic rings of the biphenyl molecules and the stretching of the CN groups have been selected as “markers” of the NLC orientation, since they occur along the long molecular axis of biphenyl molecules ( $\mathbf{z}$ -axis): the orientation of the NLC director  $\mathbf{n}$  within the POLICRYPS structure turns out to be perpendicular to its polymeric slices.

Results represent a contribute for the determination of the orientational order parameters ( $\langle P_2 \rangle$  and  $\langle P_4 \rangle$ ) in a POLICRYPS system. Moreover, they might allow to find an exact relation between the director orientation and the FWHM of the curve obtained by plotting the intensity peak at  $1610\text{ cm}^{-1}$  as a function of the angle  $\theta$ . In future, different Raman analysis (Raman mapping of large area sample) are planned in order to investigate the liquid crystal birefringence distribution in POLICRYPS systems.

Above studies will support the future work concerned with the use of POLICRYPS structures as a template to be nano-doped for fabricating metamaterials.

#### Acknowledgments

The research leading to these results has received funding from the European Union’s Seven Framework Programme (FP7/2007-2013) under grant agreement no. 228455 [NANOGOLD].

*Raman scattering enhancement associated to sodium oxide formation after thermal treatment of glass substrates*

M. Castriota, E. Cazzanelli, **A. Fasanella**, R.G. Agostino, T. Caruso and A. Policicchio

*AIP Conference Proceedings* **1267**, 998 (2010)

## Raman Scattering Enhancement Associated to Sodium Oxide Formation after Thermal Treatment of Glass Substrates

M. Castriota, E. Cazzanelli, A. Fasanella, R. G. Agostino, T. Caruso et al.

Citation: *AIP Conf. Proc.* **1267**, 998 (2010); doi: 10.1063/1.3482935

View online: <http://dx.doi.org/10.1063/1.3482935>

View Table of Contents: <http://proceedings.aip.org/dbt/dbt.jsp?KEY=APCPCS&Volume=1267&Issue=1>

Published by the [American Institute of Physics](#).

---

### Related Articles

Dynamic mechanical analysis in La-based bulk metallic glasses: Secondary ( $\beta$ ) and main ( $\alpha$ ) relaxations  
*J. Appl. Phys.* **112**, 083528 (2012)

Vapor-deposited  $\alpha,\alpha,\beta$ -tris-naphthylbenzene glasses with low heat capacity and high kinetic stability  
*J. Chem. Phys.* **137**, 154502 (2012)

Phase change behaviors of Zn-doped Ge<sub>2</sub>Sb<sub>2</sub>Te<sub>5</sub> films  
*Appl. Phys. Lett.* **101**, 051906 (2012)

Effects of rare-earth doping on femtosecond laser waveguide writing in zinc polyphosphate glass  
*J. Appl. Phys.* **112**, 023109 (2012)

Enhancement of glass-forming ability of Fe-based bulk metallic glasses with high saturation magnetic flux density  
*AIP Advances* **2**, 022169 (2012)

---

### Additional information on AIP Conf. Proc.

Journal Homepage: <http://proceedings.aip.org/>

Journal Information: [http://proceedings.aip.org/about/about\\_the\\_proceedings](http://proceedings.aip.org/about/about_the_proceedings)

Top downloads: [http://proceedings.aip.org/dbt/most\\_downloaded.jsp?KEY=APCPCS](http://proceedings.aip.org/dbt/most_downloaded.jsp?KEY=APCPCS)

Information for Authors: [http://proceedings.aip.org/authors/information\\_for\\_authors](http://proceedings.aip.org/authors/information_for_authors)

### ADVERTISEMENT



AIP Advances

*Submit Now*

Explore AIP's new  
open-access journal

- Article-level metrics now available
- Join the conversation! Rate & comment on articles

# Raman Scattering Enhancement Associated to Sodium Oxide Formation after Thermal Treatment of Glass Substrates.

M. Castriota, E. Cazzanelli, A. Fasanella, R.G. Agostino,  
T. Caruso and A. Policicchio

*INFM-LICRYL Laboratory and CEMIF.CAL., Dipartimento di Fisica, Università della Calabria, Ponte P. Bucci – Cubo 31C, I-87036, Arcavacata di Rende (CS), Italy*

An anomalous enhancement of the Raman scattering can be obtained without SERS-active noble metals components [1] or proper periodic structures [2], for tungsten oxide ( $\text{WO}_3$ ) thin films, when deposited on indium tin oxide (ITO) coated glasses, which underwent a pre-deposition annealing at 700 °C in air.

$\text{WO}_3$  was prepared via a sol-gel route [3,4]. In a first set of samples the mother solution was deposited by a spin coater (SC10 CaLCTec S.r.l.) on the as-received substrates, commercial ITO-coated glasses (Balzers); later these samples were subjected to different thermal treatments, for 1 hour in air. A second set of samples was prepared using a ‘two-step’ annealing procedure: i) pre-deposition annealing at 700 °C for 1 h of the ITO-coated glass substrates; ii) after the deposition, the samples were annealed at 300 °C, to dehydrate  $\text{WO}_3$  layer.

Micro-Raman measurements were performed by a Jobin–Yvon Labram apparatus using a 633 nm He–Ne laser. In the first set of samples, very weak Raman spectra, typical of amorphous  $\text{WO}_3$  [5-7], are observed after annealing below 500 °C, spectra of crystalline  $\text{WO}_3$  [6-9] appear for higher temperature annealings. In the samples undergoing the two-step annealing procedure, the pre-deposition treatment on the ITO/glass substrates induces the formation of micrometer sized ‘islands’ on the film surface (see Fig.1). Raman spectra, collected separately from the flat surface around the islands (Zone A), and from the top of an island (Zone B), are shown in Fig. 2, for increasing laser powers (various filters). Spectra from the islands appear much more intense of those from the surrounding surface, suggesting that materials of the ‘islands’, mainly sodium oxide due to high temperature reaction, induce an appreciable Raman scattering enhancement for the spectra of the  $\text{WO}_3$  overlayer, amorphous  $\text{WO}_3$  [5-7] at low laser powers, crystalline [7-9] at the highest power.

Photoelectron surface spectra on differently annealed samples of the  $\text{WO}_3$ /ITO/glass (with ITO substrate not pre-annealed) and ITO/glass substrates, show the following photoelectrons shallow cores peaks, all associated to oxides: In 4d states at 18.6 eV in the binding energy scale, O 2s as a broad peak at 23 eV, Sn 4d at 26 eV, the W 4f<sub>5/2,7/2</sub> doublet for  $\text{WO}_3$  at 38.2 and 36.0 eV, respectively, and the Na 2p at 31.3 eV. In the ITO/glass samples, the shallow core levels due to In, Sn and O are observed for all the annealing treatments, with comparable intensities. The Na 2p photoemission peak, instead, results appreciable after

annealing at 200 °C and its intensity strongly increases after the 700 °C annealing. In the WO<sub>3</sub>/ITO/glass samples (with ITO not pre-annealed) the photoemission signal (beside the valence band) are due to shallow cores of W, In, O and Sn, for annealing up to 500 °C. In and Sn signal are due to their high photoelectron cross section and also because the WO<sub>3</sub> film shows some fractures, allowing the detection of photoelectrons coming from deeper layers. After the 700 °C annealing an increase of the In 4d peak, and the rise of a strong Na 2p peak are observed. These data seem to rule out a metallic colloid formation, responsible for Raman enhancement even in the case of Na colloidal particles [10]. According to the literature, the Na chemical shift here observed (Na 2p peak around 31.3 eV) is compatible with a Na<sub>2</sub>O oxidation state in all the samples [11].

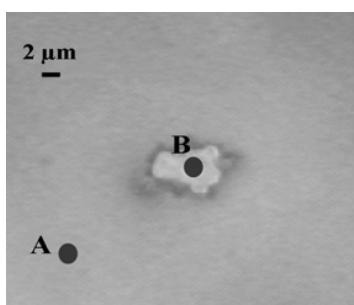


FIGURE 1: micrograph of a WO<sub>3</sub> deposit over a sodium oxide “island” .

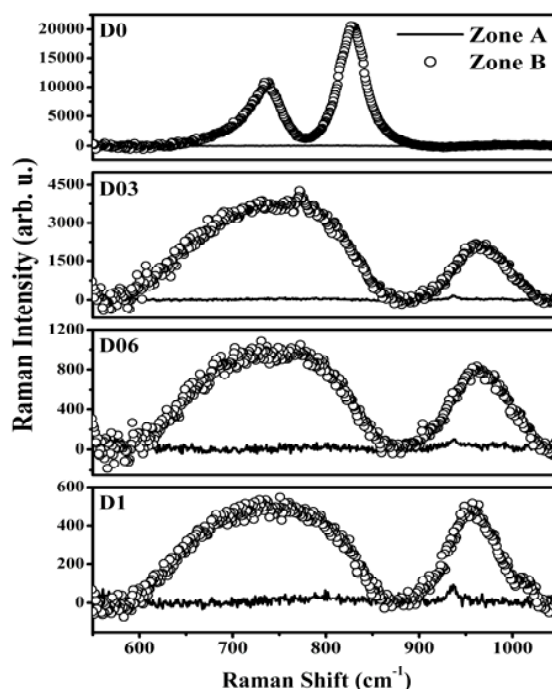


FIGURE 2: Raman spectra from WO<sub>3</sub> deposited on the island and far from the island shown in Fig.1. The optical density of the used filters are indicated inside.

## REFERENCES

1. R.P. Van Duyne, J.C. Hultheen, D.A. Treichel, *J. Chem. Phys.* 99 (1993) 2101
2. C. Zhang, A.I. Smirnov, D. Hahn, H. Grebel, *Chem. Phys. Lett.* 440 (2007) 239.
3. M. Castriota, S. Marino, C. Versace, G. Strangi, N. Scaramuzza, E. Cazzanelli, *Mol. Cryst. Liq. Cryst.* 429 (2005) 237
4. J. Livage, D. Ganguli, *Sol. Energy Mater. Sol. Cells* 68 (2001) 365.
5. K. Bange, *Sol. Energy Mater. Sol. Cells* 58 (1999) 1. 272
6. E. Cazzanelli, L. Papalino, A. Pennisi, F. Simone, *Electrochim. Acta* 46 (2001)1937
7. E. Cazzanelli, S. Capoleoni, L. Papalino, *Philos. Mag. B* 82 (2002) 453
8. A. Kuzmin, J. Purans, E. Cazzanelli, C. Vinegoni, G. Mariotto, *J. Appl. Phys.* 84(1998) 5515
9. E. Cazzanelli, G. Mariotto, C. Vinegoni, A. Kuzmin, J. Purans, *Ionics* 5–6 (1999)335
10. E. Rzepka, S. Lefrant, L. Taurel, *Solid State Commun.* 30 (1979) 801.
11. A. Barrie, F.J. Street, *J. Electron. Spectrosc. Relat. Phenom.* 7 (1975) 1

*Micro-spectroscopic Raman investigation on the canvas oil painting “Rebecca at the well”, of Neapolitan anonymous*

E. Platania, E. Cazzanelli, G. De Santo, **A. Fasanella** and M. Castriota

*Journal of Raman Spectroscopy*, **43**, 1694 (2012)

# Micro-spectroscopic Raman investigation on the canvas oil painting 'Rebecca at the well' of Neapolitan anonymous<sup>†</sup>

E. Cazzanelli,<sup>a\*</sup> E. Platania,<sup>a,b</sup> G. De Santo,<sup>a</sup> A. Fasanella<sup>a</sup> and M. Castriota<sup>a</sup>

In this work, a micro-Raman spectroscopic investigation was carried out in order to identify the pigments used in the canvas oil painting 'Rebecca at the well', which is preserved in MAON museum in Rende, southern Italy. The artwork's history is unknown, and no scientific investigation was performed on it before. Art historians believe that the painting was created in the XVIII century by an artist of the Neapolitan school. Raman spectra were collected by a Jobin Yvon micro-Raman LABRAM apparatus, with a He-Ne laser (632.8 nm) as excitation source. The main original pigments were identified and modern pigments like yellow-orange chrome and phthalocyanine were also found, providing important information about the restoration works and the painting's history. Copyright © 2012 John Wiley & Sons, Ltd.

**Keywords:** micro-Raman spectroscopy; mineral pigments; yellow-orange chrome; phthalocyanine; oil painting

## Introduction

Nowadays, optical spectroscopy, and in particular Raman spectroscopy, represents one of the most powerful and useful investigation tools in many scientific areas of interest.<sup>[1]</sup> With regard to the artistic field, the technique's application concerned different artworks and art materials: medieval manuscripts,<sup>[2,3]</sup> majolica,<sup>[4]</sup> ancient glasses,<sup>[5]</sup> ancient roman mortars,<sup>[6]</sup> frescoes,<sup>[7]</sup> canvas paintings,<sup>[8]</sup> pigments, varnishes and many others. Raman Spectroscopy presents several advantages: non-destructive analysis of materials, no chemical-mechanical preparation of desiccation necessary for specimens prior to analysis, specific recognition of biomolecular spectral marker for the identification of genuine and fake objects, high spatial resolution, analysis of organic and inorganic materials, execution of standard and *in situ* analysis.<sup>[9]</sup> In this work, Raman spectroscopy was used to investigate the pigments of the canvas oil painting 'Rebecca at the well', attributed to a Neapolitan anonymous, which is presently preserved in MAON museum of Rende (Cosenza), Italy, within the collection 'Luigi Ladaga'. This painting is a beautiful example of baroque naturalism, depicting an episode from the biblical history, also quite represented in other paintings: the old faithful servant Eliezer was sent by Abraham in his original birthplace, Upper Mesopotamia, to search a wife for the son Isaac; when arriving, very tired, to the well outside of the city of destination, he promised to ask as wife for Isaac the first girl offering to him some water. In fact, he met the young Rebecca, which, by chance, was the nephew of Nacor, brother of Abraham (Genesis 24, 17–21).

The difficulty of the investigation was due to the absence of historical and scientific documents about the painting: it is the first time that scientific analyses were performed on this artwork. Taking into account stylistic and formal studies, art historians ascribe the painting to a Neapolitan artist of the XVIII century, but many stylistic details can also support the hypothesis of a more ancient origin, going back to the XVII century. The information provided by Raman spectroscopy constitutes a significant contribute to the knowledge, not only of the pigments composition, but also of the artwork's history.

## Experimental

The painting object of the present investigation has been previously photographed in two manners: natural light and grazing light. A widespread craquelure phenomenon has been shown by the grazing light method on the paint layer. In particular, this method allows to emphasize the texture of the painting surface.

Raman spectra were recorded with a Jobin Yvon LABRAM spectrometer, interfaced with a Olympus microscope, equipped with a He-Ne (632.8 nm) laser as excitation source and a CCD detector cooled by a Peltier device. Different Olympus objectives (20×, 50× and 100×) were used to visually explore the painting and to collect the spectra.

In this work, only the spectra obtained with the 50× objective (focal length of 15 mm) are shown, being the same as those obtained with the other objectives. The spectral resolution, by using the 1800 grooves/mm grating, was estimated to be better than about 2 cm<sup>-1</sup>. The illuminated spot size was about 5 μm in diameter. Neutral filters with different optical densities, 0.3, 0.6, 1, 2, 3 and 4, were available in order to reduce the impinging laser power and avoid damages to the painting and pigment modification. Each micro-Raman spectrum was collected in 20 s and three accumulations.

\* Correspondence to: Enzo Cazzanelli, Dipartimento di Fisica, Università della Calabria, Cubo 31C, Ponte P. Bucci, 87036-Arcavacata di Rende, Cosenza, Italy. E-mail: enzo.cazzanelli@fis.unical.it

<sup>†</sup> This article is part of the Journal of Raman Spectroscopy special issue entitled "Raman spectroscopy in art and archaeology" edited by Juan Manuel Madariaga and Danilo Bersani.

<sup>a</sup> Dipartimento di Fisica, Università della Calabria, Cubo 31C, Ponte P. Bucci, 87036 Arcavacata di Rende, Cosenza, Italy

<sup>b</sup> on leave for Università di Firenze, Polo Scientifico Sesto Fiorentino, Dipartimento di Chimica, Via della Lastruccia 3-13, Sesto F.no (FI), Italy



The perimeter area has been analysed first. Since the occurrence of a 'glue paste lining' restoration treatment has been seen (this treatment consists of positioning the original canvas on a new canvas), it is thought that the paint layer was restored as well. Moreover, it has been seen that the lining canvas was larger than the original canvas. As a matter of fact, the perimeter area of the lining canvas was covered with a special material and painted, reproducing the original chromatic tonalism. For this reason, the analyses were first performed on the lateral borders of the painting in order to find possible recent pigments.

Subsequently, spectra of the painting's internal points were collected. Several problems occurred during the investigation, as the strong fluorescence phenomenon due to the decay of the thick varnish layer. Moreover, evidences were found that several areas of the painting were retouched; therefore, it was possible to observe modern pigments instead of the originals. For this reason, the painting was lighted up with a Wood lamp which allowed to distinguish the retouched areas from the originals. In particular, the different brightness observed on the painting lighted up by a Wood lamp, are function of various factors: pigments and medium chemistry composition; time gone by after their application. The new pigments are darker than the old ones, which are more fluorescent due to chemical reactions between medium and pigment established in time.<sup>[10]</sup> In this way, retouched areas were pointed out, as well as areas with thin medium layer that allowed to optimize spectral collection. The painting was subdivided in six ideal squares, performing measurements according to the numeric increasing order of the squares (Fig. 1).

## Results and discussion

Besides the suggested dating of the painting and the attributions to specific artistic schools, no written records exist on its history,

reporting some details about the specific techniques used by the artist, as well as descriptions about particular treatments on the painting during the following centuries, in particular, the occurrence of specific restoration works.

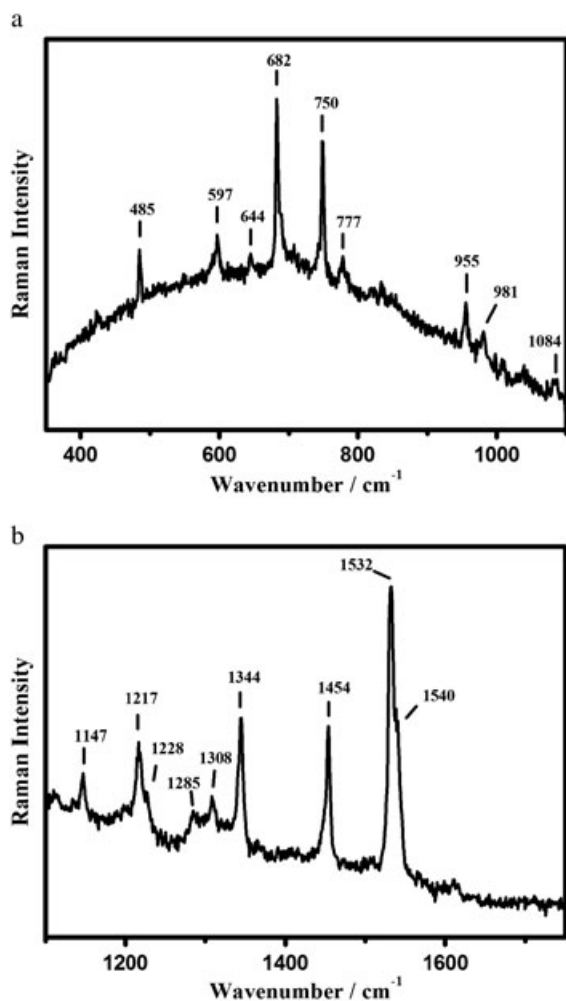
The visual inspections on the artwork reveal the restoration made on the old canvas, and the change of the frame, substituted with a greater one. Additional colours were applied to the zones around the border of the painting, to mask such changes. There is no written document reporting other restoration activities, concerning even the internal zones of the image, which can involve the application of new pigments not in use when the painting was made. These restoration works are experimentally demonstrated by the scientific investigations performed: in fact, an analysis of the fluorescence under Wood lamps reveals the existence of several areas of the painting where retouches have been performed. Thus, the micro-Raman analysis was aimed to better investigate the nature of these pigments.

All the points investigated by micro-Raman technique are shown in Fig. 1. The spectral collection started from lateral borders of the painting. Figs. 2 and 3 show representative spectra of some investigated dark areas near the borders.

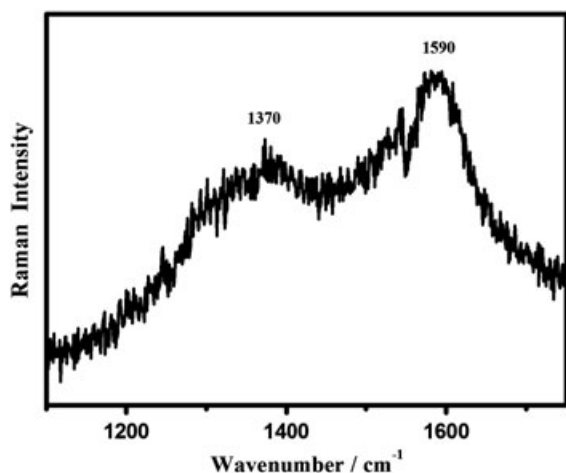
One of the most significant finding is provided by the spectrum of Fig. 2, whose spectral patterns can be found also in internal points of the painting. Some of its characteristic Raman modes, at about 683, 750, 779, 1217, 1345, 1454 and 1533  $\text{cm}^{-1}$ , have been attributed to green chlorinated copper phthalocyanine,<sup>[11,12]</sup> Moreover, Raman modes at about 486, 597, 644, 955, 980, 1148  $\text{cm}^{-1}$  show the presence of blue chlorinated copper phthalocyanine<sup>[13]</sup> (even other Raman modes, for instance the one at about 815  $\text{cm}^{-1}$ , the modes around 1300  $\text{cm}^{-1}$  and the high frequency shoulder of the 1533  $\text{cm}^{-1}$  pyrrole stretching, can be assigned to the phthalocyanine compounds, which can present polymorphism). These pigments, synthesized since 1936,<sup>[14]</sup> are chemical complexes of copper and chlorinated



**Figure 1.** Conventional division of the painting 'Rebecca at the well' in 6 different sectors, and mapping of the spots explored by micro-Raman analysis.



**Figure 2.** Representatives Raman spectra of the lateral borders, collected from dark blue–green zones, for two different spectral ranges: 350–1100  $\text{cm}^{-1}$  (a); 1100–1750  $\text{cm}^{-1}$  (b), which reveal the presence of modern organic phthalocyanine pigments.



**Figure 3.** Representative Raman spectrum of other dark zones of the lateral borders, showing the typical bands of amorphous carbon, in the 1100–1750  $\text{cm}^{-1}$  spectral range.

phthalocyanine. In particular, in the case of the phthalocyanine, a higher number of hydrogen atoms is substituted by chlorine atoms. The strong chlorine's electronegativity influences the electronic distribution of the green phthalocyanine, which is particularly stable and resistant to external agents. Chemical formulas of this pigments are:  $\text{C}_{32}\text{H}_3\text{Cl}_{13}\text{CuN}_8$  (blue phthalocyanine),  $\text{C}_{32}\text{H}_3\text{Cl}_{15}\text{CuN}_8$  (green phthalocyanine).

Well expected, on the contrary, is the spectrum of Fig. 3, collected from dark areas of the painting's lateral borders and internal points: the two Raman modes at 1370 and 1590  $\text{cm}^{-1}$  have been assigned to the well-known D and G band of amorphous carbon.<sup>[15]</sup>

Subsequently, a careful visual analysis was performed for all the zones of the painting characterized by different colours, and several sets of micro-images were obtained; an example of such set is shown in Fig. 4 for the red regions. For each image, the corresponding Raman spectrum was analysed and compared to the others collected from the same set.

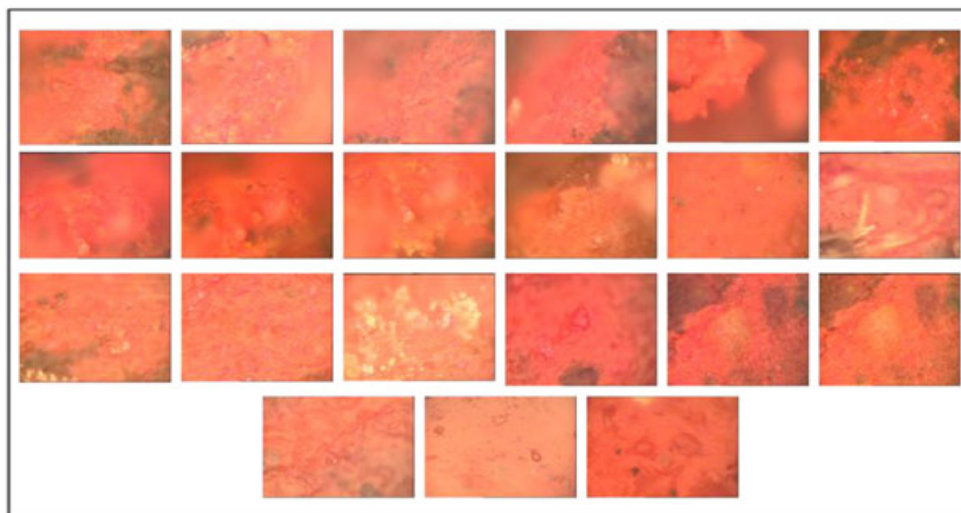
In many cases, strong Raman bands characteristic of a specific pigment can be easily identified in each spectrum, while very weak peaks can be associated to the presence of small fractions of other pigments, or even other components, whose identification is more difficult.

The most representative spectral patterns characterizing the red areas are reported in the Figs. 5 and 6 (corresponding to the micro-images of Fig. 4).

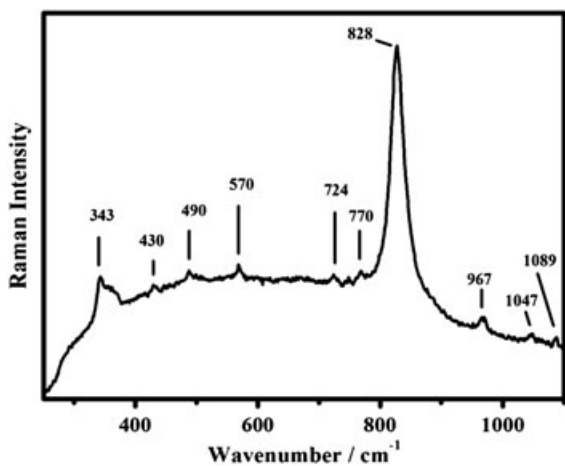
Raman features at about 343 and 828 (see Fig. 5) have been attributed to chrome yellow–orange<sup>[16]</sup> ( $\text{PbCrO}_4\cdot\text{PbO}$ ). Some of the weak modes at about 430, 490, 570, 724, 770, 967, 1047, 1089 can be tentatively attributed to phosphates and carbonates.<sup>[16]</sup> Chrome yellow–orange was introduced around about 1809 by the French chemist Louis Vaquelin, who extracted for the first time the pigment from crocoite mineral<sup>[6,17]</sup> This pigment is used in oil painting because it makes the drying process<sup>[18]</sup> of the paint layer faster. Its presence in this painting, dated to XVIII or XVII century, can indicate the occurrence of later retouches or even a restoration work.

Other pigments have been identified in the red internal zones of the painting. For instance, the Raman spectrum of Fig. 6 exhibits a quite different spectral pattern: it shows three vibrational modes at about 252, 282 and 343  $\text{cm}^{-1}$  and can be assigned to the pigment identified as 'red vermilion' ( $\text{HgS}$ )<sup>[6,19,20]</sup> This pigment, known and used since ancient times, was obtained from cinnabar (natural mineral), and it was one of the most expensive pigments. Ancient Romans, who called it *minium*, used it for parietal paintings. In particular, the most important Pompeii's families, used to paint the walls of their dwellings with red vermilion, with the purpose of boasting their richness.<sup>[21]</sup>

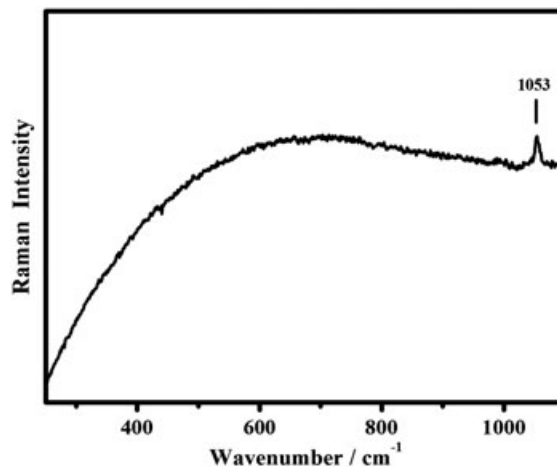
The Raman spectra collected on the white areas show a characteristic vibrational mode at 1053  $\text{cm}^{-1}$  attributed to 'lead white'<sup>[6,7]</sup>; a representative spectrum is shown in Fig. 7. This pigment, known and used since ancient times (Theophrast, Plinius and Vitruvius illustrated the wide use of the lead white for wall paintings or as siccative of linen oil in the oil painting<sup>[22]</sup>), was progressively substituted by zinc white during the half of XIX century and by titanium white in the half of XX century, due to its toxicity. Historical documents<sup>[23]</sup> say that the best quality of white lead was produced in Venice, while less precious qualities were produced in Holland and England. The lead white produces a very flexible paint layer, easy to apply and with a good opacity. For this reason, the lead white has been the most used white in the painting history, unlike the bone white which



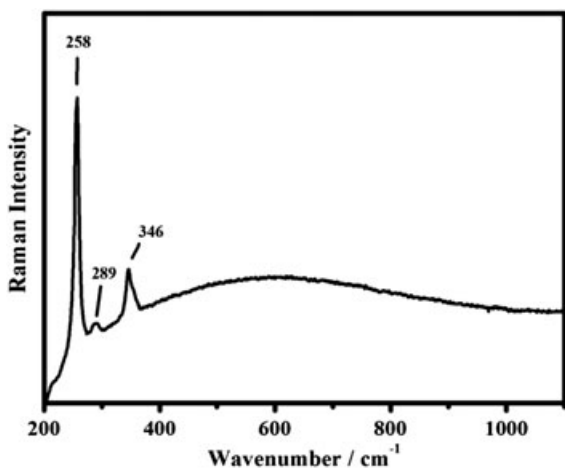
**Figure 4.** Set of optical images from of the red zone performed with the 50X objective (focal length of 15 mm).



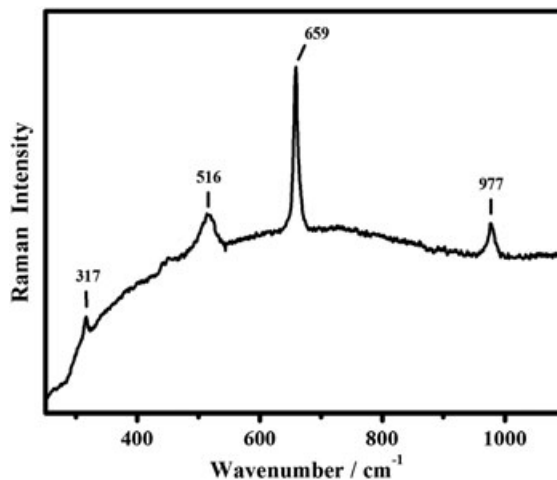
**Figure 5.** Representative Raman spectrum of 'red' internal painting's points, corresponding to prevalent yellow–orange chrome. Spectral range 250–1100  $\text{cm}^{-1}$ .



**Figure 7.** Representative Raman spectrum from white areas, attributed to lead white pigment. Spectral range 250–1100  $\text{cm}^{-1}$ .



**Figure 6.** Representative Raman spectrum of other 'red' internal spot, where is prevalent the vermilion pigment. Spectral range 200–1100  $\text{cm}^{-1}$ .



**Figure 8.** Representative Raman spectrum, from the probed yellow areas, concerning the page's yellow tunic and the horse's ornament (square 2 of Fig. 1). Spectral range 250–1100  $\text{cm}^{-1}$ . The spectral features of several pigments appear in these spectra (see text).



was extremely doughy.<sup>[24]</sup> The lead white is a basic lead carbonate ( $2\text{PbCO}_3 \cdot \text{Pb}(\text{OH})_2$ ).<sup>[6,7]</sup> In spite of the high stability of this pigment, it becomes black with the time. This behavior depends on a chemical reaction where  $\text{H}_2\text{S}$  produced by atmospheric pollution reacts with the lead white, creating  $\text{PbS}$ , also known as black galena<sup>[6,7]</sup>

The same procedure of investigation was applied for the yellow areas, concerning the page's yellow tunic and the horse's ornament (square 2 of Fig. 1). The Raman investigation provided the spectrum shown in Fig. 8: the identification of the observed Raman bands at 317, 440, 451, 516, 659 and  $977\text{ cm}^{-1}$  with well-known yellow pigments appears difficult: some frequency correspondence could be suggested with particular yellow pigments based on mixed oxide containing Pb, Sn, Sb, which had some diffusion among Italian painters in the XVII century.<sup>[25]</sup>

It is possible that the anonymous author of this painting was experimenting some similar complex oxide, but we must consider also the use of pigment mixture, making the identification even harder.

## Conclusions

In this work, some of the pigments used in the painting 'Rebecca at the well' were analysed and characterized by non-invasive Micro-Raman spectroscopic technique. This technique has been confirmed as non-invasive and effective for the diagnostic investigation. In particular, six pigments of the pictorial palette were characterized. The analysis of the white pigment showed the presence of lead white,<sup>[6,7]</sup> commonly known as 'biacca'. Among the red pigments has been identified the red vermilion,<sup>[6,10,11]</sup> a very precious pigment, known also as cinnabar (the mineral from which the pigment derives). The presence of a pigment so expensive suggests not only the importance and the richness of the purchaser, but also the fame of the artist who was able to buy such an expensive pictorial material.

The black pigment analysed has been attributed to amorphous carbon.<sup>[6]</sup> For the yellow areas, there is a problem in the identification of the exact pigments, the use of some complex oxide is tentatively proposed, taking into account the geographic and historic proximity with the complex yellow pigments based on ternary oxides containing Pb, Sn, Sb. In the areas of the artwork near the border, but also in some internal point, the presence of blue and green chlorinated phthalocyanine<sup>[2-4]</sup> has been an extremely important discovery. In fact, these pigments, synthesized since 1936, confirm the presence of retouched areas of the paint layer, seen with the Wood lamp analysis. Moreover, the presence of these pigments gives important information about the painting's restoration during the XX century, of which none historical document is available. The presence of yellow-orange chrome,<sup>[6,8,9]</sup> used since 1809, confirmed the restoration hypothesis. In particular, since the pigment was widely used

during the XIX century and rarely used during the XX century, two restoration interventions can be supposed: one during the XIX century and the other during the XX century, surely after 1936.

All these elements, deduced from micro-Raman analysis, constitute important information for the artefact history.

## Acknowledgements

The authors are indebted to dr. Tonino Sicoli, director of the MAON, for kindly providing the painting and for the help to this research.

## References

- [1] G. Compagnini, *J. Raman Spectrosc.* **2008**, *39*, 131.
- [2] R. J. H. Clark, *J. Mol. Struct.* **1995**, *347*, 417.
- [3] R. J. H. Clark, *J. Mol. Struct.* **1999**, *480-481*, 15.
- [4] K. Sakellariou, C. Miliani, A. Morresi, M. Ombelli, *J. Raman Spectrosc.* **2004**, *35*, 61–67.
- [5] P. Colombari, *J. Cult. Herit.* **2008**, *9*, e55.
- [6] M. Castriota, V. Cosco, T. Barone, G. De Santo, P. Carafa, E. Cazzanelli, *J. Raman Spectrosc.* **2008**, *39*, 295.
- [7] M. Castriota, E. Meduri, T. Barone, G. De Santo, E. Cazzanelli, *J. Raman Spectrosc.* **2008**, *39*, 284.
- [8] M. Ortega-Avilés, P. Vandenberghe, D. Tenorio, G. Murillo, M. Jimenez-Reyes, N. Gutiérrez, *Anal. Chim. Acta* **2005**, *550*, 164.
- [9] H. G. M. Edwards, T. Munshi, *J. Anal. Bioanal. Chem.* **2005**, *382*, 1398.
- [10] A. Conti, R. Cassanelli, *L'Arte. Critica e Conservazione*, Jaca Book, Milano, **1993**, p.109.
- [11] M. Bouchard, R. Rivenc, C. Menke, T. Learner, *Preserv. Sci.* **2009**, *6*, 27.
- [12] F. Schulte, K. W. Brzezinka, K. Lutzenberger, H. Stege, U. Panne, *J. Raman Spectrosc.* **2008**, *39*, 1455.
- [13] L. I. Mc Cann, K. Trentelman, T. Possley, B. Golding, *J. Raman Spectrosc.* **1999**, *30*, 121.
- [14] F. Rosi, C. Miliani, I. Borgia, B. Brunetti, A. Sgamellotti, *J. Raman Spectrosc.* **2004**, *35*, 610.
- [15] I. M. Bell, R. J. H. Clark, P. J. Gibbs, *Spectrochim. Acta*, **1997**, *53*, 2159.
- [16] L. Burgio, R. J. H. Clark, *Spectrochim. Acta*, **2001**, *57A*, 1491.
- [17] M. Sendova, V. Zhelyaskov, M. Scalera, C. Gulliford, *Archaeometry* **2007**, *49*, 655.
- [18] (<http://www.webexhibits.org/pigments/indiv/history/cryellow.html>).
- [19] T. D. Chaplin, A. Jurado-López, R. J. H. Clark, D. R. Beech, *J. Raman Spectrosc.* **2004**, *35*, 600.
- [20] D. Bersani, G. Antonioli, P. Lottici, A. Casoli, *Spectrochim. Acta*, **2003**, *59A*, 2409.
- [21] H. G. M. Edwards, D. W. Farwell, S. Rozenberg, *J. Raman Spectrosc.* **1999**, *30*, 361.
- [22] B. Wehling, P. Vandenberghe, L. Moens, R. Klockenkämper, A. Von Bohlen, G. Van Hooydonk, M. De Reu, *Microchimica Acta* **1999**, *130*, 253.
- [23] L. De Beausobre, *Introduzione generale allo studio della politica, delle finanze e del commercio*, Yverdon, Berlino, **1764**, p. 109.
- [24] B. S. Tosatti, *Trattati Medievali di tecniche artistiche*, Jaca Book, Milano, **2007**, p. 108.
- [25] S. Ruiz-Moreno, R. Perez-Pueyo, A. Gabaldon, M. J. Soneira, C. Sandalinas, *J. Cult. Herit.* **2003**, *4*, 309s.

*Chapter 6*

**GENERAL CONCLUSIONS AND PERSPECTIVES**

During this work it has been shown that Raman spectroscopy is very powerful diagnostic techniques to investigate systems which belong to the *soft matter* class defined as “complex fluids” class.

In the first three chapters a presentation of the soft material and of the technique used during this work has been given. In the chapter 4 the research activity made on the representative systems is shown. In summary, these activities lead to the following results:

- Amino acid present on the peptide skeleton, primary structure, of the GPR30 have been identified and are: tryptophan, phenylalanine, cysteine, alanine, and aspartic acid. Its secondary structure is made by disordered  $\alpha$ -helix structures.
- In biomimetic systems, it has been shown that as the temperature increases the conformation of the choline groups and of the hydrocarbon chains change from *trans* to *gauche*. In addition, it has been shown that the C-N stretching band shows a peculiar frequency shift across the transition gel-ripple-liquid crystalline phases that could even provide a useful diagnostic marker of such kind of transition.
- Polarized Raman spectroscopy has been used for the first time in order to monitor the orientation of the liquid crystal molecules in POLICRIPS holographic lattice which results to be perpendicular to the polymeric walls of the systems.
- It has been shown, that ITO coated glass subjected to a pre-annealing thermal treatment up to 600°C shows structures which can be used for surface enhancement Raman spectroscopy and a qualitative model has been proposed.
- Finally, the diagnostic studies, made on the paint, allowed the identification of the original pigments and of those used in restoration interventions which constitute important information for the artefact history.

In the future are planned deeper investigation, made also by using different laser sources, to use the resonance Raman effect, in order to investigate the interaction between the ligand and the receptor (GPR30), in order to confirm the preliminary studies which indicate that this interaction occurs between the ligand and cysteine side

chains. Furthermore, others polarized Raman investigations on POLICRYPS are planned, by changing the polarized component analyzed, to determine the order parameters,  $\langle P_2 \rangle$  and  $\langle P_4 \rangle$  of the liquid crystal molecules inside the POLICRYPS holographic grating.

Of course, the new substrate purposed will be used in order to promote the Raman scattering by the studied systems. For this reason, further consideration with regard the size control and the technological application of such structures are planned for future perspectives.